ABSTRACT

Title of Dissertation: Structural and Electrochemical Variances in Doped Lithiated Cathodes and Ionically Conducting Solid State Materials: Relationships in Solid State Electrolytes, Cathodes, and the Interfaces

Matthew Limpert, Doctor of Philosophy, 2023

Dissertation directed by: Professor Eric Wachsman,
Department of Materials Science and Engineering

Lithium-ion conducting $Li_7La_3Zr_2O_{12}$ (LLZO) garnets are being explored as a replacement for the flammable organic electrolytes used in batteries. However, LLZO garnets require high temperature sintering to densify the structure, but that microstructure and electrochemical properties can vary with lithium content as the lithium volatizes during sintering. The effects of sintering the LLZO garnet requires a detailed examination and study to determine how lithium content can affect physical properties, phase purity and density, as well as performance through ionic conductivity. Studying these parameters produced ionic conductivities above 10^{-4} S cm^{-1} in samples that had increased density by enabling liquid phase sintering through the eutectic between Al_2O_3 and Li_2O. Despite this high conductivity, the movement of Li^+ through a solid electrolyte encounters even slower kinetics through the rigid electrolyte-cathode interface to the active cathode material. A cathode for LLZO garnets requires a new design with both ionic conduction and electronic conduction pathways while reducing interfacial resistance when co-sintered. Excess lithium within

LLZO garnet reduced formation of nonconductive $LaCoO_3$ when co-sintered with the active material, $LiCoO_2$ (LCO), which enables a new completely solid-state cathode for lithium metal batteries to be designed and interfacial resistance to be minimized. LCO, however, is limited to 4.2 V to ensure long life cycle without lattice deformation. Unlocking the potential 5 V cycling with of LLZO garnet necessitated the development of a higher voltage cathode. Chlorinating the oxygen site of lithium spinel, $LiMn_2O_4$, using a citric acid method stabilizes the 2 V plateau, which increases the capacity to 180 mAhr g^{-1}, and triple doping with Co, Fe, and Ni enables customization of the properties while shifting the voltage to 5 V. The high voltage spinel and LLZO garnet enables high voltage cycling with increased safety potential enabling a pathway to a safe 400 Wh kg^{-1} cell, 150 Wh kg-1 higher than the current state of the art.

Structural and Electrochemical Variances in Doped Lithiated Cathodes and Ionically Conducting Solid State Materials: Relationships in Solid State Electrolytes, Cathodes, and the Interfaces

by

Matthew A. Limpert

Dissertation submitted to the Faculty of the Graduate School of the
University of Maryland, College Park, in partial fulfillment
of the requirements for the degree of
Doctor of Philosophy
2023

Advisory Committee:
  Professor Eric Wachsman, Chair
  Dr. Ashley Ruth
  Associate Professor Yifei Mo
  Associate Professor Isabel Lloyd
  Professor Chunsheng Wang, Dean's Representative

Dedication:

I dedicate this thesis to my family and friends who have supported me through this thesis writing process. Especially my wife who encouraged me to start this journey and never stopped supporting me. I look forward to starting the next phase of our lives when neither one of us are pursuing advanced degrees.

Acknowledgements

The research described in this dissertation was supported by funding from US Army Command, Control, Computers, Communications, Cyber, Intelligence, Surveillance, and Reconnaissance (C5ISR) Center's support through the United States Army's In-House Laboratory Innovative Research Program.

I would like to acknowledge my advisor, Dr. Eric Wachsman, who gave his scientific advice, and support through many trials while completing the work for this thesis. By joining the lab, I was able to expand my scientific horizon beyond the Army's group of scientists to solve larger energy challenges facing the present and future. I am grateful for the opportunity to learn new skills, specifically Inductively Coupled Plasma-Mass Spectrometry, which took many failed tests to feel comfortable with the results. I also appreciate the freedom you allowed me to forge the path of dissertation research, As well as the guidance that you provided to study several key areas to obtain the high quality results.

I would also like to thank Dr. Terrill Atwater, who encouraged me to take the step of going to graduate school while also working. I am grateful for both your scientific, professional, and personal advice you shared with me as I continued my journey through this process. The techniques you taught me ranged from dynamic scanning calorimetry to x-ray diffraction to cyclic voltammetry. Almost every characterization technique in this work, you either taught or explained. This was invaluable to completion of this work. I also appreciate the sound board you provided when I would have an idea that I had and providing the encouragement to follow through on a= experiments, no matter how they turned out.

I also would like to thank Army Research Labs for allowing me access to their equipment and using their supplies. I especially would like to thank Josh Allen, David Mackie, Luther Mahoney, and Jeffrey Read. Whether it was system repairs, materials, access, or just general process questions, you found a solution or provided the solution. Your help was greatly appreciated.

I also want to thank my colleagues in battery research including but not limited to: Dr. Gregory Hitz, Dr, Dennis McOwen, Dr. Lei Zhang, Jack Gritton, Dr. Yaoyu Ren, Jon O'Neill, Dr. Tanner Hamann, Ricky Hoft, and Griffin Godbey. All of Dr. Wachsman's group members who provided expertise, experimental support, and guidance all through email conversations. Their help with experiments, specifically cell cycling, XRD, and DLS, and advice on my experimental set up was invaluable. I also want to thank Annette Mateus for working through all the issues that came up for the submission process for the manuscripts.

I also want to thank my family and friends who continuously supported me continuously through the process, no matter what stage or how long it took. I am grateful you provided support and understanding through this entire process.

Finally, I would like to thank my wife, Janelle Steves, who was the first one to encourage me to embark on the journey through graduate school. Your patience as I conducted the research and writing allowed me to spend time doing the work needed to complete this dissertation. I also would thank you for your efforts while editing my many writings and teaching me parts of your writing style to improve it to where it is today. I am forever grateful for your unconditional support.

Table of Contents

List of Tables

List of Supplementary Tables

List of Figures

List of Supplementary Figures

List of Abbreviations

Å	Angstrom
APG	Aberdeen Proving Grounds
BSE	Back Scattered Electron
d	Interplannar Spacing
DEC	Diethylene Carbonate
DMC	Dimethyl Carbonate
DRT	Distribution of Relaxation Times
DSC	Differential Scanning Calorimetry
EC	Ethylene Carbonate
EDX	Electron Dispersive X-Ray
EIS	Electrochemical Impedance Spectroscopy
EV	Electric Vehicles
FEC	Fluoro Ethylene Carbonate
G_{Gb}	Grain Boundary Conductance
ICP-MS	Inductively Coupled Plasma Mass Spectrometry
IPA	Isopropanol
JT Effects	Jahn Teller Effects
Λ	Wavelength
LAGP	Lithium Aluminum Germanium Phosphate
LATP	Lithium Aluminum Titanium Phosphate
LCO	$LiCoO_2$, Lithium Cobalt Oxide
LFP	Lithium Iron Phosphate ($LiFePO_4$)
LIB	Lithium Ion Battery
LiPON	Lithium Phosphorous Oxynitride
LiSICON	Lithium Superionic Conductor
LLCZN	$Li_{6.75}La_{2.75}Ca_{0.25}Zr_{1.5}Nb_{0.5}O_{12}$
LLNO	$Li_5La_3Nb_2O_{12}$
LLZO	$Li_7La_3Zr_2O_{12}$, Lithium Garnet
LMB	Lithium Metal Battery
LMNO	$Li_xMn_{1.5}Ni_{0.5}O_4$, Lithium Spinel
LMO	$Li_xMn_2O_4$, Lithium Spinel
LTO	$Li_4Ti_5O_{12}$, Lithium Titanium Oxide
NCA	$Li_xNi_{0.8}Co_{0.15}Al_{0.05}O_2$
NMC 811	$Li_xNi_{0.8}Mn_{0.1}Co_{0.1}O_2$
Ω	Ohm
OLE	Organic Liquid Electrolyte
PTFE	Polytetratfluoroethylene
PVDF	Polyvinyldene Fluoride
PVDF-HFP	Poly(vinyldene Fluoride)-co-hexafluropropylene
PXRD	Powder X-Ray Diffraction
σ_{Bulk}	Bulk Conductivity
σ_{GB}	Grain Boundary Conductivity
σ_{Total}	Total Conductivity
ρ	Density

R_e	Electronic Resistance
$R_{electriolyte}$	Electrolyte Resistance
R_{SEI}	SEI Resistance
R_{ct}	Charge Transfer Resistance\
S	Siemens
SEI	Solid Electrolyte Interface
SEM	Scanning Electron Microscope
SSE	Solid State Electrolyte
STA	Simultaneous Thermal Analysis
TGA	Thermogravimetric Analysis
UMD	University of Maryland
V	Voltage
Wh	Watt-Hour
XRD	X-Ray Diffraction
XRF	X-Ray Fluorescence
2θ	Diffraction Angle

Chapter 1: Next Generation Lithium Metal Based Electrochemical Systems and Characterization Techniques

1.1 Overview of Batteries

Electrochemical storage devices (batteries) have been used in various forms for the past 100 years, storing energy (Watt-Hours or Whr) through electrochemical reactions that can be released on demand by the user. An electrochemical storage device (Figure 1) is typically where the reduction reaction occurs in the anode and the oxidation reaction in the cathode. This is made possible by an electrolyte that allows ion movement between the electrodes and a circuit enabling the flow of electrons, current (Amp), between the electrodes. The simplified figure of a lithium-ion battery (Figure 1) displays the operation that has allowed battery technology to become used in everyday applications.

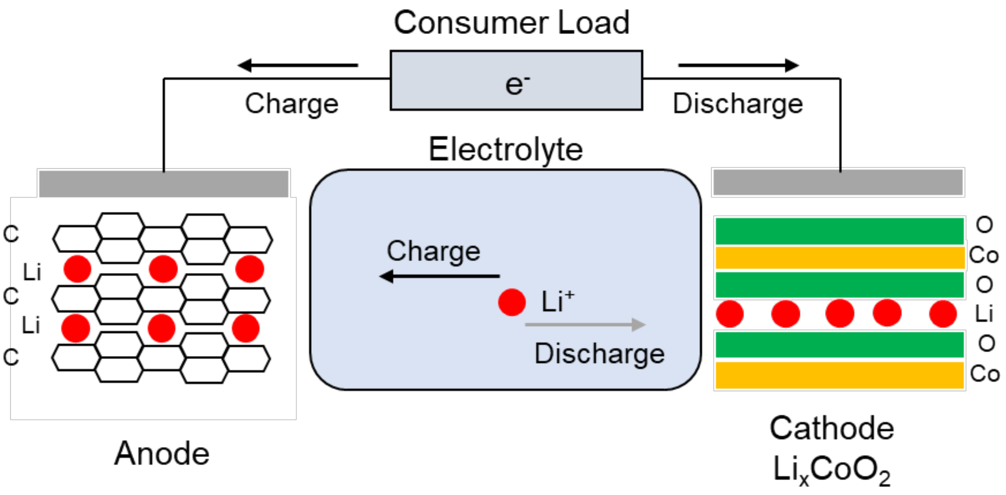

Figure 1. Diagram of a standard lithium-ion battery

Lithium-ion batteries (LIB) have grown in prevalence to be included in many everyday applications since their introduction in 1991. While considered safe since failures are one in ten million, the organic liquid electrolyte (OLE) can ignite causing catastrophic failures and injury to those using them. With the introduction and increased prevalence of electric vehicles (EV), it is imperative to not only increase safety but also energy density to meet consumer needs, which will be the focus of this work.

1.1.1 Lithium-Ion Batteries

In 1987, Goodenough reported a lithium intercalating cathode, $LiCoO_2$ (LCO), which enabled the production by the battery industry of the LIB at a specific energy of 100 Wh kg^{-1}. Through advances in engineering practices, a LIB can approach 250 Wh kg^{-1} [1] and has become the preeminent chemistry in consumer electronics over the last 20 years. Lithium-ion cells have an intercalation graphite anode and a layered cathode lattice structure, typically LCO. The intercalation process follows equations (1) and (2) when discharging, where lithium is oxidized on the cathode (1) and then reduced on the anode (2) while the electron flows through an external circuit, powering a device.

$$(1)\ Li_xCoO_2 + Li^+ + e^- \leftrightarrow LiCoO_2$$

$$(2)\ LiC_6 \leftrightarrow C_6 + Li^+ + e^-$$

With increasing usage in devices, LIB production is predicted to reach 278 gigawatt-hours per year in 2021[2]. This will put immense pressure on natural resources[3], raise safety concerns from the standard liquid electrolyte[4], and challenge recycling facilities[5] to keep up with the demand to manufacture new batteries and develop methods to handle the discarded technologies. It is critical to increase batteries' energy storage capabilities, power capabilities, life cycle, and safety to meet these future demands. For this to be possible, each part of its active material (anode, cathode, and electrolyte) will need to be optimized.

1.1.2 Anodes for Lithium Based Batteries

The anode in a commercialized LIB is where the reaction between a lithium ion and an electron occurs in graphite. Graphite has high electrochemical stability, low volumetric changes during cycling (30%)[6], and long cycle life (over 1000 cycles) at low rates. With only one lithium atom stored per six carbon atoms, there is increased weight of non-mobile material, carbon, in comparison to the active material, lithium, allowing graphite to have a capacity of 372 mAhr g^{-1}. Graphite also adds resistance to lithium-ion movement because of the small lattice spacing until lithium is inserted; limiting its rate capability. While currently an industry standard, different anode materials have garnered interest recently for electrochemical properties that improve on graphite's performance.

$Li_4Ti_5O_{12}$ (LTO) is a spinel structure and has high-rate potential as an anode because of favorable lattice spacing and 3-d channels[7] but is heavier than graphite. Likewise, LTO lowers the operating voltage (1.56 V vs lithium) from its potential difference with lithium, decreasing the gravimetric energy density. Also, LTO's electronic conductivity (energy gap 3.8 eV [8] and 3.8×10^{-6} S cm^{-1} [9]) is low and requires additional conductive carbon to overcome this deficiency without other modifications. This has also been overcome by several different methods: using nano particles to shorten Li-ion pathways, coatings to increase electrical and ionic conductivity[10,11], widening the lattice for quicker lithium intercalation[12], and designing 3-d electrodes that optimize the lithium ion and electron pathways[13]. While it is considered safer[9], it fails to increase the energy density sufficiently for most applications.

Silicon anodes can significantly increase the anode's energy density by achieving a capacity of 3600 mAhr g^{-1}, the second highest theoretical capacity for anodes, providing additional energy for most applications. However, pure silicon experiences large volumetric changes during cycling causing rapid cycle life decay from the loss of electrical connections to the conduction network[14]. Likewise, kinetic issues can occur during cycling when the solid electrolyte interphase (SEI) is formed on the anode which can degrade the electrolyte, both leading to increased resistance[15]. One method to mitigate these issues is pre-lithiating the silicon which reduces irreversible capacity loss but can also reduce the achieved capacity[16]. Similar results can be achieved through electrolyte additives, a porous anode to accommodate volume changes[17], or using nano sized silicon[18]. However, the capacity and energy density will still be lower than the theoretical capacity of a lithium metal anode.

Lithium metal is the highest capacity anode for lithium-based batteries at 3860 mAh g^{-1} while providing the lowest electrochemical potential (-3.4 V against the standard hydrogen electrode)[19]. Despite its benefits, the use of lithium metal in practice has been hindered by volumetric changes during cycling, an unstable interface in standard electrolytes, and cell failure from dendrite formation caused by uneven lithium plating[20]. Without any engineered mitigation in place, lithium plates unevenly and strips from different places leading to “dead lithium”[21]. “Dead lithium” becomes detached from the lithium metal, reducing cycle life by decreasing the lithium metal available for cycling[22]. As the cell cycles, the amount of dead lithium becomes larger and longer until finally it connects the cathode and anode; creating a short circuit. This is exacerbated in standard carbonate-based electrolytes reacting with lithium metal and forming unstable SEI layers reducing the columbic efficiency[23]. Since lithium plates unevenly and reacts with air, standard electrolytes, and water while forming lithium dendrites, its adoption has been limited[24]. However, lithium metal batteries (LMB) offer the maximum energy density for a lithium-based battery while some of these problems can be mitigated with material design changes.

The technical challenges of LMB of providing longer cycle life and higher gravimetric energy density and increasing safety are paramount to their widespread implementation. Lithium metal dendrite formation can be mitigated with surface coatings on the lithium metal such as lithium halides (LiX, X=Cl, Br, F, I) to stabilize the interface, increasing cycle life[25-28]. Solid electrolytes, i.e. replacing the liquid electrolyte with a lithium ion conducting solid, can accomplish the same thing as a lithium coating, and enable even plating of lithium[29] while also reducing safety hazards associated with standard liquid electrolytes. To increase energy density to above the standard 250 Wh kg^{-1} while increasing safety, lithium metal should be researched for implementation into solid state electrolyte rechargeable batteries. The focus of this work will be on safe SSEs, their physical, microstructural, and electrochemical properties for use in high energy density LMB.

1.1.3 Liquid Electrolytes and Safety in Lithium Based Batteries

Lithium ion cells experience failure rates at about one in ten million but with more electric vehicles being produced (5,000 to 9,000 cells per car), the amount of failures will increase because of the increase in cells usage. These failures are caused by manufacturing defects and can cause the cells to go into thermal runaway. Around 90°C, the solid electrolyte interface (SEI) can begin to exothermically decompose; starting thermal runaway[30]. Between 130°C and 150°C , exothermic reactions set in between the electrodes and electrolyte[31]. These reactions can progress from the thermal decomposition of the electrolyte, reductions of the electrolyte by the anode, and oxidation of the electrolyte by the cathode[32]. If this heat can be dissipated, the thermal runaway can be avoided but will continue if the heat cannot be removed. As the temperature increases to above 200°C, the separator melts resulting in shorting of the electrodes, the cathode begins decomposing and releasing oxygen, and finally electrolyte combustion[33, 34]. This can occur under abuse conditions or under normal conditions if there is a defect within the cell[35]. Research has been performed to develop drop-in replacements for lithium-ion cells.

Additives into the electrolyte electrolytes are designed to stop one of the thermal runaway reactions and avoid cell failure, mostly through removing the activated H· or HO· formed during decomposition of the SEI[36]. The principal being the additives releases a chemical at a temperature to reactive with the activated chemicals[37]. This can be flurocynoesters[38], resorcinol bis(diphenyl phosphate)[39], fluro ethylene carbonates[40], and modified carbene adducts[41] are just a few types of additives being explored. The additives can shutdown the thermal runaway but most would need to be modified in order to operate with lithium metal and do not remove the flammable organic liquid. A class of electrolytes that can remove that potential safety barrier are ionic liquids.

Ionic liquids as a class of electrolytes that are molten salts with a melting point well below room temperature, are typically nonflammable, have high chemical stability, and wide electrochemical stability[42]. There are two classes of ionic liquids: aprotic ionic liquids and protic ionic liquids[43]. The main difference resides in the availability of a proton on the cation in the protic ionic liquid. The anions in aprotic ionic liquids are typically the anions associated with lithium salts used with OLEs such as BF_4^-, PF_6^- ,bis(trifluoromethansulfonyl)imide, and bis(fluorosulfonyl)imide[44]. These can be combined with imidalzolium, pyridinium, pyrrolidinium, and piperifinium and with the introduction of the lithium salt is a liquid with ionic conductivity at room temperature[45]. Protic ionic liquids are easier to synthesize from neutralization of an acid and a base and thus cheaper[46]. The lithium salt is then added to increase ionic conductivity when fabricated into a full cell. While promising, more work is required in order to have longer cycle life and limit dendritic failures.

1.1.**4** Solid State Electrolytes for Next Generation Batteries

Solid state electrolytes (SSE) for LMB are lithium-ion conducting solids that can replace the OLEs in LIB. Several lithium-ion conducting solid ceramic electrolytes have been studied exhibiting high ionic conductivity on the order of magnitude of 10^{-3}-10^{-4} S cm^{-1} or higher at room temperature, as well as electrochemical stability and are chemically inert to side reactions with lithium metal or standard cathodes such as LCO[47]. The investigated SSEs include A-cation deficient perovskite-type ($La_{(1-x)/3}Li_xBO_3$)[48], Li_3N[49], Li Super Ionic Conductor (LiSICON) and thio-LiSICON ($Li_{4-2x}Zn_xGeS_4$)[50], and LLZO garnet ($Li_7La_3Zr_2O_{12}$). However, each type has its drawbacks that limits its potential applicability.

A-cation deficient perovskite-type SSE, such as Li_3N, are structurally complicated due to disordering on the B-site, like with the addition of Co and Fe[51,52]. However, each may contribute to long range ordering on the A-site[53]. That long range ordering restricts this class of SSE's potential use despite the reported conductivity of 10^{-4} S cm^{-1} [54,55]. There are also two structures of this material in commercial powders, P6*Immm* and $P6_3$*Immc*, and one is not stable at room temperature making processing difficult and it possesses a low decomposition voltage (0.45 V)[56], further limiting its widespread application.

Lithium phosphorus oxynitride (LiPON) is another promising class of lithium based solid electrolytes whose conduction mechanism is not well understood despite being studied since 1992 [57]. The basic chemical formulation involves a lithium group with a phosphorous oxinitride, PO_4N. LiPON's conductivity of 0.0064 mS cm^{-1} as well as several structural stability issues limits the appeal outside of its use in microelectronics[58]. While promising with the ability to create thin layers, scale up and the limited conductivity make it a less promising candidate for widespread use in EV markets.

Oxygen and sulfur based solid electrolytes offer wider voltage stability and higher conductivity making them more suited for the higher power required in commercial markets. $Li_{2+2x}Zn_{1-x}GeO_4$ follows a LiSICON structure, reacts with lithium metal, and has reached conductivities of 10^{-6} S cm^{-1}, two orders of magnitude less than what is desired for LIB[59,60]. Contrastingly, lithium aluminum germanium phosphate (LAGP) and lithium aluminum titanium phosphate (LATP) achieve conductivities of 10^{-3} to 10^{-4} S cm^{-1}. LATP and LAGP follow a LiSICON structure where TiO_6 (or GeO_6) form the octahedral, PO_4, the tetrahedral, and lithium substructure with vacancies allowing for higher lithium conduction. Thio-LiSICON changes the LiSICON structure to a sulfide and yields an improved conductivity of 10^{-3} S cm^{-1} due to the more polarized S^{-2} replacing the O^{-2} [61].However, lithium metal is unstable as the titanium or germanium reduces with time while its rigidity severely increases cathode interfacial resistance[62], making manufacturing less than ideal. These electrolytes above have potential with more research, but none are as balanced in terms of benefits and negatives as lithium-ion conducting garnet.

1.1.4.1 Lithium Conducting Garnet Solid Electrolytes

The lithium-ion conducting garnet structure was first reported in 2003 by Thangadurai et al. with lithium occupying the sub lattice of the garnet structure[63]. The initial reported structure was $Li_5La_3M_2O_{12}$ (M=Nb,Ta) (LLNO), measured a lattice parameter of ~12.8 Å, and obtained a conductivity of ~10^{-6} S cm^{-1}. In 2007,Thangadurai, Weppner, and Murugan then reported on a highly stuffed lithium-ion conducting garnet SSE achieving a conductivity of 1.90×10^{-4} S cm^{-1} with the formula $Li_7La_3Zr_2O_{12}$ (LLZO)[64]. This highly stuffed structure was the lower conductivity tetragonal phase (~10^{-6} S cm^{-1}) at room temperature but a highly conductive, disordered cubic phase (Figure 2b) at temperatures above 700°C, which has a partially occupied lithium substructure[65]. The higher conductivity cubic phase was stabilized at room temperature by dopants to create lithium disorder which exhibited a high bulk conductivity, ~10^{-3} S cm^{-1} [64]. Niobium is a popular choice to stabilize the cubic phase and increase the lattice parameter which correlates to increasing Li^+ conduction[66].

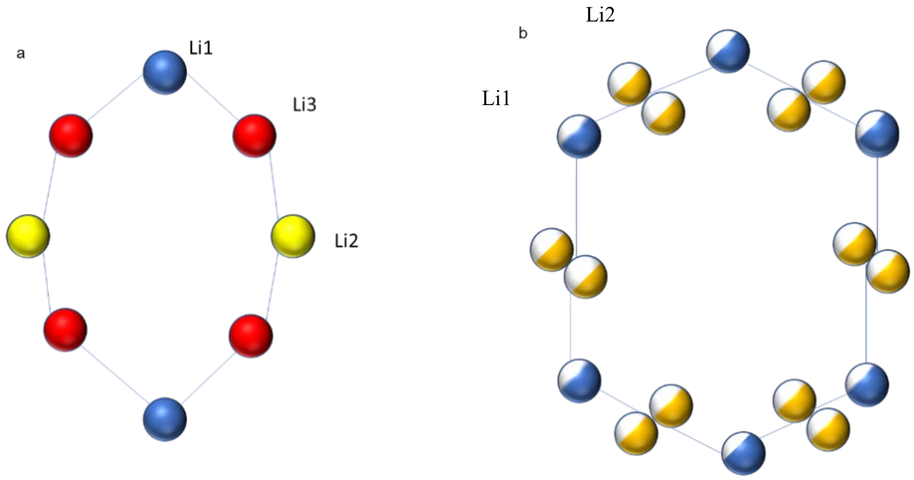

Figure 2a. LLZO garnet tetragonal with filled lithium sites. **Figure 2b.** LLZO cubic structure with partially filled lithium sites

Increasing the lattice parameter through increasing lithium content in the lattice and vacancy concentration increases lithium-ion conductivity[67,68]. Lithium content, likewise, is crucial to obtaining a dense microstructure with the correct, disordered LLZO as there are multiple phases (LLNO and LLZO) and nonconductive phases (i.e. $La_2Zr_2O_7$) that can form depending on the lithium concentration. The total conductivity, though, is a function of bulk (majority LLZO phase) and grain boundary conductivity (density and phase purity), which both are functions of lithium content. Studying the effects of lithium content should enable a deeper understanding of the role lithium content has on the three physical properties and thus the total conductivity. This will be discussed more in depth in Chapter 2 as a study on the impacts of added lithium on LLZO type electrolytes for LMB.

LLZO garnets have also been shown to be stable against lithium metal, stop dendrites when dense, and have a wide voltage range (up to 6 V), making it attractive for several high voltage cathode materials[69]. The potential cathode materials are diverse, and each has its potential but also deficiencies for next generation LMB.

1.1.5 Oxide Type High Voltage Lithium Cathodes

The final active part of an electrochemical cell is the positive electrode, the cathode. High energy, transition metal cathode materials in use in lithium-ion batteries (Table 1) follows the structure of $LiBO_2$ where B is Ni, Al, Co, or Mn with $LiCoO_2$ (LCO) being common. The lithium, oxygen, and transition metal atoms occupy sites on alternating layers with lithium intercalating between the oxygen layers. The theoretical specific capacity of LCO is 274 mAh g^{-1} but the practical reversible capacity is 145 mAh g^{-1} due to structural deformation, cracking, and loss of electrode connectivity during deep cycling (>4.2 V or up to 0.5 Li per mole) [70,71]. This limits either its cycle life (charging above 4.2 V) or useable capacity by limiting charging to 4.2 V. However, other cathodes have been developed that can meet future energy demand.

Material	**Structure**	**Potential vs. Li/Li+, average V**	**Specific Capacity (mAhr g^{-1})**	**Reference**
LCO	Layered	3.9	140	72
$LiNi_{0.8}Co_{0.1}Al_{0.1}O_2$ (NCA)	Layered	3.8	180-200	72
$LiNi_{0.33}Mn_{0.33}Co_{0.33}O_2$ (NMC 333)	Layered	3.8	160-170	72
NMC 811	Layered	3.8	200	73
$LiMn_2O_4$ (LMO)	Spinel	4.1	120	74
$LiNi_{0.5}Mn_{1.80}O_4$ (LNMO)	Spinel	4.7	140	74
$LiFePO_4$ (LFP)	Olivine	3.45	150-170	72

Table 1. List of Specific Capacity and Specific Energy Density of Widely Used Cathode Materials

LCO is similar in lattice structure to two other commercial cathodes, $Li_xNi_{0.8}Mn_{0.1}Co_{0.1}O_2$ (NMC 811) and $Li_xNi_{0.8}Co_{0.15}Al_{0.05}O_2$ (NCA) with the former having over 200 mAhr g^{-1} and the latter over 150 mAhr g^{-1}. However, each targets a different consumer market for their respective electrochemical properties with NMC for electronics due to the long stable cycle life and NCA for high power applications such as power tools[75]. The nickel in both NMC and NCA structures increases the voltage and enables more lithium to be extracted, manganese stabilizes the structure for longer cycle life, and the aluminum increases the lattice parameter, which enables higher rates. These types of higher voltage cathodes are candidates for next generation LMB using LLZO garnet type electrolytes but must overcome rigid, high resistance, connections at the cathode-SSE interface.

These types of layered cathodes due suffer from various issues depending on the cathode. LCO was the first cathode introduced but is limited to 4.2 V on charge and cobalt can account for 25 to 30% of a batteries overall cost[76]. This cost burden makes other high nickel content cathodes more attractive. NCA was introduced for power tools because of its high-rate capability from the larger lattice spacing[77] but can have degraded cycle life from the high nickel content[78]. NMC 811 also suffers from this low cycle life because of microcracks formed during cycling that results in nickel dissolution[79].

1.1.5.1 Interfacial Issues between Lithium Garnet and High Voltage Oxide Cathodes

Solid state electrolytes require stable interfaces for operation between high voltage (>4 V) cathodes and lithium metal in order to increase the state-of-the-art lithium-based batteries above 400 Wh kg^{-1}. The interface, however, between LLZO garnet and electrodes contributes large amounts of interfacial resistance that have slowed LLZO development as an SSE for LMB[80]. This interfacial resistance can be produced by the microstructure differences, volume changes during cycling, and lattice mismatch between the garnet and the electrodes[81]. Each electrode has these interfacial issues and each has various mitigation strategies to reduce interfacial resistance.

The interfacial impedance between LLZO garnet and lithium metal anodes is largely from the rigid anode/electrolyte surface, in the range of 10^2-10^3 Ω cm^2 [82]. This is further complicated by nonconductive species such as LiOH or Li_2CO_3 forming on LLZO's surface when in contact with air, specifically the moisture in air[83]. Likewise, the poor wettability of molten lithium does not assist in reducing these rigid solid-solid interfacial problems. However, the reaction between LLZO garnet and lithium is limited except in conditions above 300°C[84]. Over the last few years, reducing anode interfacial impedance has been of utmost importance towards making functional solid-state cells[85] with success in reducing the interfacial resistance to 1 Ω cm^2.

The interfacial impedance on the cathode introduces the same types of issues as the anode that also requires mitigation to make an operational electrochemical cell. Uniformity of the cathode-solid interface can reduce the interfacial impedance when the cathode matches well with the solid electrolyte[86]. However, this is hampered by the volume changes in the cathode during cycling and the loss of connectivity with LLZO causing a reduction in cycle life[87]. New designs for the cathode-solid electrolyte interface will need to be researched and engineered for solid state electrolytes to mitigate cycle life loss and reduce interfacial impedance.

Minimizing the impedance between LLZO garnet and the cathode is documented and crucial for high energy cell development[88]. High temperature processing through co-sintering the two dissimilar materials together can reduce the interfacial impedance by reducing distance between materials and provide both an ionic and electronic conduction network for cycling[89]. This can create a dense composite cathode where the solid electrolyte and composite cathode will have no physical distance between them and a uniform interface, thus reducing resistance. However, the two phases react at traditional LLZO sintering temperatures from the loss of lithium and oxygen, specifically at temperatures greater than 1050°C[90]. A study on techniques to reduce this reaction for co-sintering LCO and LLZO garnet should diminish the impedance and enable solid state cycling. The interface and technique will be studied in Chapter 3 to explore a potential path forward for co-sintering but will be limited to 4.2 V on charge because of the limitations of LCO.

1.1.5.2 Lithium Spinel Cathodes for Next Generation, High Capacity, High Voltage Cathode

LLZO garnet can operate at voltages greater than 4.5 V and one of the cathodes that can operate at those voltages is doped lithium spinel. Lithium spinel, $Li_xMn_2O_4$ (LMO) (120 mAhr g^{-1}), follows a LiA_2O_4 structure, is low cost, and environmentally friendly alternative to LCO[91]. LMO can be modified through dopants to increase the operating voltage and capacity to compete against the higher nickel content-layered cathodes like NMC 811 and NCA. Nickel doping in spinel, $Li_aMn_{1.5}Ni_{0.5}O_4$ (LMNO), has been used to increase the operational voltage to 4.75 V, which increases the cathode energy[92]. This increase in operating voltage is due to the difference between the electronic band structures of nickel and manganese. To increase the capacity further, lithium has been reported to occupy vacant tetrahedral sites to double the capacity to 240 mAhr g^{-1} but with reduced cycle life[93]. Enhancing the life cycle and maintaining the capacity in the higher capacity lithium spinel is critical for next generation lithium-ion batteries.

Lattice distortions, such as Jahn Teller (JT) effects during charging and discharging reduce lithium pathways, and manganese dissolution both limit cycle life when x approaches 0[94]. JT effects can be reduced when the transition metal sites are disordered and form the Fd-3m phase rather than the ordered $P4_332$[95]. Anion doping produces this disorder on the transition metal sites and increases structural stability at higher voltages[96]. LMO spinels with a disordered structure reduce JT effects and increased cycle life can be achieved by anion doping.

Doping and the ordering of cations[97,98], oxygen vacancies[99], and surface morphology[100] are just a couple factors that affect the structural, microstructure, and electrochemical properties of LMO cathodes. Nickel and cobalt are commonly doped on the manganese site to increase operational voltage (4.75 V from 4 V) and enhance rate capabilities[101,102]. While, chlorine doping on the oxygen site increases charge retention, temperature range, capacity, cycle life, and the voltage window[103,104]. Inserting "B site" dopants (Ni, Fe, Co, etc.) into LMO structure with chlorine doping the oxygen site will be explored in Chapter 4 by adding three transition metal dopants and a chlorine dopant to the manganese spinel structure. This spinel structure will then be used with a LLZO electrolyte to determine the operational feasibility of 5 V operation in a LMB.

1.1.6 Research Objectives for the Next Generation Lithium Based Battery

The change from an OLE to an SSE can increase the volumetric and gravimetric energy density of LMB (Figure 3a and b) by enabling the use of lithium metal and reducing the size of the separator layer. LLZO type SSEs can be utilized for high energy density, next generation lithium-based batteries, however, they require a more complete understanding of the importance of lithium content on its physical and electrochemical properties.

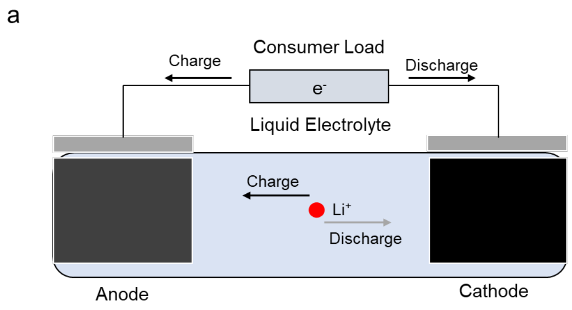

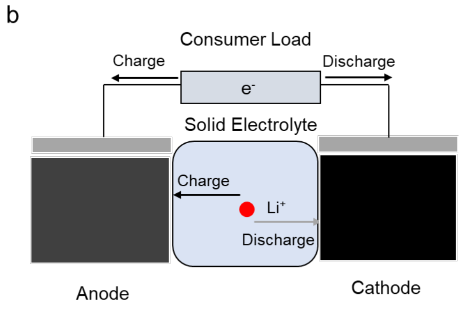

Figure 3a. Diagram of typical LIB. **Figure 3b.** Diagram of SSE LMB.

Lithium content of LLZO changes depending on the sintering conditions and that content can determine the phase purity, which greatly affects the final product's physical and electrochemical properties[105]. Bulk conductivity is a function of phase purity, while grain boundary conductance is a function of percent density and percent density is a function of phase purity and lithium content. The goal of the first section (Chapter 2) will be to determine the physical and electrochemical property shifts caused by changing lithium content during both calcination and sintering.

The focus of the next section (Chapter 3) will be an investigation on co-sintering to reduce the interfacial impedance between the cathode and LLZO garnet. Through computational analysis, lithium and oxygen losses in both phases have been shown to increase the reactivity at co-sintering temperatures[106]. Lithium and oxygen loss compensation by engineering excess lithium onto the LLZO garnet will be considered to reduce secondary phase formation. By co-sintering the SSE and cathode, the changing electrochemical properties of the composite cathode will be quantified. The goal of the second section of work will be to stabilize both phases, determine interfacial resistance, maintain LCO's electrochemical performance, and demonstrate the ability to cycle in a co-sintered cell.

Lastly, lithium spinel offers a framework for a high voltage, high-capacity cathode material that can be paired with LLZO garnet (Chapter 4). Creating and studying the increased capacity through anion doping to allow a second lithium to be inserted into the structure will be the third and final part of the research reported. The goal was to increase the capacity to 180 mAhr g^{-1} and add three separate transition metal dopants into the LMO structure to increase the operating voltage and determine the electrochemical properties of various dopants. The doped spinel will showcase the ability of the LMO structure to be tailored for high rates and high energy applications. Finally, the doped spinel will be utilized with LLZO garnet and lithium metal in a full cell to showcase the potential next generation type lithium-based battery.

Kinetics are the driving force of several of these studies. For example, in sintering processes the solid state reaction kinetics determine the degree of densification and is based on lithium content. However, the lithium vaporization at sintering temperatures is based on thermodynamic properties of Li_2O that will limit the kinetic sintering driver. This vaporization process will also drive co-sintering as lithium and oxygen are lost in both LLZO and LCO species. Finally, all of the parts (composite cathode, solid electrolyte, and lithium metal) packaged together in a full electrochemical cell will involve electrochemical kinetics of the lithium ion and electron. Both are key features needed to ensure high energy density, rate capability, and life cycle of the cell.

1.2 Kinetics of Processes Used in This Work

1.2.1 Calcination and Sintering Kinetics

The LLZO garnet used in this work was made using a solid-state synthesis, which is an inexpensive option and, outside of the precursors, only involves solvents for mixing. The method used requires the precursor solids to be well mixed, an appropriate temperature applied to below the materials melting point, and enough time at the required temperature for decomposition of all the reactants to form the product. The reactants used to form the base LLZO garnet is expressed in Eq. 3.

$$(3)\ 14LiOH + 3La_2O_3 + 3Zr_2O \rightarrow 2Li_7La_3Zr_2O_{12}$$

This reaction, however, is complicated by lithium loss through vaporization of Li_2O at calcination and sintering temperatures[107], which is typically overcome by adding 10% excess lithium to the precursor mixture but is just one factor that can influence the solid-state reaction.

Several other factors influencing solid state reactions are contact between solids, rate of diffusion (temperature dependent), and rate of nucleation[108]. The larger surface area of the particles allows for more contact area between grains for reaction, which can be overcome by increasing the rate of diffusion of the species which will rise with temperature. When the grains start to bind together, nucleation will become dominant and form a single unit. The three factors (particle size, temperature, and time) will determine the time required at the reaction temperature. These become important as more lithium from LLZO volatizes with time which will cause secondary phases to form[109]. This secondary phase formation becomes critical to avoid especially when solid electrolytes are formed into single layers through sintering.

Sintering is the reduction of free energy between particles where they are bound to one another to form a larger structure at high temperatures when the particles are in close contact with one another. The high processing temperature activates atomic movement and enables the grains to have the necessary energy to freely move making it a parameter dictating densification, along with the time spent at temperature. LLZO garnet's density needs to be optimized through its sintering conditions in order to increase lithium ionic conductivity while minimizing Li_2O losses.

The sintering process for LLZO garnet, like most ceramics, occurs over several stages: initial, intermediate, and final. Initial stages involve connection between two particles, which is referred to as "necking" but does not result in any volume decreases. Intermediate stages increase the neck width and the particles become closer; increasing the density to 70 to 90% of its theoretical density[110]. The final stage forms a single larger structure where the density reaches 100% but this step takes place on an infinite time scale. These processes can be assisted or hindered through different mechanisms depending on the powder's composition, which will become crucial during LLZO's sintering.

There are several different considerations for the SSE sintering in this work such as liquid phase sintering, coarsening, and, specifically for this work, lithium loss at high temperature. Liquid phase sintering involves a sintering species or added sintering aid that melts at the sintering temperature which drives the densification from the capillary energy of the system. Conversely, the coarsening mechanisms occur during sintering when the activation energy needed to breech densification reactions is not met, creating more necking. These mechanisms take place during the intermediate stages and without additional temperature, no amount of time will complete densification[110]. The last consideration is mass loss and loss of kinetic drivers as certain materials in the system boil or volatilize which will decrease phase purity. The typical sintering process for LLZO involves a mother powder or lithium source to reduce lithium losses (Figure 4). This system will require enough lithium to ensure it has fast kinetics to densify before lithium losses become too great and secondary phases are formed. The two considerations, time and temperature, will be studied in LLZO type garnet systems to determine the effect of lithium loss.

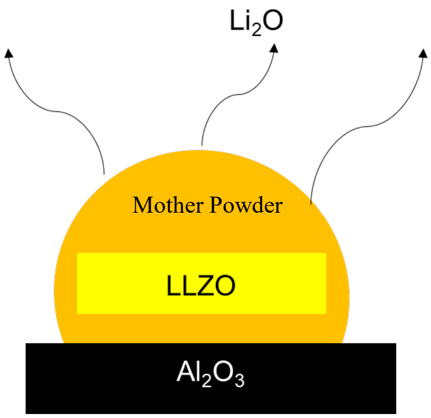

Figure 4. LLZO garnet typical sintering set up where a green body is placed in a bed of mother powder and Li_2O vaporization occurs at high temperatures

1.2.2 Kinetics of Electrochemical Cells

After sintering, solid-state electrolytes will be packaged into a full electrochemical cell with two electrodes. The ionic resistance within an electrochemical cell during operation can be fragmented into several major components: Li ion intercalation into the electrode or plating/stripping onto lithium metal, desolvating into and out of the electrolyte, movement through the electrolyte, transport through the solid electrolyte interface (SEI) layer, and the transfer into the active electrode's lattice[111]. This is coupled with the electron movement through the composite cathode to the active material where the Li^+ is reacted with the electron and stored in the active material. For faster rates, the transfer from the electrolyte to the electrode and through the SEI layer are the critical steps that can enhance Li-ion rate capability, meaning the rates will be limited unless the SEI and the charge transfer are maximized for Li^+ transfer[111]. This can be expressed in Eq. 4 in terms of separate resistances and Figure 5 shows it graphically:

$$(4)\quad R_{Cell} = R_e + R_{electrolyte} + R_{SEI} + R_{Ct}$$

This defines R_e as the electronic resistance, $R_{electrolyte}$ is the resistance of the electrolyte, R_{SEI} is the resistance of the SEI layer, and R_{ct} is the charge transfer between the SEI layer and the electrodes. Each step has its own processes that can be studied and optimized in an electrochemical cell.

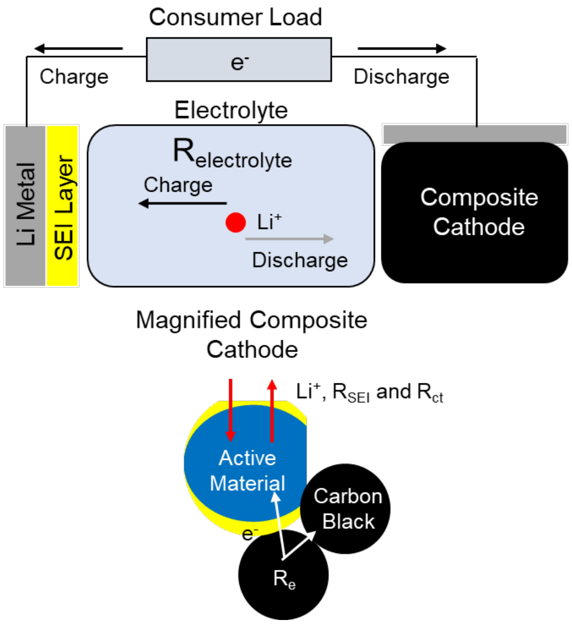

Figure 5. Resistances within a LMB

The desolvating step involves Li becoming a Li^+ before entering the SEI layer where it has been determined that at both interfaces this step is the rate limiting step in charge transfer kinetics even more so than the electrolyte[112]. This step is almost inescapable in electrochemical cells as the process involves the charge transfer over a barrier between two layers with two separate activation energies. The activation energy of the desolvating process was measured at ~50 kJ mol^{-1} for electrolyte/$LiFePO_4$ cathode interface[113]. However in a different system with $LiMn_2O_4$ as the active material, the ion transfer reaction was found to be 23-25 kJ mol^{-1} in an aqueous electrolyte system[114]. These results suggest the cathode-SEI may be rate limiting once the electrolyte layer is optimized for transport and will be different for each electrolyte/electrode system. The LLZO-cathode interface may be the rate limiting step in optimized SSE systems and will be studied through the interfacial resistance after co-sintering.

LLZO garnet has been successfully utilized in cells by several different groups[115,116], but lithium losses during sintering remains a concern[117]. Understanding this issue and relating it to structural losses with lithium loss is critical to minimizing kinetic issues in thin, sintered electrolytes, $R_{Electrolyte}$ (Chapter 2). Likewise, the de-solvating movement of Li^+ from the solid electrolyte into the cathode will need to be investigated, R_{SEI} and R_{Ct}. One way that has been used to limit de-solvating resistance and interfacial impedance has been co-sintering, which will be addressed using excess lithium to mitigate nonconductive secondary phase formation (Chapter 3). Finally, the active material of the cathode itself also can play a role in reducing these issues. By and by creating submicron grains to enable quicker lithium movement, a lower R_{Ct} can be achieved (Chapter 4). The work in this thesis will be presented through increasing conductivity in LLZO garnets by investigating lithium losses ($R_{Electrolyte}$) (Chapter 2), increasing conductivity at the interface through co-sintering (R_{SEI} and R_{Ct}) (Chapter 3), and developing a submicron spinel-type cathode that can improve the rate capacity of next generation lithium batteries (R_{Ct}) (Chapter 4). All of these parts will involve processes and experiments that will be described in the upcoming section.

1.3 Other Processes and Experimentation Used in This Work

1.3.1 Pechini Method (Citric Acid) Method

Pechini Method is a sol gel process that produces a sub-micron sized powder and, in this work, will be used to create the LMO type cathode material. The method involves separate steps: forming a chelate between metal cations in the form of precursors, which are dissolved in a solution, with a hydroxyl carboxylic acid[118]. The mixture is then cross linked with an added aid, creating a gel through esterification. After the mixture is heated to greater than 200°C, which breaks down the structure through pyrolysis (charring), the char is then be calcined at the appropriate temperature to react the carbon-metal mixture and form the final product. In this work, the final product will be a modified LMO spinel.

The modified Pechini method used in this work included stoichiometric amounts of lithium nitrate (Sigma Aldrich 99.99%<) plus an excess of 15% to compensate for lithium loss, manganese nitrate(Sigma Aldrich 98%<), lithium chloride (Sigma Aldrich 99.99%<) (replaces the 15% excess Li when added), cobalt nitrate (Sigma Aldrich 99.999%<), nickel nitrate hexahydrate (Sigma Aldrich 99.999%<), and iron nitrate nonahydrate (Alfa Aesar 98%<) mixed in methanol (Fischer Scientific 99.99%) having the stoichiometry of the following: $Li_aCo_xFe_yNi_zMn_{2-x-y-z}O_{4-b}Cl_b$ ($x<0.05$, $y<0.05$, $z<0.05$, $b<0.15$, and $a=1$)). The mixture was vigorously stirred, then citric acid was added in a 1.6:1 mol ratio with metal ions during mixing. The mixture was stirred until all the citric acid was dissolved. Finally, ethylene glycol (Sigma Aldrich 99.8%) was added in a 0.53:1 mol ratio of ethylene glycol to mol of metal ions before being mixed and simultaneously heated to evaporate the water at 100°C, completing trans esterification. Ethylene glycol has been used to better disperse materials with ions and promote polymerization of metal-citrate mixtures because of the added OH group[119]. The mixture was then heated to the pyrolysis temperature of 300°C to decompose citrate complex precursor. The remaining precursor was ground and calcined at 650°C for 10 hours in air with a heating/cooling rate of 10°C min^{-1} to limit chlorine loss and form the LMO spinel structure.

1.3.2 Sintering LLZO Garnet

Sintering processes have been previously described in the kinetics section. Sintered pellets for the work presented were prepared by pressing calcined powder into 12 mm diameter pellets. The pellets were then placed in an Al_2O_3 or MgO crucible, covered in 0.5 g of their mother powder before being placed in a furnace and heated to the specified furnace temperature. The crucible, variation in temperature, and time will be specified for each sintering experiment with the heating/cooling rate being 3°C min^{-1} for each experiment.

1.3.3 X-Ray Diffraction

X-Ray diffraction (XRD) is a materials characterization technique, which can determine lattice structure information and identify phases. X-rays are generated from the sample by the scattering of electrons in the atom, in which the strength of the signal depends on the position of the detector and the relative phase shift (i.e. the lattice structure detected will depend on the detector angle)[120]. The data obtained can confirm phase purity, lattice deformation from dopants, and crystallite sizes.

The principles for XRD detection and analysis are described by the Bragg Equation, Eq. 5. Where, XRD is in terms of a reflection of the sets of lattice planes by the angle with n as the multiple of the wavelength, λ is the wavelength, d is inter planar spacing of parallel lattice planes, and 2Θ is the diffraction angle.

$$(5)\ n\lambda = 2d\ sin\theta$$

While simplified, this principal equation is the basis for XRD, enables results to have phases prescribed to the diffraction peaks, and allows for important structural information, for example the lattice parameter, to be calculated[121].

The x-ray interaction with the sample's lattice is the crucial part of XRD. When an x-ray interacts with an atom, the electrons in the atom decelerate which emits a characteristic x-ray (scattering). If these atoms are in a structured plane as seen in Figure 6, a wave, referred to as the diffraction beam is generated. Waves that are in phase and do not interfere with one another is called diffraction, which correspond to the planes of a lattice (depending on the beam angle). The planes of the lattice are represented by the wavelength, which are then displayed by intensity vs. the angle of diffraction, Θ , the resultant diffraction peaks correspond to the plane.

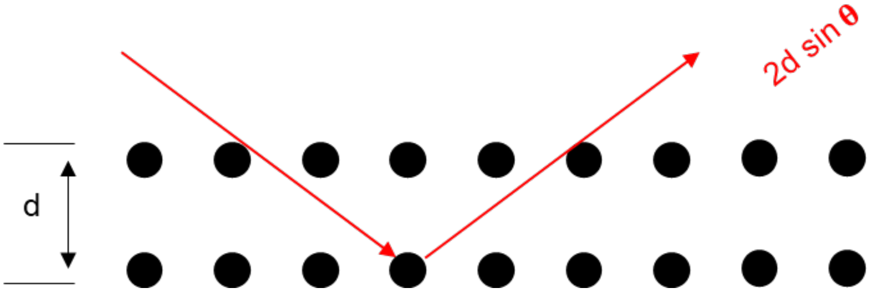

Figure 6. Graphical interpretation of Bragg's law

Samples of calcined powder or sintered pellets in this work were prepared for XRD by grounding the sample into a fine powder using a mortar and pestle before being placed into the XRD sample holder. A microscope glass slide was then used to flatten the sample before being placed into the XRD. The XRD used in this work was Bruker D8 Advance, Cu-kα and provided the basis for Rietveld Refinement calculations of lattice parameters and phase purity.

Rietveld Refinement are calculations performed to compute the lattice parameter and phase purity by fitting the XRD diffraction pattern through a complex minimization procedure. The refinement considers four main properties of the pattern: peak shape, peak width, preferred orientation, and method of calculation[122]. Peak shape depends on the deviation from a Gaussian curve and the refinement take these changes into account to minimize errors. While, peak width, full width at half maximum, is a function of the diffraction angle that will be used to fit an equation as part of refinement to find adjustable parameters. Rietveld refinement was performed on all the XRD patterns generated for this work to determine lattice parameters and phase percent.

1.3.4 X-Ray Florescence

X-ray fluorescence (XRF) chemical characterization was performed on the LMO samples calcined in this work. X-rays from the sample are generated through ionization caused by the x-rays generated from the machine and this ionization process creates characteristic x-rays from the sample (Figure 7). They are then detected in the same way as electron dispersive spectroscopy (EDS)[123]. With high enough energy, the machine generated x-ray can dislodge an electron in an orbital of the sample, creating a hole, and an outer electron falls into the hole to restore equilibrium. This act creates an x-ray, which is referred to as x-ray fluorescence. The electron orbitals of each element have a characteristic energy since each element has different orbitals filled to differing quantities[124]. In this work, this allowed for elemental amounts to be determined.

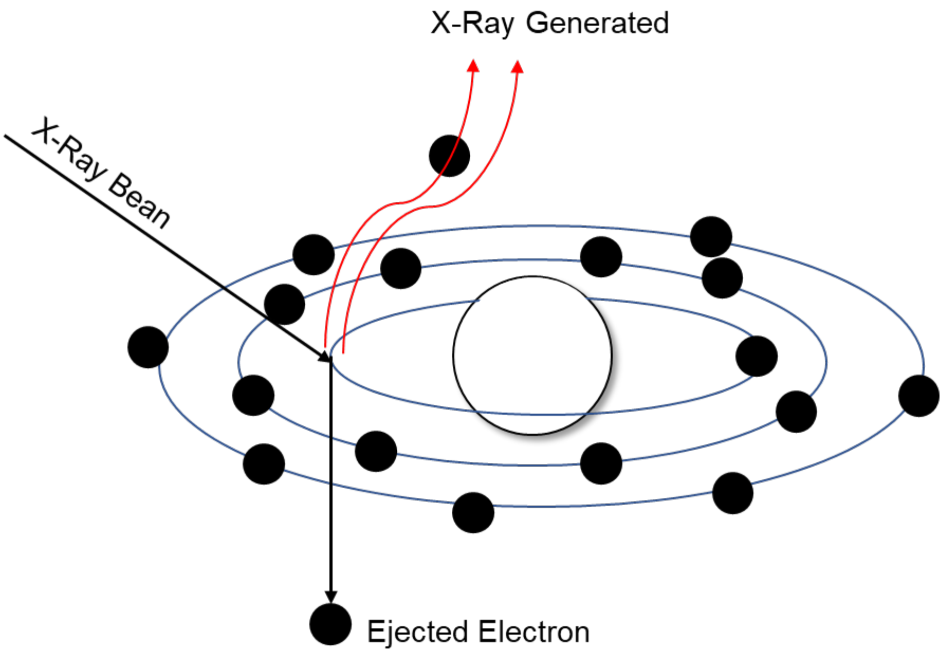

Figure 7. Process of creating an X-ray in XRF

For this work, finely ground sample powder was poured into the sample holder. The sample holder was then placed into the XRF for analysis. The data was analyzed and fitted through the software with elemental amounts of the sample and spectra that matches the quantitative amounts. XRF for this work was performed on a Bruker S2 Ranger. The elements were restricted to sodium and heavier elements, which necessitated a different technique to measure lithium in LLZO.

1.3.5 Inductively Coupled Plasma-Mass Spectrometry

While XRF is a powerful technique, lithium cannot be detected using it which necessitates Inductively Couple Plasma-Mass Spectrometry (ICP-MS) for LLZO garnets. ICP-MS instrument have been used previously for lithium concentration determination in LLZO garnets[125]. ICP-MS involves connecting an ICP unit with a mass spectrometer (MS), which can utilize several different types of sample detection, while the ICP portion of the system is generally similar across most systems. The important process of the ICP system is to create ions of single elements from a sample prior to introduction into the MS. The ion formation from the plasma is controlled between 6000-7000 K where a phonon can be produced by the excitation of outer electron in atoms. The amount of energy from the plasma can remove that outer electron, creating the free ion for mass spectrometry[126]. After the ion is free, it moves into the mass analyzer.

Mass analyzers can have different designs depending on how the ions are to be sorted: quadrupole technology, time of flight and collision/reaction cell technology are several of them but the time-of-flight analyzer is used in this work. It operates with the free ions traveling through an ion pulser to accelerate the ions before passing through a flight tube. The heavier atoms will travel more slowly towards the electrostatic magnet at the back of the tube and then directed into the detector. The detector is a semiconductor material that creates an electric signal when an ion contacts the surface where it can be translated into a count vs. the time it takes for the ions to fly through the tube, which is recorded as the atomic mass per charge[127].

Select LLZO garnet samples had ICP-MS (Perkin Elmer) performed on them for this work but required specific requirements to digest them in acid. Two percent aqua-regia from HCl and HNO_3 in distilled water was made as the stock solution to dilute both standards and samples. A custom standard was purchased and then diluted to create standards with the following elements: Li, La, and Al. The samples were digested in premade aqua regia and were allowed to fully digest before being diluted to 2%. Then, the samples were diluted with stock solution so elemental weights were between 0.1 and 10 mg/L. The samples were run and analyzed using the ICP-MS software before being normalized to a non-Li element, the lanthanum for lithium garnet.

1.3.5 Raman Spectroscopy

Raman Spectroscopy is a nondestructive, surface level technique that measures phases, crystallinity, and molecular interaction information based on the sample’s atomic interaction with light. Electromagnetic radiation is focused onto the sample which scatters the radiation and is measured it as a function of wavelength[128]. The laser is focused onto the sample and generates scattered light that is dispersed. This interaction with the laser generates multiple types of light, Rayleigh scattering, and Raman scattering[129]. Raman scattering (inelastic) accounts for <0.00001% of all phonons generated and generates all the structural information. The generated plot is a function of wavenumber, ω, as cm^{-1} against the intensity where the wavenumber corresponds to vibrations of both atoms within a structure and compounds.

Sample preparation was done similarly to XRD where the powder samples were ground in a mortar and pestle to ensure a fine powder was formed. However, sintered samples were polished with sandpaper before the measurement. The Raman measurements were performed on a Horiba EVO BX41.

1.3.6 Scanning Electron Microscope

Scanning Electron Microscope (SEM) is capable of imaging microstructures of sintered samples with submicron to nanometer level details. SEM's irradiate the area under examination with a finely focused electron beam, which produces different types of signals: secondary electrons (SE), back scatter electrons (BSE), and characteristic x-rays or electron dispersive x-rays (EDX), among other signals[130]. The beam's interaction with the sample is complex but can be defined into several steps: first, the electron beam enters the sample and then interacts with the electrical fields of the atoms. It finally interacts with the electrons in the sample, causing either the electrons to scatter elastically and laterally (secondary) or to eject electrons (backscatter). However, backscattering of electrons requires more energy from the electron beam to create enough electrons to properly image the sample. Likewise, the depth of the electron beam can create different x-rays

(EDX) and electrons[131]. The focus of this work will be on the images obtained from SE, BSE, and EDX signals.

SE signals are detected using a secondary electron detector (SED). SEDs are coated with a scintillator (fluorescent substance) which attracts the SE generated and creates a light after contacting the detector[132]. The light is then converted into an electron signal and finally into an image. The other type of detection used in this work is BSE. BSE are electrons that have been ejected from the nuclei of the sample and undergo a series of elastic scattering events in which they are emitted from the top of the sample[133]. BSE detectors are semiconductors where electron-hole pairs are formed when BSEs encounter the detector, and the generated signal is converted into an image[134]. The amount of electron-hole pairs formed corresponds to the energy of the BSE's formed, i.e. materials with high molecular weights will have stronger signals and be elementally lighter. This gives BSE images different information than SED but requires higher accelerating voltages to generate enough BSEs to be imaged. With increasing voltage and current, x-rays (EDX) can also be generated. EDX images allow differentiating between elements of the sample. At high electron beam currents and voltages, the electrons penetrate the inner electron bands where those electrons are removed and then electrons fall from the upper bands, which generate x-rays. The EDX detector has a high bias voltage applied to it so that the x-rays create current across the semiconductor; allowing the original x-ray energy to be calculated[135]. The three imaging (SE, BSE, and EDX) allow for a fuller image to be generated allowing microstructure (SE), phase (BSE), and chemical (EDX) to be determined.

Samples for each imaging technique are prepared the same and performed during the same SEM measurement session for each sample. The samples were placed onto electron conducting carbon tape on the sample holder where solid sintered samples have fractured surface imaged and powder is pressed onto the carbon tape before being placed into the SEM. Pellets were imaged with the fractured edge of the sample. Powder samples were pressed onto the carbon tape and then shaken off to ensure the powder would not become dislodged during measurements. All SEM for this work was performed on a JEOL JSM-IT100.

1.3.7 Archimedes' Method

The Archimedes' method, a density measurement technique, is accurate within 5% for small objects[136]. For this work, it was performed on sintered samples to measure their density. The method's principle arises from the pressure of the liquid exerted in all directions on the sample, including the bottom, while the pressure is proportional to depth. Thus, when an item is submerged and the weight can be measured, the difference of the weight in air and the weight in the medium (the mass displaced by the sample), divided by the density of the medium will yield the density of the solid.

Sample pellet densities in this work were measured using Archimedes' method in IPA in which density was calculated using Equation 6 where ρ is the density and w is the weight.

$$(6)\ \rho_{LLCZN} = \frac{w_{pellet}}{w_{Displaced\ Isopropanol}} \rho_{Isopropanol}$$

For this work, this method was performed primarily on LLZO to measure the degree of densification from sintering, which was described in a prior section. The sintered samples were weighed and then weigh again while submerged in IPA. The results were calculated using Equation 6.

1.3.8 Differential Scanning Calorimetry/Thermogravimetric Analysis

Differential Scanning Calorimetry (DSC) and Thermogravimetric Analysis (TGA) are thermal analysis techniques to measure heat required to increase the temperature and weight of a sample, respectively, as the temperature changes. TGAs include a microbalance to hold the sample, a thermocouple, and a programmable furnace to heat the sample. The thermocouple measures the temperature of the sample and the microbalance measures the weight: ensuring the weight change can be measured with temperature. While DSC involves two different furnaces: a sample furnace and a reference furnace with a known heat capacity. As the samples are heated, the difference in the heat required to heat the sample vs. the reference can be calculated based on the energy needed to heat the samples. In the forthcoming chapters, both processes take place in a simultaneous thermal analysis (STA) where they are measured at the same time. The samples were weighed using a micro balance and then inserted into an Argin environment in the system. The heating profile included an increase in temperature of 10°C min^{-1} to the specified temperature. While the maximum temperature will be specified for each experiment. All the experiments were performed on a Perkin Elmer STA 8000.

1.3.9 Electrochemical Cell Construction Using Organic Liquid Electrolyte

Electrochemical cells are traditionally called half cells when lithium metal is used as the anode. Half cells with organic liquid electrolyte were used to characterize the cathode, with 1M $LiPF_6$ in 50:50 mixture of ethylene carbonate:dimethyl carbonate (EC:DMC) (unless otherwise specified) as the electrolyte, glass separators, and a designed composite cathode in a CR 2025 cell. The composite cathode included polytetrafluoroethylene (PTFE), carbon black, and an active material in a weight ratio of 5:15:80 mixed in a mortar and pestle before being flatted between two rollers and punched into discs. The discs were placed into CR 2025 cells and then dried in a vacuum oven at 75°C. The cells were then assembled with three liquid electrolyte-soaked glass fiber separators between the lithium anode and composite cathode.

Each cell had electrochemical impedance spectroscopy (described the next section) performed to determine resistivity and connectivity of cell components. After, three charge discharge cycles between standard voltages (specified depending on cell chemistry) were performed at 0.5 mA cm^{-2} which is roughly 1 mA in a CR2025.The cells would then have one of multiple tests performed to characterize the electrochemical performance.

1.3.10 Electrochemical Impedance Spectroscopy

Electrochemical Impedance Spectroscopy (EIS) is a characterization technique for electrochemical devices to measure their resistances. The technique operates by applying an AC current at different frequencies to the sample with the responding electrical current measured. The simplest equation that this technique follows is Ohm's Law. EIS operates under this law but the data the technique generates is more complex. This equation only follows one circuit but in most electrochemical cells there are multiple circuits running in series and parallel[137]. This technique is crucial towards understanding the ionic movement through both solid-state electrolytes and full cells used in LIB. Each circuit will be different depending on the experimental set up and will be described in each chapter.

1.4 Conclusions

LIB have different materials, and each requires the above characterization techniques to ensure the material is the correct structure, is the desired microstructure, and has the needed electrochemical properties. Likewise, next generation batteries require material improvements to increase energy density to meet future demands. SSEs, specifically LLZO garnet, possess high conductivity, lithium metal stability, and wide voltage windows but introduces new resistances. Figure 8 describes the resistances investigated in the forthcoming work.

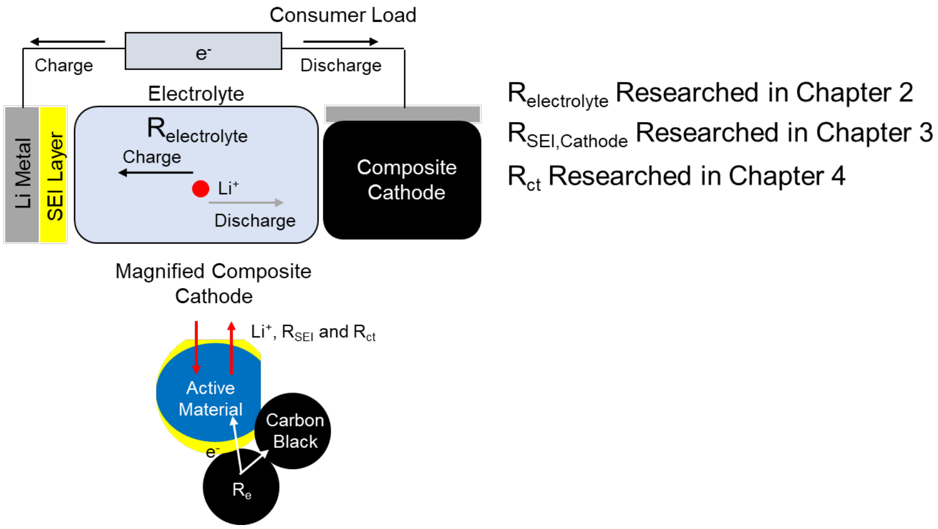

Figure 8. The resistances of a LMB and the chapters they will be investigated in

The understanding of crucial aspects such as lithium content and aluminum are paramount towards creating a manufacturing method to include quality control characterization techniques. The lithium content of sintered LLZO will be studied in the upcoming sections while, the interface between LLZO and LCO will be studied to reduce the interfacial impedance between the two. Finally, new LMO cathode materials to take advantage of the high voltage stability of the lithium garnet will be explored to create high energy density cells. The techniques needed to study next generation LMB were described in the previous sections and will be crucial to performing the forthcoming work.

Chapter 2: Achieving Desired Lithium Concentration in Garnet Solid Electrolytes; Processing Impacts on Physical and Electrochemical Properties

Reprinted with permission from Limpert, M. A.; Atwater, T.B.; Hamann, T.; Godbey, G.L.; Hitz, G.T.; McOwen, D. W.; Wachsman, E.D. Achieving Desired Lithium Concentration in Garnet Solid Electrolytes; Processing Impacts on Physical and Electrochemical Properties. *ACS Chem. Mater.* **2022**, 34, 9468-9478, DOI: 10.1021/acs.chemmater.2c01915. Copyright 2022 American Chemical Society.

Abstract

Lithium ion-conducting garnet is one of the most promising solid-state electrolytes to replace liquid organic electrolytes in lithium batteries, resulting in a tremendous and rapidly increasing number of garnet publications and commercial activity. However, these publications are typically based on a nominal lithium content with the addition of excess lithium to qualitatively supplement lithium losses during calcining and sintering, resulting in an inexact lithium composition that directly influences the sintered garnet's physical and electrochemical properties. In this study, we systematically varied the lithium content during processing of $Li_{6.75\pm X}La_{2.75}Ca_{0.25}Zr_{1.75}Nb_{0.5}O_{12}$ (LLCZN), then measured the actual lithium content, determined density and secondary phase formation, and the impact on electrochemical properties. Molar lithium content after sintering ranged from 5.5 to 7.3 lithium per mol for a desired 6.75 stoichiometric LLCZN Li-composition, depending on the starting lithium content and sintering conditions utilized. Secondary phases were detected when lithium content was outside of the designed stoichiometry, hindering sintering. Samples sintered in MgO crucibles obtained the high bulk conductivities (>10^{-4} S cm^{-1}). However, they exhibited low grain boundary conductance due to secondary phases resulting in total conductivities on the order of 10^{-5} S cm^{-1}. In comparison, when sintered in Al_2O_3 crucibles, bulk

conductivity (2.0×10^{-4} S cm^{-1}) and grain boundary conductance (1.07×10^{-3} S cm^{-1}) reached their maximum at 6.37 lithium per mol of LLCZN for a total conductivity of 1.68×10^{-4} S cm^{-1}. While similar bulk conductivities were attained when sintered in MgO crucibles, the highest total conductivities were achieved in samples contaminated with ppm levels of aluminum from the Al_2O_3 crucible.

1. Introduction

Since their commercialization in 1991, lithium-ion batteries have been utilized to power consumer electronics and more recently electric motor vehicles[138]. Current lithium-ion batteries have the potential for a catastrophic failure, igniting the organic liquid electrolyte and causing significant damage. Over the past 40 years, researchers have studied lithium-ion conducting solid state electrolytes (SSE) such as Lithium Super Ionic Conductor (LISICON) sulfides, lithium conducting phosphates, and perovskites to replace the flammable organic liquid electrolyte[139- 144]. Most of these SSEs are nonflammable and have the potential to inhibit cell failure from dendrite formation. However, each suffers from either low conductivity, reactivity with air, or instability against lithium metal[140,145], limiting their applicability in the next generation of lithium-based batteries.

Thangadurai and Weppner reported lithium-ion conducting garnet, $Li_6ALa_2Ta_2O_{12}$ (A=Sr, Ba), that is stable against lithium metal, has low reactivity with air, and possesses a total ionic conductivity (σ_{Total}) of 4.0×10^{-6} S cm^{-1} [146], which is a combination of the grain boundary conductance (G_{GB}) and bulk conductivity (σ_{Bulk}). Since then, the structure has been researched extensively leading to the reporting of a cubic phase with disordered lithium sites possessing σ_{Bulk} two orders of magnitude higher than the ordered, tetragonal phase, $Li_7La_3Zr_2O_{12}$ (LLZO) [147,148].

The cubic phase has added dopants to create lithium site vacancies to disorder the lithium sub lattice. Both phases have dodecahedral LaO_8, octahedral ZrO_6 sites, and lithium filling the interstitial sites[147]. The cubic phase has two lithium sites: tetrahedral (24d) and octahedral (96h and 48g) where they are connected and partially filled, which facilitates the higher ionic conductivity[147]. Cubic LLZO is typically prepared with 10% excess lithium to account for volatilization losses during sintering, filling the two lithium sites to an estimated 56% and 88% respectively, but actual lithium concentration can change depending on sintering conditions[146,147,149]. This impacts total conductivity and creates significant uncertainty in reported LLZO results.

In addition, the type of crucible used is a sintering condition parameter that can significantly impact the lithium concentration in LLZO type electrolytes. Garnet, like most ceramics, is typically sintered in Al_2O_3 crucibles. However, it was found that this results in a small level of aluminum contamination in the garnet due to the reaction with lithium. This has the benefit of more easily stabilizing the cubic phase resulting in higher σ_{Total}[150] by impacting σ_{Bulk} and G_{GB} through increased phase purity and density[151]. Another method to increasing phase purity is through the addition of excess lithium salts but they will also react with the Al_2O_3 crucible. Lithium deficient LLZO or nonconductive secondary phases that slow conduction over grain boundaries can form during sintering while added lithium has been shown to aid Li^+ conduction[152]. These excess lithium salts have proven to be a good binder in SSEs that can form a ‘glassy’ phase during sintering while increasing density and limiting nonconductive secondary phases[153,154]. However, excess lithium salts also cause aluminum migration from Al_2O_3 crucibles at sintering temperatures from the reaction between Li_2O and Al_2O_3, promoting liquid phase sintering thus increasing density which increases G_{GB} [151,154,155]. This reaction creates a eutectic liquid between Li_2O-Al_2O_3

at 1055°C with the reaction dependent on the quantity of excess lithium[156-158]. In contrast, sintering in MgO crucibles prevents this contamination. Al_2O_3 crucibles directly impact G_{GB} from the Li_2O-Al_2O_3 reaction through increases in density while the nonreactive MgO crucibles does not directly impact density. Therefore, the crucible material is a parameter in garnet fabrication and was also investigated herein with variations in added lithium.

How lithium content changes during sintering and the impact of the crucible utilized is crucial to understanding LLZO's physical and electrochemical properties. In this work, we report varying the lithium content in $Li_{6.75}La_{2.75}Ca_{0.25}Zr_{1.5}Nb_{0.5}O_{12}$ (LLCZN), calcined through a solid-state reaction, and sintered in either alumina or magnesia crucibles. The study includes structural characterization, chemical composition analysis, and microstructural characterization, to determine the impact of added lithium on the electrochemical properties. Herein, we offer perspective on how added lithium and its properties change with sintering time, lithium amount, and crucible.

2. Experimental Section

Stoichiometric amounts of LiOH (Sigma Aldrich 98%<), La_2O_3 (Sigma Aldrich 99.9%<), ZrO_2 (Sigma Aldrich 99%<), $CaCO_3$ (Alfa Aesar 99%<) and Nb_2O_5 (Sigma Aldrich 99.99%<) were used to synthesize LLCZN. Either -5 wt.% ,0 wt.%, 5 wt.%, 10 wt.%, 15 wt.% or 20 wt.% excess lithium was added or subtracted to the precursors, each designated as LLCZNX, where x= -5, 0,5,10,15, or 20 respectively. A standard sample size of 25 g was used for each sample. The molar amount of lithium was referred to as the added lithium content. The precursors were milled in isopropanol (IPA) (Alfa Aesar >99.7%) with 5 mm yttrium stabilized ZrO_2 milling media (Advanced Material) for 24 hours, dried, and then calcined in an Al_2O_3 crucible (>99%) in air at

900°C for 12 hours. The calcined powders (Pre-Mill) were milled using the same procedure as the first milling process, and then dried (Post-Mill). Dynamic light scattering (DLS) was performed on Pre-Mill and Post-Mill powders to determine particle size.

Half a gram of LLCZNX-Post-Mill powder was pelletized into a 12 mm pellet, placed in an MgO crucible, and covered in the corresponding LLCZNX-Post-Mill powder (0.25 g on the bottom and 0.25 g over the top, where X is the percent of added lithium) to reduce lithium loss. They were then sintered for 12 hours at 1100°C in air, ramping up and down at 3°C per minute and allowed to cool to room temperature. These samples are referred to as LLCZNX-MgO. To determine the effect of Al_2O_3 with lithium content on sintering, 0.5 g of Post-Mill powder was pelletized, placed in an Al_2O_3 crucible, similarly covered in a bed of mother powder, then sintered in air at 1100°C for 12, 18, or 24 hours, ramping up and down at 3°C per minute. Theses samples are referred to as LLCZNX-YHr, where Y is the sintering time.

The phase composition of powders and sintered samples was determined via powder x ray diffraction (PXRD) (Bruker D8 Advance, Cu-Kα with monochromatic radiation). Raman spectroscopy was also performed to measure the structural stability (Horiba LabRam HR with a 532 nm Ar^+ laser as the excitation source). Samples of the powders and sintered pellets (25-50 mg) were dissolved in 4 mL of aqua regia, diluted with deionized water to 2% acid, and then lithium, aluminum, and lanthanum quantities were determined using inductively coupled plasma mass spectrometry (ICP-MS, Perkin Elmer Elan DRC II). The results were normalized to lanthanum quantities to calculate lithium and aluminum molar amounts.

Scanning electron microscopy (SEM) was performed on the fractured edge of the cross section of a pellet for each sintering condition to detect its morphology (JEOL JSM-IT100). Energy dispersive x-ray spectroscopy (EDS) was used for local chemical analysis on the same fractured edge. Pellet densities were quantified by performing Archimedes' method in IPA. Electrochemical measurements were performed on sintered pellets after painting ion blocking Au paste on both sides, heating to 700°C for an hour to remove the organics, before placing between two stainless steel plates for Electrochemical Impedance Spectroscopy (EIS) (Solartron SI 1260). EIS measurements were taken from 1 MHz to 1 Hz at 10 mV. Zview software was used to fit the impedance data and extract the bulk (R_{Bulk}) and grain boundary (R_{GB}) resistance with conductivity determined using equation (7):

$$(7)\ \sigma = \left(\frac{1}{R}\right)\left(\frac{l}{A}\right)$$

where R, l, and A are the measured resistance, pellet thickness and pellet area respectively. The results extracted were σ_{Bulk} and the reciprocal of grain boundary contribution to the total impedance, or grain boundary conductance (G_{GB}).

3. Results and Discussion

3.1 Calcined Powder

3.1 1 Calcined Powder Results

Lithium content of the calcined powder is the starting lithium content before any pellets are sintered. For example, LLCZN-5-Post-Mill was pelletized, placed in a bed of the same LLCZN-5-Post-Mill powder, and sintered. The lithium content, phase purity, and particle size of these calcined powders impacts the physical and electrochemical properties of the sintered samples.

The ICP-MS results of the calcined powders show all samples lose lithium during the calcination at 900°C for 12 hours (Table 2). This assumes that lithium is lost to the atmosphere after forming Li_2O[159]. Over the entire calcination process, the average molar lithium loss is 7.4±1.2% at a rate of 0.045 mol Li hour^{-1} at 900°C. This yields a relationship where the measured lithium content after calcining linearly increases with the lithium amount added prior to calcination, meaning the rate of lithium lost does not appear to be influenced by the amount of lithium added. Despite the excess lithium measured in several samples, aluminum contamination from the Al_2O_3 crucible is not detected. The results show that when calcining before sintering and without a powder bed, lithium content will be reduced before a sintered product is formed.

Lithium content has an impact on the phase purity of the calcined powders and the calcined powders will be used in the sintering studies. Thus, the calcined powder will impact the phase purity of the sintered samples. PXRD patterns (Figure S1a-b and refinement in Figure S2) of Pre-Mill and Post-Mill samples displays LLCZN cubic phase (ICDD 45-0109) in every sample with secondary phases in certain low lithium content samples (Figure S3a-b). The PXRD peak at 29° and the splitting at 30° are ascribed to $La_2Zr_2O_7$ and $CaCO_3$[160]. The cubic structure can be stabilized solely by niobium doping in $Li_{6.5}La_3Zr_{1.5}Nb_{0.5}O_{12}$. This infers $CaCO_3$ begins to form when Li<6.75 and once all of the calcium leaves the garnet structure when Li<6.5 in LLCZN-5, $La_2Zr_2O_7$ begins to be detected. These secondary phases will impact the microstructure formation during sintering, which will have a deleterious impact on G_{GB}.

Lithium carbonate, which will melt during sintering and may assist in liquid phase sintering, should be the likely product when measured lithium is above the designed molar amount but may be amorphous in Pre-Mill samples[161]. The peak at ~1100 cm^{-1} in the Raman of the Post-

Mill samples (Figure S4a-b), however, also indicates Li_2CO_3 formation during the IPA ball milling step. This formation is further confirmed by the increase in weight loss during TGA between the Pre-Mill and Post-Mill samples (Figure S5a-b), the decomposition of reaction products between 300 and 800°C (Figure S6a-b), and the increase in the lattice parameters (Table 3 and fitting parameters in Table S1-3). This reaction should not be an issue as the Li_2CO_3 will decompose and add the lithium back to LLCZN during sintering, but a portion will become Li_2O vapor[159]. Above 900°C, the weight loss is minimal (~1 wt. %) but is most likely Li_2O vapor that will be lost during LLCZN's sintering, thus changing its physical and electrochemical properties.

Percent Excess Li Added	**Added Molar Li Content**	**Measured Molar Li Content of Calcined LLCZNX Powder**	**Measured Molar Li Content of Sintered LLCZNX-MgO**	**Measured Molar Li Content of Sintered LLCZNX-12Hr**	**Measured Molar Li Content of Sintered LLCZNX-18Hr**	**Measured Molar Li Content of Sintered LLCZNX-24Hr**
-5	6.413	5.914	5.53	5.756	5.616	5.412
0	6.750	6.394	6.31	6.275	6.024	5.908
5	7.088	6.558	6.48	6.370	6.297	6.035
10	7.425	6.768	6.59	6.567	6.474	6.203
15	7.763	7.189	7.11	7.106	6.757	6.543
20	8.100	7.481	7.27	7.337	7.219	7.085

Table 2. Formulated molar lithium content; and measured lithium content after calcining for 900°C at 12 hours, sintering in MgO crucibles at 1100°C for 12 hours, and after sintering in an Al_2O_3 crucible for 12, 18, and 24 hours at 1100°C.

Lastly, particle size of the calcined powder has an impact on the microstructure and thus electrochemical properties of sintered LLCZNX (Table 3)[162]. Before milling, the particle size is larger than the 3 µm maximum detection limit of the DLS. Whereas in Post-Mill samples, all are submicron as with the powder used in previous studies[163], which should be conducive for dense microstructures to limit lithium dendrite formation. The particle size of the Post-Mill samples is small enough that it should not be a large factor in the final sintered microstructures regardless of crucible.

Excess Lithium Amount (%)	Added Molar Li Amount	Measured Li Amount After Calcination	Pre-Mill Lattice Parameter (Å)	Post Mill Lattice Parameter (Å)	Particle Size of Post Mill Samples (nm)
-5	6.413	5.914	12.939	13.032	581
0	6.750	6.394	12.969	13.032	603
5	7.088	6.558	12.952	13.042	676
10	7.425	6.768	12.930	13.034	702
15	7.763	7.189	12.929	13.032	866
20	8.100	7.481	12.922	13.027	994

Table 3. Physical properties of powder after calcined at 900°C for 12 Hours

3.2 Aluminum-Free Results

3.2.1 Aluminum-Free Sintering ICP-MS Results

Every sample sintered in a MgO crucible contains less molar lithium than it did before sintering (Table 2). As with the calcined powder, the trend between the measured molar lithium content and the added lithium content for these sintered samples remains linear. However, the average cumulative lithium loss after this sintering procedure is 9.8±2.5%, a change of +2.4% from the calcined powder (Figure S7). Likewise, the rate of lithium lost during sintering (0.014 mol Li hour^{-1}) is slower by 0.031 mol Li hour^{-1} when compared to the rate during calcination. This decreased rate occurs despite a higher temperature (1100°C vs. 900°C) and the same amount of time at the processing temperature (12 hours), likely due to both reduced pellet surface area compared to powder, and the powder bed limiting but not completely stopping lithium loss. These changes in lithium will impact the physical and electrochemical properties of the sintered samples.

3.2.2 Aluminum-Free Sintering PXRD Results and Discussion

Secondary phases typically formed during processing LLZO type SSEs can be the result of lithium deficiencies, are nonconductive, and will slow conduction across the grain boundaries. PXRD data of the samples sintered in MgO crucibles (Figure 9, Figure S8, and fitting results in Table S4) displays cubic LLCZN phase but also $La_2Zr_2O_7$ and $CaCO_3$ in every sample[160] with Raman confirming their presence (Figure S9). These secondary phases are in larger quantities when compared to the calcined powder samples and may be from a reaction between MgO and $CaCO_3$[164] or Nb_2O_5[165]. However, neither EDS nor ICP-MS results indicated any Mg in the samples. LLZO type garnets generally have better performance when sintered in MgO[166], but previous studies utilize different dopants. Regardless of the cause, these secondary phases detected in PXRD will hinder Li^+ transport across the grain boundaries.

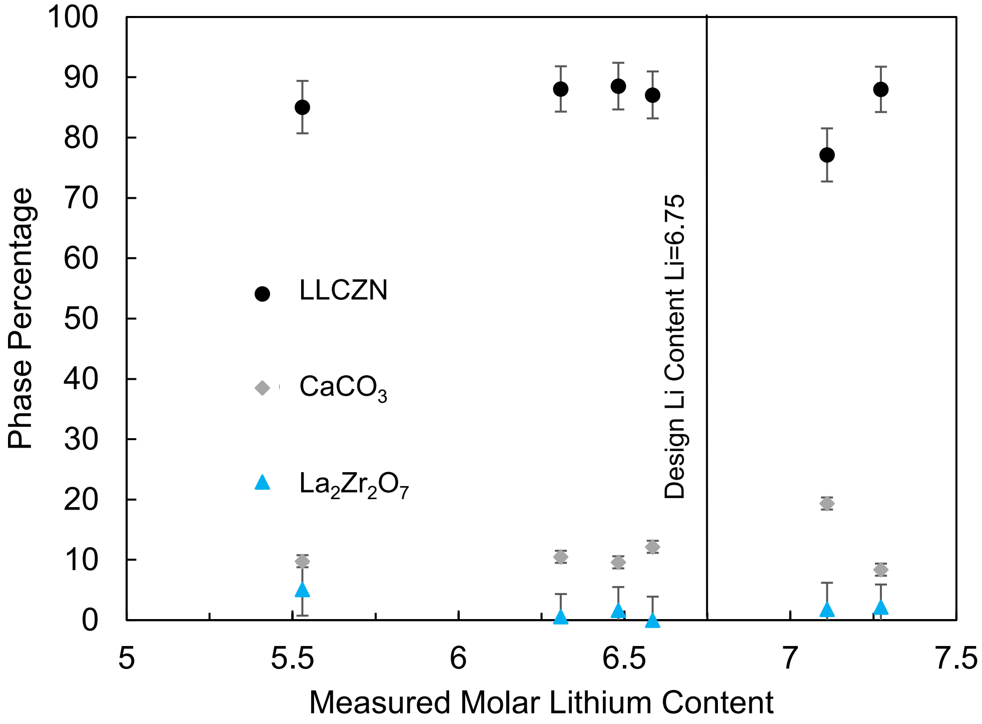

Figure 9. Cubic LLCZN and secondary phase versus measured lithium content for MgO crucible sintered samples. Circles are cubic LLCZN, triangles are $La_2Zr_2O_7$ and diamonds are $CaCO_3$.

Lattice parameters are calculated from the PXRD results and are an indicator for the resistance a lattice has to Li^+ movement, or σ_{Bulk}. As excess lithium is added, the measured lattice parameter generally expands (Table 4), but this trend falters in LLCZN5-MgO and LLCZN0-MgO. These samples increase in lattice parameter, potentially from a reaction with air or formation of a lower lithium content phase. Excluding these samples, there is an increase in lattice parameter with measured lithium between LLCZN5-MgO and LLCZN20-MgO with a percent difference between calculated and actual of 0.33% (Figure S10 and Table S5). The higher lithium content samples also exhibit higher σ_{Bulk} in part because of the larger lattice spacing being beneficial for Li^+ movement (*vide infra*).

Percent Excess Li Added (%)	**Pre-Mill Lattice Parameter (Å)**	**Post Mill Lattice Parameter (Å)**	**Lattice Parameter of LLCZNX-MgO (Å)**	**Lattice Parameter of LLCZNX-12Hr (Å)**	**Lattice Parameter of LLCZNX-18Hr (Å)**	**Lattice Parameter of LLCZNX-24Hr (Å)**
-5	12.939	13.032	12.928	12.930	12.915	12.919
0	12.969	13.032	12.932	12.927	12.930	12.916
5	12.952	13.042	12.921	12.916	12.922	12.920
10	12.930	13.034	12.926	12.919	12.916	12.920
15	12.929	13.032	12.939	12.925	12.918	12.915
20	12.922	13.027	12.943	12.919	12.906	12.921

Table 4. Lattice parameter after calcining for 900°C at 12 hours, sintering in MgO crucibles at 1100°C for 12 hours, and after sintering in an Al_2O_3 crucible for 12, 18, and 24 hours at 1100°C.

3.2.3 Aluminum-Free Sintering Microstructure Results and Discussion

Large lattice parameters are associated with high σ_{Bulk}, while a dense microstructure is an indicator for high G_{GB}. For the MgO sintered samples, the quantitatively measured density does not have a trend with measured molar lithium (Figure S11). While the numbers say the samples look promising, the SEM and EDS images tell a different story. The images qualitatively indicate all microstructures include pores, visible grains, and segregation of calcium, which are not ideal for conductivity (Figure 10). The microstructures can be divided into two distinct categories: 1) low lithium, porous samples and 2) highly lithiated samples with lower quantities of visible grain boundaries. The high lithium content samples confirm that grains can grow and eliminate pores during sintering without Al_2O_3. However, calcium is still concentrated and not dispersed throughout the microstructure in all samples, which may limit G_{GB} from the nonconductive calcium species adding resistance. Creating a dense structure would require processing changes, such as a sintering aid (e.g. Al_2O_3) or changing dopants, to ensure phase purity while determining lithium loss at with these new conditions.

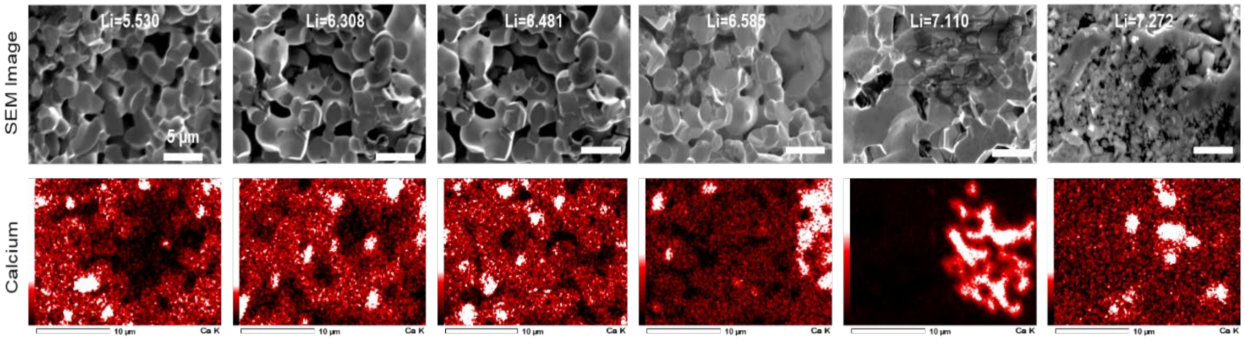

Figure 10. SEM and calcium EDS images of fractured edge of the cross section of samples sintered in MgO crucibles

3.3 Al_2O_3 Crucible Sintered Samples

3.3.1 Lithium and Aluminum Content Results and Discussion

Samples sintered in Al_2O_3 crucibles have variances in both lithium and aluminum based on the sintering time and lithium content that are different the MgO sintered samples investigated in the previous sections. The three sintering times used with the Al_2O_3 crucible (12, 18, and 24 hrs) all show linear molar lithium content versus the added lithium content but decreasing as sintering time increases (Table 2 and Figure 11). After sintering in Al_2O_3 crucibles, the rate of lithium loss from the calcined powder is 0.012, 0.018, and 0.022 mol Li in LLCZN hour^{-1} at 1100°C for 12, 18, and 24 hours. These are decreases of 0.033, 0.027, and 0.023 mol Li in LLCZN hour^{-1} from the rate during calcination. The increasing rates are also seen by the cumulative lithium losses which increases from to 9.5±1.6%, 11.8±1.0%, and 14.6%±1.7% from 12 to 24 hours of sintering. The rate of lithium loss increases with time and appears to be a quadratic formula which allows the measured molar lithium content after sintering to be estimated from the added lithium content (Figures S12-14). Lithium content and time will impact the amount of Li_2O reactant that can react with the Al_2O_3 crucible.

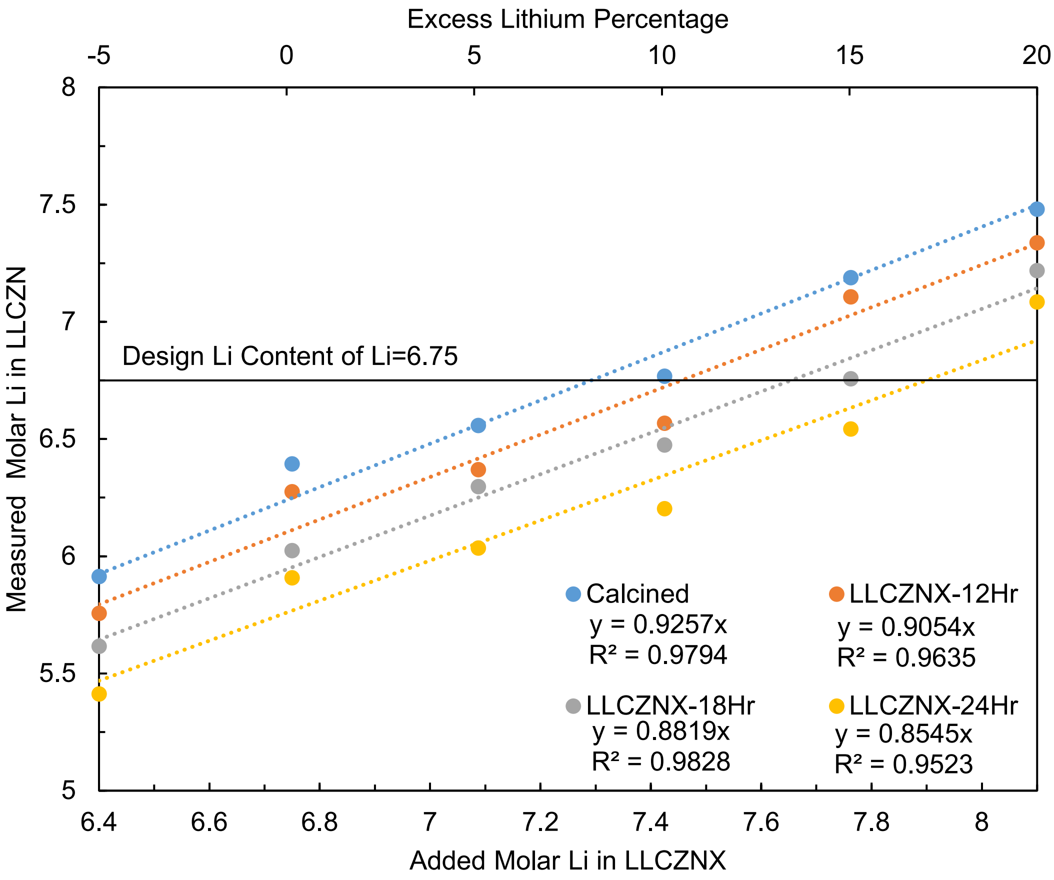

Figure 11. Measured molar lithium content vs. the added molar lithium content of samples sintered in Al_2O_3 crucibles

Aluminum migration from the crucible is related to lithium content and will influence the lattice and the microstructure, which impacts σ_{Bulk} and G_{GB} respectively. ICP-MS results of the sintered samples (Table 5) determines aluminum influx from the Al_2O_3 crucible when either the measured Li is above the designed stoichiometry of 6.75 or is measured between 6.20 and Li=6.50 (Table S6). In both cases, Li_2O reacts with the Al_2O_3 crucible during sintering, which creates a Li_2O-Al_2O_3 eutectic liquid that can also dope the LLCZN structure. As aluminum is doped onto lithium sites, lithium vacancies and Li_2O are formed as expressed by Kröger-Vink notation (Eq. 8).

$$(8)\ 6Li_{Li}^{X} + Al_2O_3 \rightarrow 2Al_{Li}^{\bullet\bullet} + 4V_{Li}' + 3Li_2O$$

For example, the measured aluminum would be sufficient in LLCZN5-12, which measures Li=6.37 and Al=0.18, to dope the lattice and maintain the structure without forming secondary phases, despite measuring below the designed Li=6.75. The amount of available lithium in this sample to react with the crucible and have Al dope the structure is self-sustaining. Li_2O reacting with the crucible creates opportunities for additional lithium to react through the resulting in greater aluminum incorporation. This aluminum contamination is correlated with lithium and will impact G_{GB} through its influence on the microstructure but may also impact σ_{Bulk} though aluminum's potential incorporation into the lattice.

Percent Excess Li Added	**Designed Molar Li Content**	**Measured Molar Al Content of Calcined LLCZNX**	**Measured Molar Al Content of LLCZNX-MgO**	**Measured Molar Al Content of LLCZNX-12Hr**	**Measured Molar Al Content of LLCZNX-18Hr**	**Measured Molar Al Content of LLCZNX-24 Hr**
-5	6.413	0.000	0.000	0.000	0.000	0.000
0	6.750	0.000	0.000	0.000	0.000	0.000
5	7.088	0.000	0.000	0.184	0.100	0.105
10	7.425	0.000	0.000	0.011	0.015	0.020
15	7.763	0.000	0.000	0.037	0.114	0.201
20	8.100	0.000	0.000	0.550	0.308	0.137

Table 5. Molar aluminum content after calcining for 900°C at 12 hours, sintering in MgO crucibles at 1100°C for 12 hours, and after sintering in an Al_2O_3 crucible for 12, 18, and 24 hours at 1100°C.

There are key similarities and differences between the ICP-MS results of the samples from the MgO crucible and the Al_2O_3 crucible. The LLCZNX-12Hr and LLCZNX-MgO samples were sintered for similar amounts of time and measure similar lithium amounts, enabling a direct comparison to ascertain crucible effects. The main difference between the sets is no aluminum is detected in LLCZNX-MgO samples, which will impact the physical and electrochemical properties. Al_2O_3 can aid sintering processes and dope the LLCZN structure, making it a versatile dopant but cannot be easily controlled through contamination. The similarities between the lithium contents allow for an investigation into the crucible effects on the lattice, microstructure, and finally the electrochemical properties.

3.3.2 Structural Characterization and Discussion of Pellets Sintered in Al_2O_3 Crucibles

As the measured quantities of lithium and aluminum varies, the phase purity of the samples changes, which will impact G_{GB}. PXRD data of the pellets sintered in Al_2O_3 crucibles shows cubic LLCZN in every sample with secondary phases becoming more common when Li<6.75 (Figure 12 and Figure S15-17, with fitting results in Table S7). As in the MgO sintered samples, the PXRD peak at 29° is $La_2Zr_2O_7$ and the splitting at 30° is $CaCO_3$. These secondary phases are reduced and finally eliminated when Li>7. However, $CaCO_3$ formation is limited in samples with high concentrations of aluminum but also low lithium, such as Li=6.37. When Li<6.2, secondary phases are detected in every sample and increases with sintering time (Figure S18a-c). PXRD of the samples indicates the Al_2O_3 crucible offers structural stability when high aluminum or lithium is detected, which will be beneficial for G_{GB}.

Ordering of the lithium sites in garnets has been investigated and can slow conduction through the lattice, rather than over the grain boundaries. When designed at Li=6.4 in garnet, the molar lithium content has been shown to limit short range ordering[149]. Ordering of the lithium sites has been previously reported using Raman spectroscopy[167], however, we did not detect ordering in this work for samples with Li>6.30 (Figure S19-21). In our work, the sample closest to Li=6.4, with measured Li=6.37, has high phase purity despite low lithium content, likely aided by the aluminum content (Al=0.184). The difference between this study (measured lithium) and others with similarly designed lithium amounts may be due to lithium loss at the differing sintering conditions, making a direct comparison difficult. It should be studied further to determine if

Li=6.37 is indeed a thermodynamically favorable lithium quantity regardless of designed lithium content and the effects on σ_{Bulk}.

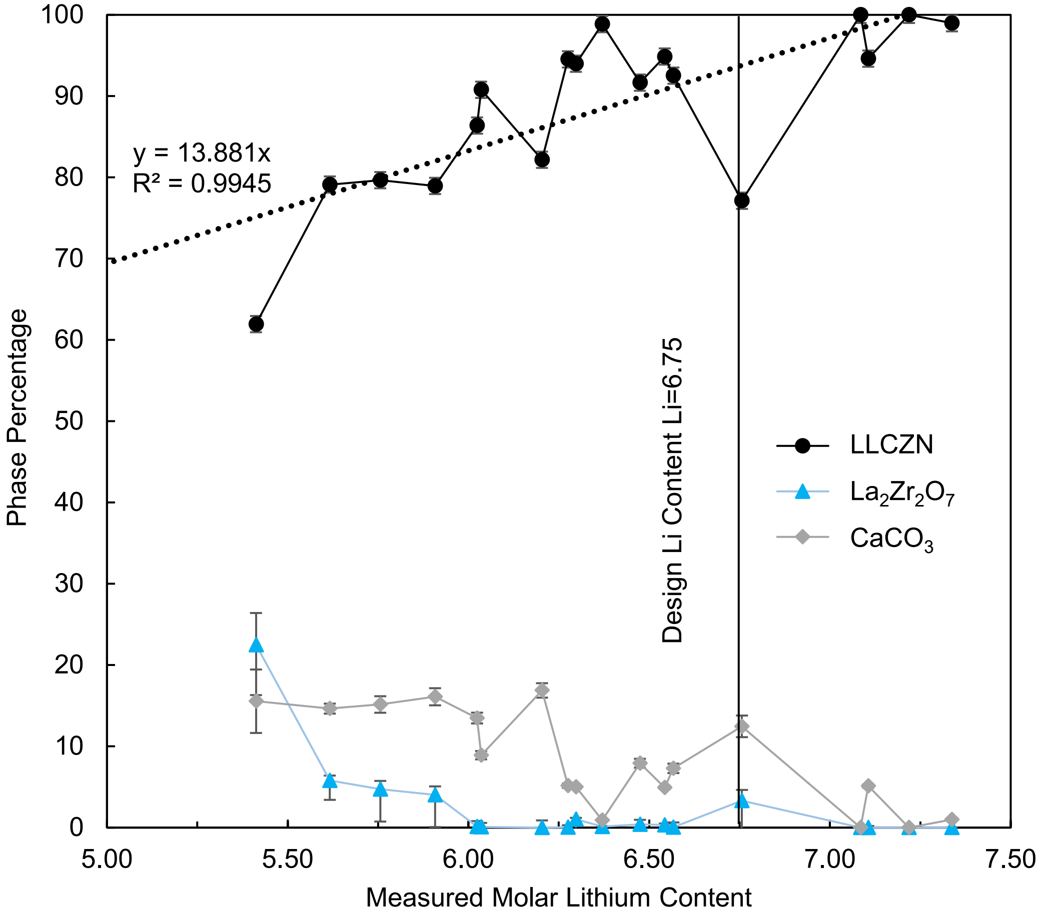

Figure 12. LLCZN phase percentage versus measure lithium content overall the sintering times. Circles are cubic LLCZN, triangles are $La_2Zr_2O_7$, and diamonds $CaCO_3$.

Bulk conductivity can also vary based on the lattice parameter of LLZO garnets and for our work, the lattice parameter of the LLCZN phase for the samples sintered in Al_2O_3 generally decreases with increasing lithium (Figure S22 and Table 4), in stark contrast to those sintered in MgO crucibles, and generally decrease with sintering time but that is a limited relationship (Figure S23). Samples highly contaminated with aluminum may have aluminum entering the lattice thereby decreasing lattice parameters[168]. Aluminum has a smaller ionic radius than lithium (53.5

pm for Al vs. 76 pm for Li) and forms two vacancies for every aluminum doped into LLCZN due to charge balancing, further shrinking the lattice[169,170]. Shrinking lattice parameters in these samples may introduce resistance to lithium movement through the lattice, decreasing σ_{Bulk}.

The phase information from PXRD, Raman, and the calculation of lattice parameters as lithium and aluminum changes will help explain their influence on both G_{GB} and σ_{Bulk}. When comparing the PXRD and Raman results, samples sintered in Al_2O_3 crucibles show better phase stability than their counterparts sintered in MgO crucibles, despite comparable lithium contents. This is clearly seen by calcium appearing more stable in the garnet lattice when there is aluminum present versus the high $CaCO_3$ concentration throughout the MgO samples. While aluminum can easily enter the garnet lattice, magnesium has not been reported to enter up to 1250°C[171]. This is a key difference in the PXRD between the two sets of samples: Al_2O_3 is more compatible with the materials system and sintering conditions than MgO. Changing dopants may allow for greater stability with the MgO crucible but in this study Al_2O_3 appears more beneficial to LLCZN's phase stability.

Lastly, the decrease in the lattice parameter of the samples sintered in Al_2O_3 crucibles with lithium is contrasted with the MgO sintered samples where the lattice parameter generally increases with lithium, showing a potential impact of the crucible. The lattice parameters of the samples sintered in MgO are mostly higher regardless of sintering time but are much higher in LLCZN15-MgO and LLCZN20-MgO. This may have operational impacts as bulk conductivities in LLZO type SSEs have been shown to be lower in samples with smaller lattice parameters[172]. The higher phase purity in Al_2O_3 sintered samples will show an increase in G_{GB} by decreasing nonconductive species that may block Li^+ conduction through the pellet while the MgO samples may have higher σ_{Bulk} enabled by the larger lattice.

3.3.3 Microstructure Results of Sintered Pellets in Al_2O_3 Crucibles

Microstructure and density impacts G_{GB} by eliminating grain boundaries and creating a single dense electrolyte layer. The green density of the pressed pellets indicates a structure with an average density of 3.6±0.075 g cm^{-3} (Figure S24) with small variations between samples. Conversely in the sintered samples (Figure S25), higher aluminum content, lithium content, or both is indicative of densities above 90% theoretical. Quantitatively the Al_2O_3 crucible sintered samples measure high densities but, like the MgO sintered samples, the qualitative images show features that will limit G_{GB}.

Preferred microstructures of LLCZN for G_{GB} should have a low quantity of pores, minimal grain boundaries, and dispersed elements[173]. In samples when Li<6.75, the quality of microstructure depends more so on the quantity of aluminum contamination from the crucible (Figure 13). EDS of the Li=6.474 sample does not detect any aluminum and has small visible grains while the calcium signal becomes concentrated rather than dispersed throughout the microstructure. This is a common microstructure in samples below Li=6.27 (Figure S26). When $CaCO_3$ is formed, which is more common when Li<6.75, calcium is concentrated in the microstructure (Figure S27), which will impact G_{GB}. As more aluminum contamination occurs, for example in Li=6.370, calcium becomes more dispersed but when aluminum decreases with decreasing lithium, the calcium signal becomes stronger and the microstructure shows more visible grains. This matches with the higher secondary phase amounts detected in the XRD results. This can occur due to charge balancing from Al incorporation into the LLCZN structure. Al^{3+} is preferred to dope on the Li sites in low quantities and removes three Li in order to balance the charge, leaving extra lithium. To remain in the structure, Ca^{2+} can dope the La^{3+} site, enabling an extra lithium to remain in the structure to balance the charge. As the lithium and aluminum in the sample decreases, calcium incorporation into the lattice ceases. Two of the samples, despite low lithium content, obtain the preferred microstructures for high conductivity in part from the reduction of secondary phase formation, likely aided by aluminum contamination.

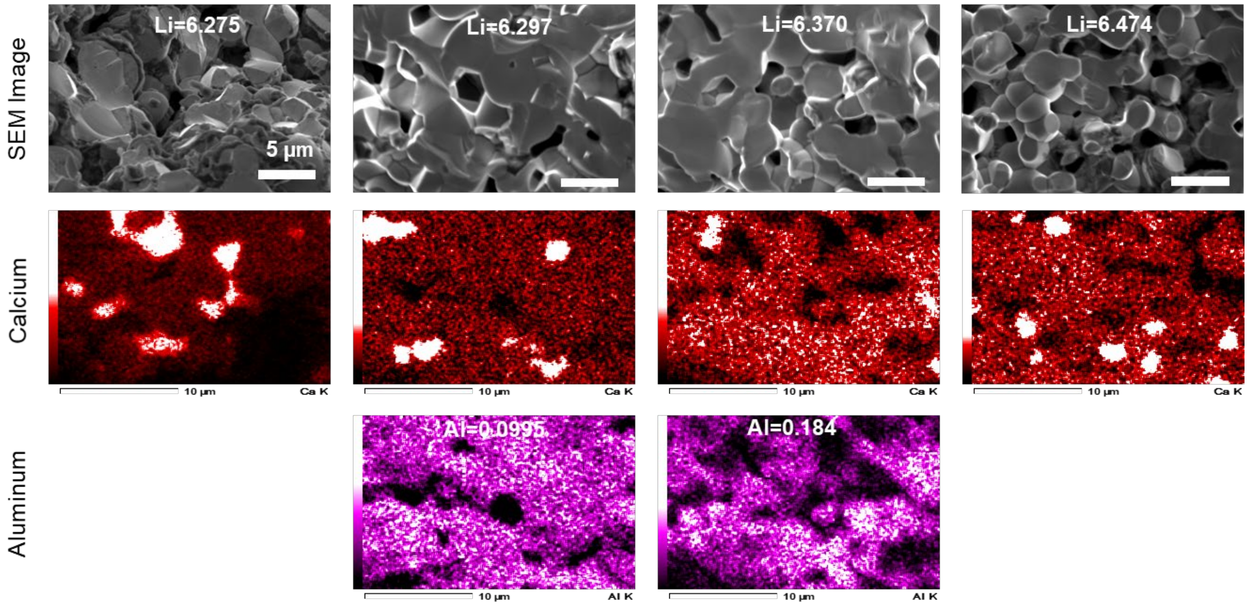

Figure 13. SEM and lithium and aluminum EDS of the fractured edge of the cross section of lower lithium contents. Measured lithium and aluminum molar contents are shown where applicable.

High lithium content samples show larger grains and dispersed calcium, aided by the high phase purity, but three of the four samples still have visible grain boundaries (Figure 14). In these samples, there is excessive amounts of aluminum causing liquid phase sintering which results in abnormal grain growth that requires longer sintering times to eliminate the pores. As lithium increases, aluminum generally becomes concentrated and not dispersed. The glassy Li_2O-Al_2O_3 phase binds the grains together and promotes grain growth[174]. However, this phase becomes concentrated at the grain boundaries which appears to stop pore elimination and may limit conduction over the grain boundaries. LLCZN15-12Hr (Li=7.106, Al=0.037) is the only sample were aluminum did not hinder pore elimination owning to the relatively low Al:Li ratio. Like calcium with the low lithium samples, the excess aluminum may slow conduction over the grain boundaries and limit G_{GB}.

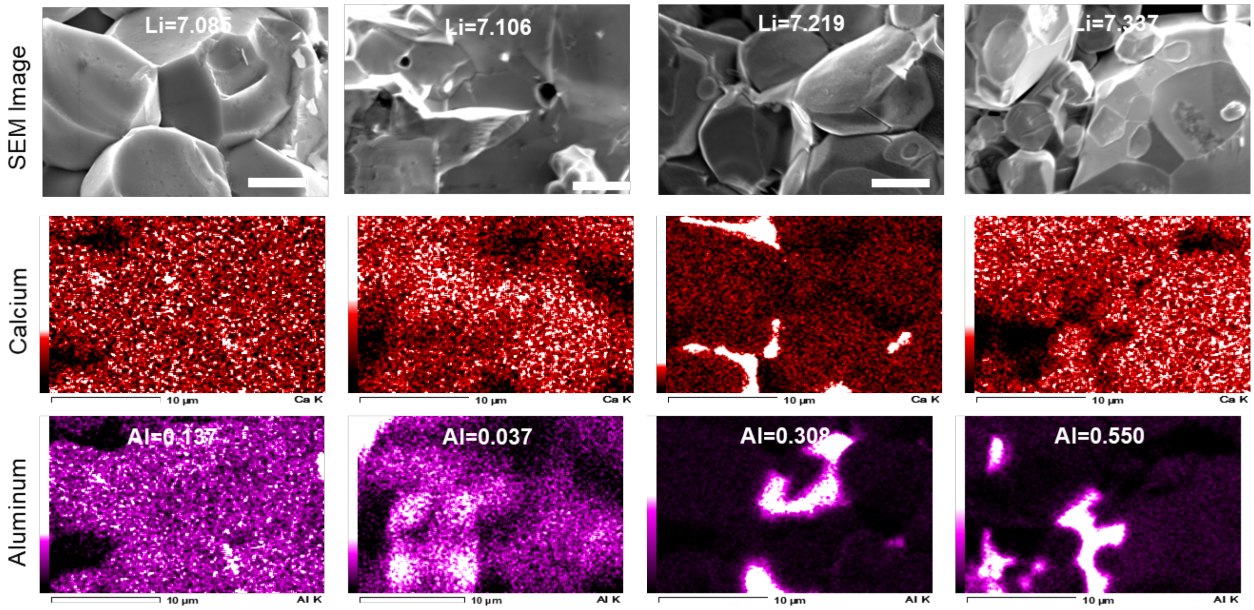

Figure 14. SEM and lithium and aluminum EDS of fractured edge of the cross section of higher lithium contents. Measured lithium and aluminum molar contents are shown where applicable.

Samples sintered in Al_2O_3 crucibles develop better microstructures for conduction than the MgO sintered samples. While they do have calcium concentrated rather than dispersed, MgO samples display density and microstructure patterns similar to their Al_2O_3 sintered counterparts, including the rise in density around Li=6.370. Unlike the MgO sintered samples, Li_2O-Al_2O_3 liquid and aluminum's stability with LLCZN's dopants leads to higher phase purity and appears to be a factor in the development of the preferred microstructures. In comparison, excess lithium melting in MgO sintered samples is not enough to offset lower phase purity, which leads to slower densification processes and calcium concentration. These differences between the two crucibles in microstructure development will impact each of their respective G_{GB} and σ_{Total}.

3.4 Electrochemical Results and Discussion

SSE's require high total conductivity (> 10^{-4} S cm^{-1}) which is the combination of σ_{Bulk} and G_{GB}, where each may be influenced by the lattice parameter and microstructure, respectively. Bulk (Figure 15) and grain boundary resistance (Figure 16) (R_{Bulk} and R_{GB}, Ohms) were ascertained by modeling the EIS data. Most Nyquist plots of the samples included two distorted semicircles and a tail in the low frequency range. These Nyquist plots and the models are included in Figure S28a-d where, σ_{Total} (Ohm^{-1} cm^{-1}, or S cm^{-1}) is a function of both the G_{GB} and the σ_{Bulk}, Equation 9,10, and 11.

$$(9)\quad \sigma_{Bulk} = \frac{1}{R_{Bulk}}\left(\frac{l}{A}\right)$$

$$(10)\quad G_{GB} = \frac{1}{R_{GB}}\left(\frac{l}{A}\right)$$

$$(11)\quad \frac{1}{\sigma_{Total}} = \frac{1}{G_{GB}} + \frac{1}{\sigma_{Bulk}}$$

R_{Bulk} is assumed to be the high frequency data and the R_{GB} is assumed to be the middle frequency data[175]. This is further confirmed through capacitance values obtained from the model, where 10^{-12} F is R_{Bulk} and 10^{-11} to 10^{-8} F is the grain boundary[176] (Table S8 and S9) in good agreement with other reported LLZO type electrolytes[177]. Another semicircle forms after the grain boundary resistance in the low frequency range and based on the capacitance values (below 10^{-8} F), it is assumed these resistances are from the Au-LLCZNX interfaces[173]. In certain samples, however, the bulk and grain boundary cannot be separated out by comparison of the capacitance values (Table S10). Distribution of relaxation times (DRT) is required to determine the different electrochemical processes for each sample.

DRT when combined with EIS data is used to identify the characteristic distribution of EIS timescales (Figures S29-34) and assists in separating out contributions to the conductivity. The

MATLAB GUI DRT tools, provided by Wan et al.[178], shows the EIS data has several distinct sections for relaxation times. The relaxation times below 10^{-6} s correspond to the fast motion of the Li^+ migration in the Wyckoff 96h↔24d↔96h route through the lattice[179]. Several samples have a second peak above this timescale that may correspond to lithium migration of 8a↔16f↔96h in tetragonal $Li_7La_3Zr_2O_{12}$ [179,180] but these are minor peaks cannot be differentiated fully from the cubic phase. As all samples have a peak above 10^{-6} s, the initial resistor in all samples is assumed to be R_{Bulk}. The middle section, between $5x10^{-5}$ and 10^{-3} s is attributed to the grain boundary contribution[181]. However, there are peaks in this section that cannot be attributed to pure grain to grain resistance[179]. These secondary peaks indicate abnormal movement over the grain boundaries potentially caused by aluminum migration from the crucible or secondary phase formation, such as $La_2Zr_2O_7$ or $CaCO_3$. This is similar to the overlap between grain and bulk resistance sections, such as in Li=6.54, where more than one peak is introduced in the bulk resistance area. More work is needed to differentiate the two sections to separate out the different EIS contributions of these abnormal grain-grain resistances. As they appear to be minor in comparison with the main grain boundary contributions, they are combined in this work to be the total grain boundary resistance. The last section of time constants which is slower than 10^{-3} s corresponds to LLCZNX-Au interface and the Li^+ blocking of the Au paste[182]. In comparison, the relaxation frequencies indicate similar results to the DRT. LLCZN5-MgO, for example, shows comparable relaxation frequencies for the third circuit in the model to the circuits attributed to the grain boundaries (Table S11 and S12). These may be the abnormal grain boundaries caused by different grain boundary compositions and are included in the total conductivity calculations. Likewise, several bulk resistances show higher relaxation frequencies than detected in the DRT, such as in the MgO sintered samples. The relaxation frequencies are computed using the results of the EIS model and project the initial circuit to higher frequencies than the measured frequencies performed during EIS. The chemical composition of the bulk can change the relaxation times by up to two orders of magnitude[179] causing some samples to measure lower frequencies. More work is required to determine if multiple phases are present in these samples and their effect on relaxation frequency. The DRT when combined with the fitting results indicate there are two contributions to the electrochemical properties of the samples, Li^+ movement through the lattice and Li^+ conductivity over the grain boundaries where the larger resistances at higher time scales are assumed to be the interfaces between Au and LLCZNX.

Bulk conductivity increases with lithium content in both crucibles (Figure 15) but is not correlated with sintering time (Figure S35 and S36) and weakly correlated with lattice parameter (Figure S37). Though it rises with lithium content, lithium content does not have as strong of an influence over the σ_{Bulk} (2.0 x 10^{-6} S cm^{-1} to 2.0 x 10^{-4} S cm^{-1}) when compared to G_{GB} (2.31 x 10^{-7} S cm^{-1} to 1.07 x 10^{-3} S cm^{-1}). Maximum σ_{Bulk} is detected in Li=6.37 and the samples above Li=6.75, which occurs in both Al_2O_3 and MgO sintered samples before decreasing again in LLCZN20-MgO. As the LLCZN is fully stabilized either through added lithium or aluminum contamination, the σ_{Bulk} increases in both MgO and Al_2O_3 sintered samples. Once the phase is stabilized above Li=6.75, the σ_{Bulk} varies minimally between samples and plateaus close to the maxima σ_{Bulk} measured in this work. While the trends are similar, the σ_{Bulk} of samples above Li=6.30 of samples sintered in Al_2O_3 crucibles are consistently near the maxima. This is contrasted with the samples sintered in MgO crucibles which only achieve higher σ_{Bulk} above Li=6.75, indicating issues with either the calcium or the aluminum.

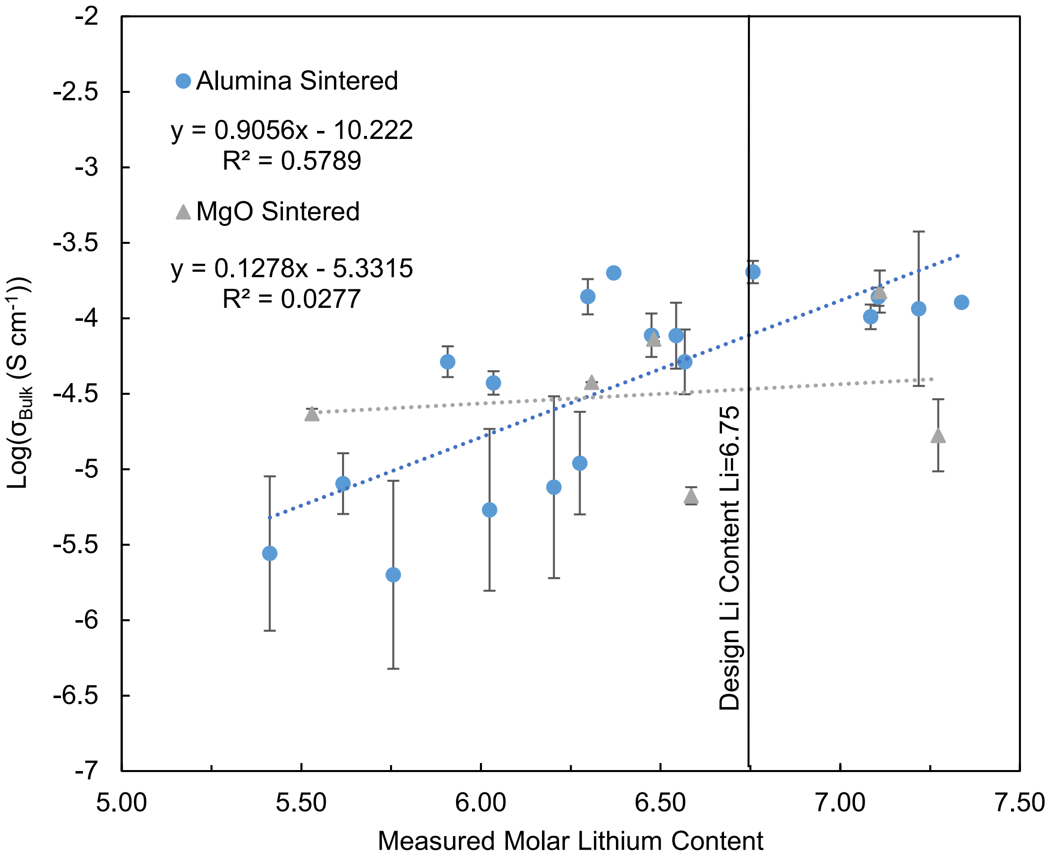

Figure 15. Measured bulk conductivity versus measured lithium content for Al_2O_3 and MgO sintered samples

The higher lithium content samples sintered in MgO crucibles measure larger lattice parameters than the ones sintered in Al_2O_3 crucibles but obtain similar σ_{Bulk}. This is indicative of two potential issues: 1) calcium having minimal impact on bulk conductivity[183] or 2) larger lattice parameters having a negligible effect on conduction when measured lithium content is above the designed lithium content. Calcium has been shown to have lower σ_{Total} when compared to other alkaline earth metal dopants in LLZO garnets[184]. Combined with the current results where calcium did not appear to be in the LLCZN lattice in the MgO samples, the impact of the calcium requires further investigation to determine if it is thermodynamically favorable to remain in the structure under certain sintering conditions. This includes sintering on MgO crucibles and then determining its impact on the electrochemical properties. Lastly, the larger lattice parameters of the aluminum free samples do not appear to enable faster conduction. This should also be studied more to determine if this trend continues for Al-free, pure phase LLCZN. It is crucial to maximize G_{GB} but should not be at the expense of slowing conduction through the lattice.

Measured G_{GB} typically rises with increasing lithium (Figure 16) in both sets of samples unless it is between Li=6.30 and Li=6.58 or above Li=7.10 (Figure S38). It also has a weak correlation with sintering time (Figure S38 and S39) but has a stronger correlation with theoretical density percentage (Figure S40). Below Li=6.28, G_{GB} generally decreases with declining lithium. While between Li=6.30 and Li=6.58, there is a local maximum conductivity of 1.07×10^{-3} S cm^{-1} at Li=6.37, which is also a LLCZN pure phase material with high aluminum content. This is not exclusive to this one sample as all samples in this range are contaminated with aluminum from the crucible and measure G_{GB} outside of the expected increase with lithium as displayed by the samples below Li=6.30. By Li=6.58, the G_{GB} decreases to follow that linear pattern displayed by the samples below Li=6.30. After this range, G_{GB} increases but begins to decrease after Li=7.10 or when aluminum content rises. In contrast, MgO crucible sintered samples have similar trends but measure about an order of magnitude lower than their Al_2O_3 crucible sintered counterparts after Li=6.75 despite similar lithium amounts. This indicates the impact on G_{GB} of the better phase purity and preferred microstructure of the samples sintered in Al_2O_3 crucibles.

Microstructure development has a direct impact on the measured G_{GB} as aluminum contamination impacts the microstructure development. MgO samples tend to be less dense, form more secondary phases, and have calcium concentrated. While their Al_2O_3 crucible counter parts, have lower quantities of secondary phases, larger grains, minimal pores, and dispersed calcium.

This offers several potential reasons for the decrease in G_{GB} from MgO to Al_2O_3 crucibles: 1) MgO is not stable with the LLCZN elements leading to development of nonconductive species and 2) Al_2O_3 crucibles has beneficial impacts on both lattice and microstructure. For example, LLCZN5-12Hr (Li=6.37) obtained the maximum G_{GB} owning to the large grains and minimal visible pores. The microstructure developed with a mix of higher phase purity from more aluminum content which may have also assisted with liquid phase sintering. LLCZN5-MgO, by contrast, also had an increase in G_{GB} around this point from potential Li_2CO_3 melting but not enough to overcome the large quantities of secondary phases slowing conduction through the microstructure and developing a microstructure with visible grains and pores. Overall, high density, minimal secondary phases, and dispersed calcium, properties not seen in MgO samples, are physical properties that indicate lower grain boundary conductance.

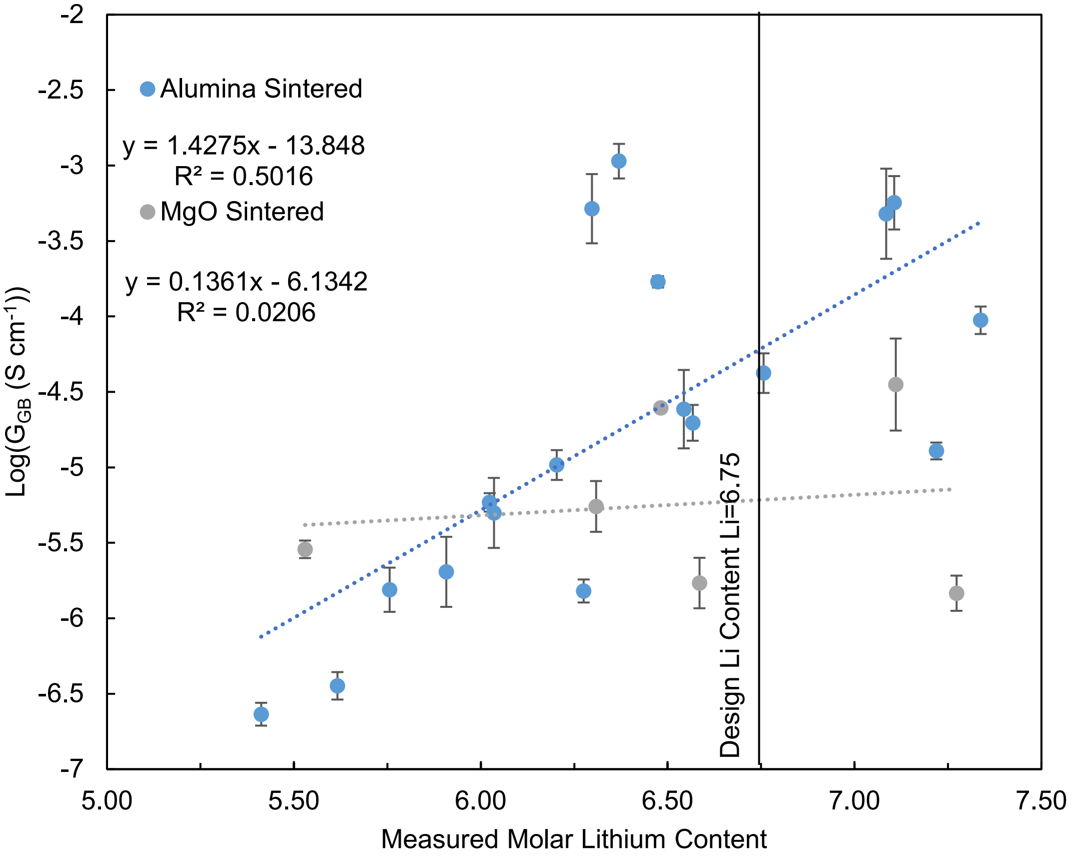

Figure 16. Measured grain boundary conductance versus measured lithium content for Al_2O_3 and MgO sintered samples

The σ_{Total} of LLCZNX generally rises with increases in lithium but reaches a maximum of 1.68×10^{-4} S cm^{-1} in LLCZN5-12Hr (Li=6.37) (Figure 17). This is similar to the MgO sintered samples where LLCZN5-MgO reaches a local maxima of 1.84×10^{-5} S cm^{-1} (Li=6.48). However, the σ_{Total} for MgO samples are more than a half an order of magnitude lower than the Al_2O_3 counterparts. Total conductivity follows the bulk conductivity and grain boundary conductance results by having a correlation with lithium more so than time (Figure S41 and S42). Samples with a measured lithium content below Li=6.30 have a linear correlation with lithium content but this does not continue when aluminum is introduced in the samples between Li=6.30 and Li=6.54. Aluminum migration reduces the linearity of the σ_{Total} trend while MgO samples showed limited linearity due to secondary phase formation throughout all samples. LLCZN5-12Hr (Li=6.37), LLCZN18-12Hr (Li=6.76), LLCZN20-24Hr (Li=7.08), and LLCZN15-12Hr (Li=7.11) combined high bulk conductivity with high grain boundary conductance. Contrastingly, secondary phase formation, such as $CaCO_3$ or $La_2Zr_2O_7$, or large amounts or aluminum migration appears to reduce σ_{Total} in the other samples.

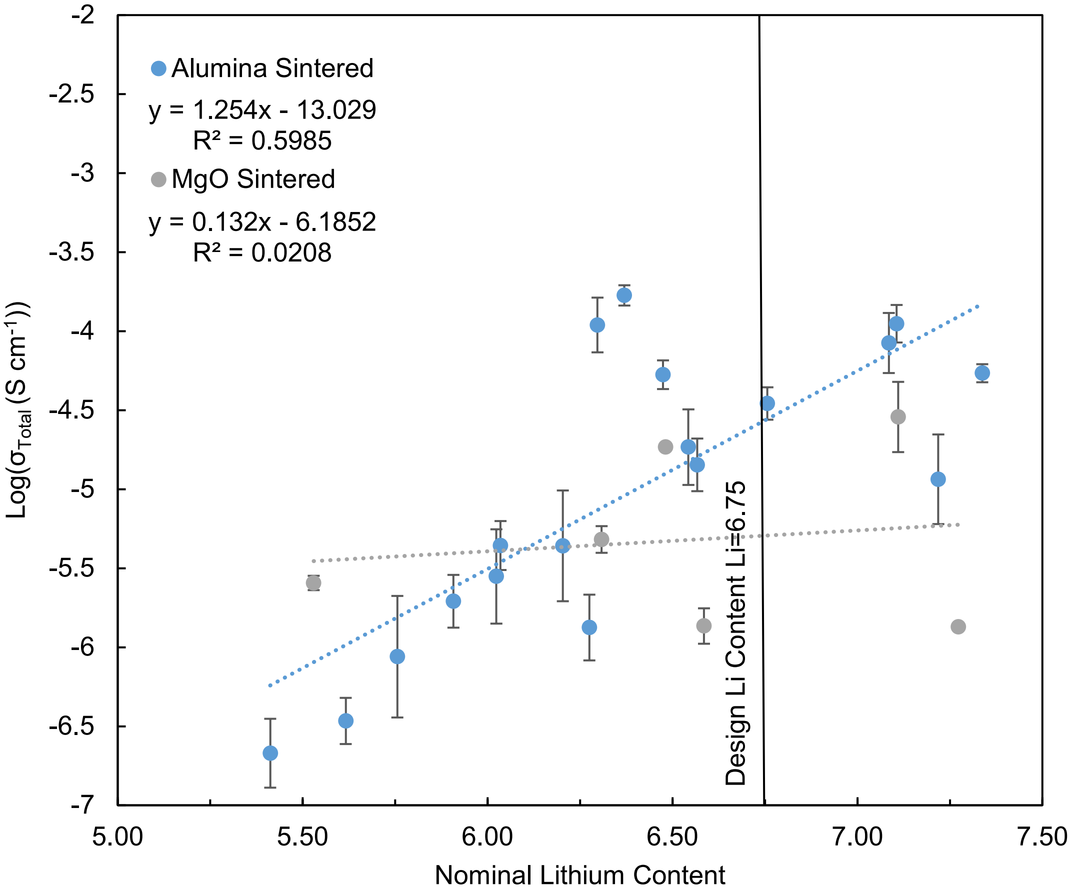

Figure 17. Measured total conductivity versus measured lithium content for Al_2O_3 and MgO sintered samples.

Crucibles play a critical role in the product's physical and electrochemical properties. An example not researched in this effort is platinum crucibles which have been shown to limit lithium loss when compared to alumina crucibles[166]. While without mother powder, MgO and platinum crucibles achieve high relative density (>90%) and σ_{Total} over 6.23×10^{-4} S cm^{-1} when sufficient excess lithium is added[185]. Excess lithium can account for lithium losses at sintering temperatures even without a powder bed but all the sintering conditions (size and type of crucible, temperature, time, rate, size of sample, etc.) will need to be optimized. The results of this study, combined with previous reported results, show lithium loss can be reduced during sintering and high bulk conductivity and grain boundary conductance can be achieved in a single sample when sufficient lithium is designed into the sintered electrolyte.

4. Conclusions

Lithium content is crucial for phase composition, microstructure formation, and ionic conductivity of LLCZN. In our work, excess lithium (X in LLCZNX) proved beneficial with a minimum of X=15% and sintered for at least 12 hours at 1100°C. Five samples sintered in Al_2O_3 crucibles had limited secondary phases and were at least 97% cubic LLCZN. While, sintering in MgO crucibles produced higher amounts of secondary phases, regardless of lithium content. Electrochemical results showed grain boundary conductance was correlated with lithium and aluminum from denser developed microstructures. This is exemplified in low lithium and low aluminum content samples that displayed porous structures and resulted in lower grain boundary conductance partially due to secondary phases blocking Li^+ conduction. Lithium rich samples sintered in Al_2O_3 crucibles, however, obtained denser microstructures and higher grain boundary conductance enabled by the Li_2O-Al_2O_3 eutectic liquid formed during sintering. Secondary phases or large amounts of aluminum appeared to reduce grain boundary conductance. In both sets of samples when measured lithium amounts were greater than Li=6.75, bulk conductivity achieved its maximum consistently at 10^{-4} S cm^{-1} as lithium measured in the correct stoichiometry. Future work will require merging the high grain boundary conductance and high bulk conductivity by maintaining sufficient lithium content and high density without excess aluminum or secondary phase formation.

Chapter 3: Improving Phase Stability during Co-sintering of LCO and LLZO for Reduced Interfacial Impedance

Abstract

Sintering improves particle-to-particle bonding thus reducing interfacial impedance, but co-sintering dissimilar materials leads to undesirable side reactions and inter-diffusion that increases interfacial impedance far more than the improved particle-to-particle bonding reduces it. This has been a major issue for co-sintering lithium ion conducting garnet and high voltage cathodes at the temperatures necessary to sinter both materials. Herein we successfully co-sintered $Li_{6.75}La_{2.75}Ca_{0.25}Zr_{1.5}Nb_{0.5}O_{12}$ (LLCZN) solid electrolyte and high voltage $LiCoO_2$ (LCO) cathode at 1050°C without detectable secondary phase formation by incorporating excess lithium into the LLCZN garnet prior to sintering. Thermal analysis indicates a reduction of the reaction between LLCZN and LCO when excess lithium was incorporated into LLCZN. The interfacial resistance between the composite cathode and LLCZN also decreased from 7000 to 2040 Ω cm^2 when excess lithium was introduced into the composite cathode. A solid-state cell was constructed by drop casting a composite cathode of LLCZN incorporated with excess lithium, and LCO, which was then co-sintered with an LLCZN solid electrolyte layer. The cell showed reduced interfacial resistance and achieved 84 mAhr g^{-1} while operating at 45°C.

Keywords

Solid State, LLZO garnet, Co-Sintering, Lithium Cobalt Oxide

1. Introduction

Lithium ion-conducting solid-state electrolytes (SSE), such as lithium garnet $Li_7La_3Zr_2O_{12}$ (LLZO), have achieved ionic conductivities comparable to liquid electrolytes[186]. SSEs may also operate with high voltage cathodes (>4V) to obtain practical gains in energy density over state-of-the-art rechargeable lithium based batteries. Transition metal oxide cathode materials, such as $LiCoO_2$ (LCO), offer an opportunity to achieve high voltage operation with LLZO SSEs[187]. In commercial lithium ion batteries, LCO is combined with a binder and electronically conducting material, such as carbon black, to form composite cathodes where the liquid electrolyte is infiltrated between cathode particles to provide pathways for ionic conduction[188]. Without a liquid electrolyte, ionic transport between active cathode particles would be insufficient for practical operation[189]. Therefore, solid state batteries similarly require a continuous SSE network through the cathode for ionic conductivity, as has been demonstrated for solid-state lithium-sulfur cells with lower operating voltages[190].

SSEs have additional interfacial resistances between the solid electrolytes and the electrodes. High interfacial resistance (10^2-10^3 Ω cm^2) between LLZO electrolytes and lithium metal anodes can be caused by the rigid solid contact on the anode/electrolyte surface[191]. This is further complicated through the reaction of LLZO with air where non-conductive species are formed on the surface of LLZO, increasing interfacial resistance[192]. Likewise, the interfacial impedance of the cathode introduces similar issues where cathode and solid electrolyte preparation play a role in the uniformity of the cathode-solid interface. The interfacial impedance will be reduced if the cathode uniformly coats the solid electrolyte and minimizes voids between itself and the SSE[193,194].

Additionally, volume changes in the cathode during cycling can cause delamination at the cathode-electrolyte interface, reducing the interfacial contact area and increasing interfacial resistance in the composite cathode[195]. This volume expansion and contraction can be alleviated by using a lithium ion conducting polymer as a soft ion conducting interface in composite cathodes[196]. However, the additional layer can contribute to increased impedances due to impedances inherent to the polymer itself as well as at the SSE-polymer-cathode interfaces.

Solid oxide fuel cells encounter similar conduction and interfacial issues. One mitigation strategy is to co-sinter an electron-conducting electrode and an ion-conducting electrolyte material to create two different solid conduction networks through a composite electrode. This is complicated by the movement of the transition metals from one species to the other during sintering, reducing oxygen conductivity and leading to cell failure[197-199]. However, matching the sintering temperatures of the two materials can improve transport properties by creating a denser network[200]. The ionic and electronic conductivities of the co-sintered electrodes require phase stability and minimized inter-diffusion to operate efficiently.

In co-sintered composite cathodes for LLZO electrolytes, LCO acts as both the active cathode material and the electronic conductor where LLZO garnet provides ionic conductivity. However, co-sintering temperatures cause lithium and oxygen losses in both phases, where the lithium-deficient cobalt oxide and the lithium-deficient garnet react and form non-conductive species such as $LaCoO_3$, hindering both ionic and electronic transport[201]. Studies show $LaCoO_3$ formation occurs rapidly at 1085°C but can be potentially controlled below that temperature[202-203]. Previous computational results suggest that lithium coatings may protect both species[204] by forming a reservoir of lithium for LLZO and LCO to consume during co-sintering without forming $LaCoO_3$. This is further strengthened by recent computational results indicating additional lithium in the garnet phase can improve thermodynamic stability for co-sintering[205]. In that paper a potential reaction pathway is discussed where lithium content was found to play a role in the stability of both species. The decomposition products of a delithiated $Li_{0.5}CoO_2$ with LLZO was computed to find decomposition of the LLZO into nonconductive $La_2Zr_2O_7$ and La_2O_3. This is in addition to previous reported experimental results (Table 6) that vary in stability between LLZO and LCO at different temperatures and times, sintering aids, and composition [201,206-214].

Preparation of Composite Cathode	Temperature (°C), Time (hr.)	Cathode (wt%)	LLZO Garnet (wt%)	Sintering Aid (wt%)	XRD Detected Secondary Phase Formation?	Citation
LCO Deposited on Sintered Garnet	500	N/A (LCO)	N/A	N/A	No	206
Mixed Powders	790, 48	42% (LCO)	23%	35% (L_3BO_3)	Yes	207
Powders Mixed in Solvent and Caste on Lithium Garnet Pellet	700, 1	58% (LCO)	30%	12% ($Li_{2.3}C_{0.7}B_{0.3}O$)	Yes	208
Mixed Powders	700, 10	50% (LCO)	50%	None	No	209
LCO Pulse Deposited onto Sintered Garnet	700, 2	50% (LCO)	50%	None	No	210
Mixed Powders in Slurry and Pasted on Sintered Lithium Garnet	700, 1	75% (LCO)	25%	None	Inter-diffusion Detected	211
Mixed Powders in Slurry and Pasted on Sintered Lithium Garnet	700, 1	58% (NMC)	30%	12% (Li_3BO_3)	Yes	212
Mixed Powders in Slurry and Pasted on Sintered Lithium Garnet	700, 1	43% (NMC)	30%	27% (Li_3BO_3)	Yes	213
Powders Ball Milled and Dried	900, 24	50% (LCO)	50%	None	Yes	214
Mixed Powders Including 20% Excess Lithium in Lithium Garnet Powder	1050, 2	50% (LCO)	50%	None	No	201
Mixed Powders with 40% Excess Lithium in LLZ Powder	1050, 4	50% (LCO)	50%	None	No	This Work

Table 6. Reported examples of co-sintering cathode materials with lithium garnet at various temperatures and times vs. the degree of phase stabilization.

Table 6 displays mixed stabilization results during co-sintering with differing amounts of lithium, various sintering conditions, and different cathode materials. At the high temperatures typically employed for sintering, above 1000°C, lithium volatizes out of the LLZO and begins to form secondary phases, but this can be stopped with additional lithium[215]. LCO also undergoes a loss of oxygen above 250°C and forms Li_xCoO_2 (layered), $Li_xCo_{3-x}O_4$ (spinel), and $Li_xCo_{1-x}O$ (rock-salt)[216], which all may react with LLZO and $La_2Zr_2O_7$. Excess lithium during annealing of LCO has been shown to stabalize $LiCoO_2$ under atmospheric conditions, stopping the decomposition of the structure[217]. Without additional lithium when co-sintering LCO and LLZO, $La_2Zr_2O_7$ begins to form starting at 600°C before reacting with the LCO and forming $LaCoO_3$ at 700°C, well below the required sintering temperature of LLZO[218] (eq 12). Excess lithium has been shown to stop the decomposition of both LLZO and LCO during annealing, which may prove beneficial during co-sintering (eq. 13).

$$LLCZN + LiCoO_2 \rightarrow Li_{6.75-x}La_{2.75-y}CZN + (1-y)LiCoO_2 + yLaCoO_3 + xLi_2O \tag{12}$$

$$Li_{6.75+x}LCZN + LiCoO_2 \rightarrow Li_{6.75}LCZN + LiCoO_2 + xLi_2O \tag{13}$$

The relationship between high temperature co-sintering and lithium content should be explored for co-sintered LLZO and LCO to optimize the necessary transport pathways and decrease interfacial resistances. In this study, various amounts of excess lithium were added to LLZO and co-sintered with LCO. The structural stability of the resulting co-sintered LLZO/LCO phases was determined and microstructural differences were analyzed to examine the structure of the conductive pathways formed. Half-cell cycling explored co-sintering effects on the electrochemical performance of the LCO to further evaluate the conductive pathways formed during co-sintering.

2. Experimental

In this work, $Li_{6.75}La_{2.75}Ca_{0.25}Zr_{1.5}Nb_{0.5}O_{12}$ (LLCZN) was prepared via previously reported LLZO garnet processing methods[219] with compositions of -10, 10, 30, or 40% deficient or excess weight percent of lithium. The prepared LLCZN is denoted by LLCZNX, where X indicates the weight percent of lithium, e.g. LLCZN10 corresponds to LLZCN with 10 wt% excess lithium. The calcined LLCZNX was ball-milled in IPA (isopropanol, Alfa Aesar >99.7%) for 24 hours to ensure the breakup of larger conglomerates. Raman spectroscopy was performed on these ball milled powders (Horiba LabRam HR with a 532 nm Ar^+ laser as the excitation source)

Mixtures of LLCZNX and LCO (Sigma Aldrich, 99.8%) in ratios of 50/50 wt% were ground and mixed in a mortar and pestle, designated as LLCZNX/LCO. Dynamic scanning calorimetry (DSC) and thermal gravimetric analysis (TGA) were performed on the mixtures in an argon environment between 200°C and 1100°C at 10°C $minute^{-1}$ (Perkin Elmer STA 8000). LLCZNX/LCO powder samples were co-sintered in an Al_2O_3 crucible under atmospheric conditions at 3°C $minute^{-1}$ to 1050°C and held for 4 hours before cooling to room temperature. X-ray diffraction (XRD) was performed on the co-sintered powders to characterize phase purity (Bruker D8 Advance, Cu-kα), with lattice parameters and phase percentages calculated using Rietveld refinement. The fitting parameters used for LLCZN, LCO, and $LaCoO_3$ are included in Table S13-15.

Composite cathodes were constructed using co-sintered LLCZNX/LCO powders, electronically conducting carbon black, and polytetrafluoroethylene (PTFE) in 80/15/5 weight ratios. The composite cathodes were formed by mixing the three species in a mortar and pestle, calendaring, and then cutting into 16 mm discs. The discs were placed into CR 2025 cells topped with three glass separators that were flooded with 1 M $LiPF_6$ in 50:50 v/v% ethylene carbonate and dimethyl carbonate mixture (Sigma Aldrich) as the organic liquid electrolyte (OLE), and lithium metal (MTI 99.9%) as the anode. These half cells were cycled at 1 mA (0.5 mA cm^{-2}) between 4.2 V and 3.0 V for 50 cycles to determine the electrochemical performance of co-sintered LLCZNX/LCO. All cycling was performed on an ARBIN MSTAT4 battery cycler.

LLCZN with 5% excess lithium (LLCZN5) was prepared and calcined as previously performed for LLCZNX. LLCZN5 was used as the solid electrolyte (SE) for partially solid-state cell testing with the co-sintered cathode. To prepare the SE pellet, 0.3 grams of LLCZN5 was pressed into a 12 mm pellet, placed in an Al_2O_3 crucible, and covered in a bed of mother powder to reduce lithium loss. The pellet was sintered in air at 1100°C for 12 hours, with temperature ramp of 3°C per minute, and allowed to cool to room temperature. Meanwhile, mixtures of LLCZNX and LCO were prepared with the weight percent listed in Table S16 and ball milled using 5 mm yttrium stabilized ZrO_2 milling media (Advanced Material) for 1 hour. The mixtures were drop cast onto the sintered LLCZN5 and dried for an hour at 80°C. Bilayer cells and symmetric cells were constructed with cathode on one side (bilayer) or on both sides (symmetric), respectively. The pellets with cathodes were placed in Al_2O_3 crucibles and heated in air to 700°C at 3°C per minute, held for 30 minutes to remove organics, then heated to 1050°C at 3°C per minute and held for 12 minutes to sinter before cooling to room temperature.

Raman spectroscopy was performed on the co-sintered cathode for phase analysis and scanning electron microscope (SEM) images were taken on the fractured edges for microstructure analysis. A carbon-PTFE mixture (85-15 wt%) was prepared using the same procedure as for the composite cathodes and placed on top of the electrodes of the symmetric cell as an ion blocking layer. The symmetric cells were placed between two stainless steel plates for EIS measurements with 10 mV magnitude and 1 MHz to 0.1 Hz frequency range (Solartron SI 1260). Partially solid state half-cells were also constructed with lithium metal, a single glass separator soaked in an OLE of 1M $LiPF_6$ 45:45:10 v% of diethyl carbonate (DEC):ethylene carbonate (EC): fluoroethylene carbonate (FEC) for LLCZN stability[220], a LLCZN pellet with one co-sintered composite cathode (bilayer), and the carbon-PTFE mixture on top of the co-sintered cathode as a current collector. The partially solid-state half-cell was placed between two stainless steel plates. EIS measurements were taken of each solid-state cell using the same parameters as previously mentioned. The LLCZN40/LCO bilayer partially solid-state cell was cycled between 4.2 and 2.7 volts at 45°C.

3. Results and Discussion

3.1 Powdered Composite Samples

Co-sintering LLCZNX/LCO powder at 1050 °C for four hours elucidates the effects of supplemental lithium with LLCZN on the LLCZNX/LCO co-sintering process. The XRD patterns of the co-sintered powders (Figure 18) show that 40% excess lithium minimizes detection of the non-conductive, secondary phase $LaCoO_3$. Likewise, as the ratio of lithium to LLCZN decreases, the magnitude of the $LaCoO_3$ peaks increases, demonstrating the impact of lithium deficiency on $LaCoO_3$ formation. This trend also occurs with the lattice parameters where larger lattice parameters are seen in samples with more lithium (Table S17). This method of dispersing lithium species throughout the powder is like previous reports in which Li_2CO_3 and Li_3BO_3 are used as sintering aids during co-sintering at 700 °C[208.] However, our results demonstrate structural stability closer to typical sintering temperatures of LLCZN.

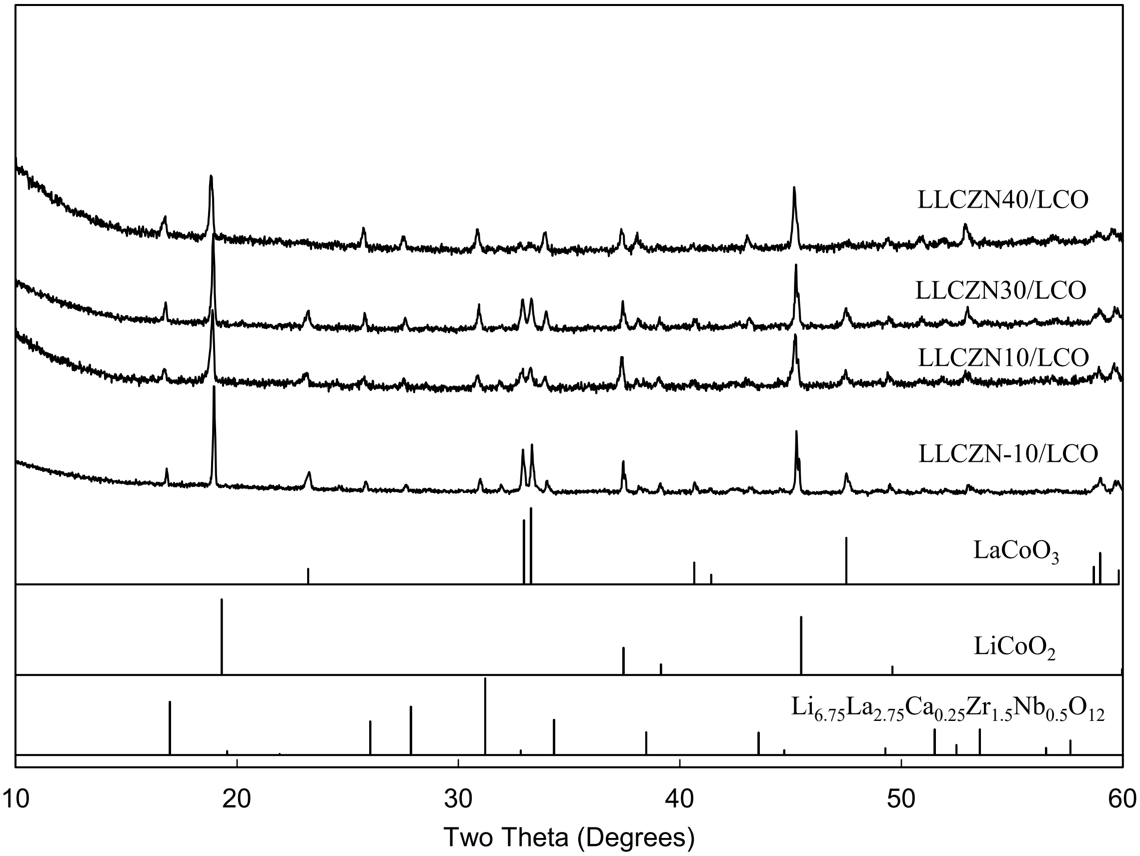

Figure 18. X-Ray diffraction pattern of LLCZNX/LCO powder mixtures calcined at 1050°C for four hours. Bottom patterns are LLZO ICDD-PDF 00-019-8837, LCOI*CDD*-PDF No. 01-070-2685, and $LaCoO_3$ ICDD-PDF 00-048-0123[221].

The calculated phase percent of LLCZN, LCO, and $LaCoO_3$ phases is plotted against X in LLCZNX (Figure 19). The Rietveld refinement fitting results are included in Table S17 and an example of the fit in Figure S43. A mass balance of the results and comparing them to the original weights of LLCZNX and LCO shows the mass of the original reactants are below 50% of the original mixture (Table S19). The 50/50 weight ratio of the samples prior to co-sintering included LLCZNX powders that had undergone a reaction during ball milling in IPA, resulting in weight gain as indicated by peak in the Raman spectroscopy results at 1100 cm^{-1} (Figure S44) [222]. This weight gain during the secondary ball milling step in IPA has been shown to be over 15% of the sample, with more reactions potentially occurring from the water in the air[215]. Thus, the co-sintered mixtures could not maintain the 50/50 wt. % ratio after these reaction products decomposed during co-sintering. Nonetheless, the phase percent trend does match $LaCoO_3$ peak intensities in the XRD patterns. There is an increase in phase retention in LLCZN10/LCO and LLCZN30/LCO compared to LLCZN-10/LCO. In LLCZN40/LCO, the two conductive phases, LCO and LLCZN, increase by 9% as $LaCoO_3$ is minimized. The extra supply of lithium in the mixture indicates a reduction in the reaction between LLCZN and LCO, enabling an increase in phase percentage of both desired phases.

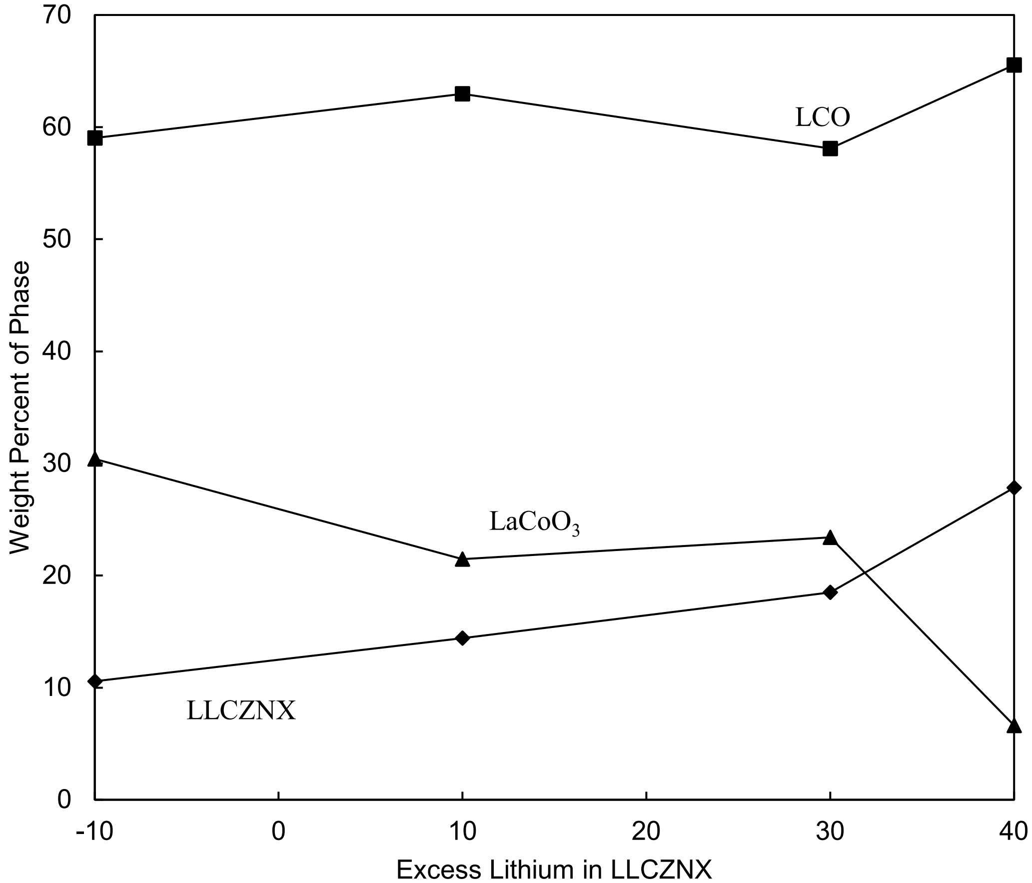

Figure 19. Weight percent of phases found in XRD patterns. Squares are LCO, diamonds are LLCZN, and triangles are $LaCoO_3$.

The TGA thermograms (Figure 20) of the LLCZNX/LCO powder mixtures demonstrate weight loss over several temperature ranges. The weight decrease at 400°C is the breakdown of the secondary species on the surface of LLCZNX, further indicated by the TGA results of the individual powders (Figure S45a). Between 400 and 600°C, the weight loss in the mixtures can be attributed to the breakdown of the hydroxides on the LLCZNX to oxides[223] while the final products of the reaction formed during ball milling begin decomposition at 700°C and are very similar magnitudes. However, there is an increase in peak height as X in LLCZNX increases between 800 and 900°C (Figure 20b). Based on previously reported results, it appears this is caused by a reaction between LLCZNX and the IPA ball milling step and is observed in the neat LLCZNX powders as well[215]. After this weight loss, all mixtures experience significant weight reductions starting at the co-sintering temperature used in this work, 1050°C. This weight loss is not detected at the same magnitude in the neat LLCZNX samples but is detected in the neat LCO samples (Figure S45a), meaning a higher percentage of weight loss can be contributed to the reaction with LCO.

Thermal analysis via DSC (Figure 21) of the LLCZNX/LCO powder mixtures reveals endothermic reactions between 300°C and 400°C in the same temperature range where TGA analysis conveys weight loss due to breakdown of secondary species Li_2CO_3 melting is also indicated by the peak at 723°C, which grows in peak height as lithium content increases in LLCZNX as seen in DSC data of the individual powders (Figure S45b) and in the DSC data of LLCZNX/LCO mixtures (Figure 21). The differences between LLCZNX/LCO samples with varied lithium contents are explicit after 1050°C where plots of LLCZN-10/LCO, LLCZN10/LCO, and LLCZN30/LCO show two visible peaks at 1055°C and 1085°C. LLCZN40/LCO data has only one visible peak indicating limited reaction between the LLCZN and LCO phases before 1085°C caused by excess lithium content.

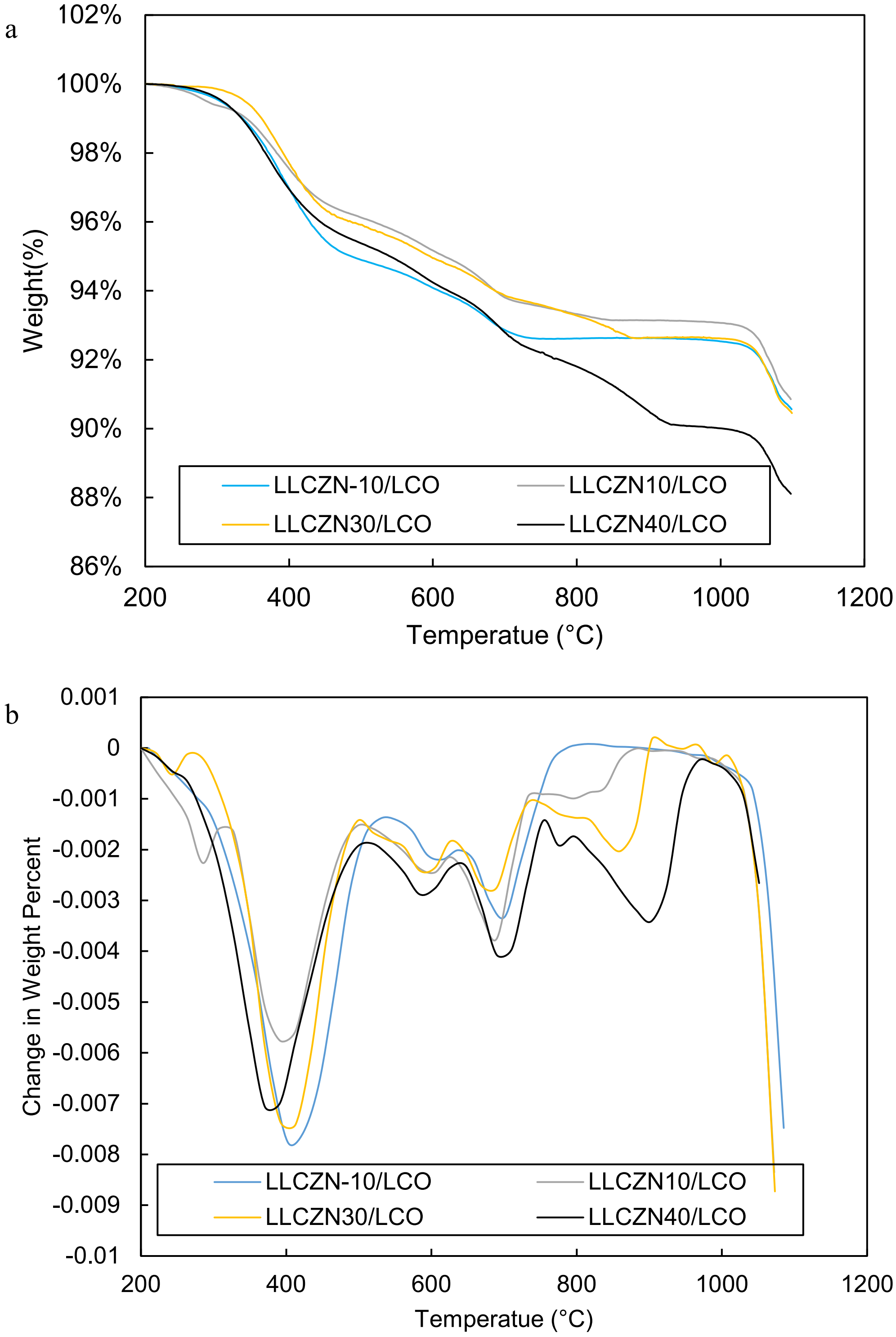

Figure 20. TGA thermograms of the LLCZNX/LCO samples. **Figure 20a.** Weight percent of the LLCZNX/LCO samples. **Figure 20b.** Change in weight percent by change in temperature of the samples in Figure 3a. Larger peaks in Figure 3b indicate steeper slopes of weight loss in Figure 3a.

Excess lithium in LLCZN40 limits the detectable reaction that can form either nonconductive species $La_2Zr_2O_7$[205] or $LaCoO_3$ (eq. 12), during co-sintering between LLCZN and LCO. These nonconductive phases can reduce the impedance in a dense co-sintered cathode and hinder performance. This can be mitigated with the excess lithium to reduce the decomposition of the LLCZN and LCO, which decreases $LaCoO_3$ formation (eq. 13). The XRD in Figure 18 showcases this benefit but there does appear to be peak broadening in several samples. This may indicate some interdiffusion between species, which will need to be studied further. Nevertheless, the two phases can be co-sintered to reduce nonconductive phase formation and can create separate ionic and electronic dense conduction networks which will eliminate carbon and binders from the composite cathode, potentially increasing volumetric and gravimetric energy densities. Likewise, co-sintering limits resistance by forming two solid conducting networks without forming the secondary phases that can increase grain-grain resistance. Lastly, this method has the potential to create a solid electrolyte and composite cathode in a single sintering step thereby eliminating Li_2CO_3 formation on the SSE-cathode interface that would increase interfacial impedance on the cathode-SSE interface. However, the time and temperature of the sintering step require optimization to ensure secondary phases are not formed and pathways for conduction are sufficient.

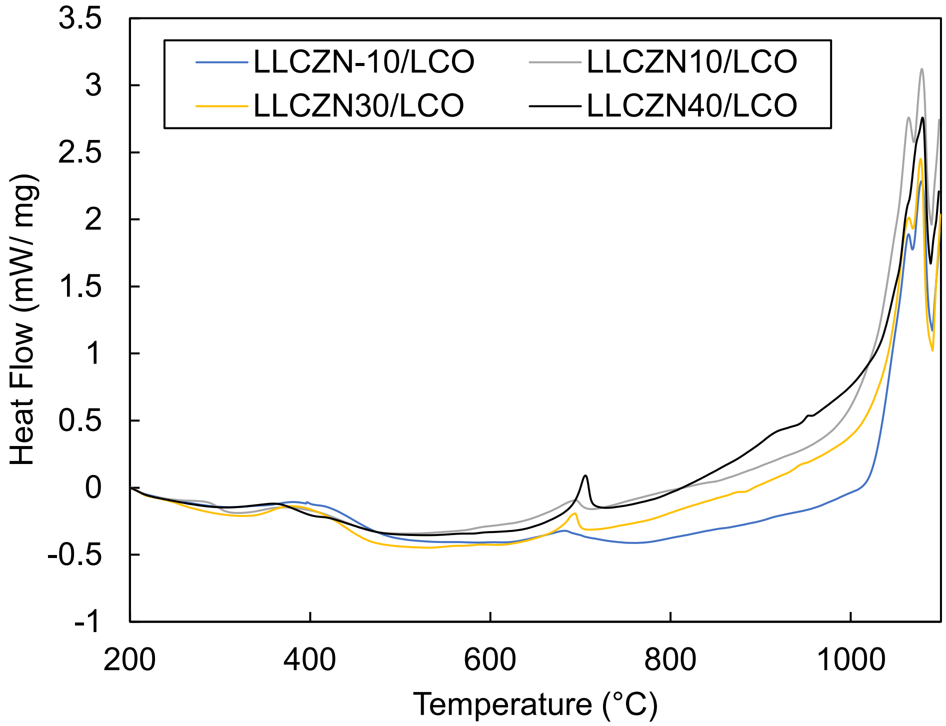

Figure 21. DSC traces for the LLCZNX/LCO mixtures. Endothermic is up and exothermic is down.

3.2 Co-sintered Cathode with a Solid State Electrolyte

Raman spectra (Figure 22) of the co-sintered LLCZNX/LCO composite cathode on LLCZN5 conveys comparable information as the XRD patterns of the corresponding co-sintered powder. The bands below 150 cm^{-1} are credited to the lanthanum cations in LLCZNX[224]. While the low frequency range for Raman (<300 cm^{-1}) corresponds to the LiO_6 octahedral ($96h_{Li1}$ position), the middle frequency (300-550 cm^{-1}) to the LiO_4 tetrahedral ($24d_{Li1}$ position), the band at 690 cm^{-1} is to the ZrO_6 octahedral[225], and the band at 717 cm^{-1} is assumed to be Nb signal, all in LLCZN. The two large peaks at 478 and 590 cm^{-1} are attributed to vibrational modes of LCO[226]. There does not appear to be secondary phase detection in any sample. However, there exists difficulty in detecting small amounts at the interfaces between the species. Overall, as lithium content increases, the LLCZN bands become more prominent, which may be a result of LLCZN phase remaining more intact with increasing lithium. Furthermore, the niobium peak is only detected in LLCZN40/LCO showing that LLCZN structure maintains niobium detection while the other samples do not. The elimination of the La peak at 125 cm^{-1} in LLCZN-10/LCO is similar to the powdered sample XRD analysis that concluded LLCZN is a minor phase with limited excess lithium in LLCZNX. In contrast, the garnet peaks in LLCZN40/LCO become less distorted, indicating excess lithium decreases the reaction between LLCZN and LCO even when drop casted onto an SE. This is beneficial for the electrochemical properties of the composite cathode.

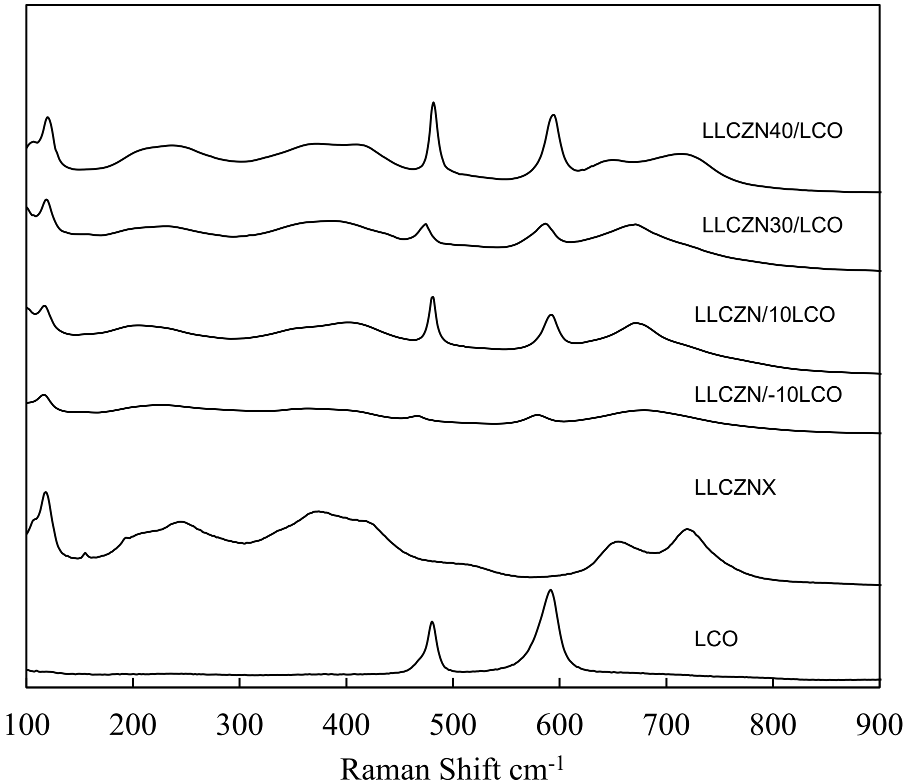

Figure 22. Raman spectra of co-sintered composite LLCZNX/LCO pellets.

SEM and back scatter electron (BSE) images (Figure S46a-d) of the co-sintered LLCZNX/LCO composite co-sintered cathode display similar microstructures independent of lithium content. Additionally, two separate phases are observed in the BSE images, showing the

LCO and LLCZN are separate phases. This is important for creating two separate conduction networks. The images also show a uniform coating on the LLCZN5 dense layer, minimizing the effects of physical differences between cathode and electrolyte on the interfacial resistances. The reported onset densification temperature of LCO is 800°C[227] and appears to sinter into a dense network in most of the samples. LCO densification activation and sintering may occur independent of the lithium content in LLCZNX, meaning the electronic transport attributed to LCO should remain high in these samples.

Conversely, LLCZNX, independent of X, appears to have grain boundaries which will increase Li^+ resistance and limit ionic transport during cell operation. This may be due to a combination of factors, not limited to the decreased sintering temperature, sintering dissimilar materials, and reduced time at the sintering temperature. Lower sintering temperatures are reported in literature but most utilize sintering aids such as Al[228], CeO[229], and glass additives[230] or dopants like Mg[231]. The use of sintering aids would beneficially reduce the amount of lithium required and allow for longer sintering times. Future work should focus on reducing the sintering temperature of LLZO garnet to increase the density of the composite co-sintered cathode.

3.3 Electrochemical Performance

Ionic and electronic conduction has been shown to occur through LLZO when doped with cobalt, but the reported electronic conductivity of 2.75×10^{-6} S cm^{-1} was orders of magnitude lower than the reported ionic conductivity of 10^{-4} S cm^{-1} [232]. Charge transport of Li^+ and e^- also occurs over the interfaces of both phases, making the mixture behave differently than the sum of the individual components. Thus, co-sintering will require electrochemical cycling to determine operational feasibility. In examination of the effect of co-sintering on capacity, co-sintered powders in liquid cells show increases in both capacity and capacity retention with increasing lithium content in LLCZNX (Figure 23a and b, and Figure S46). The first cycle shows a standard discharge curve for most but LLCZN-10/LCO and LLCZN10/LCO do show a second discharge plateau, potentially from interdiffusion between the LLCZN and LCO. With further cycling, the increase in capacity occurs from 50 mAhr g^{-1} in LLCZN-10/LCO to 120 mAhr g^{-1} in LLCZN40/LCO at cycle 50. LLCZN-10/LCO is mainly $LaCoO_3$ that blocks Li^+ and e^- resulting in 60% capacity loss to 50 mAhr g^{-1}. With increasing lithium, LLCZN10/LCO and LLCZN30/LCO had ~20 wt% of $LaCoO_3$ and reduces their performance to 101 and 106 mAhr g^{-1}, respectively. This may be the result of $LaCoO_3$ formation slowing Li^+ and e^- conduction into the LCO grains. LLCZN40/LCO measures 113 mAhr g^{-1} after several cycles where the lower capacity may be from cell construction and the small amount of $LaCoO_3$. The capacity results indicate co-sintering does not severely damage achievable capacity in LLCZN40/LCO but will need to be designed into a solid-state cell to determine its full effect.

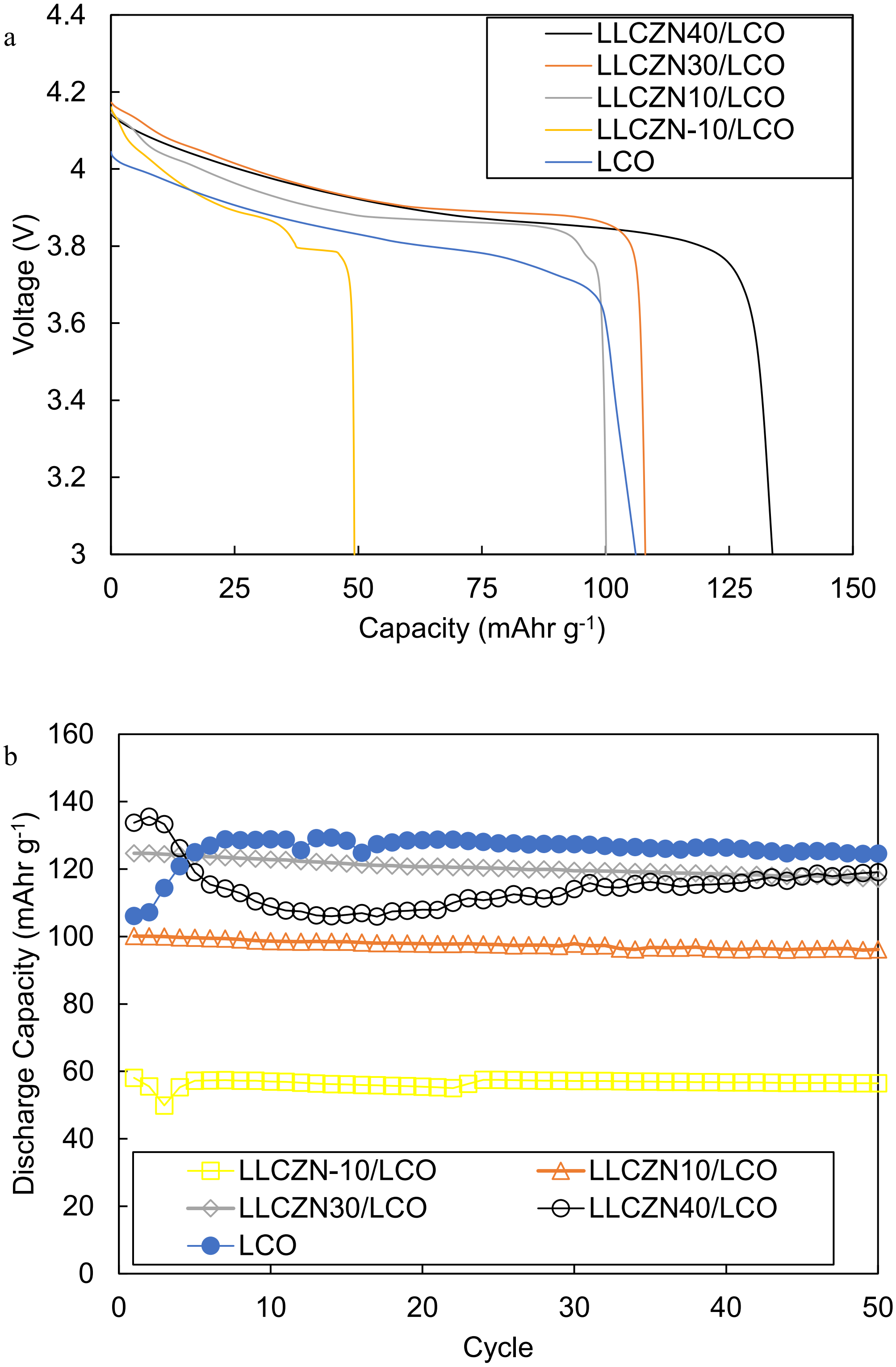

Figure 23. Liquid cycling of composite cathode. **Figure 23a**. First cycle of composite cathode in a liquid cell. **Figure23b**. Capacity vs. cycle for liquid cell

Using the pellets with one (bilayer) or both electrodes (symmetric) attached to the SSE requires pure LLCZN as the solid SSE layer. The phase purity and dense microstructure of the SSE layer in both configurations are confirmed through Raman and SEM (Figure S48 and S49) analysis. Interfacial resistance (R_{INT}) of the co-sintered cathodes in the symmetric cells with two electrodes shows a reduction of resistance with increasing lithium content (Figure 24a and b). The type of resistance is confirmed through capacitance values[233] and an appropriate fitting (example and model in Figure S50). There are two visible semicircles with a Warburg tail in each sample where the second semi-circle reduces in magnitude in samples with larger quantities of lithium. The samples, based on the sample set up, have four resistances that were also identified using the capacitance values. The capacitance values show four areas: the first 10^{-11} to10^{-10} F is bulk resistance, 10^{-9} to 10^{-8} F is grain boundary resistance, 10^{-6} F is the interface[234], and 10^{-4} F is the electrode/current collector. These contributions can also be further analyzed by transforming the EIS data using distribution of relaxation frequency (DRT) (Table S20).

DRT when combined with EIS data is used to identify the characteristic distribution of EIS timescales and help inform parts of the EIS model. The MATLAB GUI DRT tools, provided by Wan et al.[235], shows the EIS data has four distinct sections for relaxation times (Figure S51). The first section around 10^{-6} s can be attributed to the bulk resistance. The next section between 10^{-5} and 10^{-2} s includes a major peak and several minor peaks. These peaks, along with the capacitance values, indicate grain boundary resistance of the LLCZN5 layer[236]. The peaks do not occur at consistent time constants, which may indicate different compositions of the grain boundaries based on the lithium content. The next section around 10^{-1} s is presumed to be the interface between LLCZX and LCO. The capacitance values range between 10^{-7} and 10^{-5} F, which is within other interfacial impedance ranges for LLZO type electrolytes and the electrodes. Much like the grain boundary section, the time constants shift of LLCZN-10/LCO indicates a slower time constant. The last impedance section in DRT is between the cell and the current collector as evidenced by the slow conduction time and the capacitance values below 10^{-5} F. Using these frequencies, the model can be compared to the physical system under test. Using the model results, the relaxation frequencies can be calculated and then compared to the capacitance and DRT results.

Relaxation frequencies can be calculated with the EIS fitting results to determine if there is overlap between the fitting results. The results show four distinct areas going from bulk (fast) to electrode (slow) (Table S21). These calculations can also assist in determining electrochemical processes in the modeled EIS and confirm the DRT peaks. The DRT peaks, the capacitance values, and the relaxation frequencies each indicate there are four distinct sections for each resistance: bulk, grain boundary, interface, and electrode. The results allow for the interfacial impedance to be determined in our samples.

Increasing lithium content in the LLCZNX appears to maintain the LLCZN and LCO structures indicated by the Raman results. Non-detected secondary phases on the surface of LLCZNX/LCO would increase R_{INT} and negatively impact cell operation. These secondary phases may be present in LLCZN-10/LCO and LLCZN10/LCO as both have larger interfacial resistances and reduced signals of both the added elements in Raman results. Meanwhile, LLCZN30/LCO and LLCZN40/LCO have strong LLCZN and LCO signals in the Raman spectra while also having lower interfacial resistance. This does not preclude formation of other phases, such as $LaCoO_3$, but even with limited formation, there is a detected electrochemical benefit of adding lithium. However, there is an increase in R_{INT} from LLCZN30/LCO to LLCZN40/LCO that could result from a combination of Li_2CO_3 formation on the surface that has not been consumed or the benefit of added lithium on R_{INT} reaches a long plateau with increasing lithium. Either way, the benefit of adding extra lithium to the LLCZNX is seen in the EIS and fitting results as shown in Figure 24.

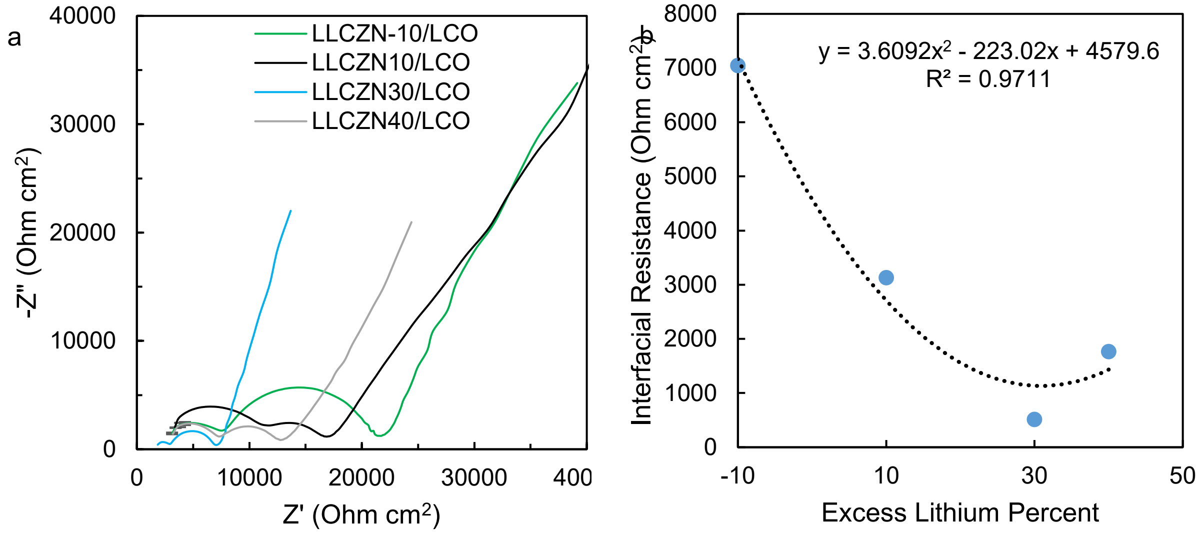

Figure 24a. EIS data of the symmetric pellet with co-sintered cathodes as electrodes and LLCZN5 as the SSE layer. **Figure 24b.** R_{INT} vs. excess lithium from the fitting of the EIS results.

Percolation theory considers the surface area of species, radii, and uniformity of the particles to determine a 30% volumetric threshold is required to enable complete pathways for conduction in two phase systems[237]. LLZO type SSEs have a theoretical density of ~5.1 g cm^{-3} [230] and LCO has a density of 5.05 g cm^{-3} [238]. Incorporating Rietveld refinement results of the powder reveals the volume percentage of LLCZN40, the Li^+ conductor, is ~30 v% of the composite cathode, barely clearing the 30 v% threshold but within the error of falling below it. The volume percentage analysis indicates the ionic conductivity of the LLCZNX species may have a limited contribution to the ionic conductivity of the composite cathode. Higher amounts of LLCZNX can be used to increase the ionic conductivity and rate potential of full cells but would potentially reduce the energy density of the composite cathode by reducing the amount active material present. However, depending on the thickness of the composite cathode, more LLCZNX would be beneficial to allow full cathode utilization. Future work should focus on the optimal amount of LLCZNX to optimize cell operation and energy density. The operational implications for this work, such as cathode utilization, can be determined using a partially solid cell with a single fully solid cathode.

The cycling of the partially solid-state cell with the co-sintered LLCZN40/LCO that operates at 45°C shows stable performance for 50 cycles when cycling at 6.75 μA cm^{-2} (Figure 25a and b). The initial rate of 12.5 μA cm^{-2} was not stable and results in quickly decreasing capacity, partially from high total cell resistance (Figure S52). LLCZN-10/LCO, LLCZN10/LCO, and LLCZN30/LCO also measure high resistance, but none can charge, likely from the amount of LLCZNX being below the 30% volumetric threshold and $LaCoO_3$ formation. However, the LLCZN40/LCO cell is able to achieve 90 mAhr g^{-1} after slowing the rate at cycle 7 and continuing through cycle 50 while measuring 45 mAhr g^{-1} at termination. The loss of capacity can be explained by non-optimized sintering conditions that did not create a fully dense microstructure. This is further confirmed by the differential capacity plot (Figure 25c) which indicates a shrinking peak during cycling, rather than a shift to the left or right, a typical indicator for increasing resistance. The loss of capacity is most likely from disconnection of the LCO from the conduction network in the all-solid-state cell. This will need to be overcome with optimized sintering conditions that promote sintering the conduction networks or a softer conduction network that can be used to expand and contract during cycling. Likewise, the results do not preclude electrolyte leakage where the OLE from the anode leaks to the cathode, which would reduce resistance. Nonetheless, the results indicate the potential for creating a cell with a co-sintered cathode and SE.

Future work should focus on densifying the composite cathode and LLCZN layer in a single sintering step that sinters both the cathode and electrolyte layer while utilizing a lithium metal anode without an OLE sufficiently to reduce capacity loss during electrochemical cycling.

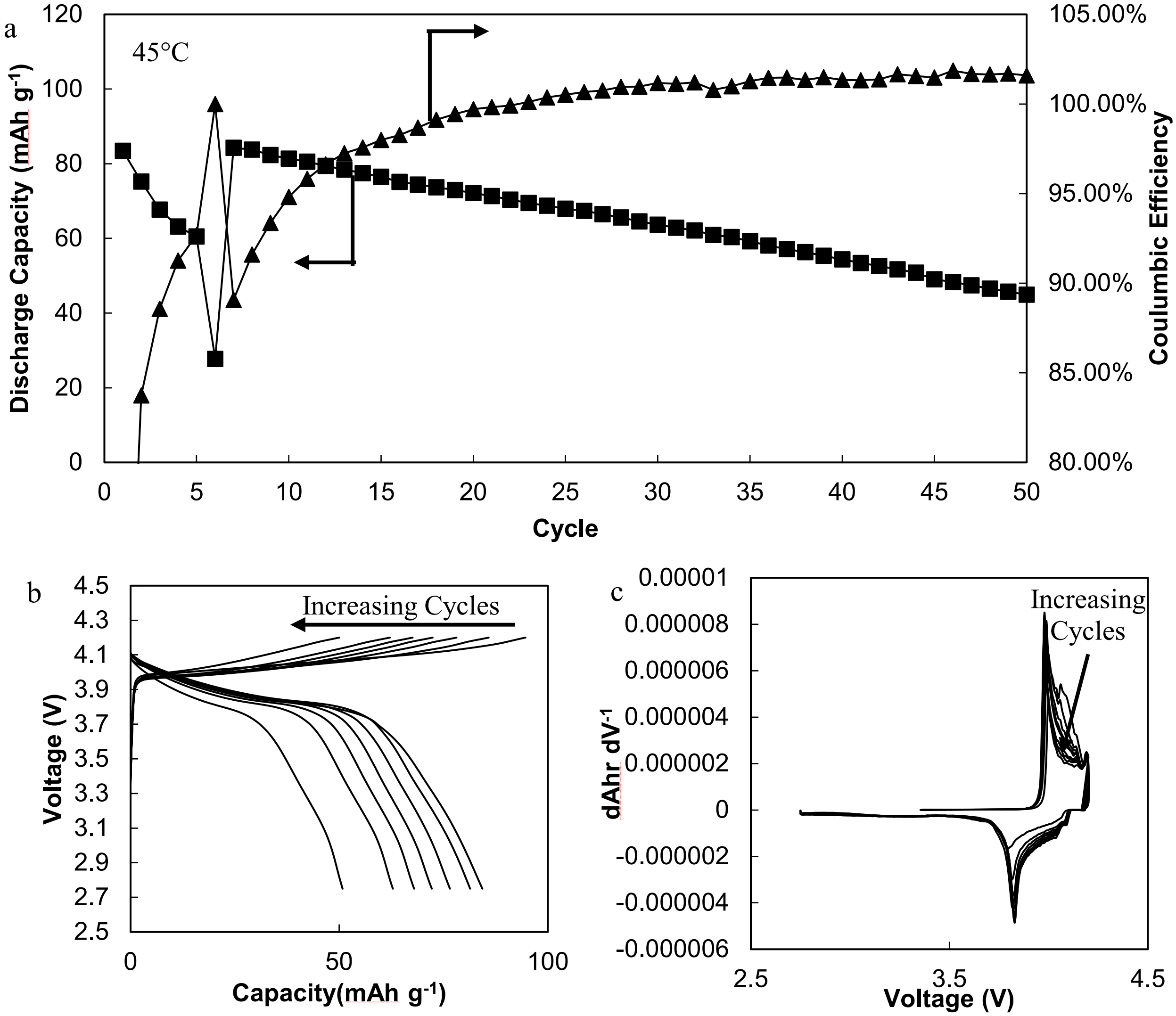

Figure 25. Results from solid state cell cycling at 45°C. **Figure 25a.** Discharge capacity and columbic efficiency vs. cycle life at 12.5 μA cm^{-2} for 6 cycles and 6.25 μA cm^{-2} until cycle 50. Squares are discharge capacity at triangles are columbic efficiency. **Figure 25b.** Voltage vs. capacity for various cycles when discharging at 6.25 μA cm^{-2}. **Figure 25c**. Differential capacity at various cycles at 6.25 μA cm^{-2}.

4. Conclusions

Lithium ion conducting garnet and $LiCoO_2$ composite cathodes were co-sintered without forming detectable secondary phases. However, 40% excess lithium calcined with the lithium garnet was required to achieve phase stabilization at 1050°C for four hours. Increasing lithium content reduced the measured reactivity between LLCZNX and LCO below 1085°C, which limited $LaCoO_3$ formation. Interfacial resistance was decreased from 7000 to 510 Ω cm^2 with increasing lithium content despite similar microstructures in all samples. LLCZN40/LCO measured high capacity from the LCO and longer cycle life compared to samples with less excess lithium in LLCZNX when cycled in liquid half-cells. Meanwhile in partially solid-state samples with solid co-sintered cathodes, the resistance was reduced and 90 mAhr g^{-1} was achieved during cycling. The cycle life was hindered by reduction of capacity and lack of densification but confirmed the potential of co-sintering LLCZN and LCO. Future work should focus on designing a co-sintered composite cathode with an electrolyte layer to create a fully solid-state battery in a single sintered step.

Chapter 4: Enhancing Capacity of Lithium Spinel via Chlorination and Triple Doping with Transition Metals for Next Generation Lithium Based Batteries

Reprinted with permission from Limpert, M.A.; Baroncini, E.B.; Gritton, E.J.; Atwater, T.B.; Wachsman, E.D. Enhancing capacity of lithium spinel via chlorination and triple doping with transition metals for next generation lithium based batteries. *Journal of Power Sources.* **2022,** 528, 231225, DOI:10.1016/j.jpowsour.2022.231225. Copyright 2022 Elsevier.

Abstract

Lithium spinel ($LiMn_2O_4$) possesses a lower theoretical specific capacity compared to layered oxide cathodes ($LiCoO_2$, $LiNi_{0.33}Mn_{0.33}Co_{0.33}O_2$, etc.) but offers an environmentally safe alternative by eliminating the cobalt used in current cathodes. $LiMn_2O_4$ requires dopants to increase the operating voltage, maximize energy density, and be competitive with current cathodes. Through a modified Pechini method, this is demonstrated with multiple dopants. The process and spinel structure enable multiple transition metal dopants (nickel, iron, and cobalt) to be added on the Mn site, which increases the specific capacity up to 110 mAh g^{-1} when charging up to 5.25 V. Chlorine doping in $LiMn_2O_4$ expands the lattice from 8.189 to 8.215 Å, allowing for the insertion and removal of additional lithium when cycling down to 2 V. This results in a nearly two fold increase in specific capacity to 200 mAh g^{-1} when discharging at 0.5 mA cm^{-2}. However, cycling between 5.25 V and 2 V with standard liquid electrolytes increases cell resistance from 63 to 314 Ω due to instability of the electrolyte at voltages greater than 4.5 V. The chlorinated spinel is then paired with a >5 V stable $Li_{6.75}La_{2.75}Ca_{0.25}Zr_{1.5}Nb_{0.5}O_{12}$ garnet to validate 5 V cycling, achieving 190 mAh g^{-1} for 5 cycles with limited specific capacity decay.

1. Introduction

Goodenough reported the initial lithium-ion cathode, $LiCoO_2$ (LCO),[239] in 1981, which culminated in Panasonic's introduction of lithium-ion technology using LCO in 1991. Since then, the technology has proliferated widely, utilized in cell phones, laptops, electric vehicles, and almost all portable electronic devices. Their production is predicted to reach 278 gigawatt-hours per year in 2021 [240], which will put immense pressure on natural resources[241], safety[242], and recycling facilities[243] to meet the demand to manufacture new batteries while safely disposing of the discarded technologies. It is critical to increase batteries' energy storage capabilities, power capabilities, life cycle, and safety while using environmentally friendly materials to relieve pressure on these issues.

Lithium spinel, $Li_aMn_2O_4$ (LMO), follows a $Li_aA_2O_4$ structure with 3-D lithium pathways and is a low cost, environmentally friendly alternative to standard LCO cathodes due to manganese abundance which relieves environmental concerns of using cobalt-based cathodes[244]. The spinel structure consists of lithium at the 8a tetrahedral sites and manganese at the 16d octahedral sites with oxygen attached to three manganese and one lithium[245]. The lithium sites completely fill during discharge to 3.5 V while the manganese sites remain half-filled[245]. During discharge, a fraction of lithium can occupy the octahedral site while manganese occupies the tetrahedral sites[246].

Lattice distortions in LMO during charging and discharging, such as Jahn Teller (JT) effects and manganese dissolution, reduce specific capacity and cycle life as Li-site occupancy (a) approaches zero[247]. However, JT effects can be reduced or eliminated when the manganese sites are disordered and LMO forms the Fd-3m phase rather than the ordered $P4_332$ phase[248]. Anion doping produces this disorder and increases structural stability at higher voltages[249], increasing both cycle life and the energy density of LMO spinel. However, LMO also requires transition metal dopants to increase the operating voltage for higher energy. LMO has an energy density of 440 Wh kg^{-1} and without dopants to enhance either its working voltage or adding additional capacity compares poorly to LCO (518 Wh kg^{-1}), and $Li_aNi_{0.8}Mn_{0.1}Co_{0.1}O_2$ (760 Wh kg^{-1})[250]. To surpass the energy density of NMC-811, LMO can be engineered to optimize its power, energy, and capacity through doping and the ordering of cations[251,252], oxygen vacancies[253], and surface morphology[254].

Recently, lithium has been reported to occupy the empty tetrahedral sites of LMO when discharging below 3 V to double the specific capacity to 240 mAh g^{-1} but with reduced cycle life [255]. Through operando X-ray diffraction, filling these sites significantly increases the volume change during cycling from 5.87% to 12.9% in LMO[256]. However, researchers were able to introduce cationic disorder to suppress Jahn-Teller effects and achieve better cycle life[257]. Likewise, glass coating on the $Li_aNi_{0.5}Mn_{1.5}O_4$ (LNMO) particles can suppress some of these degradations, increasing lithium diffusivity and stopping cycle life degradation[258]. Enhancing the life cycle with higher specific capacity lithium spinel offers a pathway to increase energy density in next generation lithium-ion cathodes.

"A" site dopants can improve LMO's electrochemical performance by reducing Mn^{3+} in the lattice, such as a combination of copper, aluminum, and titanium in a total dopant amount of 0.06 which has been shown to improve cycling stability and increase discharge rates to 12C [259]. Copper as the lone dopant up to 0.1 shows high specific capacity (108.5 mAh g^{-1}) and retention for over 1000 cycles at 1C rates through favorable diffusion kinetics from the unique octahedral structure [260,261]. While separately, aluminum in dopant amounts up to 0.16 distorted the lattice but provided 89.5 mAh g^{-1} [262]. Dopants can decrease the initial capacity achieved when Mn^{4+} in the lattice is maximized. However, the combination of low dopant amounts can provide enhanced rate capability while simultaneously distorting and minimizing capacity loss.

Nickel and cobalt are commonly doped on the Mn site to increase operational voltage (from 4 to 4.75 V) and enhance rate capabilities[263,264]. In low dopant quantities (0.1), nickel has been shown to achieve specific capacities of 87.1 mAh g^{-1} between 4.5 and 3.5 V and maintain the lattice structure at 5C discharge rates[265]. Likewise, the interaction between Ni and Fe with a dopant total of 0.05 was investigated to show better capacity retention after 50 cycles when compared to LMO[266]. Separately, Ni and Co in small amounts (0.025 each), enhances lithium diffusion through the spinel for faster rates with increased specific capacity of 113 mAh g^{-1} [267]. Separately, chlorine doping has been previously investigated and demonstrates increased specific capacity and a widened voltage range[268]. Chlorine can also create oxygen vacancies and increase the amount of Mn^{4+} in the lattice, limiting JT effects[269]. Combining anion and cation dopants (F^- and Mg^{2+}) on the Mn and O sites help improve the cycle life properties of LMO [270]. This is further investigated with La and S in LMNO with higher capacity retention at 10C rates and higher specific discharge capacity than the non-doped LNMO[271]. While changing the anion dopant to Cl, allowed for rates of 10C from the larger lattice caused by the substitution of Cl^- (0.181 nm) for O^{2-} (0.140 nm)[272]. In this work, sol-gel methods were investigated with iron, nickel, and cobalt as “A site” dopants and chlorine as an oxygen dopant to vary their physical and electrochemical properties. The maximum transition metal dopant amount for this work was 0.15 in contrast to the commonly used 0.18, as 0.15 was reported to yield the longest cycle life [273] while minimizing potential costly dopants[274], and mitigating initial capacity decay. Herein we report a sol-gel process and resulting spinel material that can be doped with three transition metals and chlorine, which results in a more than 50% increase in specific capacity to 200 mAh g^{-1}.

2. Experimental

2.1 Sol-Gel Method

Stoichiometric amounts of the following chemicals were used to calcine $Li_aCo_xFe_yNi_zMn_{2-x-y-z}O_{4-b}Cl_b$ (where a=1, $x<0.05$, $y<0.05$, $z<0.05$, $b<0.15$): $LiNO_3$ (Sigma Aldrich 99.99%<) plus an extra 15 wt%, LiCl (Sigma Aldrich 99.99%<) that replaces the 15% extra $LiNO_3$ when used, manganese nitrate hydrate (Sigma Aldrich 98%<), cobalt nitrate hexahydrate (Sigma Aldrich 99.999%<), nickel nitrate hexahydrate (Sigma Aldrich 99.999%<), and iron (II) nitrate nonahydrate (Alfa Aesar 98%<). The precursors were vigorously stirred in a beaker on a hot plate in methanol (Fischer Scientific 99.9%) before citric acid (Alfa Aesar 99.5%) was added in a 1.6:1 citric acid to metal ions molar ratio and then continued to mix. Finally, ethylene glycol (Sigma Aldrich 99.8%) was added in a 0.53:1 molar ratio of ethylene glycol to metal ions before being mixed and heated to 100°C to complete evaporation of the methanol and water. The stir bar was removed and the mixture was then heated to the pyrolysis temperature of 300°C on the hot plate for at least 2 hours to breakdown the precursor before allowing to cool to room temperature. The remaining powder was ground and calcined in a ceramic crucible at 650°C for 10 hours in air with a heating/cooling rate of 10°C/min starting and ending at room temperature.

2.2 Characterization

Dynamic scanning calorimetry (DSC) and thermal gravimetric analysis (TGA) was performed on the precursor material between 200°C and 650°C in an argon environment with temperature increasing by 10°C minute^{-1} (Perkin Elmer STA 8000). X-ray diffraction (XRD) was conducted on the calcined samples to identify secondary phases and confirm the spinel structure (Bruker D8 Advance, Cu-Kα monochromatic radiation source operated between 40 kV and 40 mA) with Rietveld refinement completed to determine the lattice parameters. X-ray florescence

(XRF) measured chlorine content in select samples (Bruker S2 Ranger). Raman spectroscopy was performed to differentiate between the disordered Fd-3m phase and the ordered $P4_332$ phase (Horiba Jobin Yvon Labram). The CDD detector operated with a 532 nm Ar^+ laser as the excitation source. Scanning electron microscope (SEM) images were taken to characterize the microstructure of the material along with electron dispersive X-ray spectroscopy (EDS) to determine the elemental distribution in the powder (JEOL JSM-IT100).

2.3 Electrochemical Characterization

The resultant spinel powder was mixed in a mortar and pestle with conductive carbon black and polytetrafluoroethylene (PTFE) in a weight ratio of 80:15:5 (~25 mg cm^{-2}) and constructed into a CR2025 half-cell with a lithium metal anode (MTI). The cathode was pressed into an aluminum screen and anode into a nickel screen. The half cells included glass fiber separators soaked in an electrolyte solution of 1 M $LiPF_6$ in dimethyl carbonate (DMC): ethylene carbonate (EC) 50:50 v% (Sigma Aldrich). Select constructed half-cells were cycled between 0.5 mA cm^{-2} and 20 mA cm^{-2} with a voltage range of 3.5 to 4.5 V to determine rate capability. Other constructed half-cells were cycled at 0.5 mA cm^{-2} from 2.5 to 4.5 V, 2 to 4.5 V, and 3.5 to 5.25 V to explore the specific capacity gained from 2 V and 5.25 mV cycling. Life cycle testing at 0.5 mA cm^{-2} between 3.5 and 4.5 V was performed on select samples. All electrochemical cycling was performed on ARBIN MSTAT 4 battery cycler system controlled by MITS Pro software. During select cycling, EIS was performed between 100 kHz and 1 Hz at an amplitude of 10 mV every hour while performing a 0.2 mAh cm^{-2} rate on an Arbin MSTAT4 outfitted with a Gamry Interface 1010E.

For 5 V cycling, calcined lithium ion conducting garnet was prepared as previously reported[275] with the stoichiometry of $Li_{6.75}La_{2.75}Ca_{0.25}Zr_{1.5}Nb_{0.5}O_{12}$ (LLCZN), 0.3 g of the calcined

LLCZN was pressed, and sintered in mother powder in an Al_2O_3 crucible at 1100°C for 18 hours. SEM, Raman, and EIS for structural and electrochemical characterization of LLCZN are included (Figure S53 and S54). A glass separator soaked in 1M $LiPF_6$ 45:45:10 v% of diethyl carbonate (DEC):EC: fluoroethylene carbonate (FEC) was used as an interlayer between LLCZN and the electrodes as FEC has been shown to provide stability both at 5 V and against lithium metal[276]. The cell was cycled between 5 and 2.2 V at a rate of 17 $\mu A\ cm^{-2}$ at room temperature.

3. Results and Discussion

3.1 Structural Characterization

The spinel phase is the sole phase detected in four out of the five XRD patterns of the calcined samples (Figure 26a) with the exception of $Li_aMn_{1.90}Co_{0.05}Fe_{0.05}O_{4-b}Cl_b$ (LMFC). The impurity in LMFC is nonconductive Mn_2O_3 that is not detected with the addition of nickel in $Li_aMn_{1.85}Ni_{0.05}Co_{0.05}Fe_{0.05}O_{4-b}Cl_b$ (LMNCF). Likewise, Li_2MnO_3 is detected in $LiMn_2O_4$ (LMO) which limits capacity in that sample. With the addition of chlorine in $Li_aMn_2O_{4-b}Cl_b$ (LM-Cl), the spinel structure stabilizes with an expanded lattice (Table 7) and does not measure secondary phases. The ionic radii of oxygen is 1.38 while chlorine is 1.81 [277]; resulting in increased lattice parameter of the chlorinated spinel. A sample of the fit and fitting parameters are included in Figure S55 and Table S22. The extra spacing in all chlorinated samples enlarges the 3-d channels and increases the specific discharge capacity by at least 50% when discharging to 2 and 2.5 V.

Sample	Lattice Parameter (Å)	Specific Discharge Capacity (2-4.5 V) (mAh g^{-1})	Specific Discharge Capacity (2.5-4.5 V) (mAh g^{-1})	Specific Discharge Capacity (3.5-4.5 V) (mAh g^{-1})	Specific Discharge Capacity (3.5-5.25 V) (mAh g^{-1})
$Li_aMn_2O_4$	8.189	N/A	N/A	55.2	N/A
$Li_aMn_2O_{4-b}Cl_b$	8.215	119.5	102.0	68.0	100.7
$Li_aMn_{1.95}Co_{0.05}O_{4-b}Cl_b$	8.203	138.4	127.8	53.0	114.7
$Li_aMn_{1.90}Fe_{0.05}Co_{0.05}O_{4-b}Cl_b$	8.206	148.2	119.3	52.5	97.5
$Li_aMn_{1.85}Fe_{0.05}Co_{00.5}Ni_{0.05}O_{4-b}Cl_b$	8.196	163.5	144.3	86.7	103.2

Table 7. Lattice parameters for all the samples, discharge capacities charged at various voltages and discharged at 0.5 mA cm^{-2} (~C/6 at 120 mAh g^{-1}) to various voltages.

Raman scattering data (Figure 26c) of the calcined spinel powder shows pure spinel phase in four of the five samples with a secondary phase in LMFC. The nonconductive secondary phase, Mn_2O_3, is indicated in the Raman by the sharp band at 660 cm^{-1} [278] and will reduce specific capacity. In the rest of the spectra, the peak at 630 cm^{-1} is assigned to the Mn-O stretching vibration of MO_6 groups belonging to the Ag mode [279]. The peaks at 590 and 625 cm^{-1} would be assigned to the Ni^{+2}-O stretching mode [280], 585 cm^{-1} to the Co-O stretching mode [281], and Fe-O at 630 cm^{-1} [282]. However, these peaks are convoluted in one another due to the low dopant amounts. The addition of chlorine, nonetheless, disorders the structure as evidenced by the sharp peaks in LMFC and LMO but those peaks are excluded in the other samples (Figure S56).

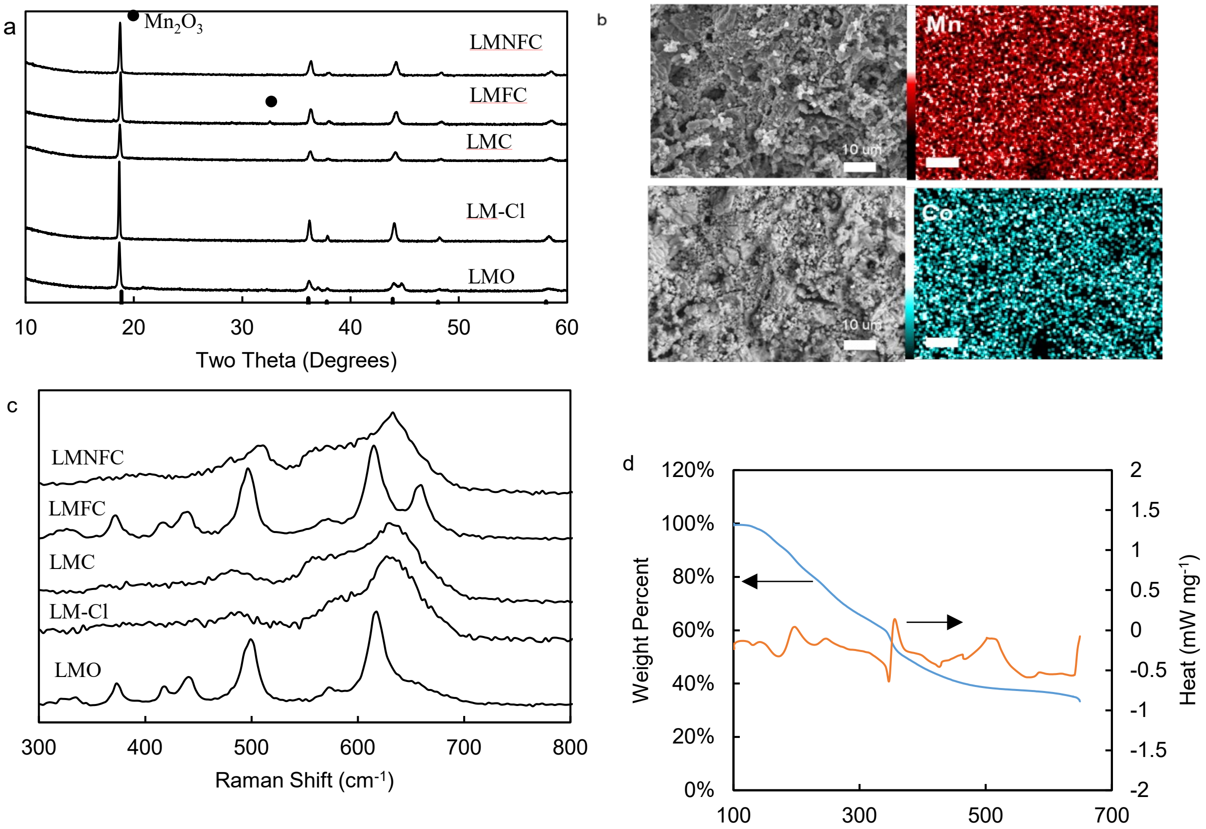

Figure 26a. XRD data for all samples. $Li_aMn_2O_4$ ICCD No. 00-035-0782 peaks are included in the bottom of the figure. The samples are listed as LMO for $LiMn_2O_4$, LM-Cl for $LiMn_2O_{4-b}Cl_b$, LMC for $Li_aMn_{1.95}Co_{0.05}O_{4-b}Cl_b$, LMFC for $LiMn_{1.90}Fe_{0.05}Co_{0.05}O_{4-b}Cl_b$, and LMNFC for $Li_aMn_{1.85}Ni_{0.05}Fe_{0.05}Co_{0.05}O_{4-b}Cl_b$. Mn_2O_3 is in two samples. **Figure 26b.** SEM. Back Scattered Electron, and EDS Images of $Li_aMn_{1.85}Ni_{0.05}Fe_{0.05}Co_{0.05}O_{4-b}Cl_b$. **Figure 26c**. Raman spectroscopy of all the samples. **Figure 26d.** DSC and TGA of $Li_aMn_{1.85}Ni_{0.05}Fe_{0.05}Co_{0.05}O_{4-b}Cl_b$ precursor powder. Endothermic is up and exothermic is down

The SEM and EDS images (Figure 26b) of the $Li_aMn_{1.85}Ni_{0.05}Fe_{0.05}Co_{0.05}O_{4-b}Cl_b$ (LMNFC) illustrate a submicron powder with manganese and cobalt dispersed throughout. The other elements are not imaged in EDS because their low amount in the spinel. Nonetheless, the small micron sized powder and dispersed elements is important for high rate cycling [283]. XRF data (Figure S57) confirms chlorine (b=0.014 for LMNFC) and the other transition metals are included in LMNFC in the appropriate quantities. The rest of the samples have porous microstructures, a network of interconnected small grains, and do not have detectable microstructure differences between them (Figure S58) showing that the sol-gel method produced consistent microstructures.

Precursor material is thermally characterized through TGA/DSC (Figure 26d) and the data shows a 65% weight loss when heated to 650°C. The weight loss is most likely carbon and nitrogen species from the transesterification reaction as those are the main species from the precursors. The peaks at 200°C are likely excess ethylene glycol and water being evaporated while the peaks at 400°C are the polymeric chains with transition metal nitrates decomposing, thereby releasing the nitrogen, carbon, and oxygen species[284]. A small endothermic peak at ~610°C indicates LiCl melting[285] while the endothermic peak after 640°C is in good agreement for our calcination temperature of 650°C.

3.2 Electrochemical Measurements

Life cycle testing between 3.5 and 4.5 V in a half-cell with LMNFC did not induce a loss of specific discharge capacity over 100 cycles or a loss of structural integrity (Figure 27a and 27b). The specific discharge capacity does not experience a significant decline, measuring 95.9 mAh g^{-1} on the first cycle to 95.8 mAh g^{-1} on the last. At cycle 35, there is a small increase in specific capacity to 99 mAh g^{-1} but the specific discharge capacity retains 96% of that higher capacity at 100 cycles. The Coulombic efficiency begins to decrease at cycle 25 which is likely weaknesses from the cell build, i.e. the lithium metal, electrolytes, seal, etc. Lithium metal can be unstable with the liquid electrolyte and form a solid electrolyte interface that is consuming the electrolyte. This is further evidenced by decreasing Coulombic efficiency but stable specific discharge capacity which is indicative of increasing charging capacity. The transition metals dopants and chlorine, though, did not adversely affect cycle life but the full capacity is seen above 5 V and below 3 V (Table 7).

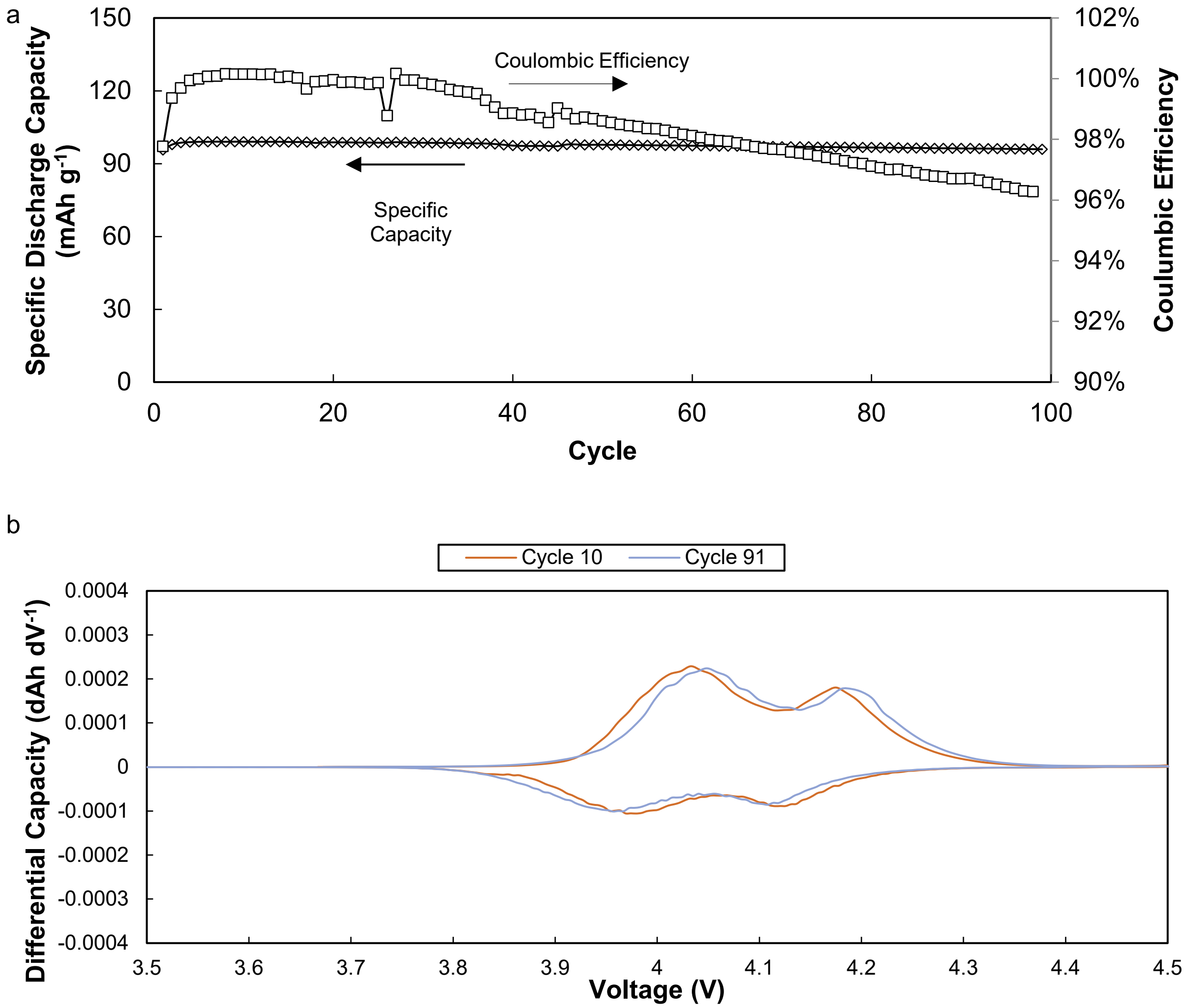

Figure 27a. The specific discharge capacity and Coulombic efficiency vs. cycles for LMNCF between 4.5 and 3.5 V at 0.5 mA cm^{-2} (~C/6 at 120 mAh g^{-1}). **Figure 27b.** Differential capacity of the 10th and 91st cycle. Charge is positive and discharge is negative.

The differential capacity plot in Figure 27b analyzes the 10th and 91st cycle in which an overcharge is indicated by the rightward shift in cycle 91, demonstrating increasing resistance within the cell. The lower peak at 4.05 V on charge is $LiMn_{1.8585}Ni_{0.05}Co_{0.05}Fe_{0.05}O_4$ going to $Li_{0.5}Mn_{1.85}Ni_{0.05}Co_{0.05}Fe_{0.05}O_4$, where the lithium remaining is in an ordered structure. While the peak at 4.18 V is from $Li_{0.5}Mn_{1.8585}Ni_{0.05}Co_{0.05}Fe_{0.05}O_4$ to $Li_aMn_{1.8585}Ni_{0.05}Co_{0.05}Fe_{0.05}O_4$ where “a” is less than ~0.25. This difference between the upper and lower peaks is from the Mn^{4+}/Mn^{3+} redox couples, which is in good agreement with the voltage difference of ~0.15V in good agreement with other reports[286]. There is no change in the shape of the curve aside from the shift to the right on charge and to the left on discharge. The similar shapes indicate the increase in the overall cell resistance is not attributed to rate changes and the lattice has not been damaged. The cathode maintains its specific capacity and the lattice structure during the 100 cycles, but Coulombic efficiency and charge retention begins to decrease, necessitating better cell construction.

Cycling between 3.5 and 5.25 V (Figure 28 and Table 7) demonstrates an increase in the cathode's measured specific capacity and energy when compared to cycling to 4.5 V. This excludes LMO which could not operate at 5.25 V. LMC achieves the highest energy density (484 Wh kg^{-1},114.7 mAh g^{-1}), followed by LMNFC (466 Wh kg^{-1}, 103.2 mAh g^{-1}), LM-Cl (389 Wh kg^{-1},100.7 mAh g^{-1}), and finally LMFC (380 Wh kg^{-1}, 97.5 mAh g^{-1}), which has low specific capacity from Li_2MnO_3 formation. The higher voltage plateau in the samples occurs from the difference in binding energy between the top valence band of Ni^{2+} and Mn [287]. The lower specific capacity in LMNFC when compared to LMC may be due to Mn_2O_3 formation but also the interaction between Co and Fe has been shown to increase the working voltage above 5.25 to 5.40 V [288]. Some capacity in LMNCF in our experiments may be not accessible with the voltage limits. Every dopant added to LMO has an effect on the band structure increasing the reduction/oxidation reaction to different operating voltages. However, there is a large overcharge in the differential capacity plot, which is also seen in cyclic voltammetry (Figure S59). Likewise, there appears to be differences between the charge and discharge curves specifically in LMFC, which may be due to Mn_2O_3 formation as evidenced by XRD results in Figure 1 and associated effects on cell cycling. Despite the instability of the electrolyte above 5 V, the cells are able to achieve a specific discharge capacity of ~110 mAh g^{-1}.

As LMNFC approaches its lithium poor state during charge, there are a number of different reactions that could occur above 5 V. If the material has insufficient lithium in this state, the care capacity is expected to increase on the subsequent cycle. However, the succeeding charge-discharge cycle (Figure S60) shows LMNFC reduced its specific capacity to 99.8 mAh g^{-1}. The charge capacity decreased with the reduction in discharge capacity in LMNFC showing the material did not have insufficient lithium to maintain charge balance in LMNFCs charged state.

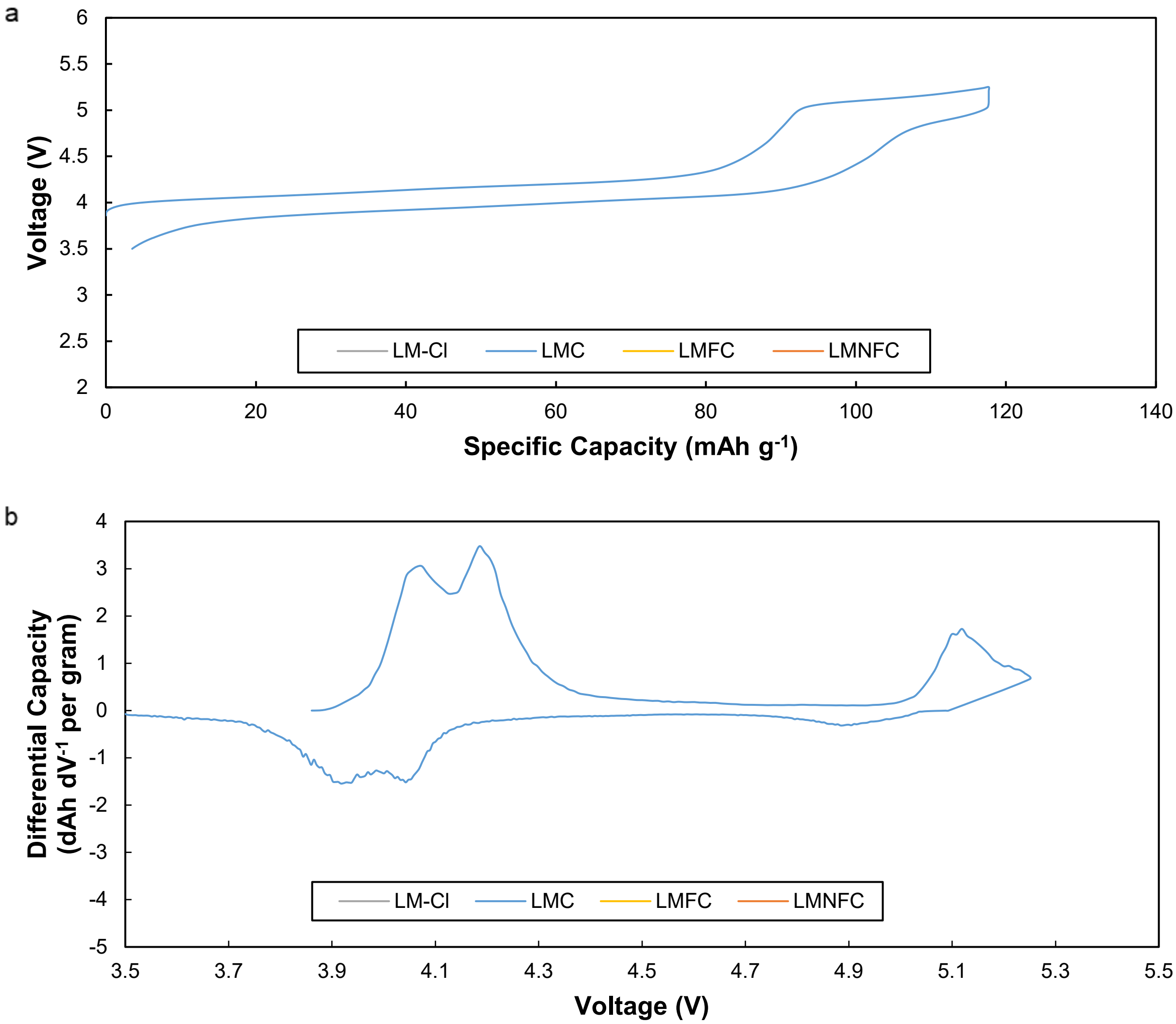

Figure 28a. Specific capacity vs. voltage of samples cycling between 5.25 and 3.5 V at 0.5 cm^{-2} (~C/5). **Figure 28b**. Differential capacity normalized to active material vs. voltage of samples charging and discharging between 5.25 and 3.5 V. Charge is up and discharge is down

Iron dopants in lithium spinel have been reported to deliver rates of 10C with 100 mAh g^{-1} when appropriately placed in the lattice [289], making it an attractive dopant. Fe below 0.1 doping levels also shows considerably longer cycle life at 120 mAh g^{-1} and occupies the 16d site while reducing Mn occupation of the 8a sites[290]. LMNFC in half cells with an active loading of 23.7 mg cm^{-2} and operating between 3.5 and 4.5 V obtains 50 mAh g^{-1} at 5 mA cm^{-2} (Figure 29a). LMNFC is capable of high rates due to the iron and other dopant inclusions aiding the lithium insertion and extraction without manganese dissolution but hindered by the high cathode loading, especially at

10 mA cm^{-2}. Increasing dopants in LMO do demonstrate better rate capability (Figure S61) but LMNFC displayed the highest capacity retention with increasing charge and discharge rates.

Charge/discharge curves of the LMNFC rate tests (Figure 29b) display surface polarization at all rates indicated by increasing over potential. This is seen by the shift in the differential capacity peaks (Figure 29c) to the right on charge and to the left on discharge due to increased kinetic resistance at the high rates. However, the shapes of the curves do not depress or change suggesting the lattice structure is still intact. This is further specified by the differential capacity curves before and after high rate cycling (Figure S62 and S63) that show little change. The high rate cycling causes increased polarization but did not damage the spinel structure.

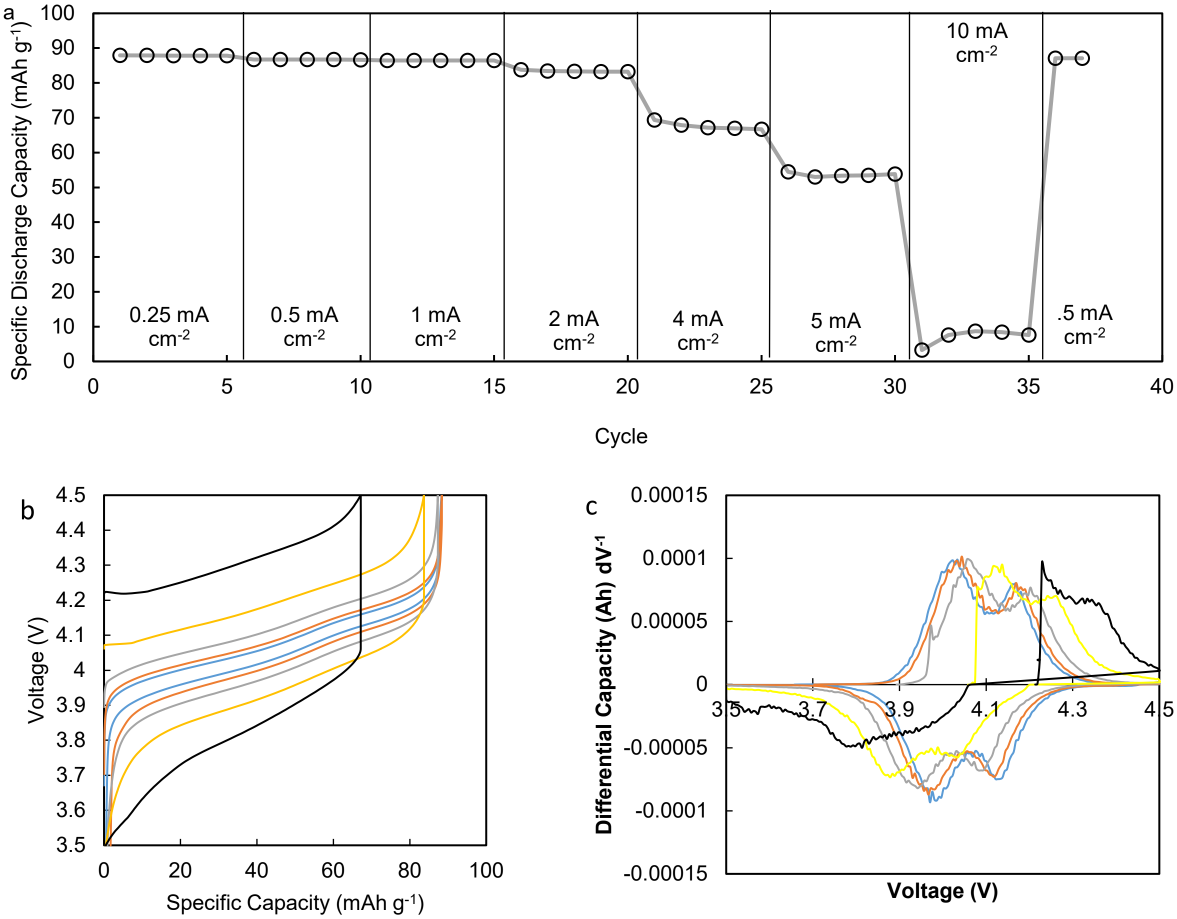

Figure 29a. Capacities of the rate capabilities of the LMNFC. Rates were at ~C/10 to 4C. **Figure 29b.** Voltage vs specific capacity of LMNFC cathode. Blue is 0.25 mA cm^{-2}, orange is 0.5 mA cm^{-2}, gray is 1 mA cm^{-2}, yellow is 2 mA cm^{-2}, and black is 4 mA cm^{-2}. **Figure 29c.** Differential capacity vs. voltage of LMNFC at different rates where the up direction is charge and down is discharge.

Rate capability of spinel is enhanced by the multiple dopants without loss of the lattice structure. The inclusion of the iron dopant enables better resistance to transition metal dissolution at higher rates while the smaller particle size enhances rate capability [283]. Although, the nickel and cobalt dopants allow lithium to remain in the structure when charged to 4.5 V, limiting *a* from approaching 0. To determine the effects of high voltage where more lithium is extracted from the spinel, a LMNCF half-cell was attempted to charge to 5.25 V (Figure S64) at high rates. However, decreasing achievable capacity is observed due to increased resistance from electrolyte instability, necessitating an optimized high voltage stable electrolyte.

Cycling the various materials in half-cells between 2.5 and 4.5 V (Figure 30a) displays the expanded lattice from the chlorine permits lithium insertion below 3.5 V, allowing a >1. XPS results have shown the binding energies are greater in chlorine doped samples than LMO from higher electron affinity of Cl compared to O which may also have an impact on the enhanced capacity[291]. Likewise, LMO data is not included since it cannot accept more lithium because it is not disordered and the lattice parameter is not expanded. In the chlorinated samples, a large resistance is observed by the voltage difference between the charge plateau at 3V and the discharge plateau at 2.6 V. This voltage difference is most likely kinetic resistance to accepting lithium into the unoccupied spinel sites. The difference is also seen by the peaks in the differential capacity curves (Figure 30b) where extra capacity is required to accommodate initial structure shifting from the extra lithium. However, degradation and anomalous peaks from the initial discharge to 2.5 V is not detected between 3.5 and 4.5 V in the differential capacity plot. The extra specific discharge capacity achieved at 2.5 V, for example LMNFC from 86.7 to 144 mAh g^{-1} (540 Wh kg^{-1}), is beneficial for doped LMO cathodes.

The addition of chlorine enables the chlorinated LMO samples to increase specific capacity by up to 50% in most of our samples in which lithium is assumed to be occupying the empty octahedral sites. Researchers have discovered the lattice shifting and accommodating a second lithium per mol of material via this extra site[93]. The chlorine possibly attracts electrons from the transition metal outer orbitals widening the lattice and allowing a second lithium to insert into the open manganese site when discharging below 3 V. With further optimization, this will enable the spinel material to compete with higher energy density cathodes.

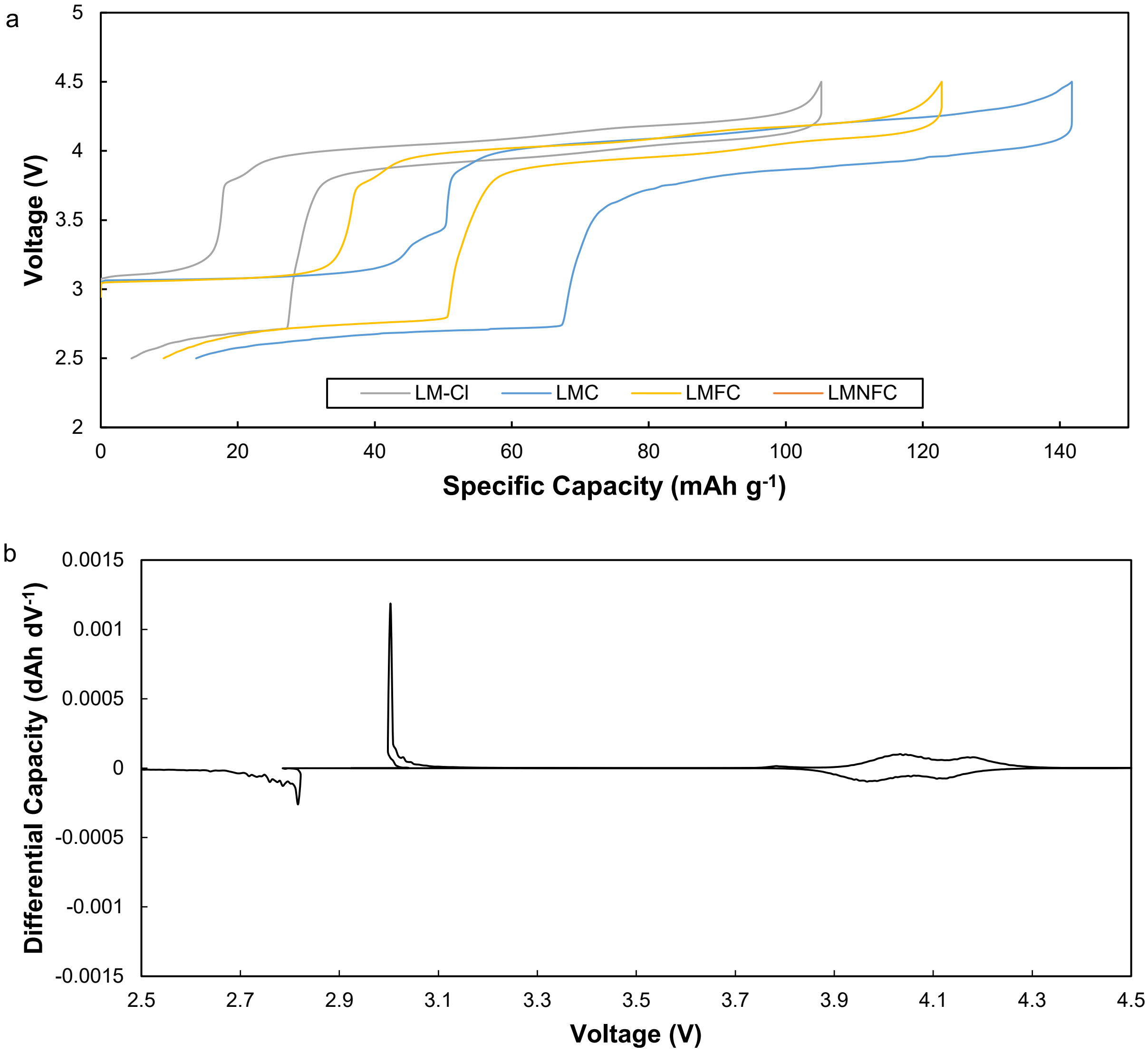

Figure 30a. Voltage vs. specific capacity of all samples to 2.5 V at 0.5 mA cm^{-2} (C/10 at 120 mAh g^{-1}). **Figure 30b.** Differential capacity vs. voltage of LMNFC.

Half cells discharged (Figure 31a) to 2 V demonstrate a specific capacity increase of only an additional 10 to 30 mAh g^{-1}. Previous reports indicated the specific capacity can be increased another 60 mAh g^{-1} when discharging to 2 V albeit with 0.05 chlorine doped at the oxygen site[292] versus the 0.0114 shown in this work via XRF. Another plateau appears to form, though not seen in the differential capacity (Figure 31b), in our samples but the increasing polarization limits acceptance of more lithium. The 15% excess LiCl, high calcination temperature, and long processing time may have reduced the chlorine that is available to enter the structure but nonetheless LMNFC still achieves a 60 mAh g^{-1} increase at 2.5 V.

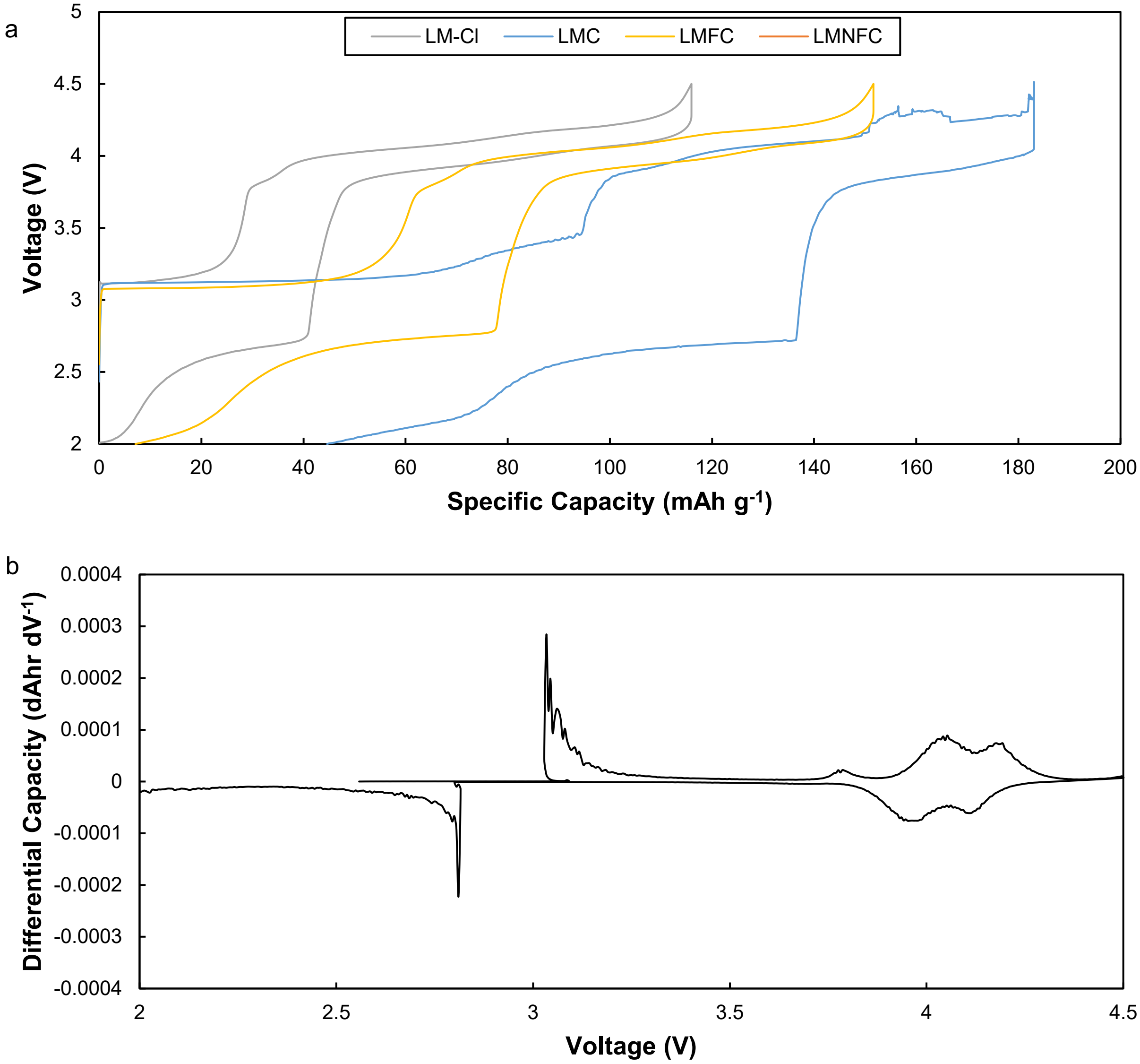

Figure 31a. Discharge curves of all samples to 2 V at 0.5 mA cm^{-2} (~C/10 for 120 mAh g^{-1}). **Figure 31b.** displays the differential capacity plot of LMNFC discharging to 2 V.

Charging above 5 V and discharging to 2.5 V creates pressure on the lattice and cell components, namely the electrolyte. Figure 32a and 32b displays charge and discharge results of a half-cell with LMNCF for two cycles between 2.5 and 5 V with EIS measurements performed every hour. An example of the model[293] used to fit the EIS data, which generates the fitting results

(Table 8), is included in the inset. The initial resistor in the series is defined as the electrolyte (Rsolv), the next resistor/capacitor pairing (Ra/Ca) is the anode, followed by the double layer or the solid electrolyte interface (SEI) on the cathode (Rp/Cp), and the last resistor/constant phase element pairing is diffusion into the active cathode material (Rad/Cad). An example of the EIS is included in Figure S13 and Figure S14 with full reporting of EIS fitting results in Tables S23-26. Despite assuming electrolyte instability, the electrolyte resistance did not increase over any of the tests but several other resistances increased.

During the first charge, the total resistance decreases between the point at 2.5 V (Point 2, 26.0 Ω) and the 3 V plateau (Point 3, 19.6Ω). Above 4.5V, the total resistance begins to increase again to 66.1 Ω at 5 V. However, the measured resistance does not decrease back to initial levels upon discharge to 2.5 V but rather increases to 149.8 Ω. This difference is the degradation of components from 5 V cycling, such as electrolyte[294] and aluminum[295], as well as cell stress from cycling to 2.5 V. Cycling that same cell again between 2.5 and 5 V shows the resistance increase (63 Ω to 161 Ω) is not reversible. This can also be seen in the reduced specific discharge capacity, 187.5 mAh g^{-1} (640 Wh kg^{-1}) vs. 172.5 mAh g^{-1} (595 Wh kg^{-1}). Concentration polarization in the discharge at 2.5 V is missing in the second discharge, accounting for the lower specific capacity. The calculated resistance in the cathode pores increases (Rad, Tables S1-4) after the 1st cycle and in the SEI layer after the 5 V cycle (Table 2), stopping lithium insertion. The lower rate helps achieve higher specific capacity in this set of experiments but could not maintain the cell specific capacity for multiple cycles from increased resistances.

To analyze the effect of charging to 5.25 V and discharging to 2 V, the same experiment was performed between 2 and 5 V and then between 2 and 5.25 V (Table 8 and discharge curves in Figures S65a and b). For the 5-2 V cycle, there is an increase in resistance between Point 4 (4.1

V, 74.01 Ω) and Point 5 (5 V, 243.5 Ω), which is most likely due to electrolyte instability and structural limitations from lithium exiting the spinel structure. However, the final total resistance increased by 80 to 211 Ω and is mainly the increased electrolyte resistance in the interaction with the electrodes. The specific capacity increases to 202 mAh g^{-1} (639 Whr kg^{-1}) but the increased resistance will lead to loss of capacity over time.

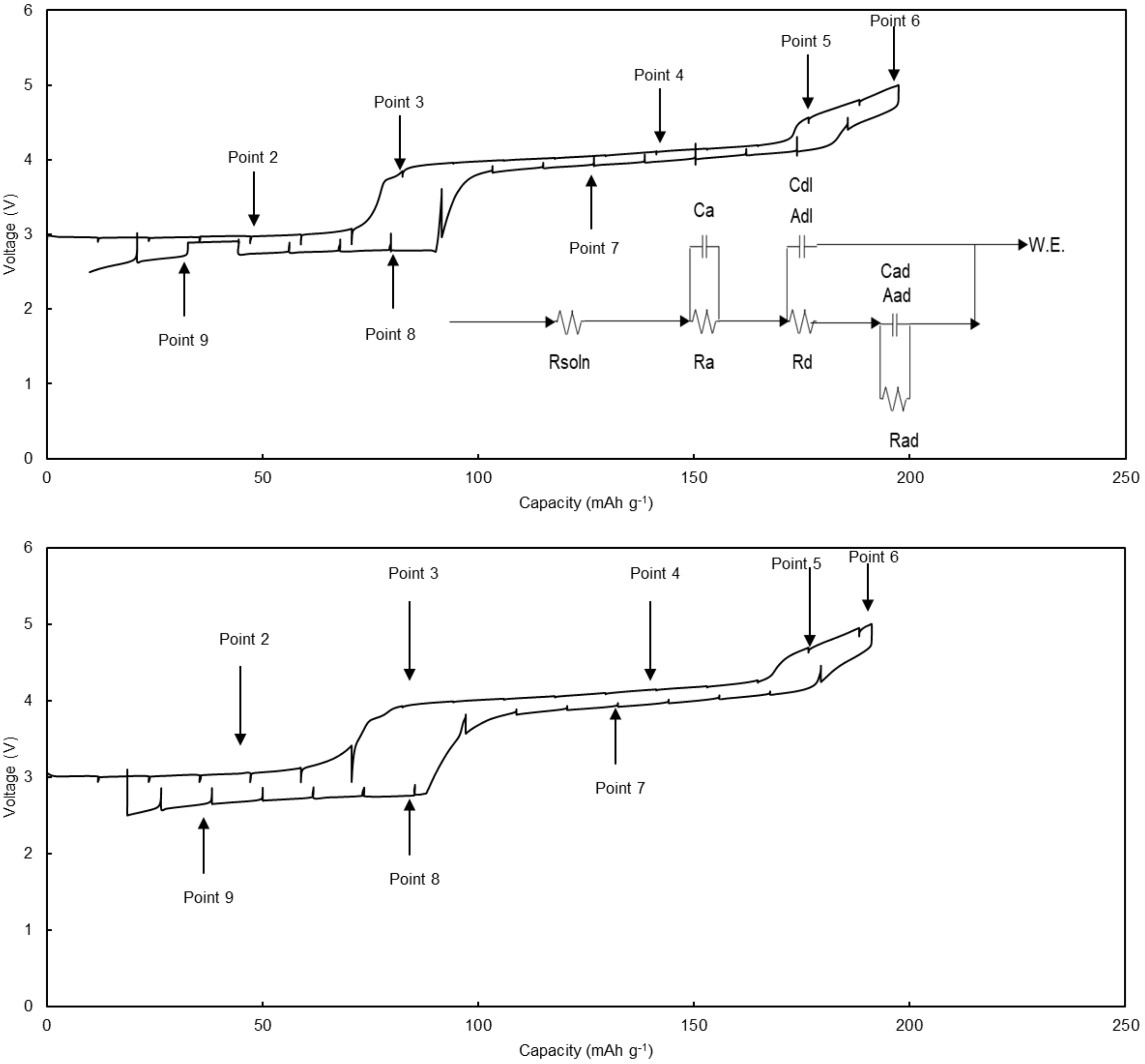

Figure 32a. Voltage vs. specific capacity for LMNCF between 5 and 2.5 V at 0.2 mA cm^{-2} (~C/10 for 120 mAh g^{-1}) with EIS measurements every hour. **Figure 32b.** Voltage vs. specific capacity for LMNCF between 5 and 2.5 V at 0.2 mA cm^{-2} with EIS measurements every hour for a second time.

Total Resistance (Ω)	**Initial**	**Point 2**	**Point 3**	**Point 4**	**Point 5**	**Point 6**	**Point 7**	**Point 8**	**Point 9**	**Point 10**	**Point 11**	**Final**
5-2.5 V First Cycle	63.64	25.99	19.55	18.13	27.71	66.08	109.67	80.23	95.62	N/A	N/A	149.86
5-2.5 V Second Cycle	161.21	70.45	49.50	34.73	311.92	66.42	94.39	126.90	137.98	N/A	N/A	139.58
5-2 V Cycle	134.05	117.81	100.78	74.01	245.34	130.31	122.64	172.78	219.66	199.23	N/A	211.28
5.25-2 V Cycle	229.67	112.95	105.34	69.01	66.36	236.86	254.52	265.88	349.54	377.60	315.98	314.27

Table 8. The total resistance measured from the EIS measurements at different points during different charge and discharge voltages. Performed on same cell in sequential order from top to bottom.

Cycling to 5.25 V increases cell resistance from electrolyte degradation and SEI products, slowing lithium-ion kinetics from the increased nonconductive films. This is indicated when charging to 5.25 V where the overall resistance increases from 66.36 (point 5, 4.6 V) to 236 Ω (point 6, 5.25 V). When cycling between 5-2.5 V, the overall resistance does decrease to ~140 Ω but increases substantially when further expanding the range to 5.25- 2 V. The operational impact of increasing resistance from the wider voltage range (5.25-2 V) is a decrease in both specific capacity and energy, 202 mAh g^{-1} and 639 Wh kg^{-1} to 185 mAh g^{-1} 567 Whr kg^{-1}. Without further optimization of the spinel material through more chlorine and better electrolytes, the voltage range will need to be reduced.

Lattice rearrangements are a consideration when a >1 in lithium spinel. In the first 5-2.5 V cycle, the cell resistance decreases on discharge between Point 7 (3 V) and Point 8 (2.6 V) while it increases between Point 2 (3.1 V) and Point 3 (3.7 V), signaling that cell stress from a >1 may not be a concern. Despite the low rate, however, the specific capacity is not recovered in the following cycle. This is in good agreement with past reported results where decreasing cycle life was found when discharging to 2 V[93]. However, Atwater and Taveras showed longer cycle life when discharging to 2 V with more chlorine in the lattice and a different electrolyte[292]. Although for our material, reducing the voltage range may reduce specific capacity loss when charging to 5 V and discharging to 2 V.

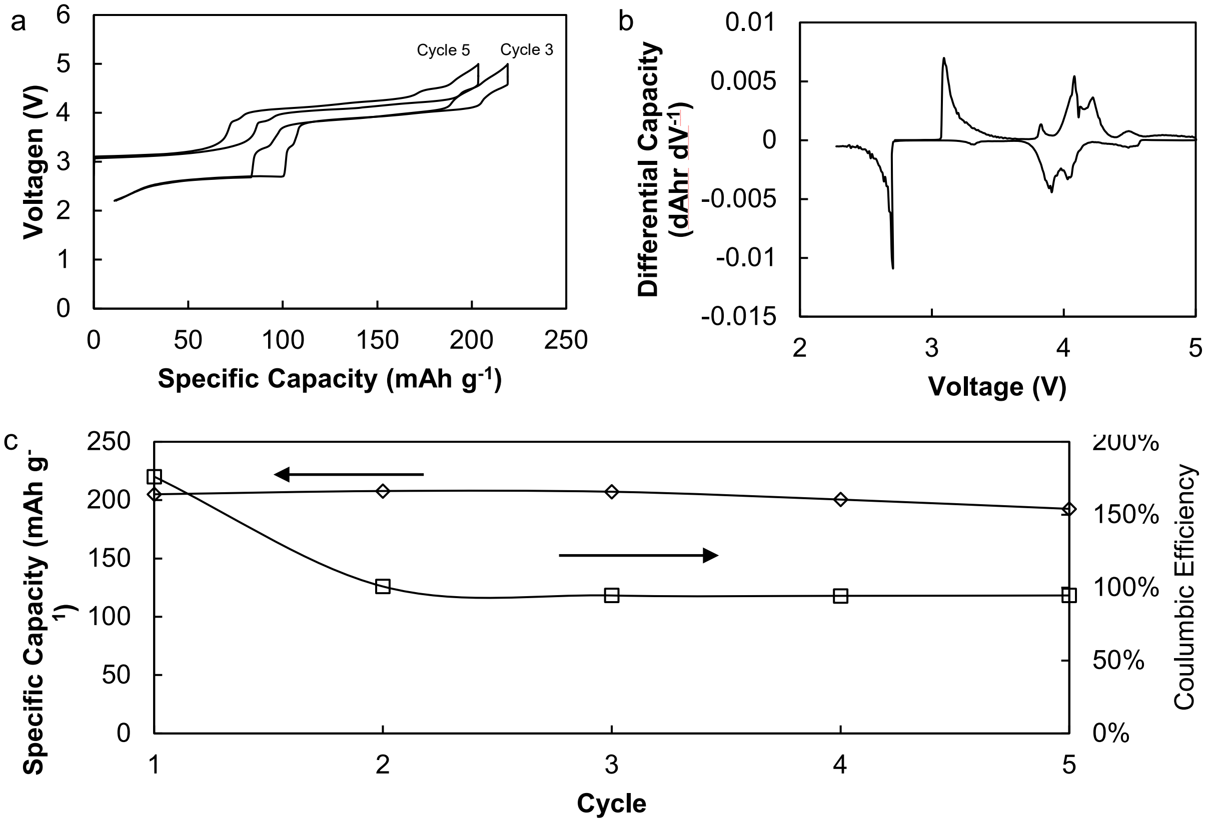

Figure 33a. Cycles 3 and 5 for LMNFC-LLCZN cell. **Figure 33b.** Differential capacity of cycle 3 on LMNFC-LLCZN cell. **Figure 33c.** Specific capacity and Coulombic efficiency vs. cycle number of LMNFC-LLCZN cell. Squares are Coulombic efficiency and diamonds are specific discharge capacity.

Validating the performance of LMNFC between 5 and 2.2 V to maximize specific capacity without an overcharge can be performed with 5 V stable LLCZN garnet (Figure 33a and b). The spinel material is calcined with *a*=1. On the initial cycle, the Coulombic efficiency (Figure 33c) is 176% because when lithium is removed on charge but a>1 when discharged to 2.2V. LMNFC displays 200 mAh g^{-1}, which is similar to what was achieved in liquid cells between 5 and 2 V. However, the energy density within the cathode is measured at 694 Wh kg^{-1} versus 639 Wh kg^{-1} in liquid cells. This is mainly from the increased specific capacity above 3V of 118 mAh g^{-1} versus

90 mAh g^{-1} at 2.5 V. Unlike with the fully liquid cells, there is not an overcharge detected by differential capacity at 5 V, showing the benefit of the solid state electrolyte. With increasing cycles, there is a slight reduction in specific capacity from 208 to 192 mAh g^{-1} from the loss of capacity at the 2.5 V plateau. Nevertheless, the LLCZN solid state electrolyte shows the potential of 5 V cycling with triple doped, chlorinated spinel but more work is required to stabilize the extra lithium within the spinel structure.

4. Conclusions

A sub-micron, chlorinated, triple transition metal doped lithium spinel was calcined using a citric acid method. The submicron nature of the spinel enabled high rates at 5 mA cm^{-2} in thick cathodes with an active loading of 23.7 mg cm^{-2}. While, the addition of chlorine expanded the lattice and enabled cycling to 2.5 V which increased specific capacity by 60 mAh g^{-1} by allowing more lithium into the structure. Finally, the transition metal dopants, specifically cobalt and nickel, allowed for an increased operating voltage to 5.25 V. The increased voltage range used to maximized specific capacity of the cathode material, however, increased resistance in standard liquid electrolytes. This increase in resistance will decrease cycle life and reduce rate capability. The lithium spinel paired with high voltage stable LLCZN garnet proved to reduce electrolyte instability when cycling to 5 V and provides a viable pathway for 5 V cycling. In future work with high nickel content, the inclusion of chlorine, and other stabilizing dopants, lithium spinel should display an increase in specific capacity that can rival state of the art cathodes.

Chapter 5: Lithium Garnet and Lithium Spinel Conclusions and Future Work

1. Varying Lithium Content in LLZO Garnet

1.1 Conclusions

Lithium-ion conducting LLZO type garnets have the potential to replace organic liquid electrolytes in lithium based rechargeable batteries but optimized processing conditions are needed to ensure the electrochemical properties (namely ionic conductivity) are improved. By varying the lithium content, as shown in Chapter 2, before calcining the precursors, the physical and electrochemical properties were varied over a range of sintering conditions, including utilizing different crucibles. The lattice parameter changed in the calcined powder as the lithium content varied, which was a sign of phase deformation, but the techniques used could not detect these minor differences in the garnet structure outside of the lattice parameter. After sintering in Al_2O_3 crucibles, however, aluminum contamination may have contributed to decreasing lattice parameters in the lithium and aluminum rich sintered samples, which allowed the cubic phase to be stabilized below the designed lithium content. By contrast, the MgO crucible sintered samples displayed larger lattice parameters than the Al_2O_3 crucible sintered samples. These variations in the lattice parameter between the crucibles did not severely impact the bulk conductivity. However, aluminum contamination did prove beneficial to forming denser microstructures.

The microstructure and electrochemical results reveal that lithium is a larger factor for microstructure development and thus grain boundary conductance than it is for bulk conductivity, especially when aluminum contaminates the SSE. This occurs for two reasons: 1) better phase purity and 2) liquid phase sintering. The secondary phases detected in the sintered samples were mainly $La_2Zr_2O_7$ and $CaCO_3$ which were formed primarily in lithium and aluminum poor samples and in every MgO sintered sample. These secondary phases slow sintering processes and hinder transport over the grain boundaries. Secondly, the liquid phase sintering from Al_2O_3-Li_2O melting appeared to greatly enhance the density and G_{GB} of the LLCZN SSE. However, Al_2O_3 contamination is difficult to control at sintering temperatures and may dope the LLCZN lattice, potentially slowing Li^+ conduction through the lattice. The MgO sintered samples displayed a half an order magnitude greater bulk conductivity from the larger lattice, but an order of magnitude lower grain boundary conductance from the less desirable microstructures and the nonconductive phases. The lithium carbonate melting in MgO sintered was not enough to offset the lower phase purity slowing conduction over the grain boundaries. This will need to be studied further to determine if a pure phase LLCZN sample can be sintered in MgO crucibles.

Eliminating the aluminum contamination to maintain the high bulk conductivity while maintaining the high grain boundary conductivity will be preferable as the contamination cannot be controlled. To do this, the particle size should be decreased, the excess lithium should be optimized, and the sintering conditions will need to eliminate secondary phase formation while limiting lithium losses. Preliminary work has shown that utilizing small particle sizes can reduce the sintering temperature[296], which would reduce lithium losses. This should be explored further with varying the lithium to understand the effect of changing the sintered sample size while creating thin electrolyte layers.

1.2 Future Work

As mentioned in the previous section, particle size and lithium content play a role in the densification processes during sintering. The different shapes of the sintered body also may have an effect, where there will be larger amounts of lithium loss at sintering temperatures as greater surface area is exposed to the sintering environment. Preliminary studies with reducing the sintered body size from 0.5 to 0.3, 0.2 and 0.1 g in LLCZN15 after sintering at 1100°C for 18 hours (utilizing the same set up in Chapter 2) displays an increasingly dense fractured edge as the size of the sample decreases (Figure 34). This indicates the size of the green body impacts the density of the finished sample. As the size shrinks, the sintered sample becomes denser and appears more conducive to Li^+ conduction. This is most likely due to the lithium content of the samples changing with each sample. For example, the smaller sample should have larger lithium losses than the larger cells due to increased specific surface area. This could make the lithium content closer to the desired stoichiometry of the cells. Therefore, the sizes of the sintered body should be investigated while measuring lithium content to determine how to consistently sinter LLZO garnet.

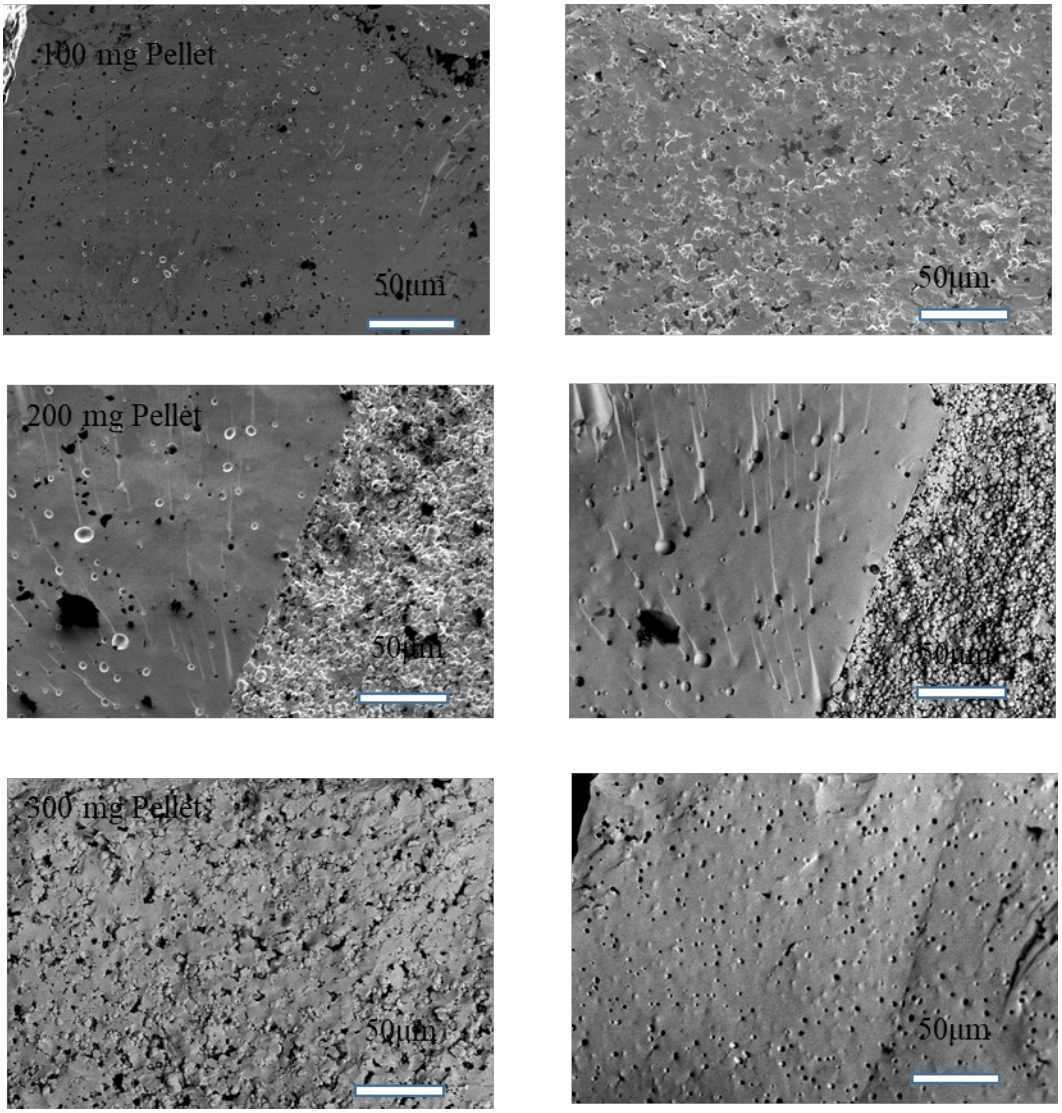

Figure 34. SEM and BSE images of LLCZN20 using different weights of powder pressed into pellets and sintered according to the sintering procedures in Chapter 2

Another option is to eliminate the sintering step all together as it may prove to be a costly with a high scrap rate if not optimized. One approach is to construct a hybrid solution utilizing ceramic LLZO powders, a lithium conducting polymer, and a small amount of OLE. This can be achieved by using poly(vinylidene fluoride-hexafluoropropylene) (PVDF-HFP) as the polymer and LiTSFI dopant to the PVDF-HFP to provide ionic conductivity[297]. By combining up to 30 wt% of $Li_{6.4}La_3Zr_{1.4}Ta_{0.6}O_{12}$, the Young's modulus can be increased to 52.1 MPa and achieve ionic conductivities of 3.2 x 10^{-4} S cm^{-1}. This compares favorably to lithium garnet which has been reported 150 GPa[298] and 10^{-4} S cm^{-1} [299].Traditionally, liquid electrolyte is also added to PVDF-HFP membranes in small amounts to aid conduction over the electrode-electrolyte interfaces and grain to grain conduction in the cell, which can increase the ionic conductivities to 1 x10^{-3} S cm^{-1} when introduced in higher quantities[300]. Combining this with the design of the reported tri-layer structure for all-solid-state batteries[301], a new electrolyte design can be explored.

The tri-layer structure for semi solid-state batteries includes a porous cathode layer, dense solid electrolyte layer, and a porous anode layer. Applying this design to a hybrid cell of PVDF-HFP and LLCZN, three layers can be constructed. On the anode side a high ratio of LLCZN to PVDF-HFP to potentially allow for space for lithium is utilized. The next layer will require a thin dendrite blocking layer in order to increase energy density by decreasing the weight of the electrolyte. This layer will have high amounts of PVDF-HFP but lower amounts of LLCZN10. The last layer will be a duplicate of the anode layer with future designs incorporating active cathode material into the design to allow for ionic conductivity to be added directly into the cathode. In these initial designs the OLE use in Chapter 4 will be added to the CR2025 cell at 20 μL for each 16 mm sample (3.34 μL cm^{-2}).

The detailed design of the cell used in the preliminary results for the rest of the section is shown in Figure 35. The design allows for a standard composite cathode to be utilized, i.e. no changes in the weight ratios utilized in Chapter 4, but does require an ion conductor to be applied (liquid) to allow for full capacity utilization. The next layer, polymer in ceramic, is 85% LLCZN10-PreMill (fabricated as the same procedure in Chapter 2), 10% PVDF-HFP (Sigma Aldrich), and 5% LiTFSI (Sigma Aldrich, 99.99%) in acetone (Fischer Chemical, 99.5%). The mixture was cast on a substrate to create a single thin layer and 16 mm discs were cut out. This layer will also require a liquid infiltration to reduce resistance between itself and the other layers. The last electrolyte layer is ceramic in polymer with 80% PVDF-HFP, 15% LiTSFI, and 5% LLCZN. The anode is a standard lithium metal anode (MTI). This is packaged into a CR2025 cell for evaluation. The tri-layer design is not utilized in this initial testing to determine if the ceramic in polymer layer can limit dendritic failures.

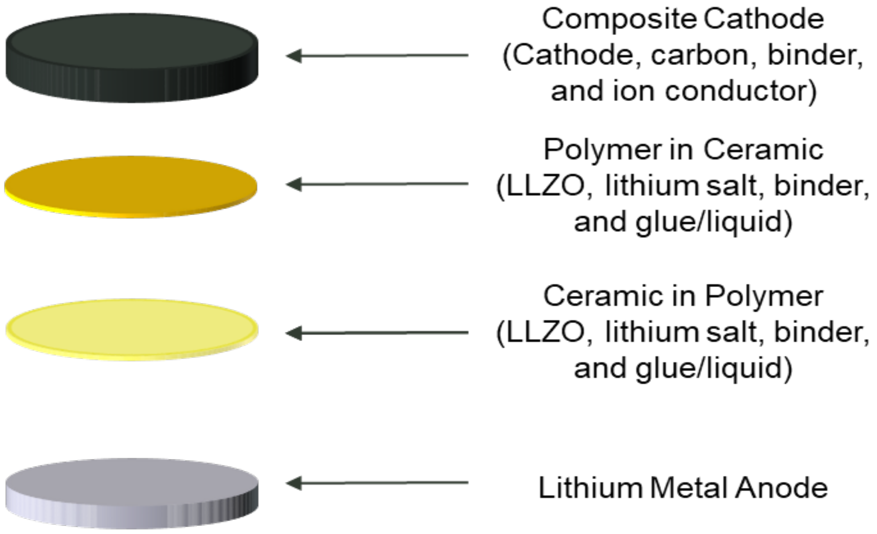

Figure 35. Design of the bilayer design using the polymer in ceramic and ceramic in polymer

Using the design in Figure 35, but constructing a symmetric cell with lithium metal electrodes, lithium is plated and stripped from one lithium metal electrode to the other. The current applied is 0.5 mA for 30 minutes for both charge and discharge and performed at room temperature. The data indicates there does not appear to be much of a side reaction or dendritic formation throughout the experiment (Figure 36). Likewise, the voltage appears stable over long periods of time. This is confirmed in the magnified section of the graph showing the lithium cycling enables a stable voltage despite the long amount of time performing this experiment. However, there are some limitations to the data. This system is limited as there is internal pressure in a CR2025 cell and thirty minutes is a limited amount of time to cycle any device, meaning the amount of lithium plated and stripped is limited to 0.25 mAhr. The data does show that lithium can be successfully stripped and plated over many cycles with limited to no secondary reactions. More research should be performed to plate and strip greater quantities of lithium.

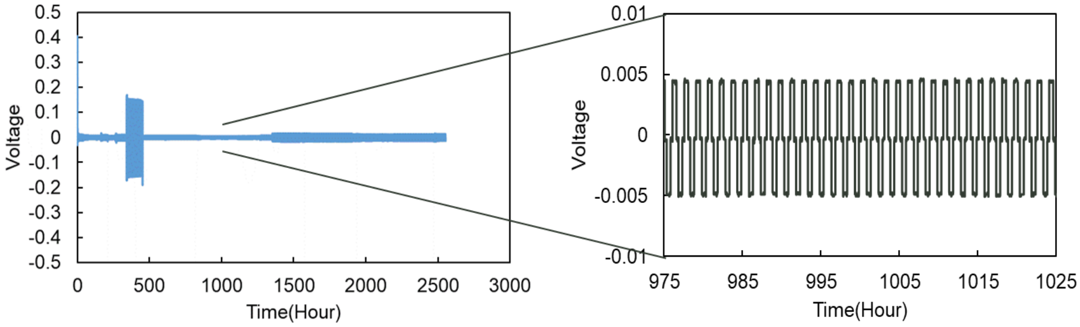

Figure 36. Lithium-lithium cycling of a cell using the design shown in Figure 35

Replacing one of the lithium electrodes from the cell used in Figure 36 with a cathode (80:15:5 LCO:PTFE:C wt%, same percentages as Chapter 4), allows the electrochemical cycling of a full cell (Figure 37). Cycled between 4.2 and 3 V at room temperature, the cells obtain 120 mAhr g^{-1} for five cycles at 0.5 mA cm^{-2}, which is the measured capacity of the LCO used in this work when used with a standard OLE. This captures the promise of the design to deliver high capacity despite limited organic electrolyte. The estimated energy density of the cell is ~125 Wh kg^{-1}, less than the 200-250 Wh kg^{-1} of state-of-the-art lithium-ion batteries but there are optimizations to increase the energy density further.

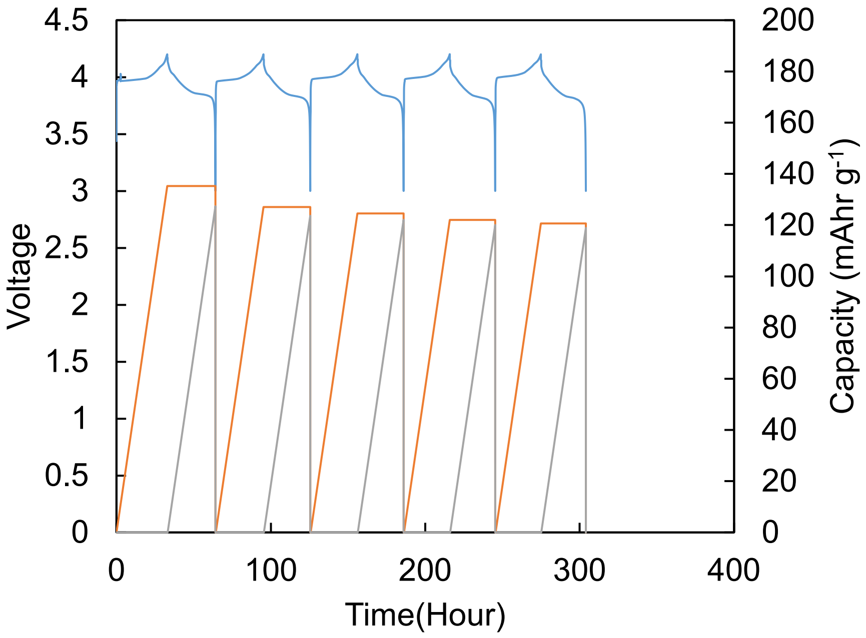

Figure 37. Full cell cycling at 25°C and using the cell design in Figure 35. Blue line is the voltage, orange line is the charge capacity, and gray line is the discharge capacity.

The energy density of the designed cell can be optimized with different materials and processing improvements. Firstly, switching the LCO cathode for a higher energy density cathode, such as NMC622 or the chlorinated, 5 V spinel shown in Chapter 4 will increase the cathode's energy density from 480 to ~750 Wh kg^{-1} without changing the cathode design. Increasing the cathode loading, either through thickness or through reduction of conductive species (carbon) to 35 mg cm^{-2} would increase the cell energy to 350 Wh kg^{-1}. The final change would be to decrease the size of the electrolyte layer to below 9 mg cm^{-2}. With these optimizations, a cell that is 400 Wh kg^{-1} can be constructed but more work is required to determine the viability of these proposed changes.

Future work should also determine if lithium metal is plating through the dendrite blocking layer and causing shorting. While the data shows stability, there are several decreases in voltage that may indicate dendrite formation[302]. Another potential reason is that lithium is plating inside the polymer in ceramic layer as that one will have more pores for plating. This may offer a potential layer to plate lithium and have space without penetrating the dendrite blocking layer, which reduces the overall resistance of the cell. All of these different systems will require structural characterizations (PXRD, Raman, SEM, etc.) to optimize all the parts for a cell that is above 400 Wh kg^{-1}.

2. Interface between LLZO and High Voltage Cathodes

2.1 Conclusions

Lithium content was shown to be an important factor for stabilizing the LCO and LLCZN phases at co-sintering temperatures of 1050°C. The temperatures used were below 1080°C because of the reaction that was shown in the DSC measurements to occur between the two phases above that temperature, regardless of lithium content. When co-sintering at 1050°C for four hours, however, 40% excess lithium added prior to mixing the precursors of LLCZN was required to eliminate detection of secondary phases. The electrochemical cycling performance did show 120 mAhr g^{-1} for 50 cycles in a liquid cell, meaning the co-sintering process did not reduce the capacity of the active material and there was reaction. This is crucial towards understanding co-sintering and how it would impact performance of the active cathode material. However, only 30% excess lithium was required for the best interfacial properties when a thin composite cathode tape was drop caste onto a sintered LLCZN pellet. Co-sintered cells did show promise by cycling at low rates for 50 cycles at elevated temperatures. LCO is a material that has fallen out of favor with the battery market due to concerns of mining[303] and cost[304]. Utilizing the manganese material developed in Chapter 4 or another nickel-based cathode, would be preferable for higher energy densities.

2.2 Future Work

Initial co-sintering experiments between LLCZN40 (formulated as specified in Chapter 3) and $LiMn_2O_4$ (Sigma Aldrich Battery Grade) were performed at 350°C and 800°C for 1 hour at each temperature. The powders were mixed in 50/50 wt % mixtures as performed in the initial experiments in Chapter 3. Without coatings and despite the excess lithium during co-sintering, $LiMn_2O_4$ (LMO) reacts with LLCZN at a lower temperature than LCO as seen in the PXRD (Figure 38). Secondary phases (specifically $La_2Zr_2O_7$) become common after 800°C, in agreement with reported literature[305,306]. The manganese reacts with the lithium garnet regardless of lithium content, meaning the technique shown in Chapter 3 is not valid for LMO type cathodes and the reaction is a different mechanism than with LCO. A coating on the lithium spinel may be required that, unlike lithium, will not be consumed during co-sintering in order to successfully increase the co-sintering temperature.

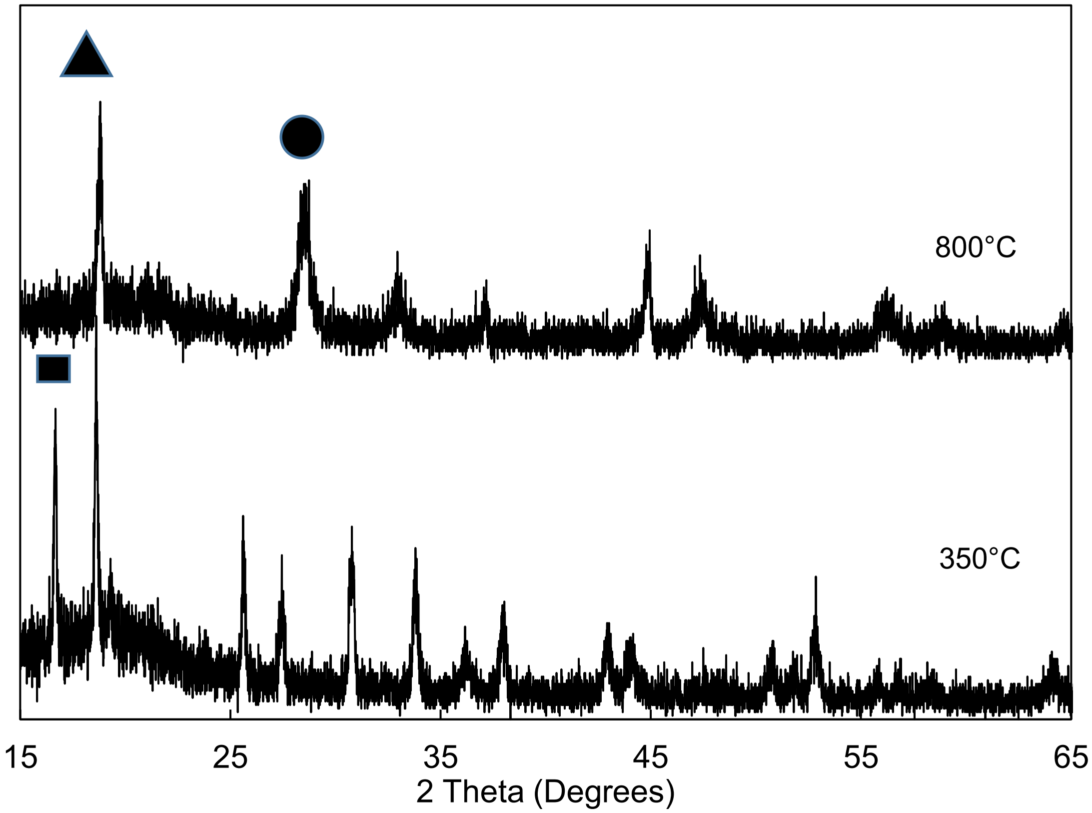

Figure 38. LLCZN40 and $LiMn_{1.85}Ni_{0.05}Fe_{0.05}Co_{0.05}O_{4-d}Cl_d$ co-sintered at 350°C and 800°C. Squares are LLCZN40, triangles are LMO, and circles are $La_2Zr_2O_7$.

LCO was shown to withstand deformations with excess lithium in LLCZN at 1050°C in Chapter 3. Coating LCO onto the spinel surface may offer similar benefits. LCO was coated onto lithium spinel successfully using a sol gel method and heating the mixture to 400°C to calcine the LCO onto the LMO at a 50/50 mol%. The XRD does not show any reaction during the process and indicates pure phase of both materials. The XRD pattern of LCO and LMO do overlap and are difficult to differentiate (Figure 39) [307,308]. However, $La_2Zr_2O_7$ forms in large quantities regardless of lithium content when 50/50 weight mixtures are heated to 800°C. The LCO structure may not be completely covering the LMO particles or the LCO species at this high of content is a favorable molar content for secondary phase formation through the coating layer. This may necessitate a coating that does not include a transition metal.

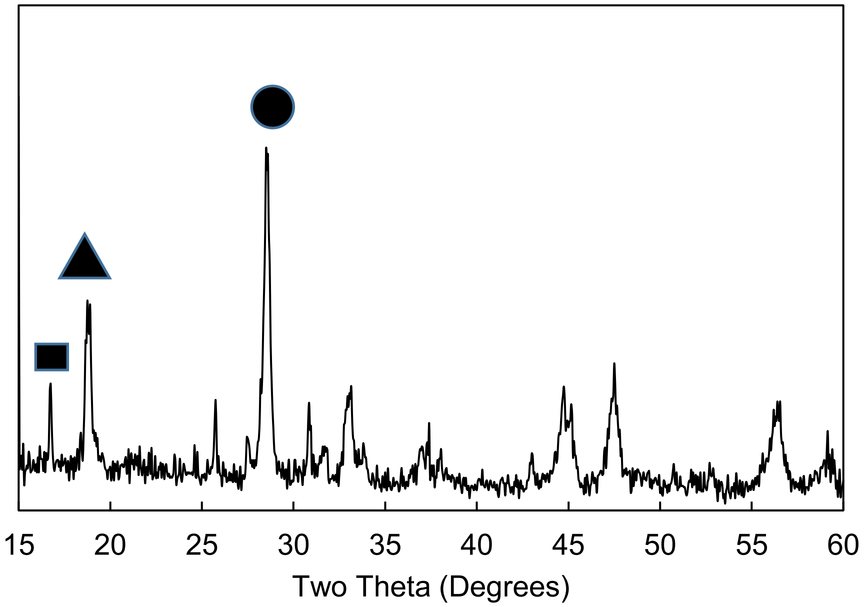

Figure 39. XRD of LCO-coated LMO co-sintered with LLCZN40 at 800°C for one hour. Squares are LLCZN40, triangles are LMO, and circles are $La_2Zr_2O_7$.

Alumina coating on lithium spinel has been shown to limit lattice distortions and manganese dissolution into OLEs [309,310]. Alumina was coated onto LMO particles by the Pechini method. Aluminum nitrate (Sigma Aldrich, 99.997%) was mixed with reagent alcohol (Fisher Scientific) and citric acid in the same ratios as used in Chapter 4. Ethylene glycol and LMO were then added at the same ratio as Chapter 4 to make 2% Al_2O_3 and 98% LMO. The procedure continued as specified in Chapter 4 but the calcination was reduced to 600°C for one hour. Initially when mixed in a 50/50 wt. % mixture with LLCZN40 as in Chapter 3, the coating appears to maintain the stability of both phases at 500°C for one hour. However, despite the coating, the stability of LMO and LLCZN did not increase to 800°C, which is within the sintering temperatures of LLZO electrolytes when dopants or sintering aids are utilized. The secondary phase appears to be $La_2Zr_2O_7$. The oxygen loss that occurs around 800°C causes Li_2MnO_3 formation and a change in oxidation state of the Mn[311]. This change may be driving the reaction with both the LLCZN and LCO or Al2O3 coating is applied to the surface.

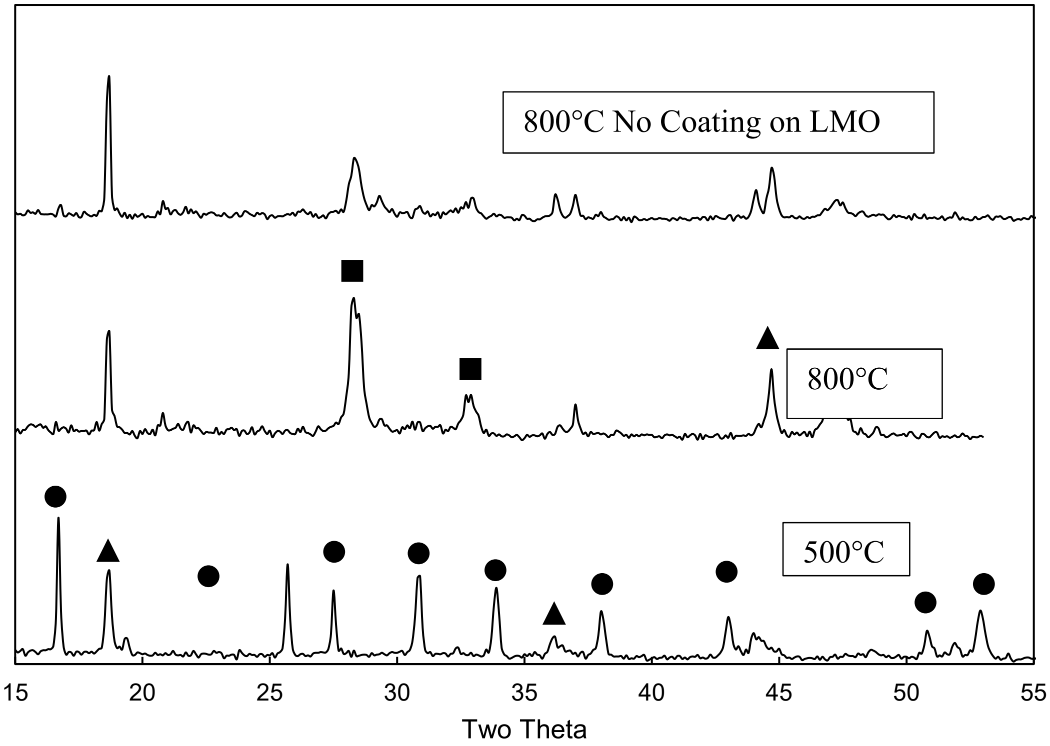

Figure 40. PXRD of resultant mixtures of LCO particles with different coating mixed with LLCZN and co-sintered to various temperatures. Circles are LLCZN, triangles are lithium spinel, and square are secondary species from the reaction between the two.

These preliminary results show some potential for co-sintering a coated spinel with LLZO type electrolytes. However, more work will be needed to confirm stability at temperatures closer to 800°C and a decrease in interfacial resistance with LLZO electrolytes. Transmission electron microscope or other surface level techniques should also be used to confirm the stability of the coating. EIS using the symmetric cell system outlined in Chapter 3 can be performed at various temperatures and coatings to determine the decrease in R_{INT}. Determining these properties with an LLZO type system, the dopants or sintering aids in LLCZN can be varied to better match the co-sintering temperature to create a solid electrolyte and solid cathode in a single step.

3. Lithium Spinel Cathode and Composite Cathodes for LLZO

3.1 Conclusions

The LMO type spinel structure was shown to be capable of three different transition metal dopants on the A-site that enabled higher voltage operation and the chlorine as an anion dopant, increases capacity when operated at voltages down to 2 V. The transition metal dopants increased capacity by 20% when increasing the charging voltage from 4 V to 4.75 V and another 10% above 5 V. However, the stress on the cell from cycling to 5 V through the decomposition of the liquid electrolyte, indicated by the increase in resistance, caused the cells to quickly lose capacity. Despite these issues, a material that has high rates and can provide a long cycle life, albeit with reduced capacity, was demonstrated.

Chlorine was added as an anion dopant to increase capacity to 240 mAhr g^{-1}, effectively making the spinel structure $L_{i2}Mn_2O_4$-Cl_d when discharge to 2 V. The electronegativity of the chlorine draws in the oxygen atoms widening the 3-d channels of the spinel enabling a second lithium to be cycled into and out of the structure. This extra capacity achieved makes the doped LMO spinel an attractive cathode for next generation lithium-based batteries as it has more capacity than NMC based cathode materials and employs manganese rather than nickel or cobalt. Utilizing this cathode with LLZO sintered pellets developed in the varying lithium content section, the potential for cycling between 5 V and 2 V was displayed for five cycles, albeit at a slow rate. More work though is needed to lengthen the cycle life and increase rate capability with the LLZO garnet. through the use of thinner solid-state layer to increase rates. Additionally, the liquid used as a catholyte should be optimized to increase coulombic efficiency to decrease secondary reactions.

3.2 Future Work with Anion Doped Spinel

Future work should focus on the impact of chlorine on the structure and its interaction with the other sites in the lattice structure. Chlorine has higher electronegativity than oxygen and despite being in lower quantities does show an impact when doped in LMO on the performance, the lattice parameter, and the lattice ordering. Similar anion dopants in lithium spinel such as, fluorine and sulfur, has been shown to decrease the oxidation state of manganese[312] , greater thermal stability[313], and better SEI formation[314]. While sulfur doping on the anion site has been shown to increase electrical conductivity[315], increases capacity to 183 mAhr g^{-1} [316], and increased electrochemical properties[317]. All of these studies should be performed to determine chlorines impacts on the structure, conductivity, and SEI formation to name a few of the potential impacts of chlorine.

Lithium spinel offers the opportunity to operate at 5 V and above but requires and electrolyte that is stable above 4.5 V. Lithium conducting garnet can operate at those voltages but requires more studies to determine a design to minimize the resistance of the SSE layer, which requires studying the lithium lost during high temperature sintering. Once sintered, the interface resistance between the cathode and SSE will need to be minimized and those ionic pathways to be dispersed through the cathode to allow for operation of a solid-state battery with an environmentally friendly cathode that will achieve over 400 Wh kg^{-1}.

Appendices

Appendix A: Supplementary Information for Chapter 2

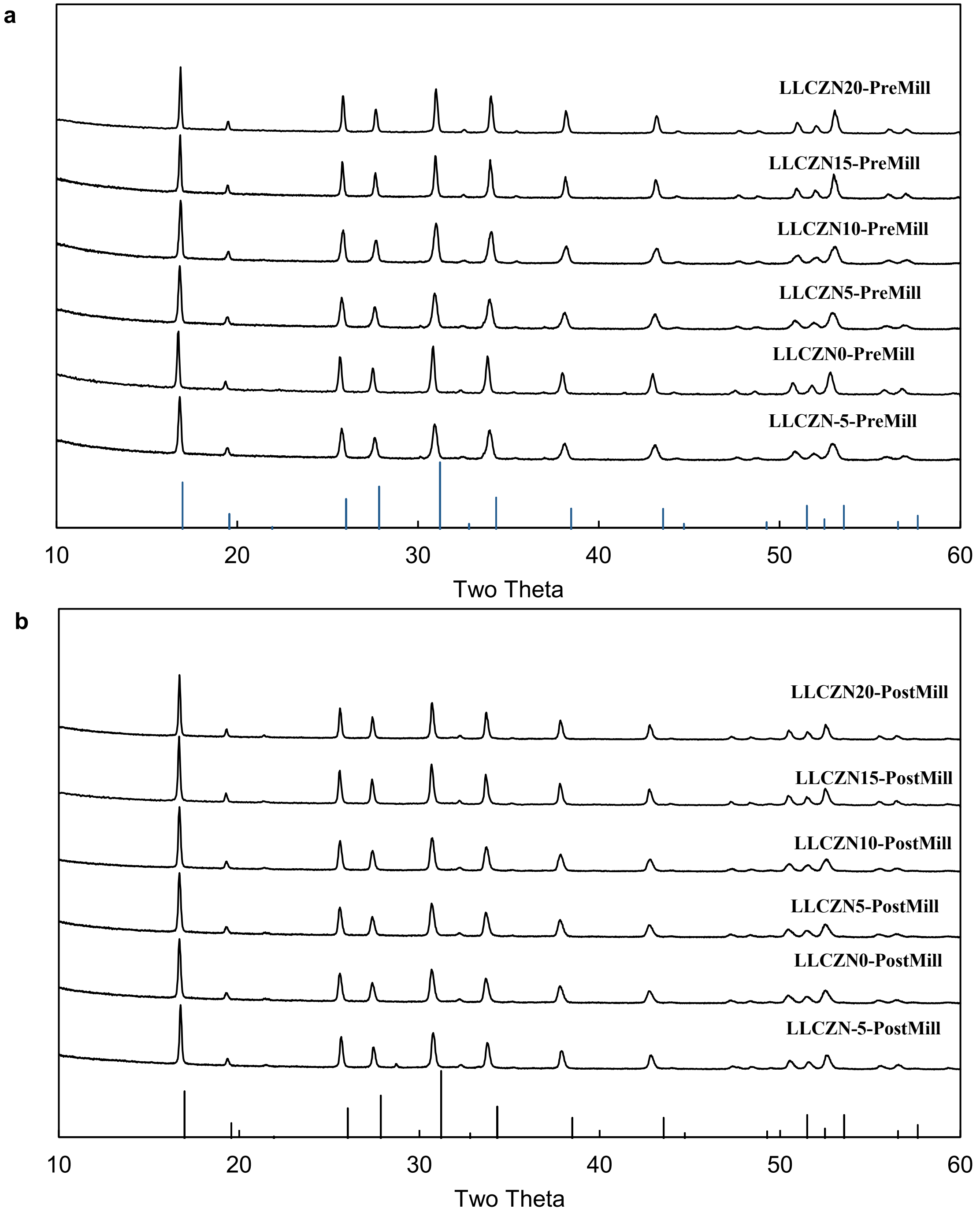

Figure S1. XRD of calcined powders. **1Sa.** PreMill LLCZN powder. **1Sb.** PostMill LLCZN powder. The bottom pattern is ICDD 45-0109

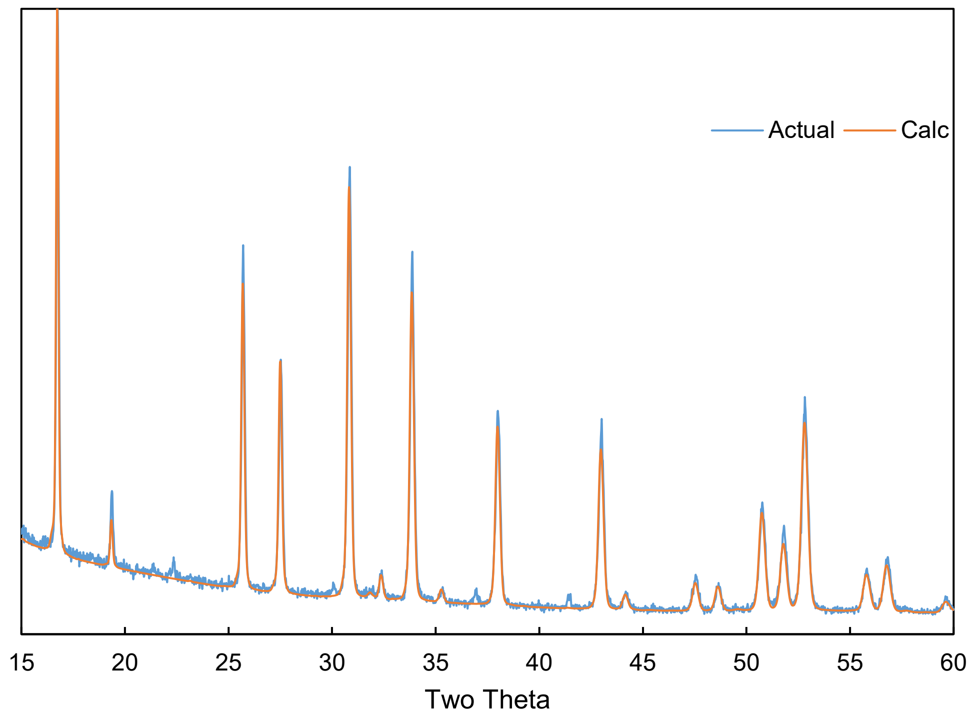

Figure S2. Refinement fit of XRD

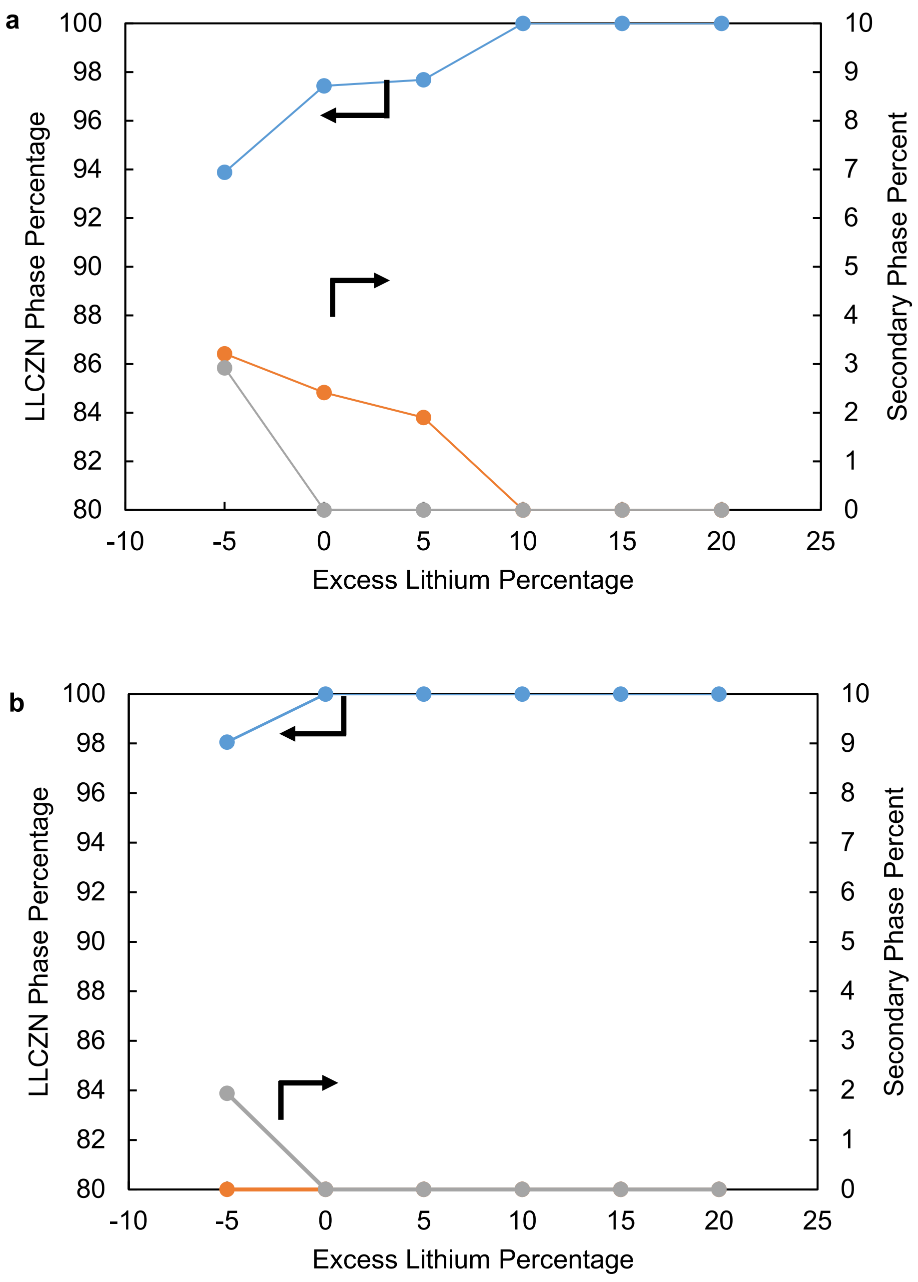

Figure S3. Phase plot vs. lithium content. Blue is LLCZN phase, orange is $CaCO_3$, and gray is $La_2Zr_2O_7$. **S3a.** PreMill LLCZN powder. **S3b.** PostMill LLCZN powder.

In the PXRD results, there does appear to be an increase in phase purity after milling. However, the TGA, DSC, and Raman results indicate a reaction during the ball milling step. The added 10% of weight from this step may lower the secondary phases under the detectable limit of the PXRD.

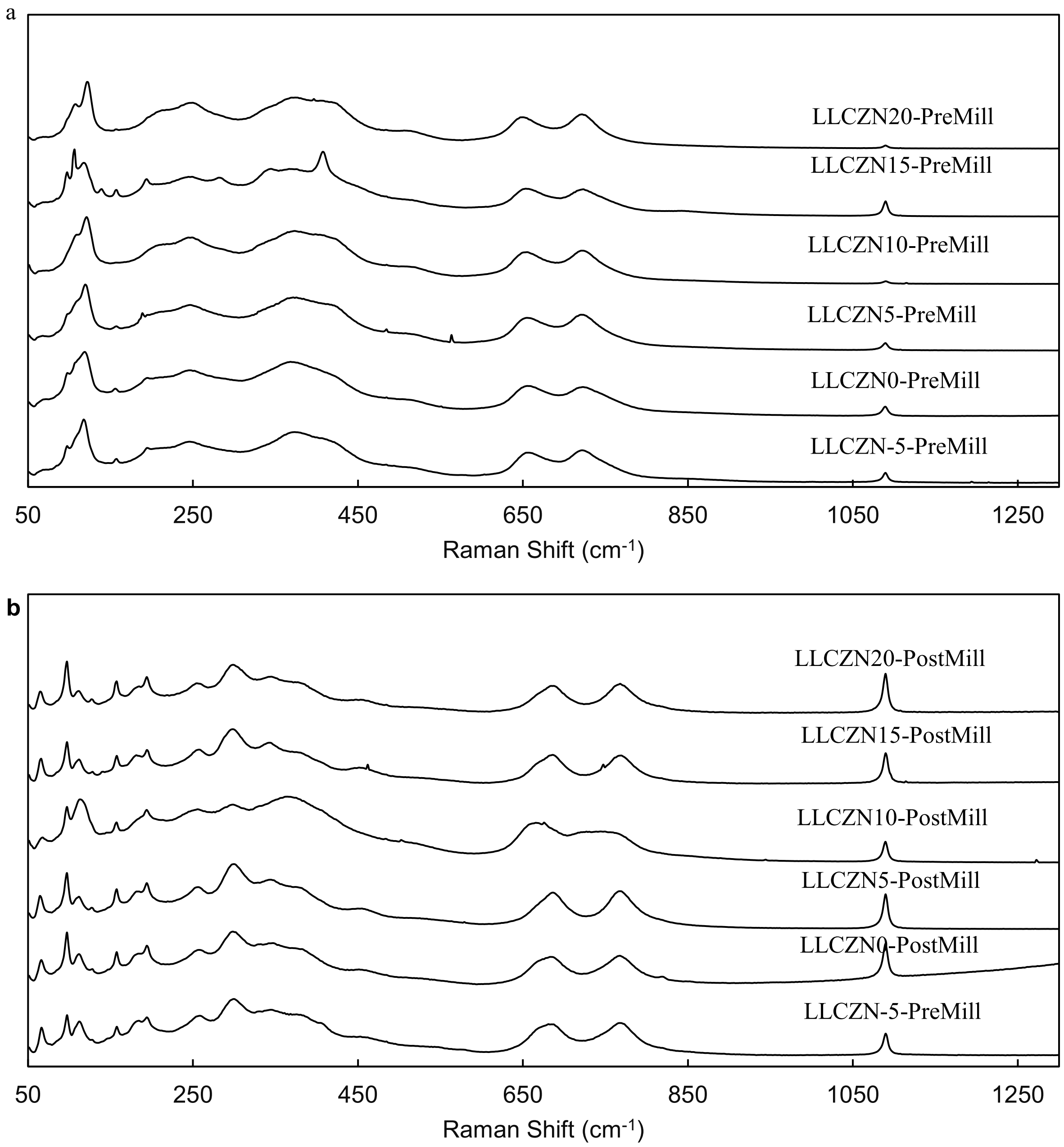

Figure S4. Raman spectra of calcined powders. **S4a.** PreMill LLCZN powder. **S4b.** PostMill LLCZN powder.

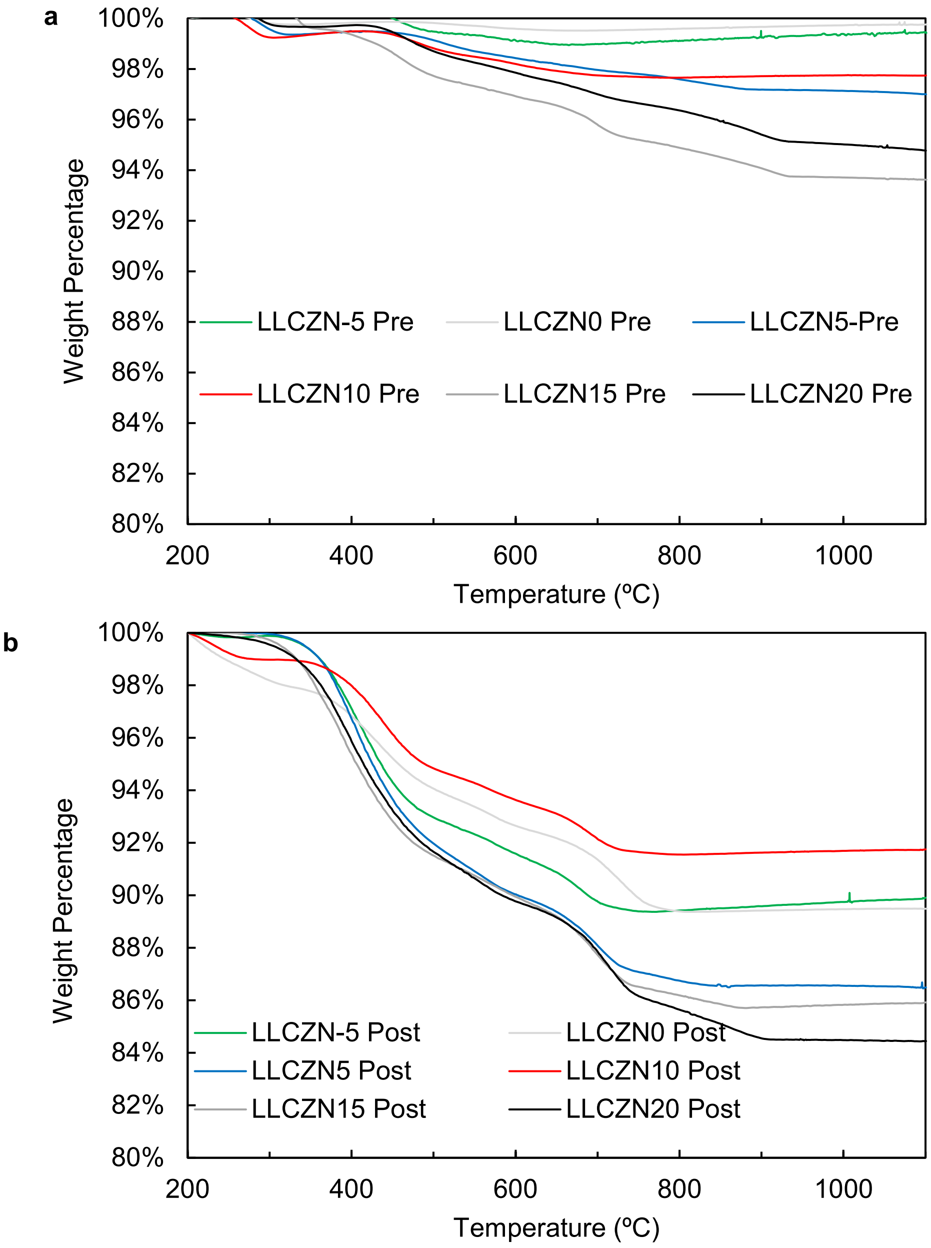

Figure S5. TGA of calcined powders. **S5a.** PreMill LLCZN powder. **S5b.** PostMill LLCZN powder.

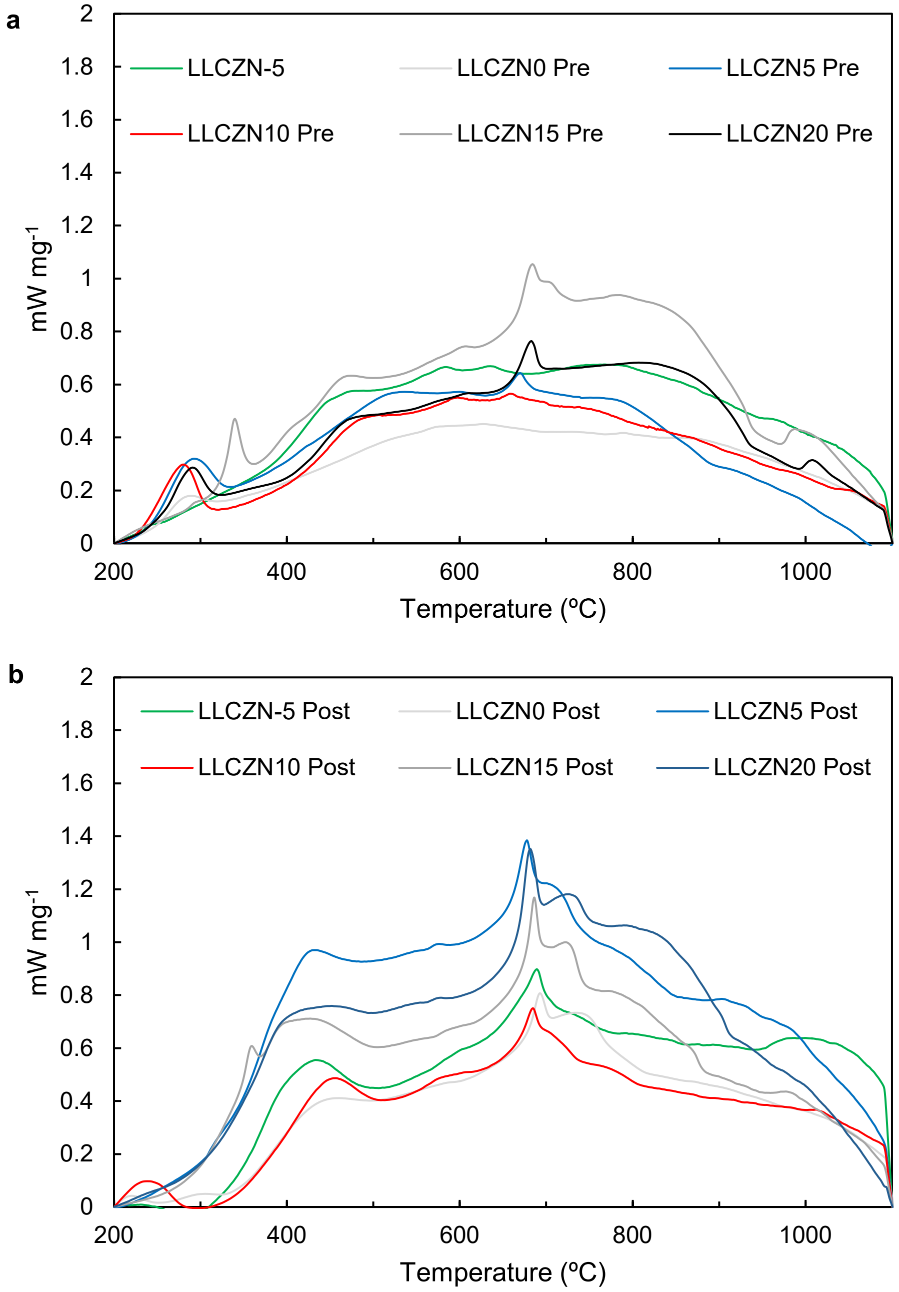

Figure S6. DSC of calcined powders. **S6a.** PreMill LLCZN powder. **S6b.** PostMill LLCZN powder.

	x	**y**	**z**	**Occupancy**
Lithium 1	0.3750	0.0000	0.2500	0.9400
Lithium 2	0.0959	0.6900	0.5731	0.3500
Lanthanum	0.1250	0.0000	0.2500	0.9190
Calcium	0.1250	0.0000	0.2500	0.0810
Zirconium	0.0000	0.0000	0.0000	0.7500
Niobium	0.0000	0.0000	0.0000	0.2500
Oxygen	-0.0316	0.0538	0.1500	1.0000

Table S1. Fitting Parameters of LLCZN PXRD

LLCZNX	**RWP**	**X2**
LLCZN-5-PreMill	7.18	2.47924
LLCZN0-PreMill	6.5	1.98804
LLCZN5-PreMill	6.39	1.88841
LLCZN10-PreMill	6.25	2.04549
LLCZN15-PreMill	6.31	1.72813
LLCZN20-PreMill	6.72	2.3115
LLCZN-5-PostMill	9.08	4.95281
LLCZN0-PostMill	8.51	3.156371
LLCZN5-PostMill	9.82	4.913778
LLCZN10-PostMill	9.22	5.795145
LLCZN15-PostMill	9.89	5.790405
LLCZN20-PostMill	10.72	6.453045

Table S2. Refinement results of varying lithium content

The calculated lattice parameter before sintering can give an indication for the lattice spacing free of aluminum and how it changes with lithium content. Rietveld refinement data of the Pre-Mill samples indicates a decrease in the lattice parameter between LLCZN0 to LLCZN20 (fitting parameters in Table S1 and S2). The lattice parameters can be used to estimate the lithium content of certain samples (Table S3). In comparison, the lattice parameter of the Post-Mill powder shows slighter variations as a function of lithium owning to the small atomic radius of lithium and the reaction during the IPA ball milling step. The lattice parameter will revert back to the range closer to the Pre-Mill samples when Li_2CO_3 decomposes but the final sintered sample's lattice parameter will be dependent on lithium loss and aluminum contamination, which will impact σ_{Bulk}.

Percent Excess Li Added	Designed Molar Li Content	Measured Molar Li Content of Calcined LLCZNX	Calculated Molar Lithium Content	Absolute Percent Difference
-5	6.413	5.914	N/A	N/A
0	6.750	6.394	6.297	1.5%
5	7.088	6.558	6.642	1.3%
10	7.425	6.768	7.089	4.7%
15	7.763	7.189	7.109	1.1%
20	8.100	7.481	7.252	3.1%

Table S3. Measured molar lithium content after calcination and the calculated molar lithium content using the lattice parameter with the error between the calculated and the actual.

Calculating lithium content from the lattice parameters would enable the measurement of lithium content without performing ICP-MS. By not utilizing certain samples where $La_2Zr_2O_7$ is formed (LLCZN-5), the lithium content of calcined powder can be estimated from the PreMill lattice parameter (Table S3). By doing so, the average error between the measured and calculated molar lithium content is 2.3%. This error may be from lithium garnets reaction with air or other experimental errors but the results indicate the possibility to estimate lithium content without performing ICP-MS.

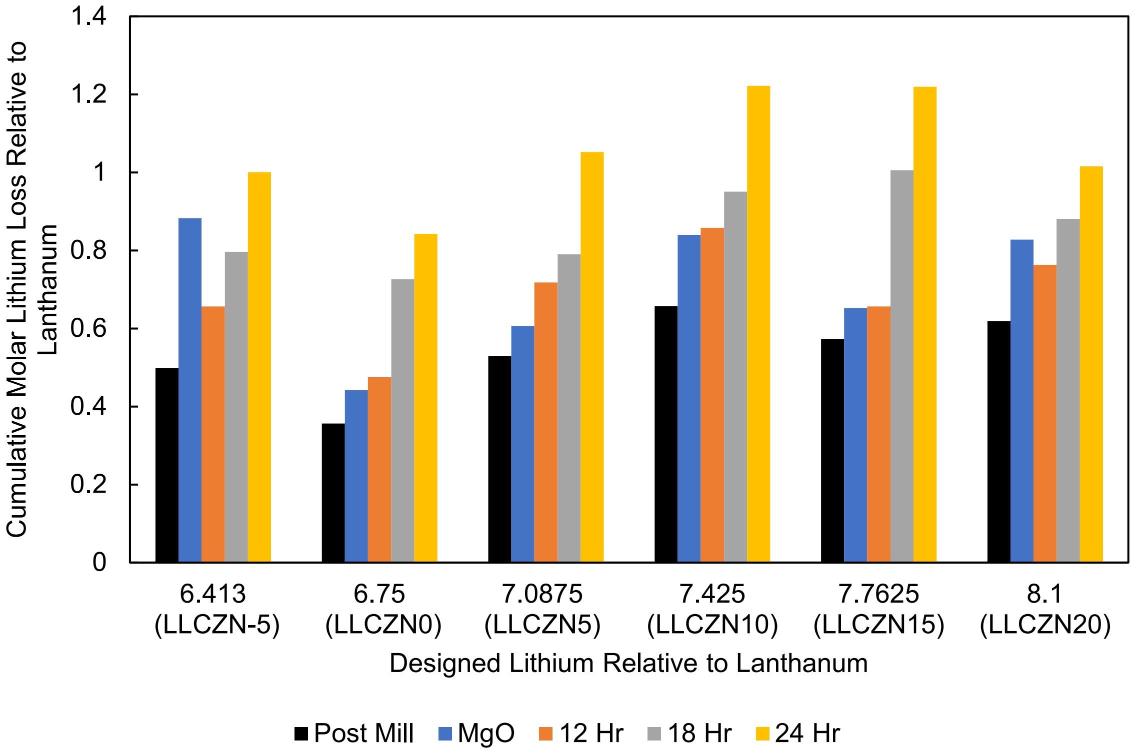

Figure S7. Percent lithium loss from added molar lithium content vs. the added lithium content.

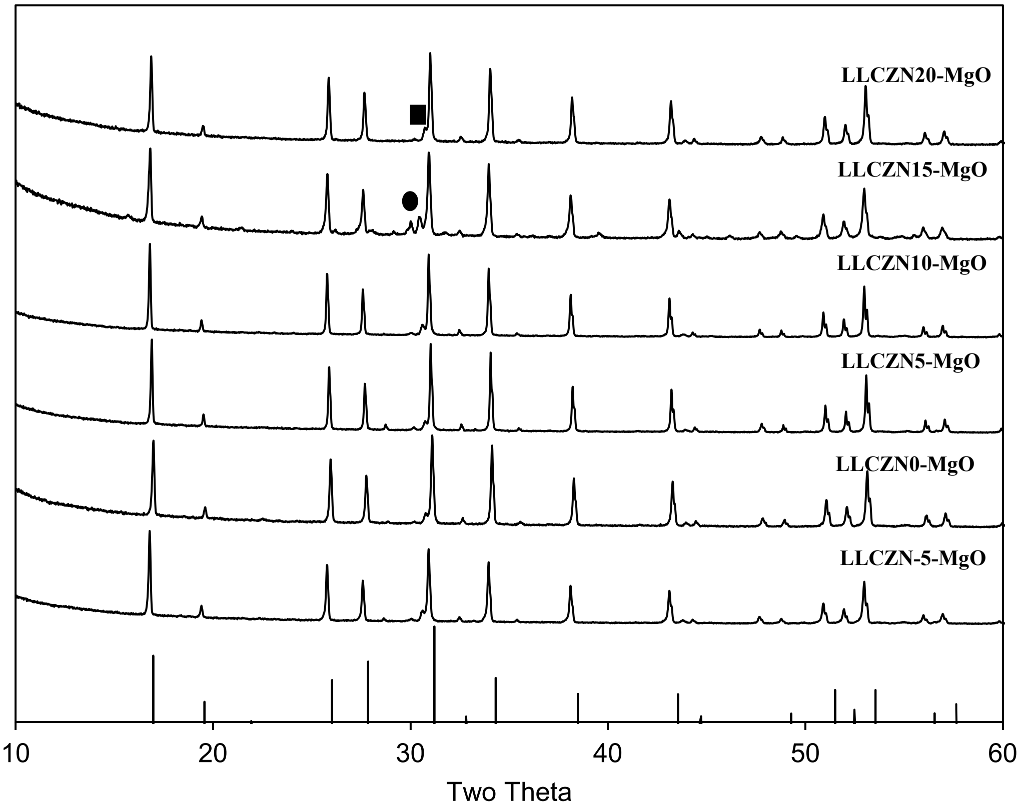

Figure S8. Structural characterization data for LLCZNX-MgO. PXRD where the bottom pattern is ICDD 45-0109. Circles are $La_2Zr_2O_7$ and squares are $CaZrO_3$.

LLCZNX-MgO	RWP	X^2
-5	9.22	5.83
0	8.35	4.25
5	8.29	4.40
10	8.16	4.56
15	10.42	6.96
20	7.82	3.78

Table S4. Fitting results of PXRD from LLCZNX-MgO

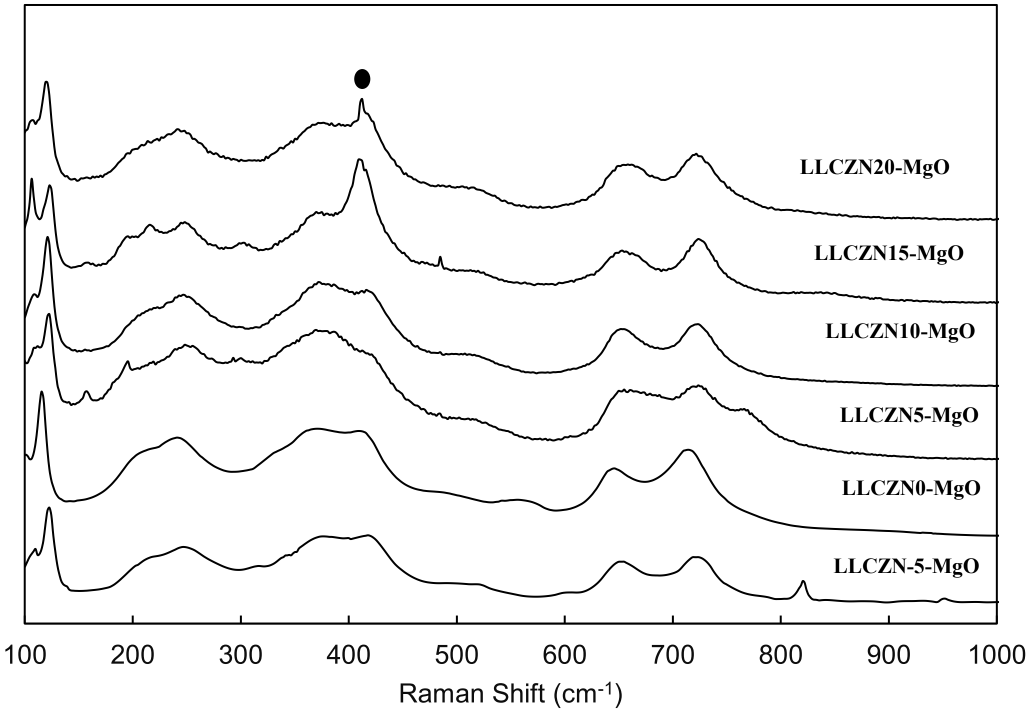

Figure S9. Raman Spectra of LLCZNX-MgO. Circles are $La_2Zr_2O_7$

Bands below 150 cm^{-1} are ascribed to lanthanum cations[318]. The low frequency range (<300 cm^{-1}) matches LiO6 octahedral (96h$_{Li1}$ position) vibrations and the middle frequency (300-550 cm^{-1}) to the LiO_4 tetrahedral (24d$_{Li1}$ position). Lastly, the bands greater than 550 cm^{-1} are associated with the Zr octahedral vibrations[319] and Nb-O sites. Sharp peaks indicate secondary phases as either $La_2Zr_2O_7$ (300 cm^{-1})[320] or $CaCO_3$ (250 and 550 cm^{-1})[321] and are detected in samples that are contaminated with aluminum or out of the lithium stoichiometric range = 6.75 and 6.4. As lithium content is reduced, the band at 400 cm^{-1} begins to weaken. The bands at 400 cm^{-1} are ascribed to $La_2Zr_2O_7$ formation[320].

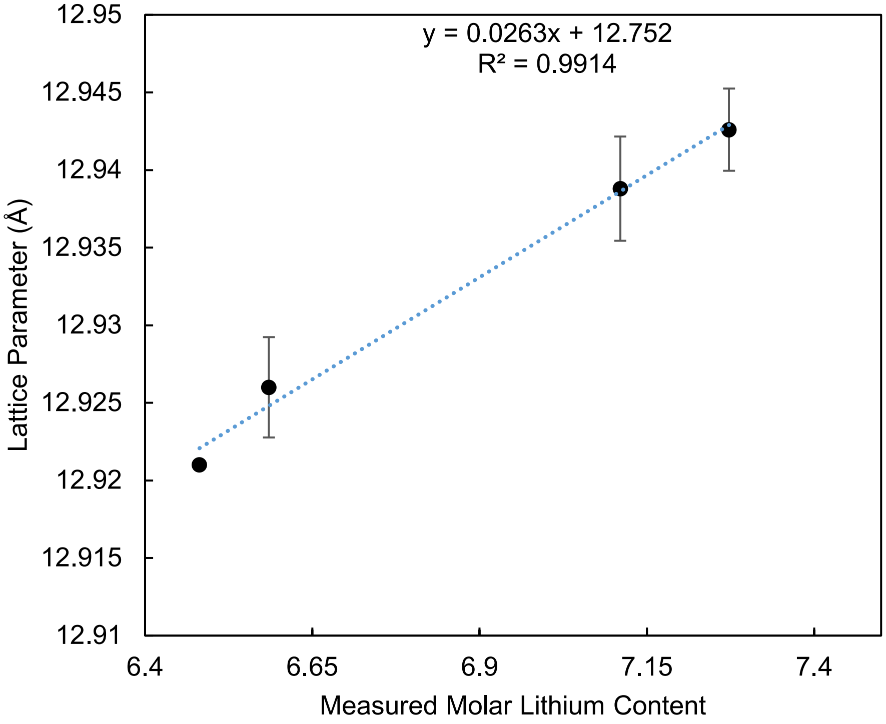

Figure S10. Lattice parameter versus measured lithium content of LLCZNX-MgO

Percent Excess Li Added	Designed Molar Li Content	Measured Molar Li Content of LLCZNX-MgO	Calculated Molar Lithium Content	Percent Difference
-5	6.413	5.53	N/A	N/A
0	6.750	6.31	N/A	N/A
5	7.088	6.48	6.447	0.50%
10	7.425	6.59	6.632	0.64%
15	7.763	7.11	7.112	0.02%
20	8.100	7.27	7.259	0.15%

Table S5. Measured molar lithium content after sintering in MgO and the calculated molar lithium content using the lattice parameter with the error between the calculated and the actual.

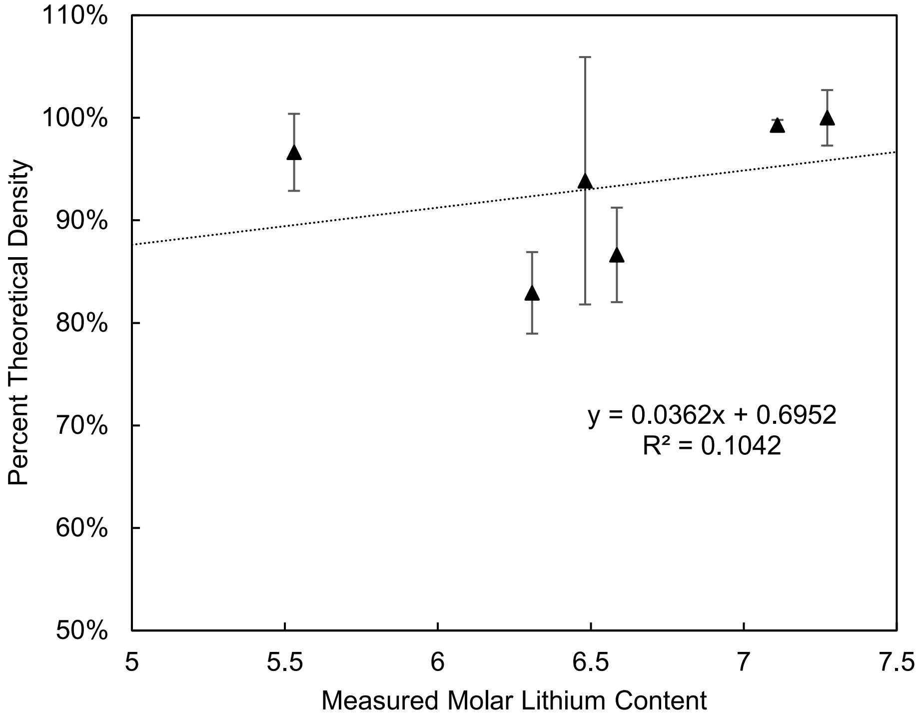

Figure S11. Density percent versus measured molar lithium content of LLCZNX-MgO

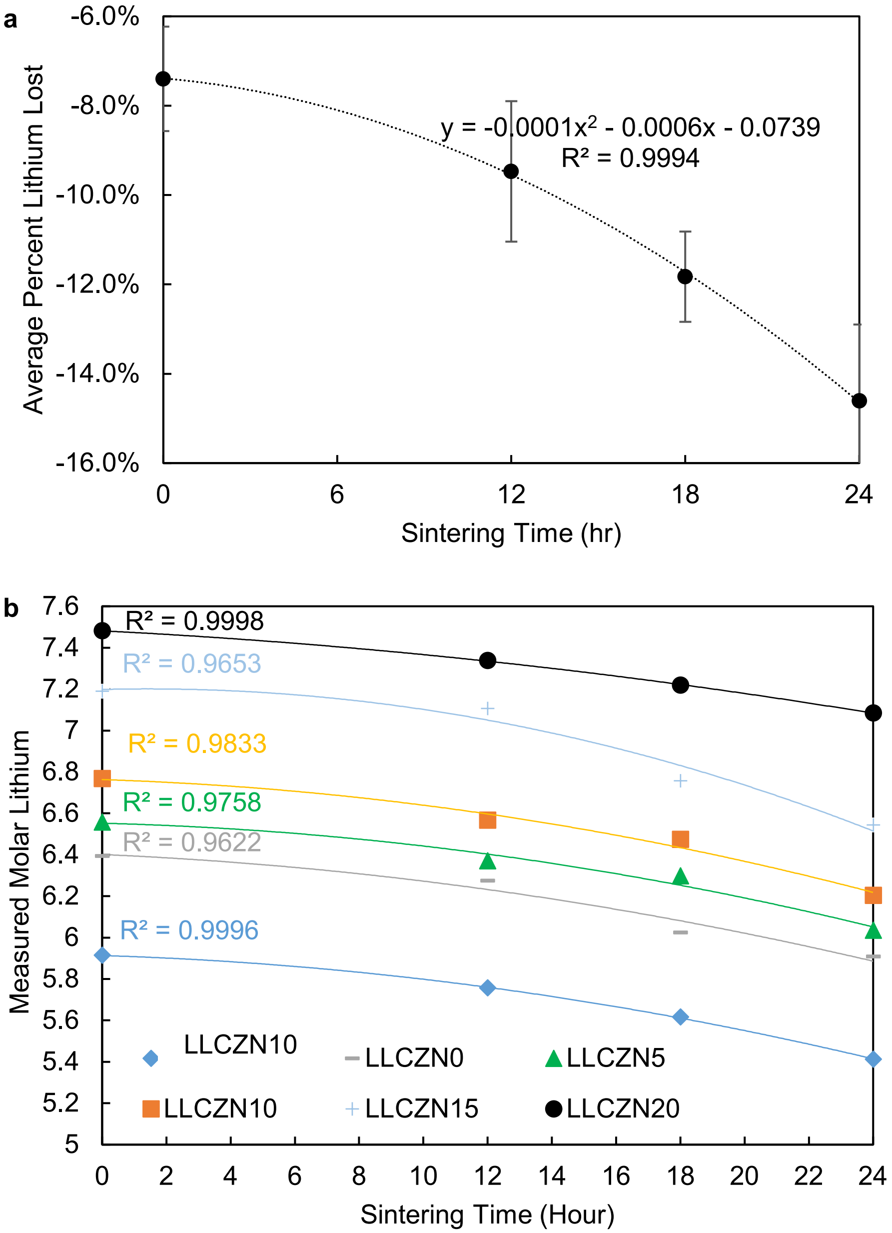

Figure S12a. Average lithium loss and aluminum gain versus sintering time. Circles are lithium loss. **Figure S12b.** Measured molar lithium amount by lithium content vs sintering time. Circles are LLCZN20, plusses are LLCZN15, squares, are LLCZN10, triangles are LLCZN5, minuses are LLCZN0, and diamonds are LLCZN-5

Estimating the lithium percentage from added lithium content would be beneficial and eliminate the need for destructive analysis using ICP-MS. In this work, the percentage of lithium lost from the added lithium, follows a linear trend (Figure S12a) between 12 and 24 hours. The linear data though is limited to between these times, but some inferences can be made as the sintering time approaches zero where the trend becomes quadratic. Li_2O vapor pressure occurs above 500°C and increases with temperature[322]. In our experimental set up, the samples are exposed to these temperatures for 6.67 hours between 500°C and 1100°C as the furnace heats and cools during which time Li_2O vapor pressure will form. The rate of lithium loss (mol Li hour^{-1}) further exemplifies this by its rise from 0.012 to 0.022 mol Li hour^{-1} with increasing sintering time from 12 to 24 hours. However, as the sintering time gets closer to zero, the lithium losses may be dominated by the lower vapor pressure rates at the heating and cooling times, meaning the losses per sintering time (rate) will be slower. Despite these losses, the weight change at 12 hours appears be the primary influence of weight loss and not the losses during heating and cooling.

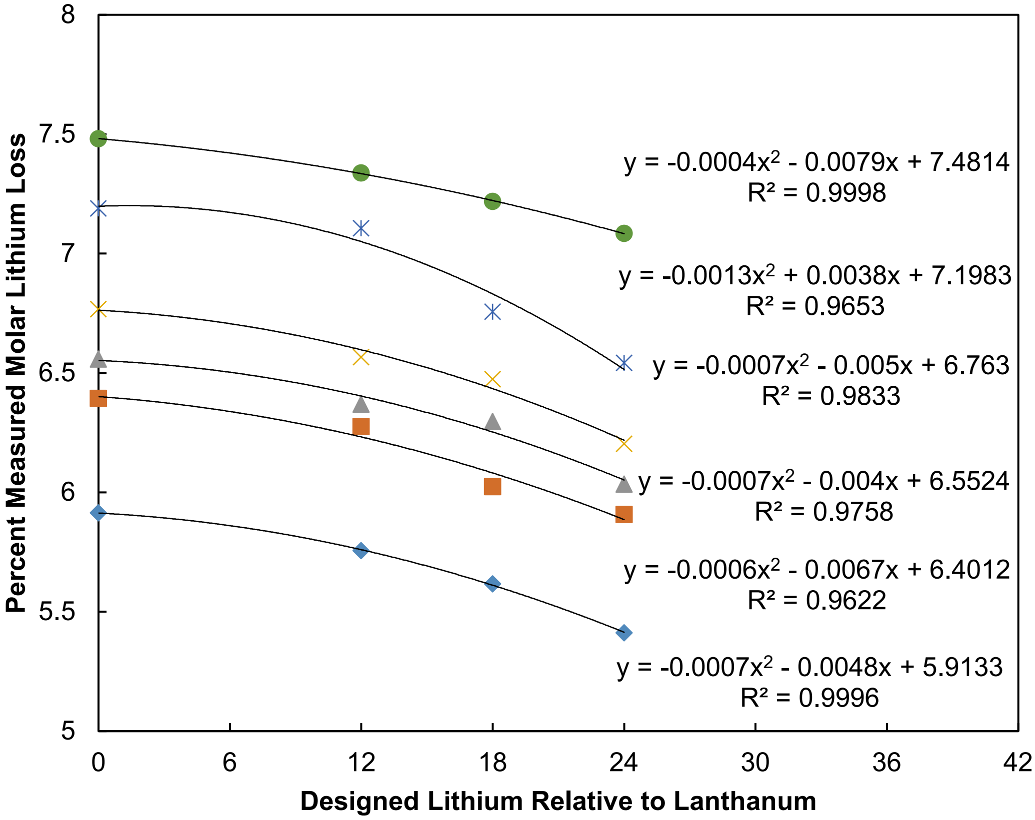

Figure S13. Sintering Time vs. Measured Molar Lithium Amount in Various Excess Lithium Amounts Circles are LLCZN20, plusses are LLCZN15, squares, are LLCZN10, triangles are LLCZN10, minuses are LLCZN0, and diamonds are LLCZN-5. Trend lines are quadratic.

Lithium content versus sintering time also appears to be quadratic for each individual LLCZNX sample as lithium loss slows when approaching the Post-Mill lithium content for all samples (Figure S13b). With the equations listed in Figures 3, the lithium content in the sintered samples can be estimated from the added lithium content, which would then not be required to be measured when using this sintering procedure. The quadratic equations in Figure 10b follow the standard quadratic formula (Eq. 12)

$$(12) \qquad y = ax^2 + bx + c$$

Meanwhile, the quadratic formulas for each individual trend line with constants “a” and “b” (listed in Figure S13) can be averaged (Eq. 13) where y is the molar lithium content after sintering and x is the sintering time.

$$(13) \qquad y = -0.00073x^2 - 0.00335x + c$$

Lastly, the “c” constant for each individual powder can be replaced by the molar lithium content for the calcined powder equation to become Eq. 14.

$$(14) \qquad y = -0.00073x^2 + 0.925x$$

This equation is able to use the added lithium molar contents and compare to the measured lithium contents listed in Table S6. The results show a fit with a relative error between calculated and the actual of 1.15% (Figure S14). LLCZNX-MgO samples can also be compared to the results of the equation where the error was found to 2.2% but may not be a proper comparison with the larger crucible utilized during that procedure.

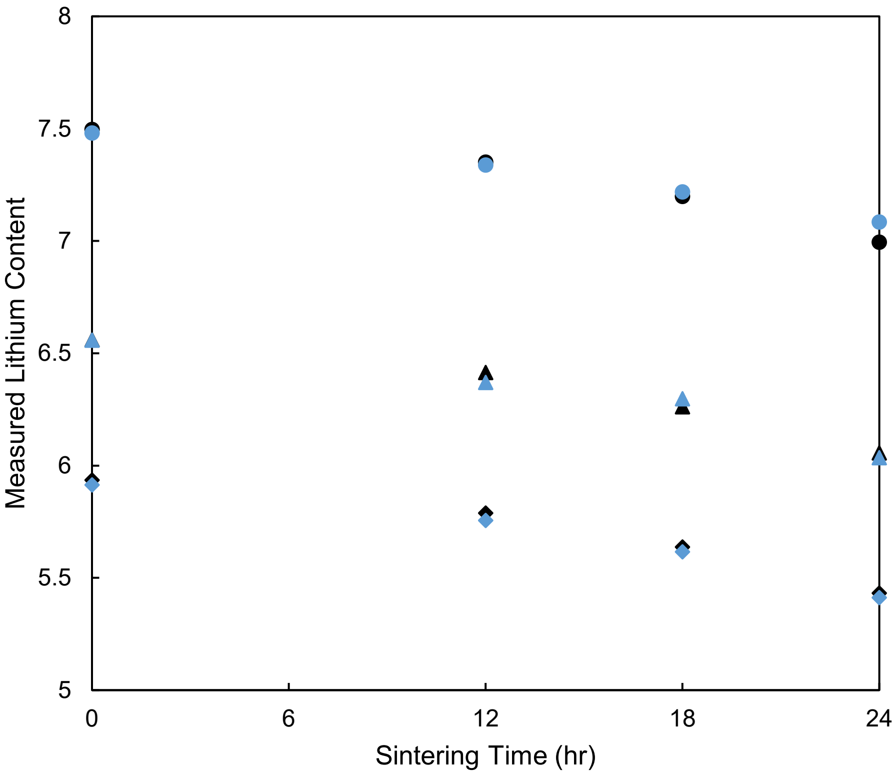

Figure S14. Molar lithium content vs. sintering time. Circles are LLCZN20 squares, triangles are LLCZN10, and diamonds are LLCZN-5. The blue data points are actual while the black are calculated with equation 12.

Researchers desire to limit sintering times in order to make garnet financially feasible for use in lithium-ion batteries[323] and thus several inferences can be made based on our results. Each of the constants in the calcined powder and the sintering equations will be influenced by either the calcination or the sintering conditions. The sintering constants (a and b) and the calcination equation are influenced by atmosphere[324], powder bed[325], and sample size[326]. With no powder bed and higher rates of lithium loss at the operational temperature, the a constant may approach zero as the losses become linear. That will make the "b" constant larger in contrast, which may be the case for powder bed free sintering in tape casted samples[327]. Other issues like equipment variations may be factors but are not likely to be as large of a factor as the lithium loss in absence of a powder bed. The variations of lithium content of LLZO type garnets impacts physical and electrochemical properties and are critical to understand for large scale manufacturing, especially as new sintering techniques are developed.

Sintering Time (hr)	Excess Lithium Percentage	Measured Lithium Content	Percentage Change in Lithium from Calcined Results	Measured Aluminum Content
12	-5	5.76	-3%	0.00
12	0	6.28	-2%	0.00
12	5	6.37	-3%	0.18
12	10	6.57	-3%	0.01
12	15	7.11	-1%	0.04
12	20	7.34	-2%	0.55
18	-5	5.62	-5%	0.00
18	0	6.02	-6%	0.00
18	5	6.30	-4%	0.10
18	10	6.47	-4%	0.02
18	15	6.76	-6%	0.11
18	20	7.22	-4%	0.31
24	-5	5.41	-8%	0.00
24	0	5.91	-8%	0.00
24	5	6.03	-9%	0.11
24	10	6.20	-8%	0.02
24	15	6.54	-9%	0.20
24	20	7.08	-5%	0.14

Table S6. ICP-MS results for samples sintered in alumina crucibles

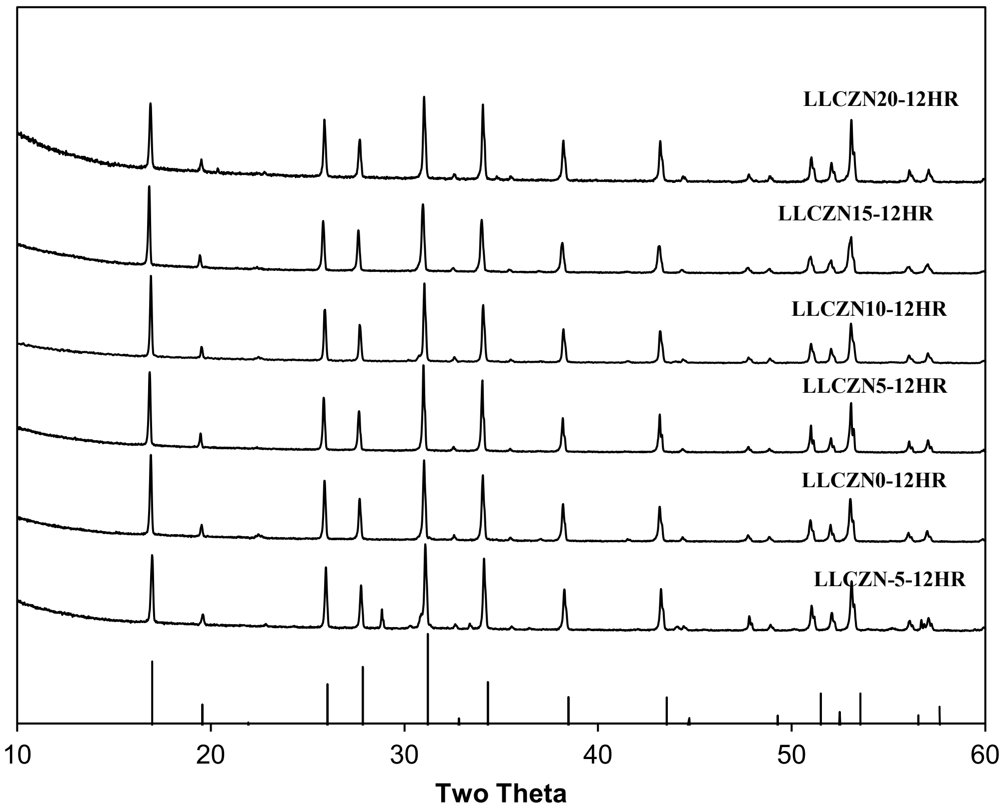

Figure S15. PXRD of LLCZNX-12HR sintered in alumina crucibles. Circles are $La_2Zr_2O_7$ and squares are $CaZrO_3$.

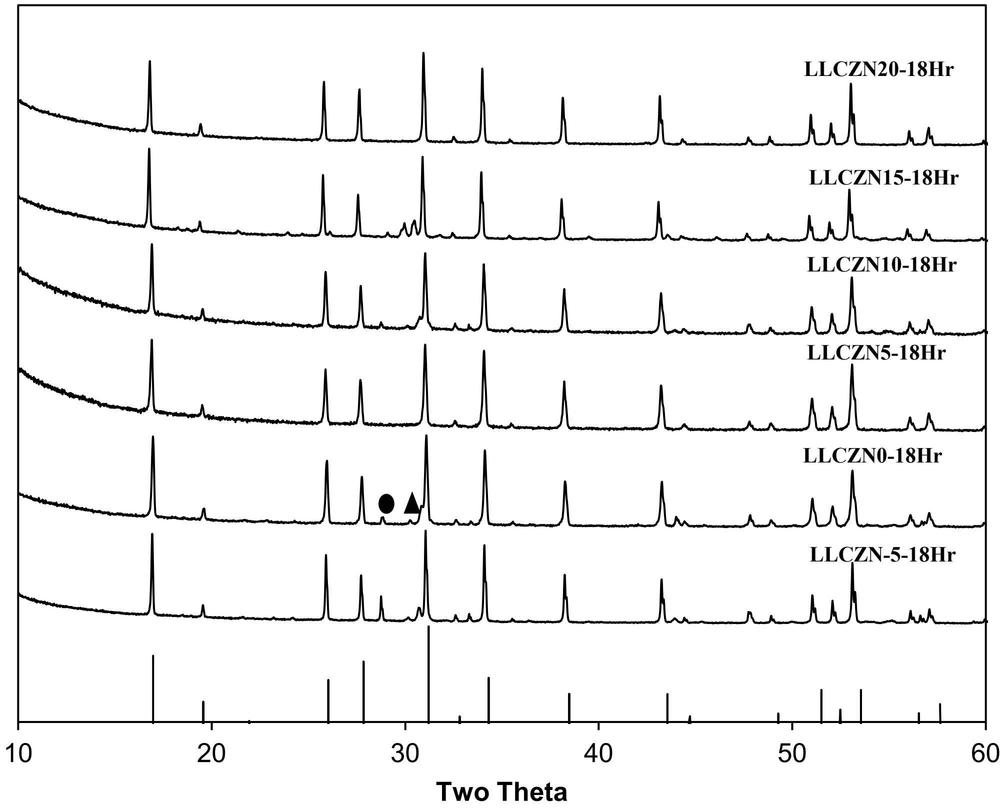

Figure S16. PXRD of LLCZNX-18HR sintered in alumina crucibles. Circles are $La_2Zr_2O_7$ and triangles are $CaZrO_3$.

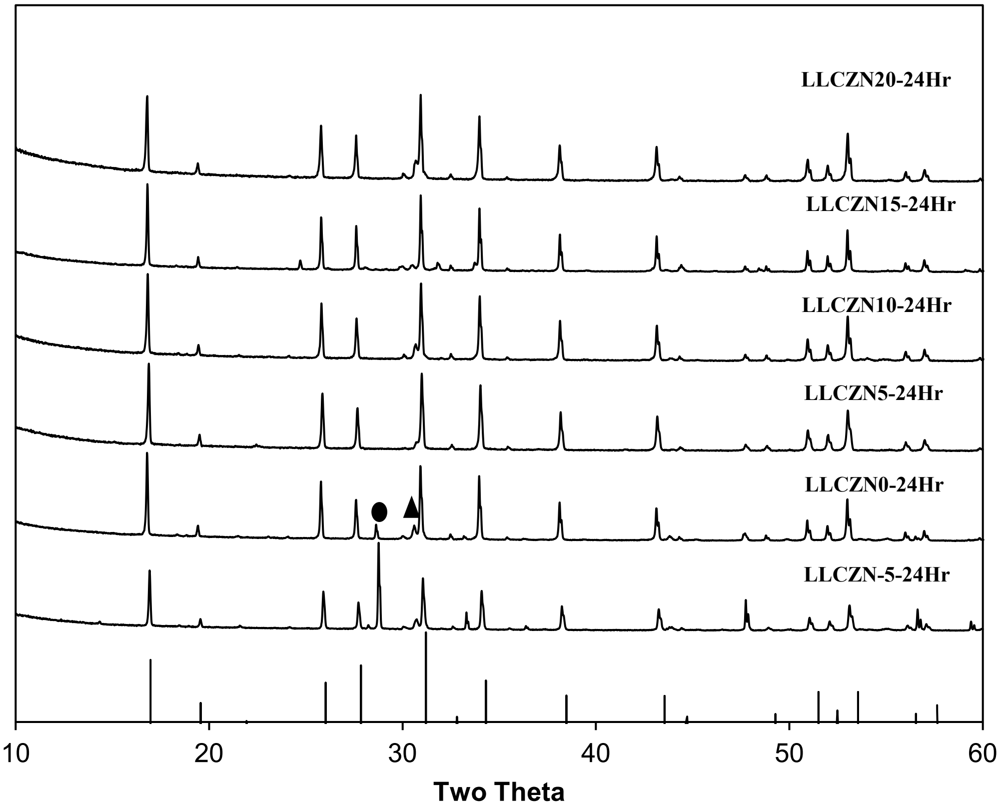

Figure S17. PXRD of LLCZNX-24HR sintered in alumina crucibles. Circles are $La_2Zr_2O_7$ and triangles are $CaZrO_3$.

Lithium Content	**Sintering Time**	**RWP**	**X^2**
-5	12	8.42	4.20
0	12	8.28	4.42
5	12	6.55	2.99
10	12	7.01	3.00
15	12	7.46	4.00
20	12	7.18	2.76
-5	18	9.19	6.70
0	18	7.65	3.87
5	18	6.91	2.46
10	18	6.16	2.55
15	18	9.09	6.86
20	18	7.50	4.44
-5	24	9.51	6.17
0	24	9.98	4.61
5	24	7.93	3.89
10	24	9.18	6.88
15	24	7.25	2.52
20	24	8.43	5.90

Table S7. Fitting results of XRD from LLCZNX-Y

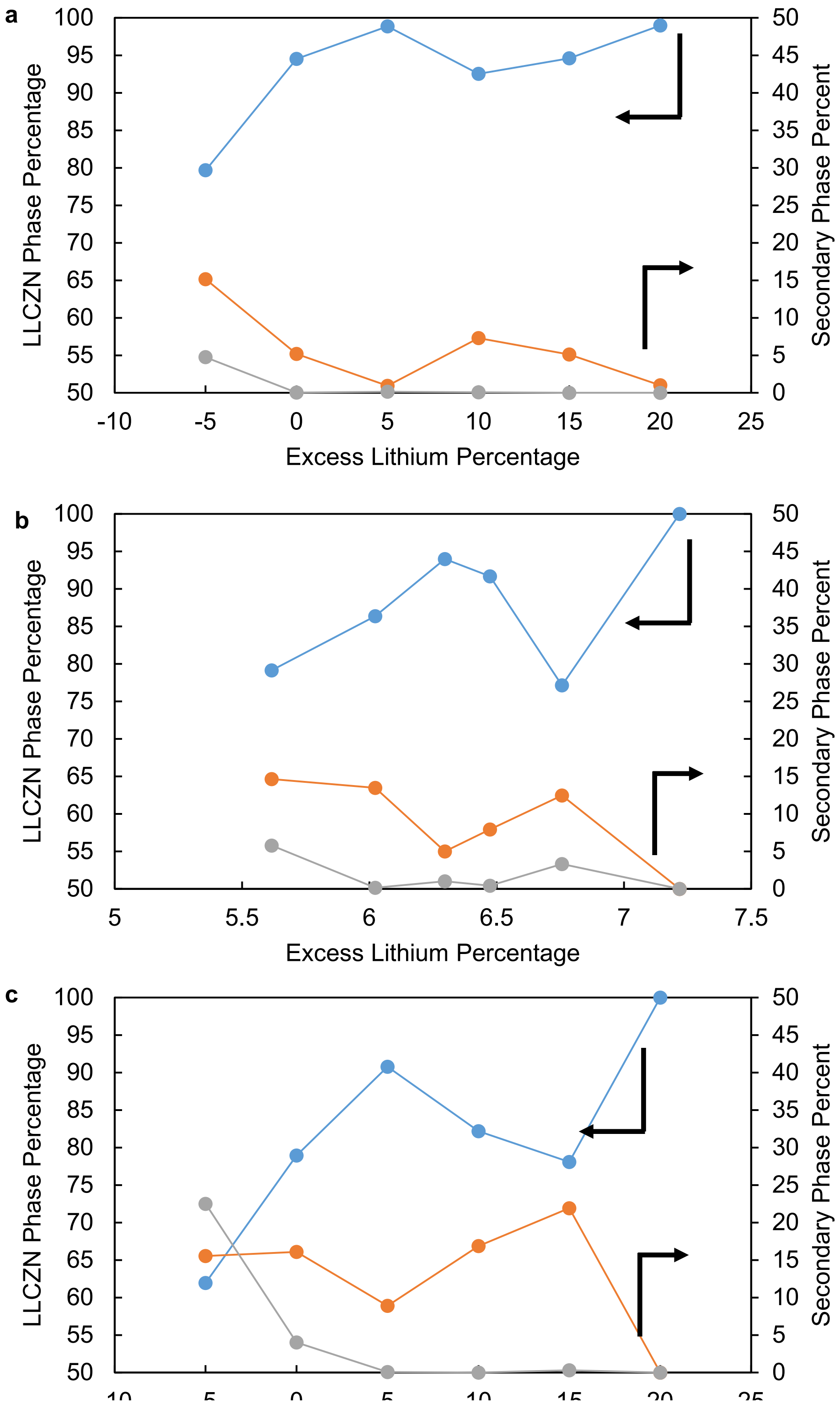

Figure S18. Phase plot vs. lithium content. Blue is LLCZN phase, orange is $CaCO_3$, and gray is $La_2Zr_2O_7$. S18a. LLCZNX-12Hr. S18b. LLCZNX-18Hr S18c. LLCZNX-24Hr

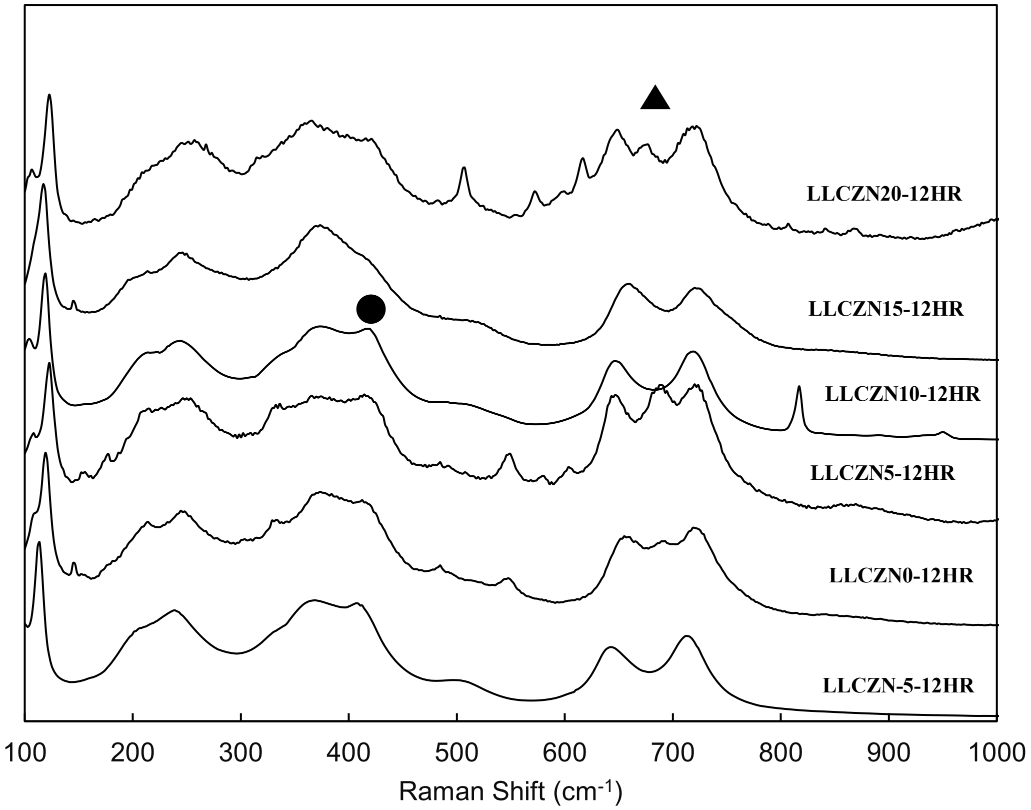

Figure S19. Raman spectra of LLCZNX-12HR sintered in alumina crucibles. Circles are $La_2Zr_2O_7$ and triangles are Al_2O_3.

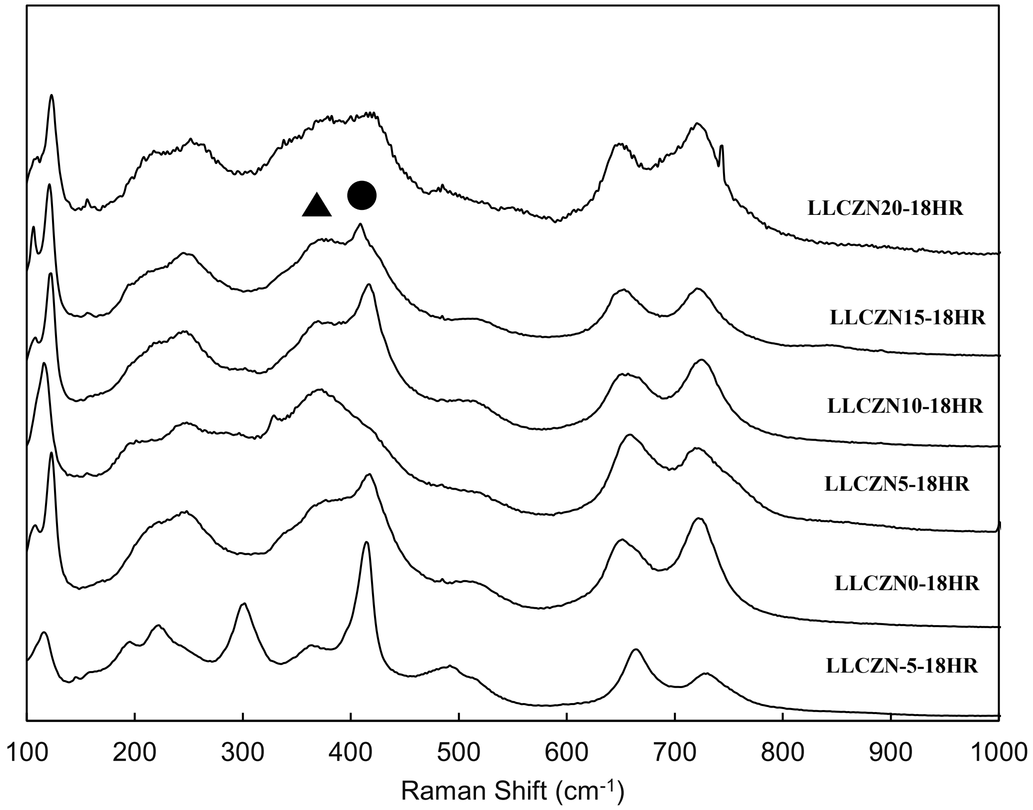

Figure S20. Raman spectra of LLCZNX-18HR sintered in alumina crucibles. Circles are $La_2Zr_2O_7$ and triangles are Al_2O_3.

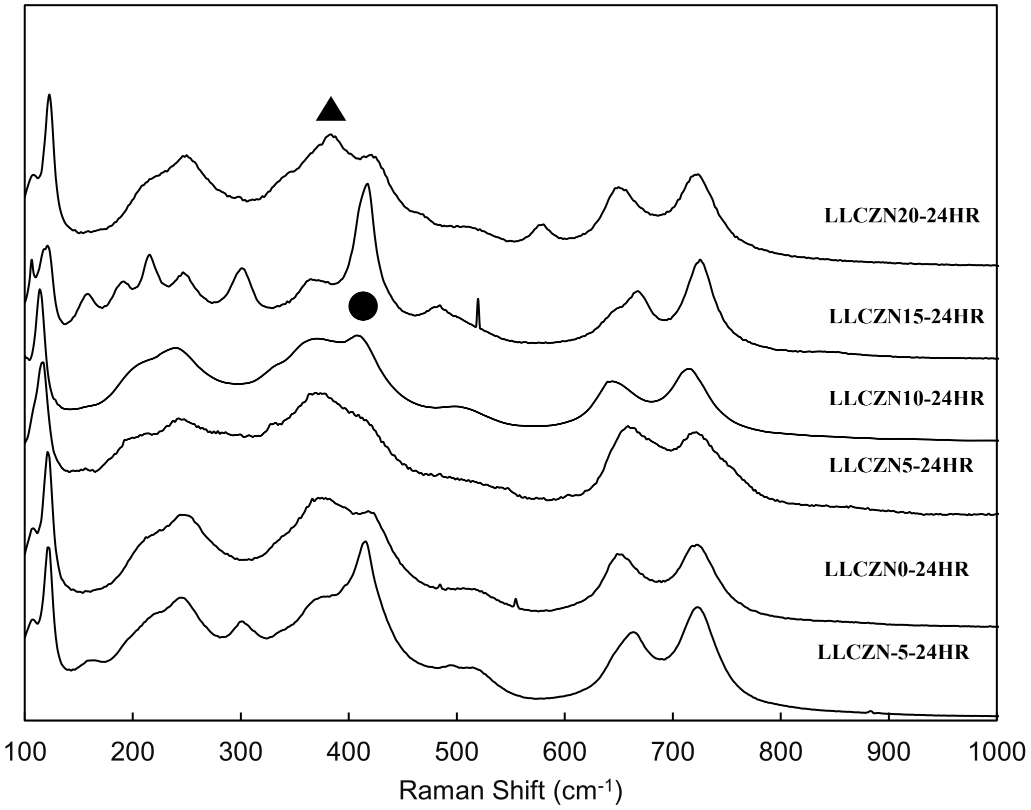

Figure S21. Raman spectra of LLCZNX-24HR sintered in alumina crucibles. Circles are $La_2Zr_2O_7$ and triangles are Al_2O_3.

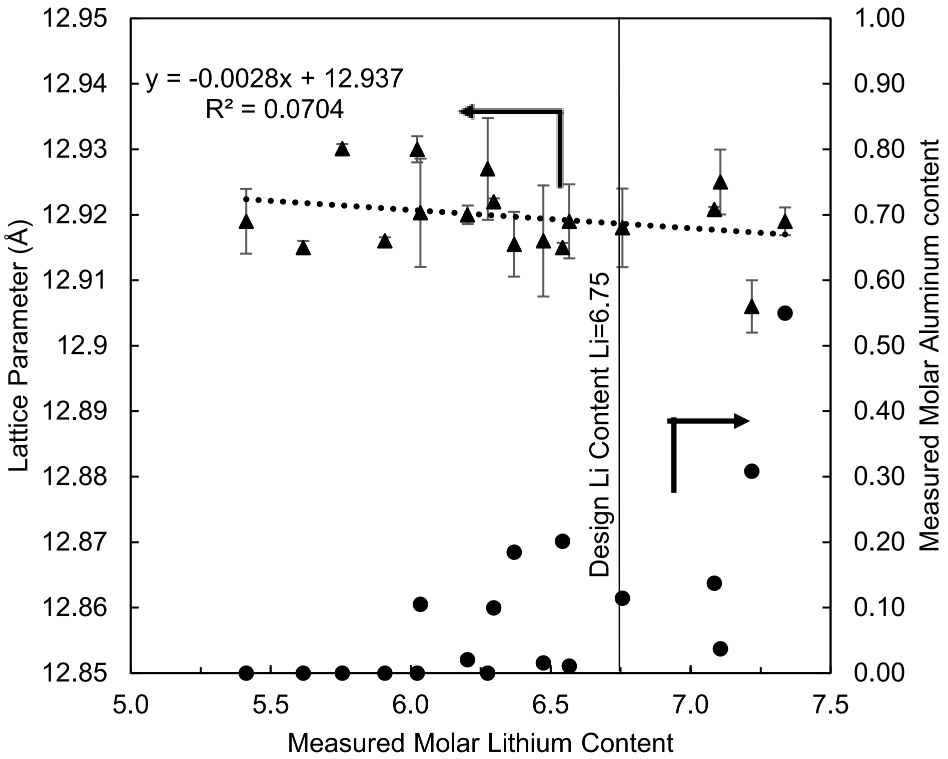

Figure S22. Measured aluminum content and lattice parameter versus measured lithium content. Triangles are lattice parameters and circles aluminum content.

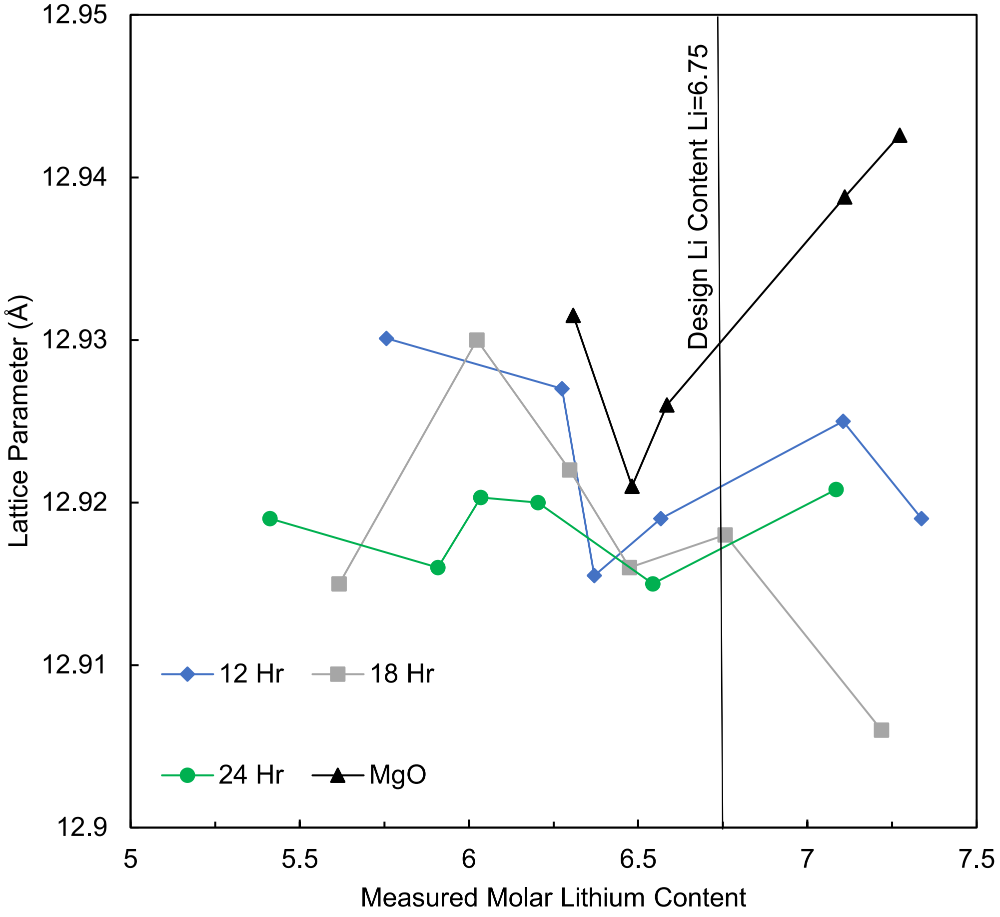

Figure S23. Lattice parameter vs. measured molar lithium content. Diamonds are LLCZNX-12Hr. Squares are LLCZNX-18Hr. Circles are LLCZNX-24Hr. Triangles are LLCZNX-MgO.

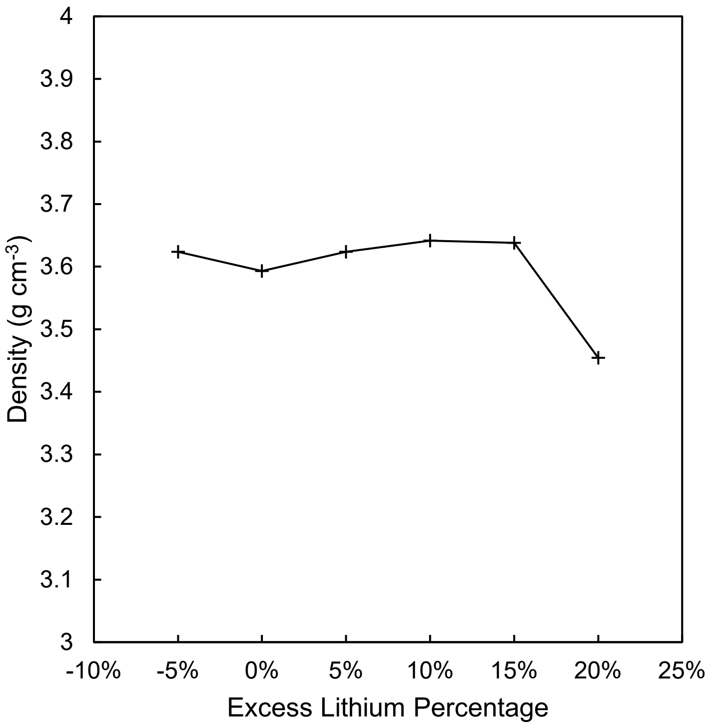

Figure S24. Density vs excess lithium of the green pellets before sintering

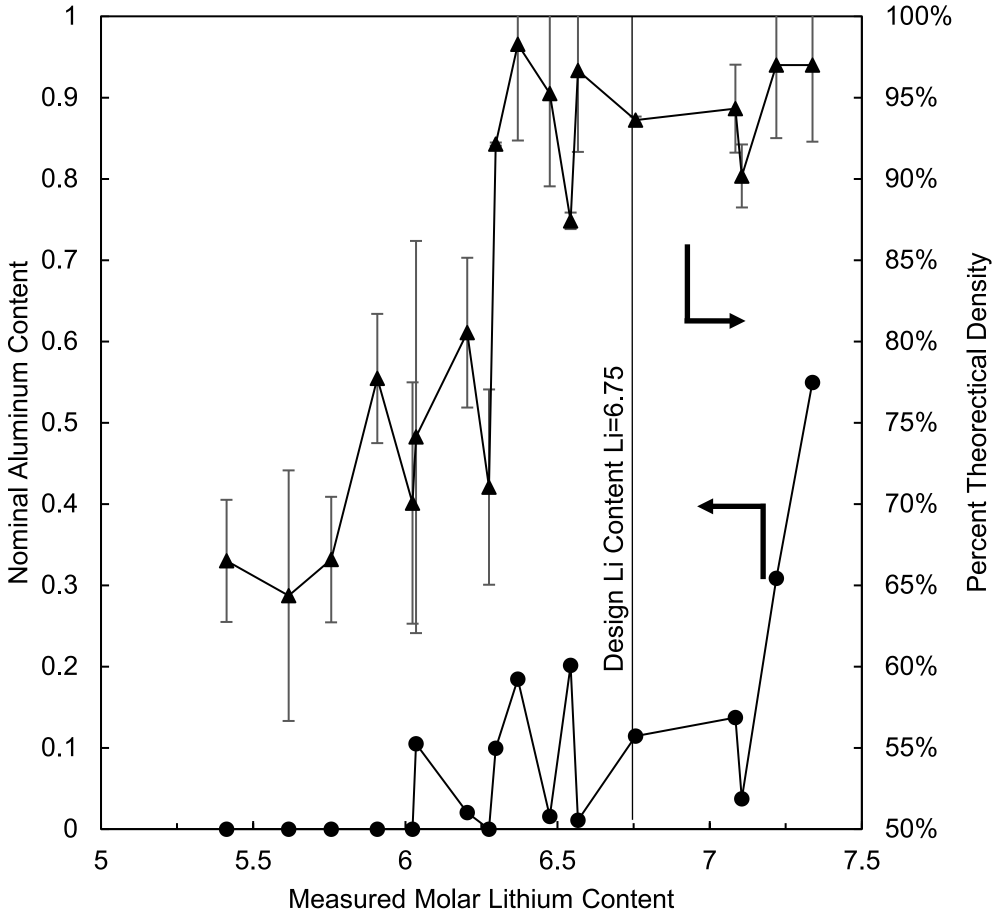

Figure S25. Measured aluminum content and density percentage versus measured lithium content. Triangles are density and circles aluminum content.

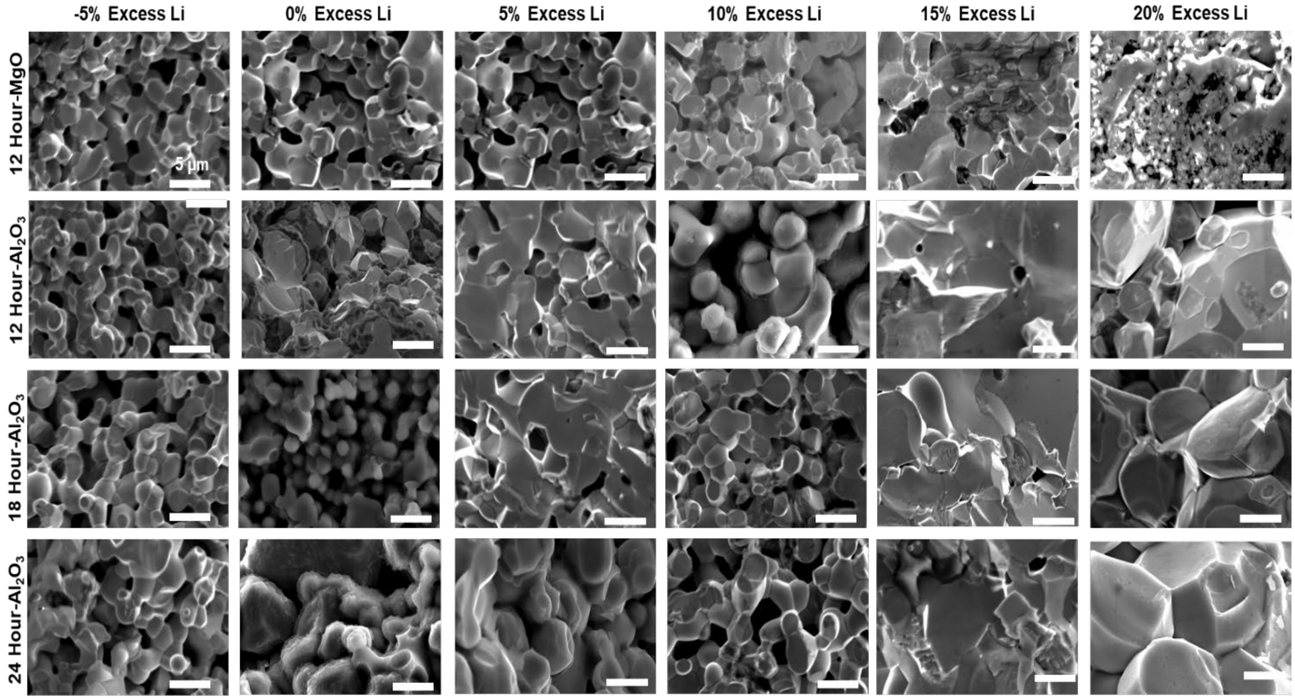

Figure S26. SEM images for all the sintered LLCZN samples

The SEM images of samples sintered in Al_2O_3 crucibles show interconnected grains and denser microstructures as lithium increases. LLCZN-5 and LLCZN0 did not achieve dense microstructures, displaying grain necking but not pore elimination, hindered by secondary phases slowing densification. LLCZN5 exhibits larger interconnected particles with some pores owning to the high aluminum content causing coarsening without pore elimination. While LLCZN10 contains smaller, visible grains with pores; indicating 10% excess lithium is insufficient to create a dense microstructure with these conditions. LLCZN15 shows consistent structures with minimal grain boundaries and limited visible pores which will limit dendrite growth[328]. LLCZN20 has visible grains but abnormal grain growth when Y=12 and 18 but at Y=24 the slower pore elimination processes begins with the larger grains[329]. At our sintering conditions in Al_2O_3 crucibles, at least 15% excess lithium is required to consistently create dense microstructures.

The inverse displays growing concentration of calcium at grain boundaries with decreasing lithium content and increasing sintering time. This implies there is a small nominal lithium range (between 6.3 and 7.34 mol of Li) where calcium will be dispersed and Al will assist in achieving high density without coarsening or secondary phase formation. However outside of that range, the secondary phases are likely to be concentrated at the grain boundaries and hinder densification processes. Any deviations to the sintering conditions would require similar analysis to ensure LLZO is sintered consistently.

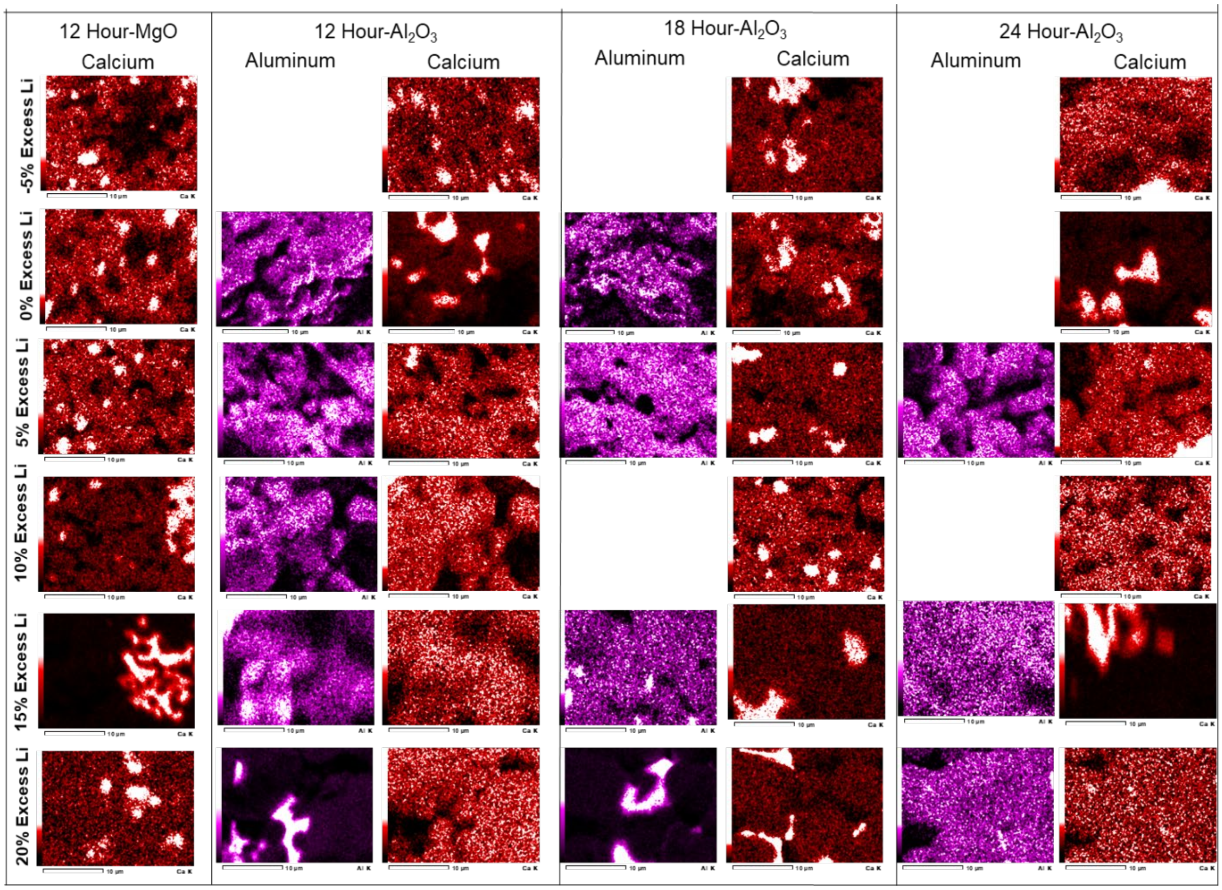

Figure S27. Calcium and aluminum EDS signals of all sintered LLCZN samples

a

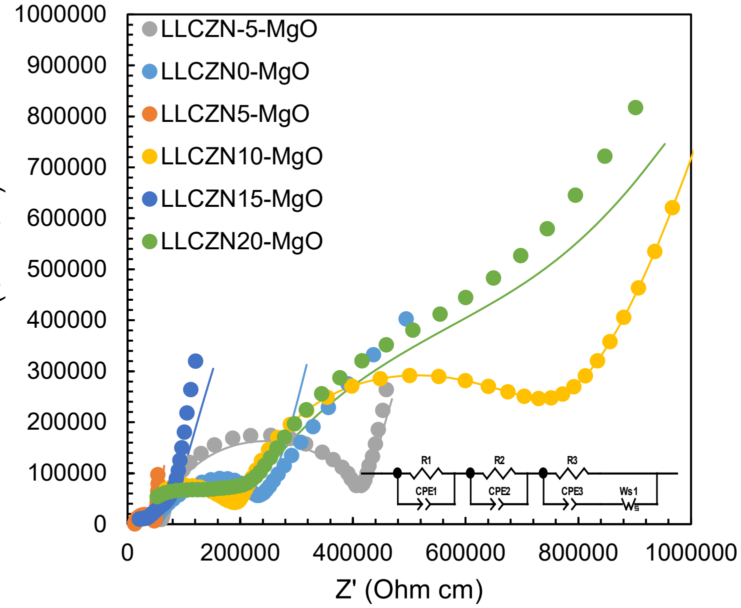
LLCZN-5-MgO
LLCZN0-MgO
LLCZN5-MgO
LLCZN10-MgO
LLCZN15-MgO
LLCZN20-MgO
-Z " (Ohm cm)
Z' (Ohm cm)
0
100000
200000
300000
400000
500000
600000
700000
800000
900000
1000000
0
200000
400000
600000
800000
1000000
R1
CPE1
R2
CPE2
R3
CPE3
Ws1

b

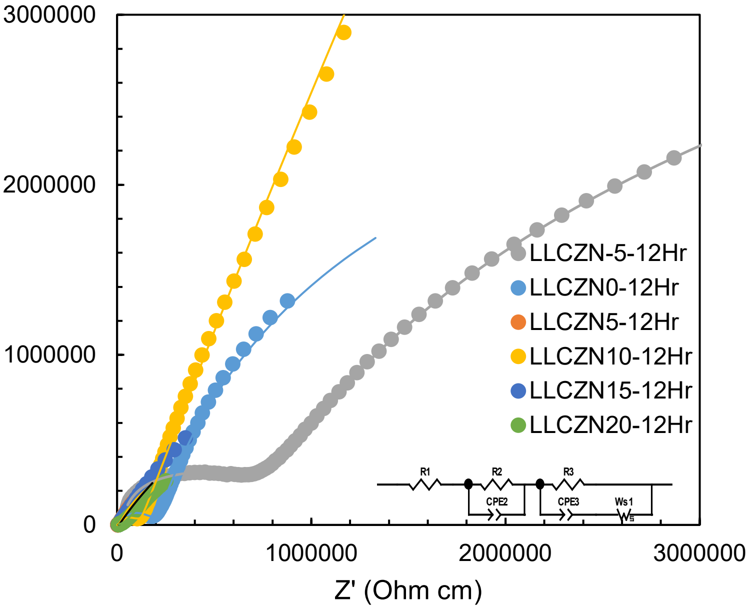
LLCZN-5-12Hr
LLCZN0-12Hr
LLCZN5-12Hr
LLCZN10-12Hr
LLCZN15-12Hr
LLCZN20-12Hr
-Z " (Ohm cm)
Z' (Ohm cm)
0
1000000
2000000
3000000
0
1000000
2000000
3000000
R1
R2
CPE2
R3
CPE3
Ws1

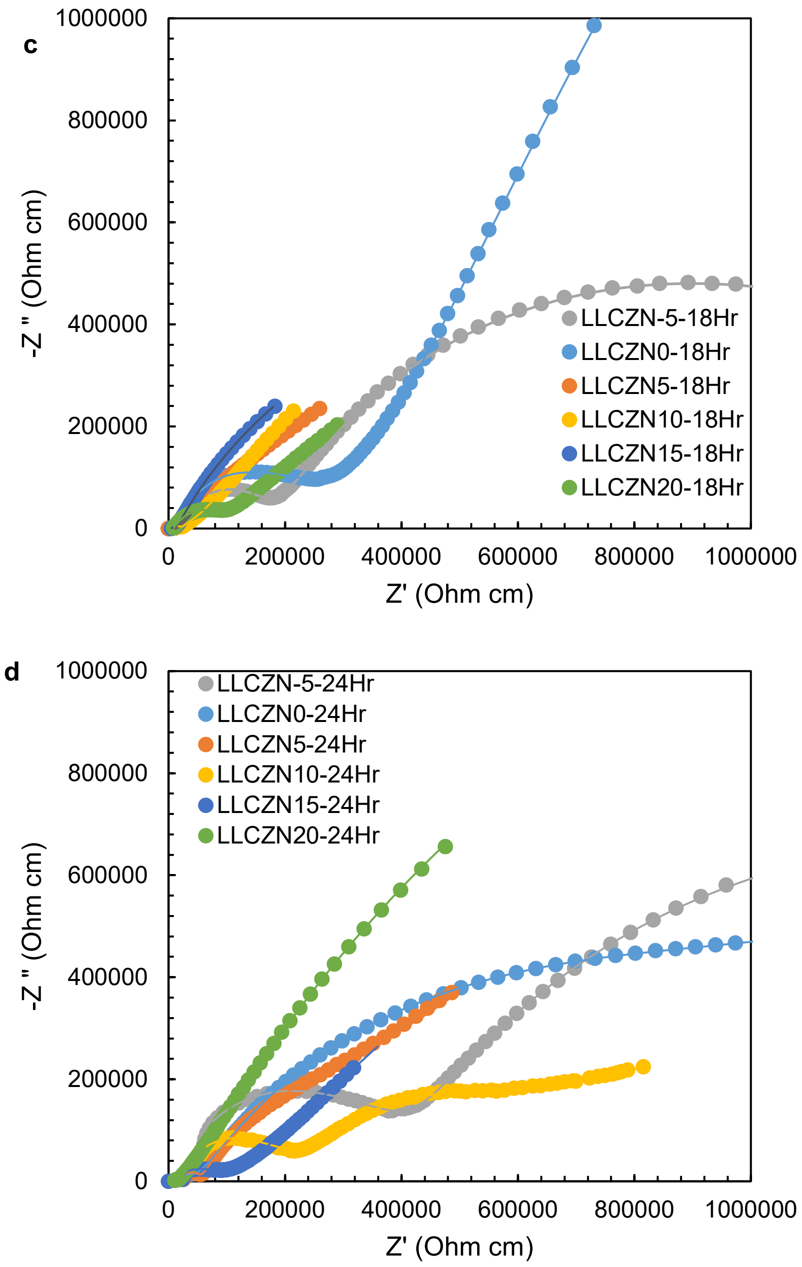

Figure S28. Example of EIS data obtained In LLCZNX-MgO with the model used to fit the data as an inset. **S28b.** Example of EIS data obtained In LLCZNX-12Hr with the model used to fit the data as an inset. **S28c.** Example of EIS data obtained In LLCZNX-18Hr. **S28d.** Example of EIS data obtained In LLCZNX-24Hr. Lines are the model fits and dots are the actual data.

Sample	R_{bulk} (Ohms)	CPE_{Bulk}	N_{bulk}	C_{bulk} (F)	R_{GB} (Ohms)	CPE_{GB}	N_{GB}	C_{GB} (F)	X^2
LLCZN-5-MgO	5265	1.1E-10	8.8E-01	1.6E-11	42825	5.49E-09	9.38E-01	3.16E-09	2.26E-05
LLCZN0-MgO	3324	1.1E-10	9.1E-01	2.6E-11	22742	8.21E-09	9.10E-01	3.51E-09	2.23E-05
LLCZN5-MgO	2691	N/A	N/A	N/A	6794	6.27E-09	9.66E-01	4.40E-09	2.13E-04
LLCZN10-MgO	19000	3.8E-10	7.7E-01	1.0E-11	73920	1.10E-08	8.56E-01	3.33E-09	2.44E-04
LLCZN15-MgO	981	9.2E-10	1.0E+00	9.1E-10	4161	2.92E-09	8.00E-01	1.72E-10	1.22E-04
LLCZN20-MgO	9269	4.0E-11	9.6E-01	2.2E-11	106000	2.16E-08	7.35E-01	2.41E-09	1.57E-04

Table S8. Fitting results of EIS data for samples sintered in MgO crucibles

Sample	**R_{bulk} (Ohms)**	**CPE_{Bulk}**	**N_{bulk}**	**C_{Bulk} (F)**	**R_{GB} (Ohms)**	**CPE_{GB}**	**N_{GB}**	**C_{GB} (F)**	**X^2**
LLCZN-5-12Hr	60829	6.41E-12	9.62E-01	3.57E-12	78554	2.7E-11	1.0E+00	2.6E-11	4.60E-04
LLCZN0-12Hr	11935	1.3E-11	1.1E+00	3.6E-11	10964	2.09E-09	8.28E-01	2.26E-10	2.43E-05
LLCZN5-12Hr	759.6	N/A	N/A	N/A	142	7.65E-08	8.88E-01	1.82E-08	1.65E-05
LLCZN10-12Hr	2836	N/A	N/A	N/A	7381	1.62E-11	1.10E+00	6.64E-11	1.56E-04
LLCZN15-12Hr	1181	N/A	N/A	N/A	289.2	7.29E-11	1.21E+00	1.51E-09	2.00E-04
LLCZN20-12Hr	1237	N/A	N/A	N/A	1669	5.22E-08	7.44E-01	2.09E-09	1.43E-04
LLCZN-5-18Hr	15235	5.6E-11	9.6E-01	2.9E-11	107160	1.15E-08	8.39E-01	3.19E-09	2.26E-04
LLCZN0-18Hr	25873	8.3E-11	9.2E-01	2.7E-11	23713	3.79E-10	1.07E+00	8.35E-10	3.24E-05
LLCZN5-18Hr	972.7	4.4E-10	8.2E-01	1.9E-11	260.7	4.34E-07	7.65E-01	2.66E-08	1.79E-06
LLCZN10-18Hr	1803	N/A	N/A	N/A	687.8	1.27E-10	1.08E+00	4.41E-10	2.58E-06
LLCZN15-18Hr	898.1	N/A	N/A	N/A	859.5	3.19E-08	8.05E-01	2.50E-09	6.64E-05
LLCZN20-18Hr	1000	N/A	N/A	N/A	8994	2.31E-08	7.90E-01	2.43E-09	1.04E-04
LLCZN-5-24Hr	42003	3.2E-10	7.7E-01	1.1E-11	184970	1.18E-08	7.78E-01	2.05E-09	2.00E-05
LLCZN0-24Hr	2681	1.8E-13	1.3E+00	1.5E-11	68000	4.40E-10	1.19E+00	2.37E-09	3.42E-05
LLCZN5-24Hr	3835	6.3E-11	1.0E+00	8.6E-11	28620	5.83E-08	8.17E-01	1.39E-08	8.78E-05
LLCZN10-24Hr	15807	4.6E-11	9.9E-01	3.8E-11	11573	9.17E-09	1.03E+00	1.18E-08	3.34E-04
LLCZN15-24Hr	2371	N/A	N/A	N/A	1608	3.23E-12	1.28E+00	2.10E-10	6.57E-05
LLCZN20-24Hr	1409	N/A	N/A	N/A	300	2.09E-09	1.00E+00	2.09E-09	2.47E-05

Table S9. Fitting results of EIS data for samples sintered Al_2O_3 crucibles

Sample	RINT (Ohms)	CPEINT	NINT	CINT (F)
LLCZN-5-MgO	822840	1.77E-08	0.68	2.32E-09
LLCZN0-MgO	75300	1.39E-08	0.84	3.91E-09
LLCZN5-MgO	7007500	8.41E-07	0.78	1.39E-06
LLCZN10-MgO	23909000	1.72E-08	0.96	1.67E-08
LLCZN15-MgO	609890	4.89E-07	0.71	2.96E-07
LLCZN20-MgO	715490	1.54E-06	0.60	1.65E-06
LLCZN-5-12Hr	235160	6.40E-07	0.52	1.11E-07
LLCZN0-12Hr	1596000	1.09E-08	0.83	4.59E-09
LLCZN5-12Hr	133390	2.49E-06	0.63	1.31E-06
LLCZN10-12Hr	1.08E+05	1.34E-06	0.85	9.53E-07
LLCZN15-12Hr	3453	1.14E-06	1.05	1.45E-06
LLCZN20-12Hr	316100	2.88E-06	0.76	2.80E-06
LLCZN-5-18Hr	36717	6.25E-09	1.14	1.76E-08
LLCZN0-18Hr	7000000	1.10E-07	0.83	1.05E-07
LLCZN5-18Hr	1620000	4.27E-07	0.58	3.26E-07
LLCZN10-18Hr	248700	1.32E-06	0.35	1.73E-07
LLCZN15-18Hr	5863	2.02E-09	0.83	2.02E-10
LLCZN20-18Hr	524740	3.90E-07	0.79	2.53E-07
LLCZN-5-24Hr	822840	1.77E-08	0.68	2.32E-09
LLCZN0-24Hr	75300	1.39E-08	0.84	3.91E-09
LLCZN5-24Hr	7007500	8.41E-07	0.78	1.39E-06
LLCZN10-24Hr	23909000	1.72E-08	0.96	1.67E-08
LLCZN15-24Hr	609890	4.89E-07	0.71	2.96E-07
LLCZN20-24Hr	715490	1.54E-06	0.60	1.65E-06

Table S10. Continued fitting result for the interfaces of the EIS data

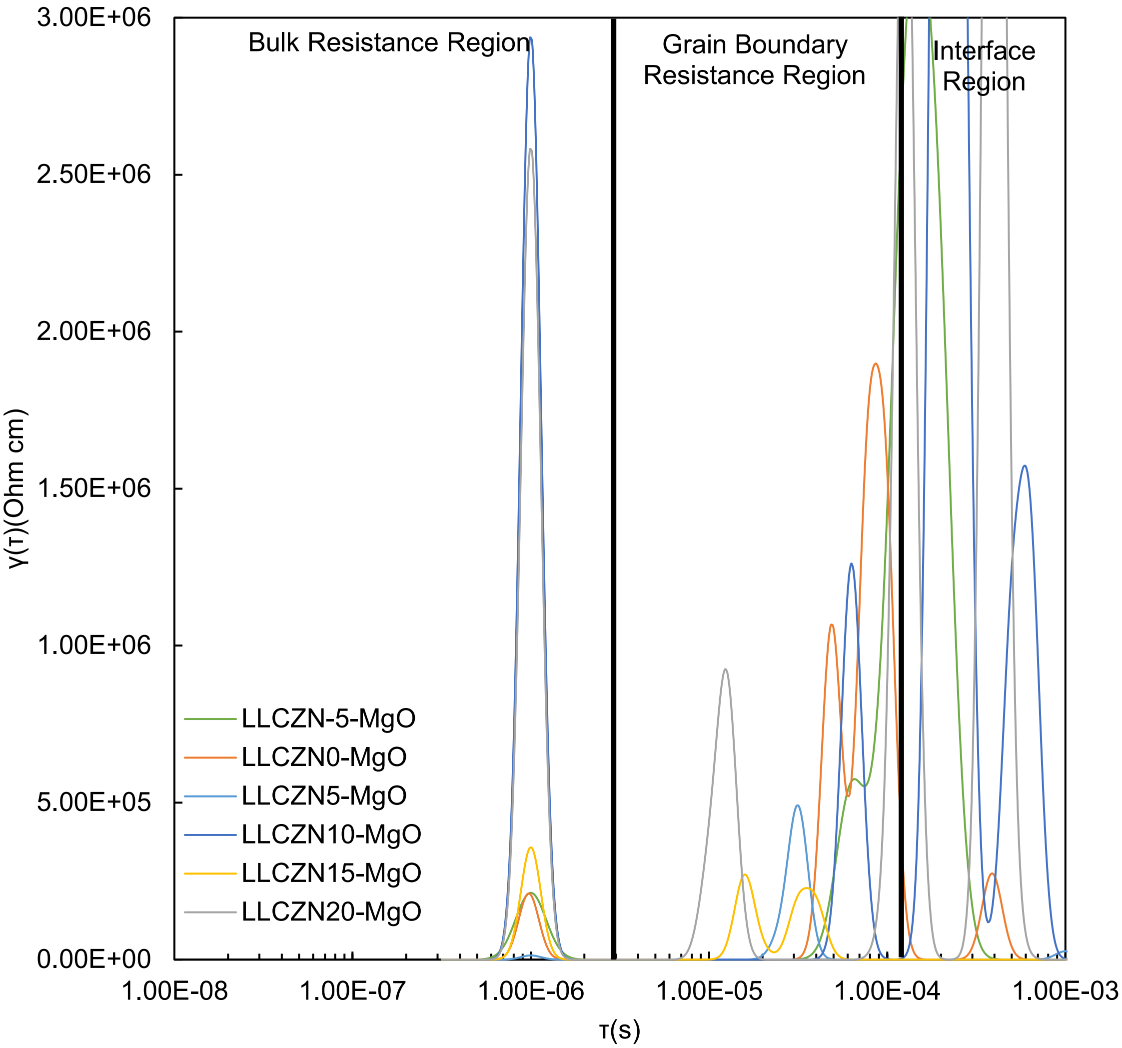

Figure S29. DRT of EIS results of samples sintered in MgO crucibles

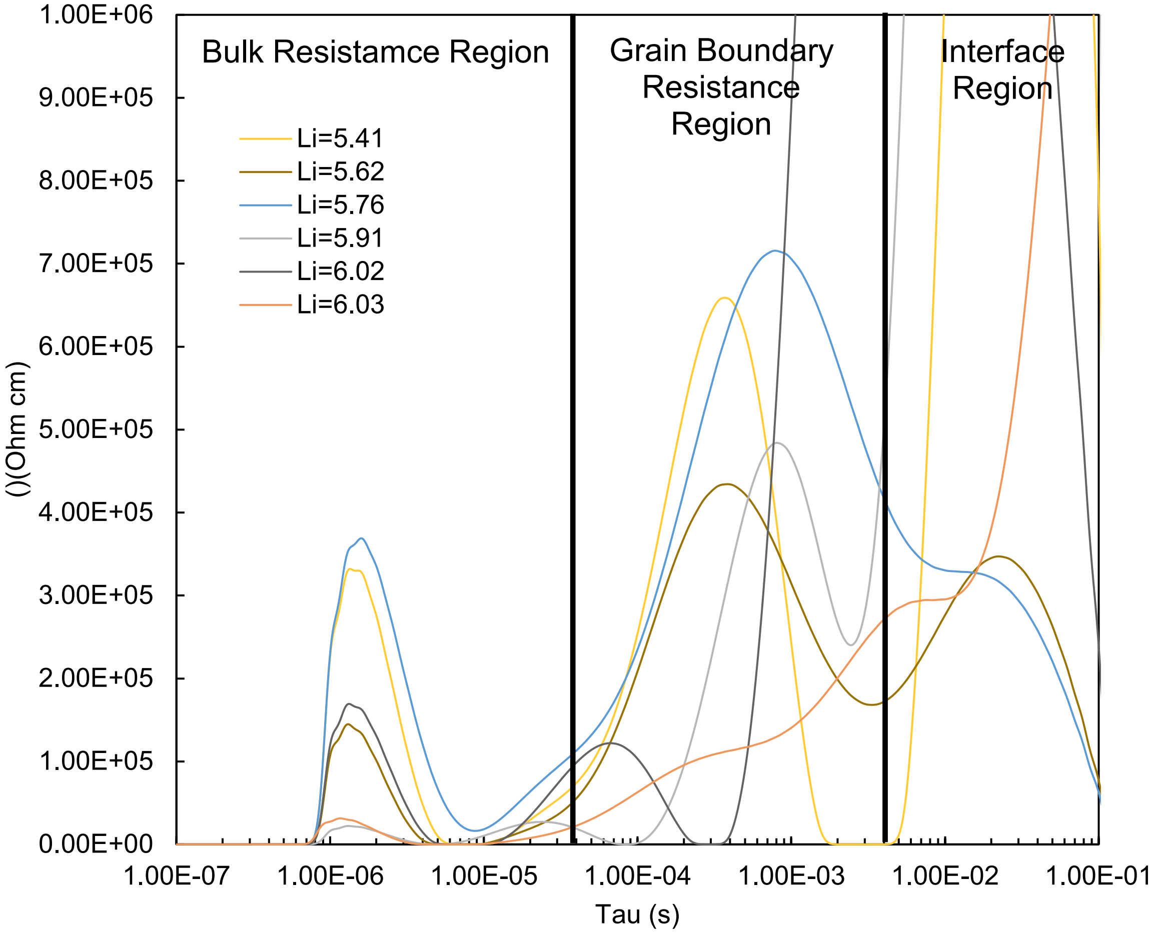

Figure S30. DRT of EIS results of lowest six lithium content samples sintered in Al_2O_3 crucibles

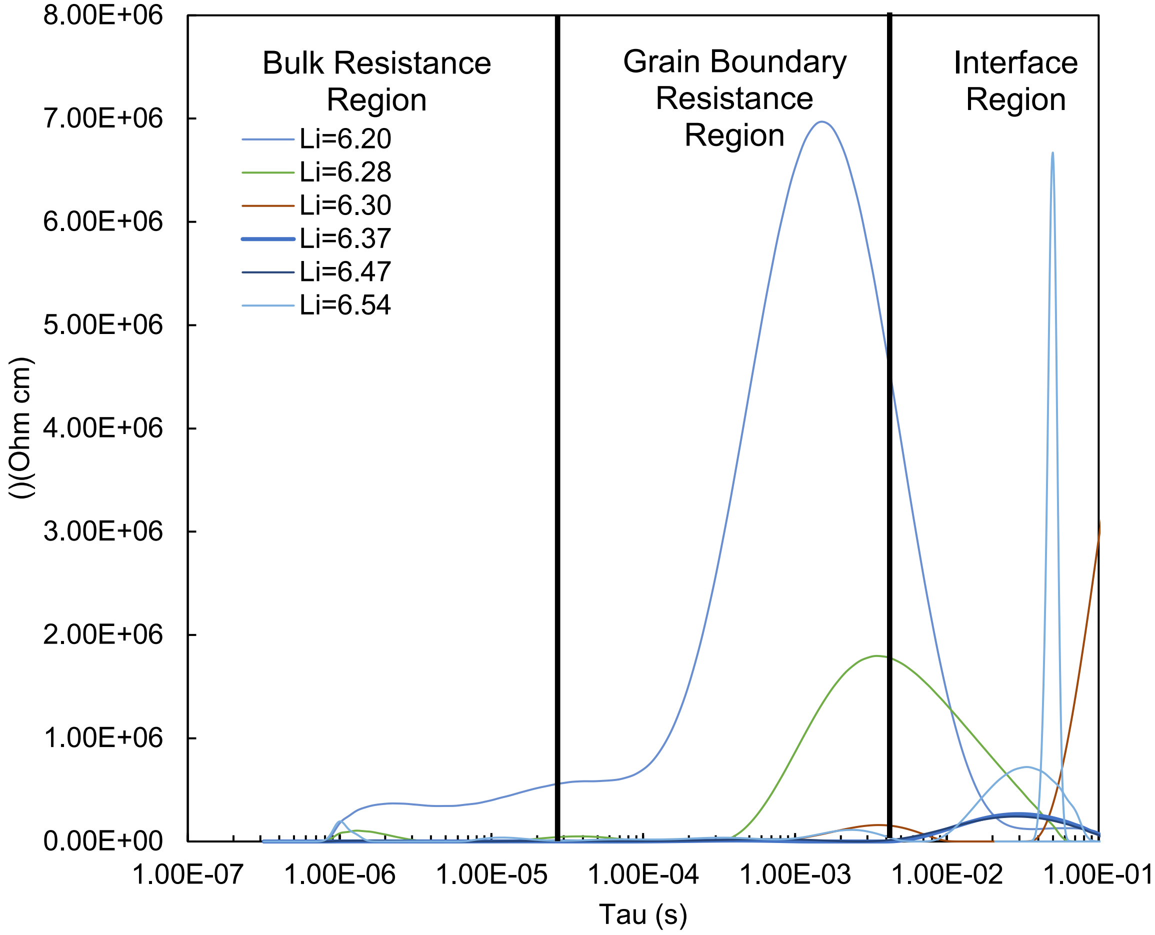

Figure S31. DRT of EIS results of middle six lithium content samples sintered in Al_2O_3 crucibles

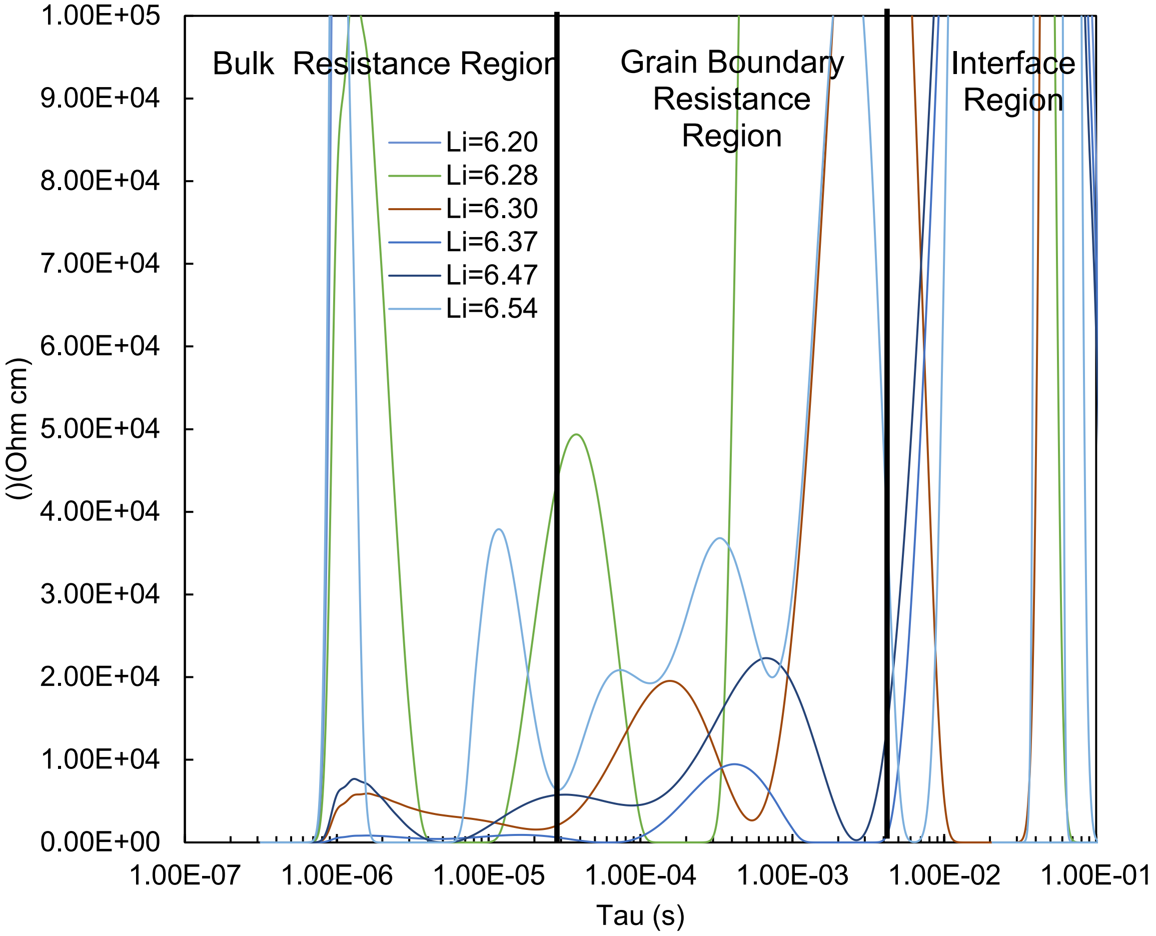

Figure S32. DRT of EIS results of middle six lithium content samples sintered in Al_2O_3 crucibles. Magnified to visualize high conductivity samples.

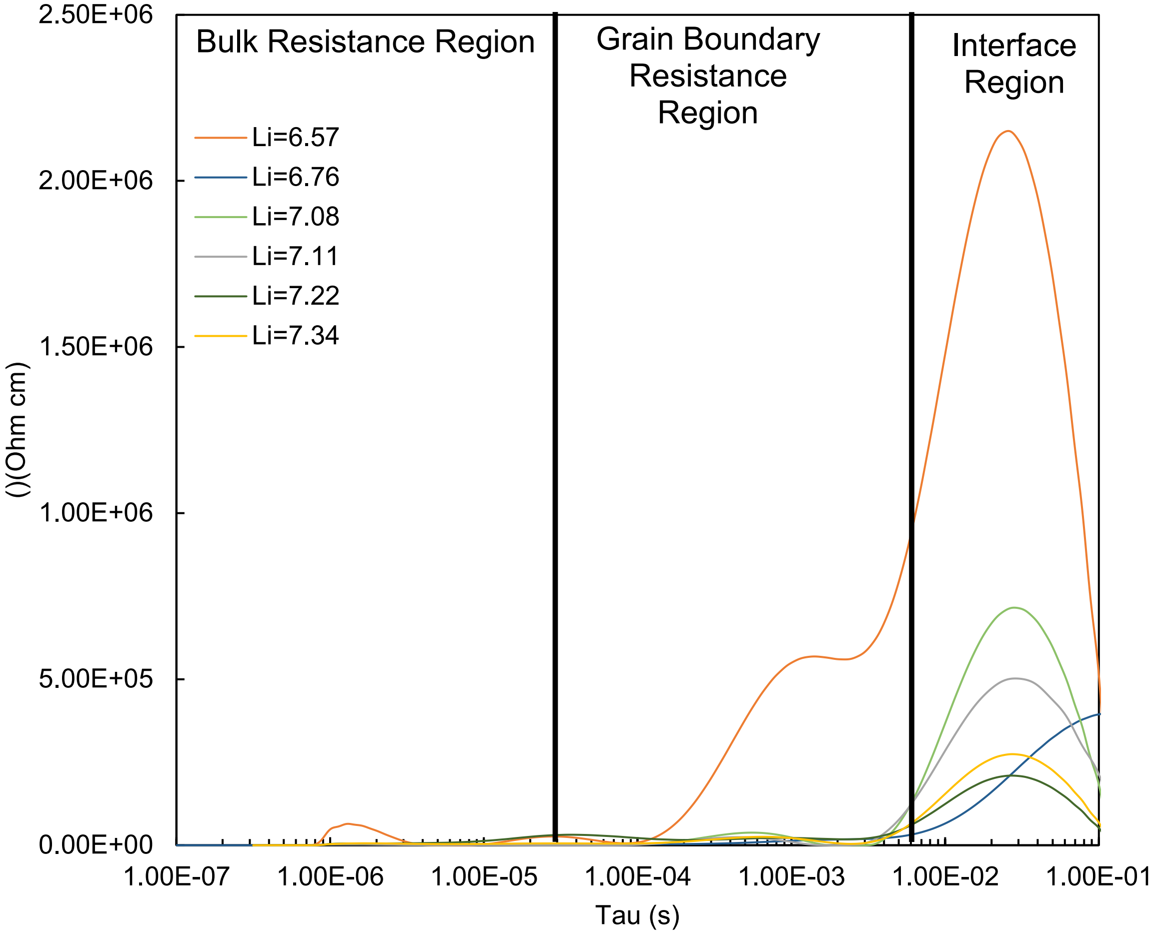

Figure S33. DRT of EIS results of highest six lithium content samples sintered in Al_2O_3 crucibles.

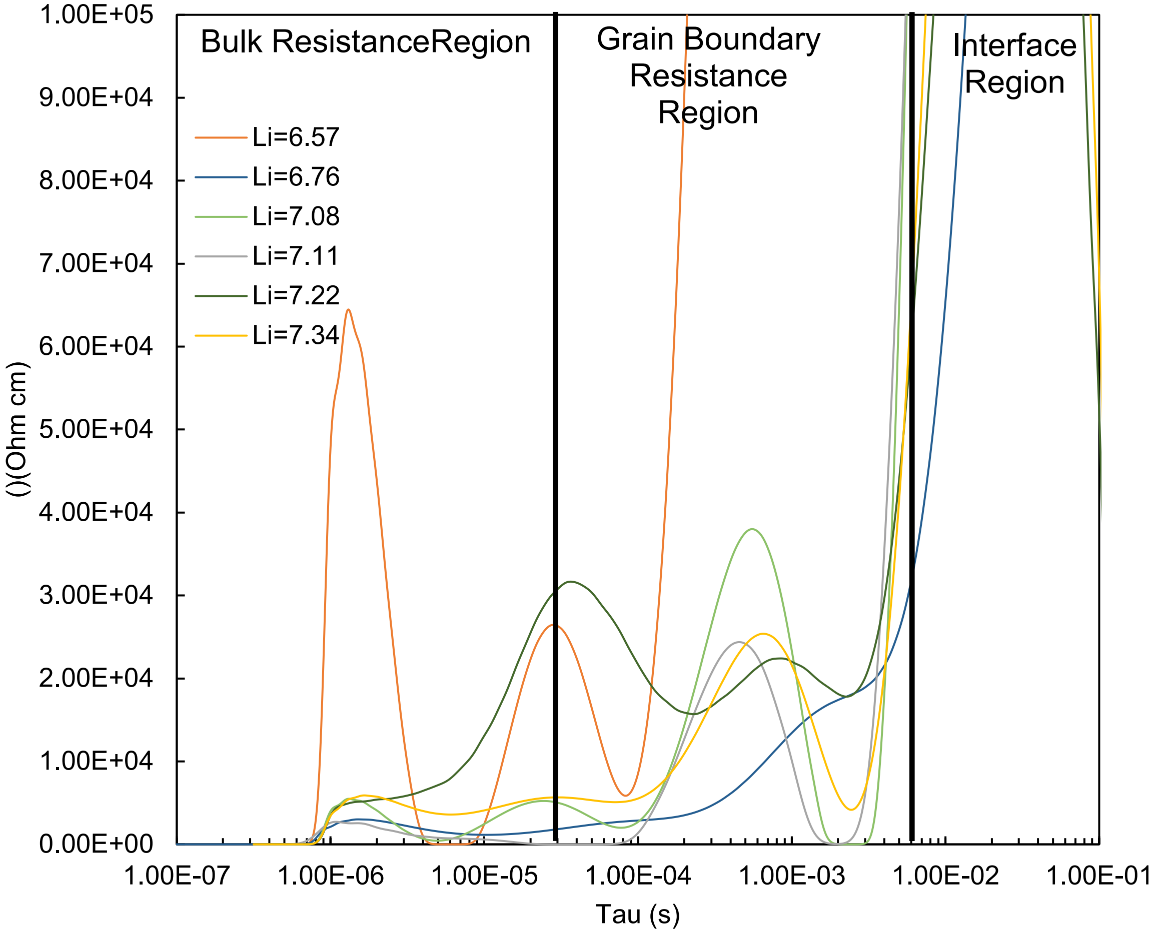

Figure S34. DRT of EIS results of highest six lithium content samples sintered in Al_2O_3 crucibles. Magnified to visualize high conductivity samples.

‘

Sample	**Relaxation Frequency 1 (Hz)**	**Relaxation Frequency 2 (Hz)**	**Relaxation Frequency 3 (Hz)**
LLCZN-5-MgO	1.9E+06	1.18E+03	1.02E-07
LLCZN0-MgO	1.8E+06	2.00E+03	1.69E-08
LLCZN5-MgO	N/A	5.33E+03	2.30E+02
LLCZN10-MgO	8.3E+05	6.47E+02	1.56E-02
LLCZN15-MgO	1.8E+05	2.17E+06	7.97E-01
LLCZN20-MgO	7.7E+05	6.22E+02	2.60E-08

Table S11. Relaxation frequencies of EIS of samples sintered in MgO crucibles

Sample	Relaxation Frequency 1 (Hz)	Relaxation Frequency 2 (Hz)	Relaxation Frequency 3 (Hz)
LLCZN-5-12Hr	7.3E+05	7.79E+04	8.34E+01
LLCZN0-12Hr	3.7E+05	6.43E+04	5.41E+02
LLCZN5-12Hr	N/A	6.16E+04	1.64E-02
LLCZN10-12Hr	N/A	3.25E+05	3.99E-01
LLCZN15-12Hr	N/A	3.64E+05	8.81E-01
LLCZN20-12Hr	N/A	4.56E+04	1.35E-01
LLCZN-5-18Hr	3.6E+05	4.66E+02	6.07E+00
LLCZN0-18Hr	2.3E+05	8.04E+03	2.17E+01
LLCZN5-18Hr	8.8E+06	2.29E+04	9.13E-01
LLCZN10-18Hr	N/A	5.25E+05	7.10E+03
LLCZN15-18Hr	N/A	7.39E+04	3.19E+01
LLCZN20-18Hr	N/A	7.29E+03	1.80E-01
LLCZN-5-24Hr	3.4E+05	4.20E+02	2.46E+02
LLCZN0-24Hr	4.0E+06	9.86E+02	2.17E-01
LLCZN5-24Hr	4.8E+05	4.00E+02	3.01E-01
LLCZN10-24Hr	2.7E+05	1.17E+03	3.70E+00
LLCZN15-24Hr	N/A	4.72E+05	1.34E+05
LLCZN20-24Hr	N/A	2.54E+05	1.20E+00

Table S12. Relaxation frequencies of EIS of samples sintered in Al_2O_3 crucibles

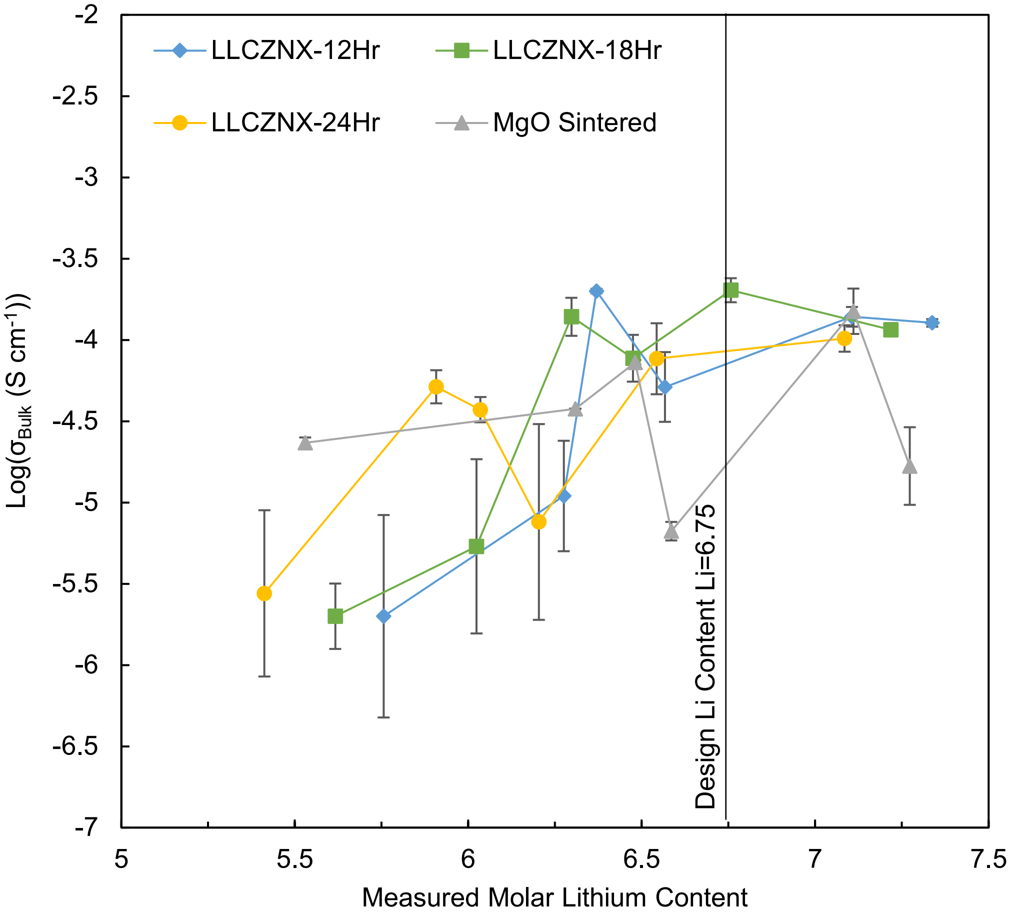

Figure S35. Log bulk conductivity versus lithium content at the four sintering conditions. Diamonds are LLCZNX-12Hr, squares at LLCZNX-18Hr, circles are LLCZNX-24Hr, and triangles are LLCZNX-MgO.

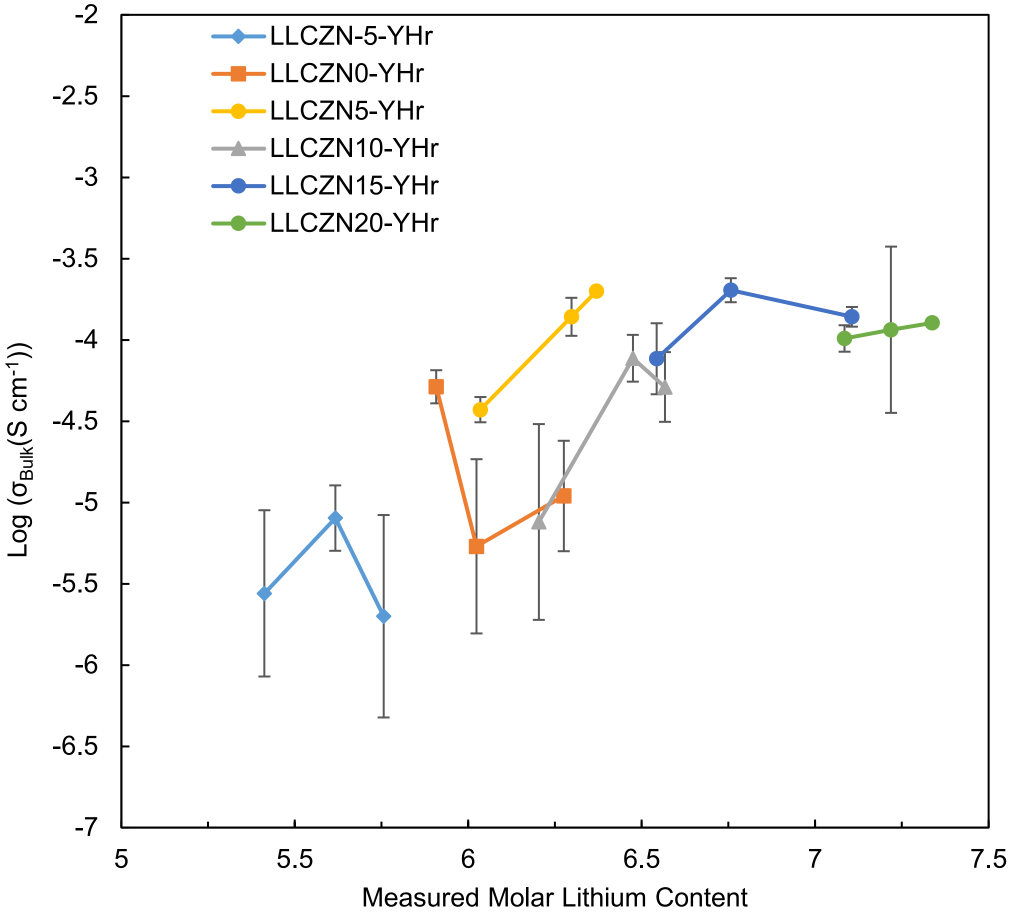

Figure S36. Log bulk conductivity vs the measure molar lithium content of LLCZNX-YHr

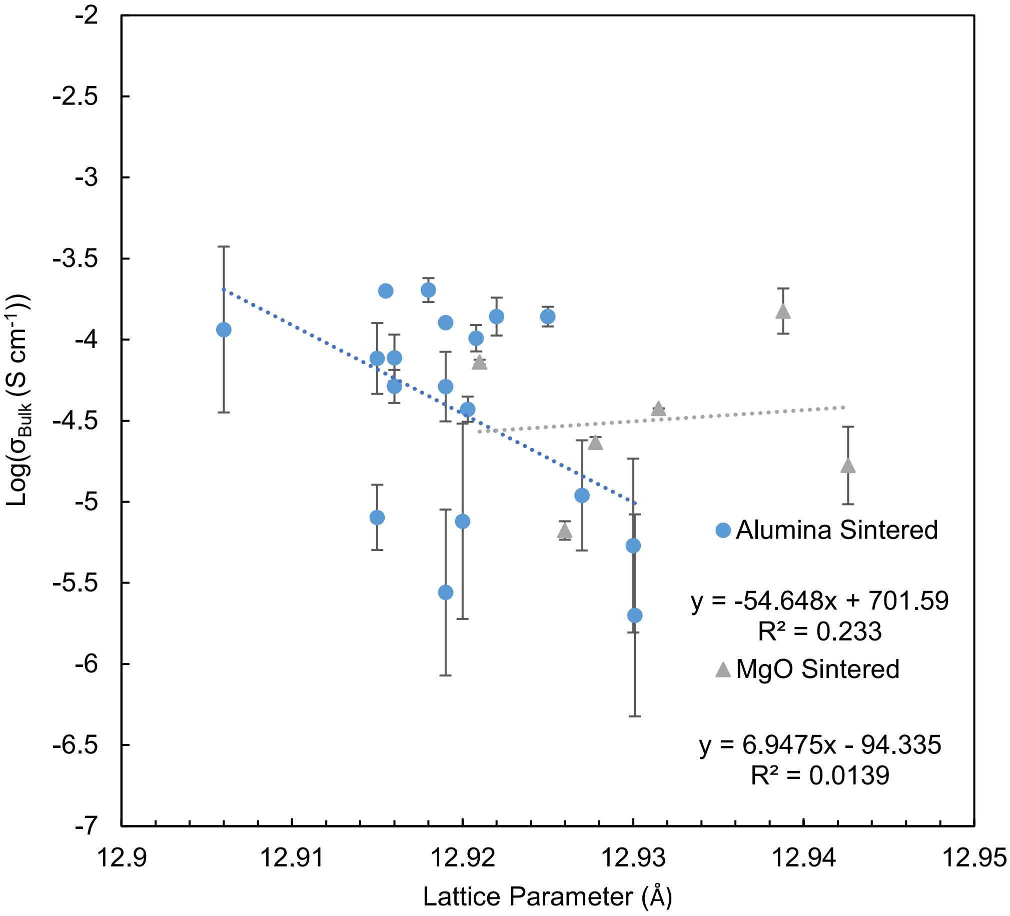

Figure S37. Bulk conductivity vs. lattice parameter for Al_2O_3 and MgO sintered samples

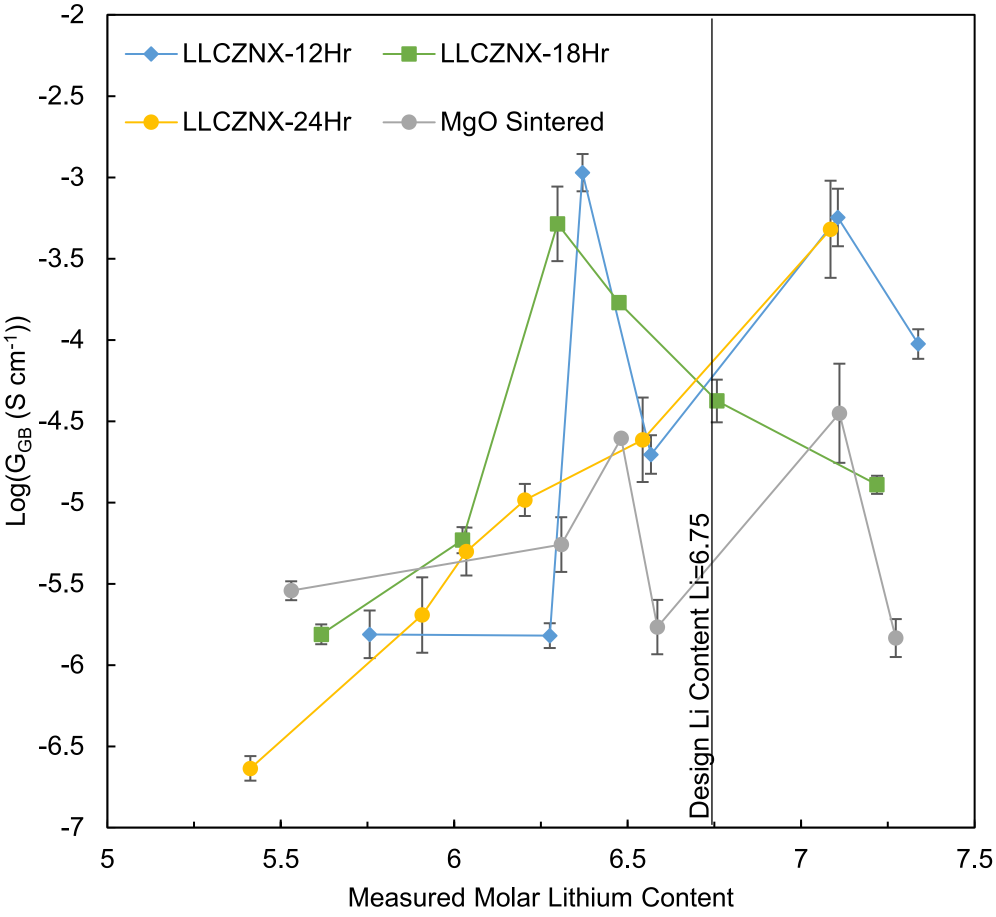

Figure S38. Log grain boundary conductance versus lithium content at the four sintering conditions. Diamonds are LLCZNX-12Hr, squares at LLCZNX-18Hr, circles are LLCZNX-24Hr, and triangles are LLCZNX-MgO.

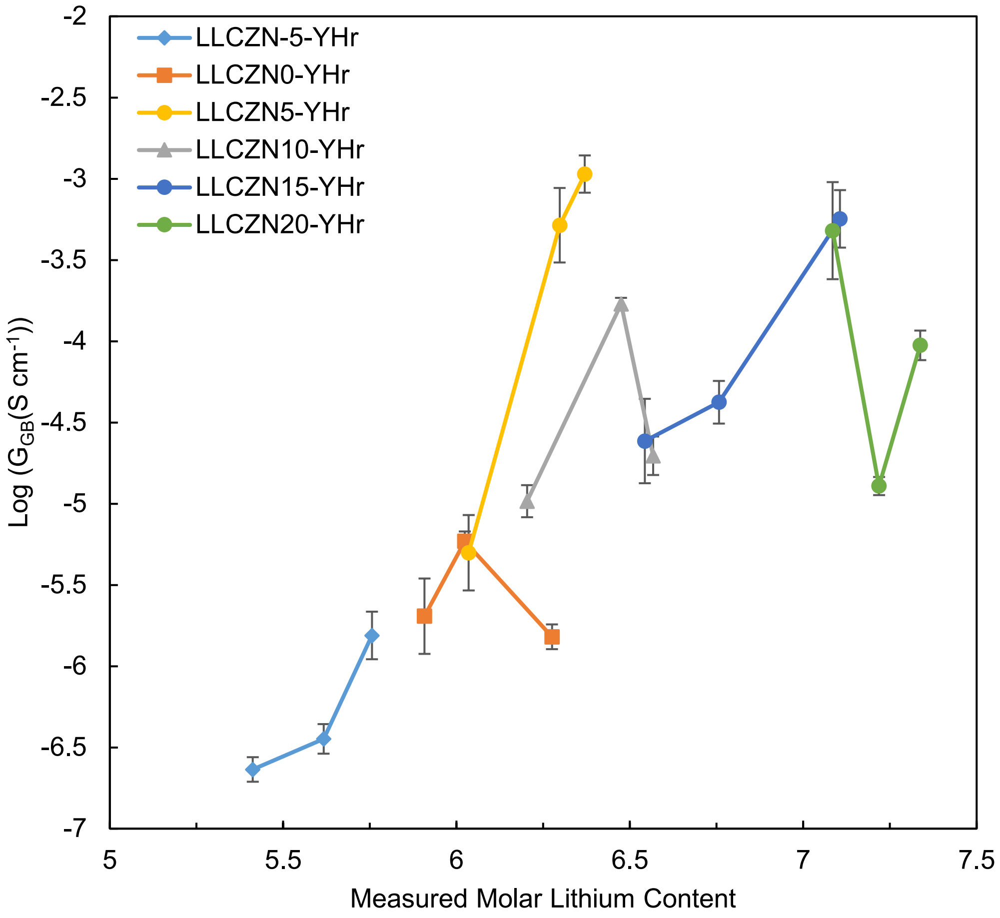

Figure S39. Log grain boundary conductance vs the measure molar lithium content of LLCZNX-YHr

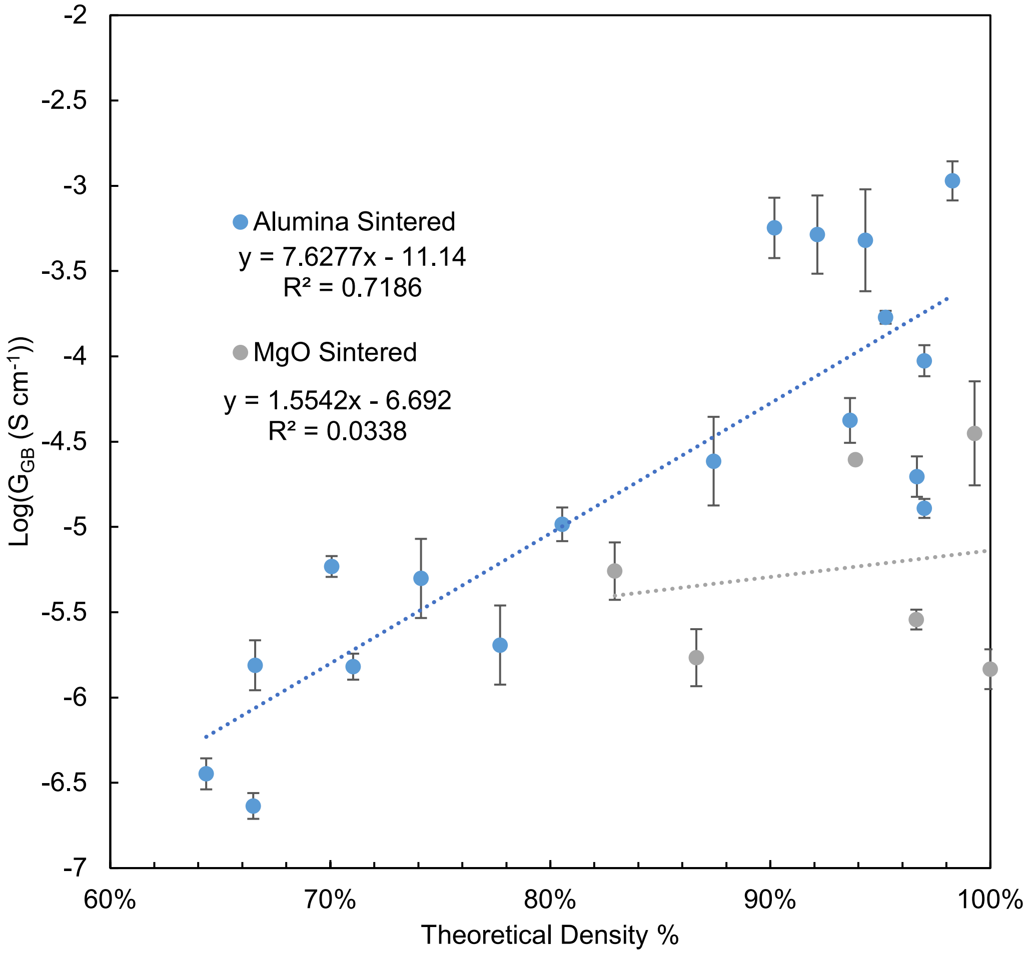

Figure S40. Log grain boundary conductance versus the theoretical density

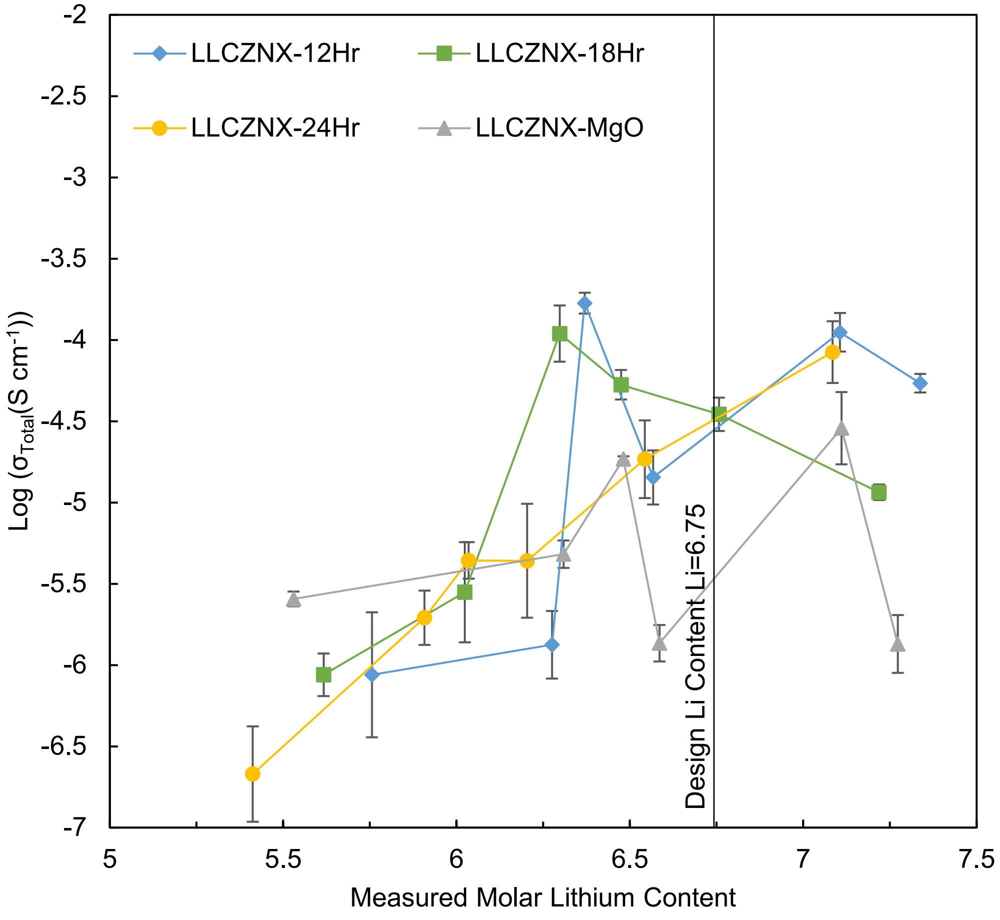

Figure S41. Log total conductivity versus lithium content at the four sintering conditions. Diamonds are LLCZNX-12Hr, squares at LLCZNX-18Hr, circles are LLCZNX-24Hr, and triangles are LLCZNX-MgO.

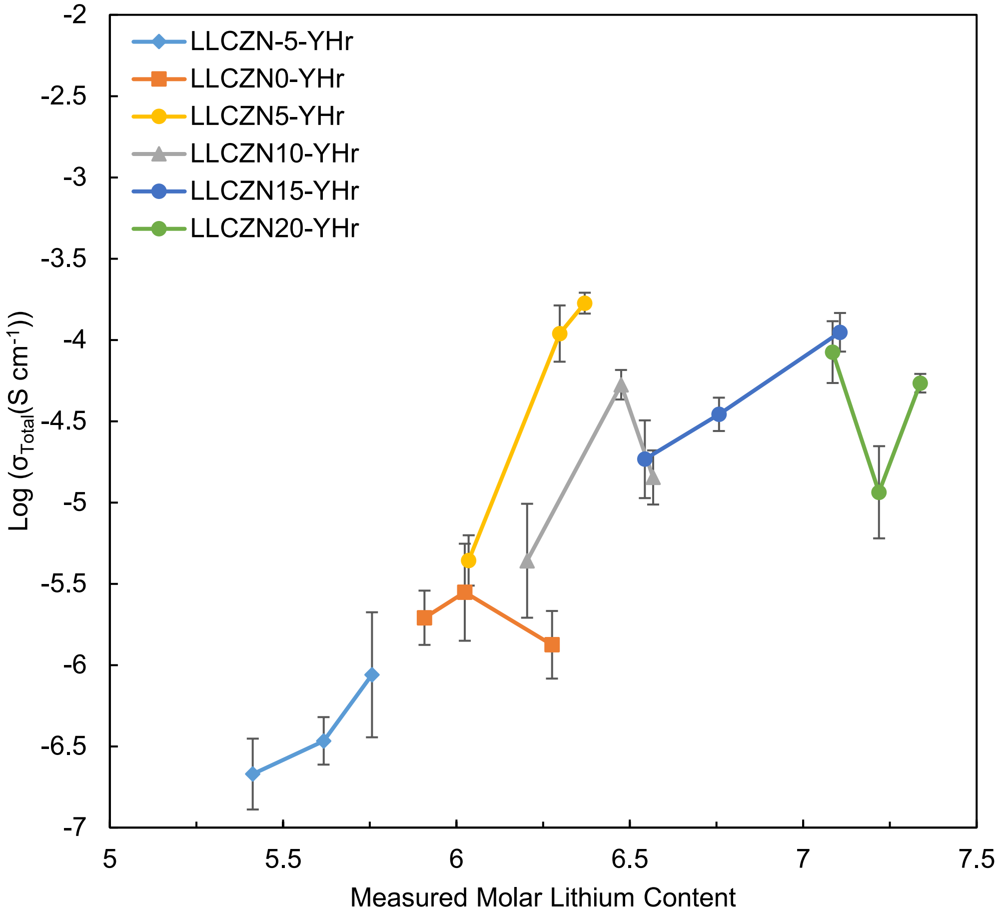

Figure S42. Log the total conductivity vs the measure molar lithium content of LLCZNX-YHr

Appendix B: Supplementary Information for Chapter 3

Element	x Coordinate	y Coordinate	z Coordinate	Occupation
Li1	0.375	0.000	0.250	0.940
Li2	0.096	0.692	0.570	0.300
La	0.125	0.000	0.250	0.921
Ca	0.125	0.000	0.250	0.079
Zr	0.000	0.000	0.000	0.750
Nb	0.000	0.000	0.000	0.250
O	-0.032	0.540	0.150	1.000

Table S13. Refinement parameters for LLCZN

Element	x Coordinate	y Coordinate	z Coordinate	Occupation
Li	0.000	0.000	0.000	0.906
Co	0.000	0.000	0.500	1.000
O	0.000	0.000	0.250	1.000

Table S14. Refinement parameters for LCO

Element	x Coordinate	y Coordinate	z Coordinate	Occupation
La	0.000	0.000	0.250	1.000
Co	0.000	0.000	0.000	1.000
O	0.000	0.000	0.250	1.000

Table S15. Refinement parameters for LaCoO3

Material	**Weight Percent**
LLCZNX	16.28%
LCO	16.28%
Polyvinyl Butryal (Sigma Aldrich)	5.72%
Benzyl Butyl Phthalte (Sigma Aldrich, 98%)	8.37%
IPA	31.60%
Acetone (Sigma Aldrich, >99.5%)	21.57%
Fish Oil (Sigma Aldrich)	0.18%

Table S16. Tape cast recipe for composite cathode for co-sintering

Lithium Content (%)	**LLCZN(Å)**	**LCO-a (Å)**	**LCO-c(Å)**
-10	12.917	2.815	14.052
10	12.920	2.815	14.045
30	12.920	2.813	14.050
40	12.924	2.814	14.070

Table S17. Lattice parameters of the mixed LLCZNX/LCO powders with varying lithium excess content. LLZO is fit using ICDD-PDF 00-019-8837, LCO is fit ICDD-PDF No. 01-070-2685, and $LaCoO_3$ is fit using ICDD-PDF 00-048-0123[330].

The lattice parameters of the LLCZNX and LCO phases were calculated by performing Rietveld refinement from the XRD data. The refinement data show minor lattice expansion in the LLCZNX phase as the lithium content increases. In contrast, when forming $LaCoO_3$, LCO maintained similar lattice parameters until the secondary phase was not detected in LLCZN40/LCO. The "a" lattice constant of LCO does not change with the increasing lithium content, but the "c" lattice constant expands from 14.050 to 14.070 Å upon reaching 40% excess lithium in the garnet powder. Despite these changes, the species' lattice parameters have a minor dependence on the lithium content of the co-sintered system.

Sample	RWP	X2
LLCZN-10/LCO	2.81	1.92
LLCZN10/LCO	2.8	1.37
LLCZN30/LCO	2.96	1.45
LLCZN40/LCO	3.24	1.23

Table S18. XRD refinement results

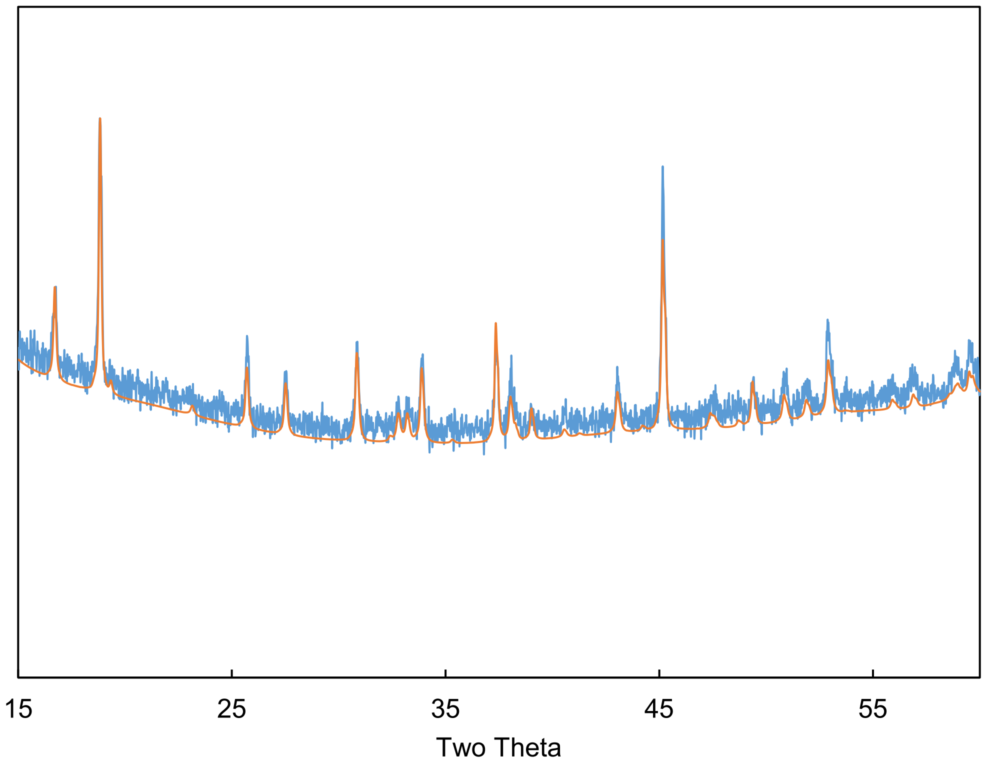

Figure S43. LLCZN40-LCO Fit. Blue is actual data and orange is the fitted data.

LLCZN in Product (g)	LCO in Product (g)	$LaCoO_3$ in Product (g)	Mol of $LaCoO_3$	Mol of LLCZN in Reactants	Mol of LCO in Reactants	Weight of LLCZN Reactant(g)	Weight of LCO in Reactants (g)	Percent of LLCZN in Reactants	Percent of LCO in Reactants
0.106	0.590	0.304	1.24E-03	1.58E-03	7.27E-03	0.482	0.711	40%	60%
0.144	0.630	0.215	8.73E-04	1.35E-03	7.31E-03	0.410	0.715	36%	64%
0.185	0.581	0.235	9.55E-04	1.56E-03	6.89E-03	0.476	0.674	41%	59%
0.278	0.655	0.066	2.70E-04	1.18E-03	6.97E-03	0.360	0.682	35%	65%

Table S19. Mass balance of Reitveld Refinement results

Mass balance was performed on a 1 gram basis of the Reitveld refinement results. The weights were then used to find the mol of each species. The total Co and La in the products should be the same amount as what was in the reactants, LLCZN and LCO. Those mols were calculated into the weight of each reactant species and then the percentages were calculated.

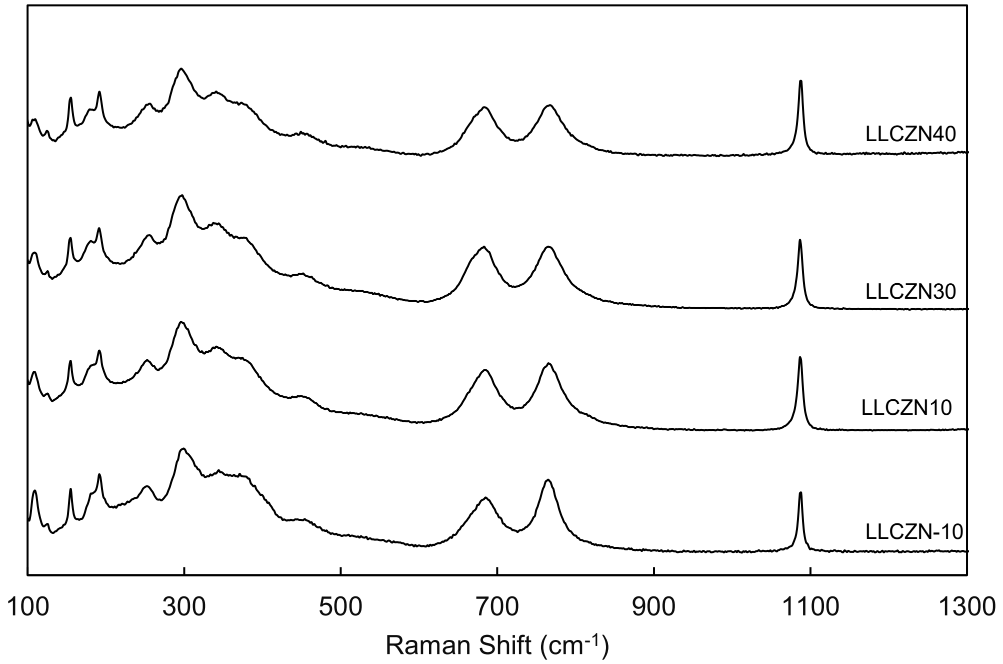

Figure S44. Raman spectroscopy of the ball milled LLCZNX material before mixing with LCO

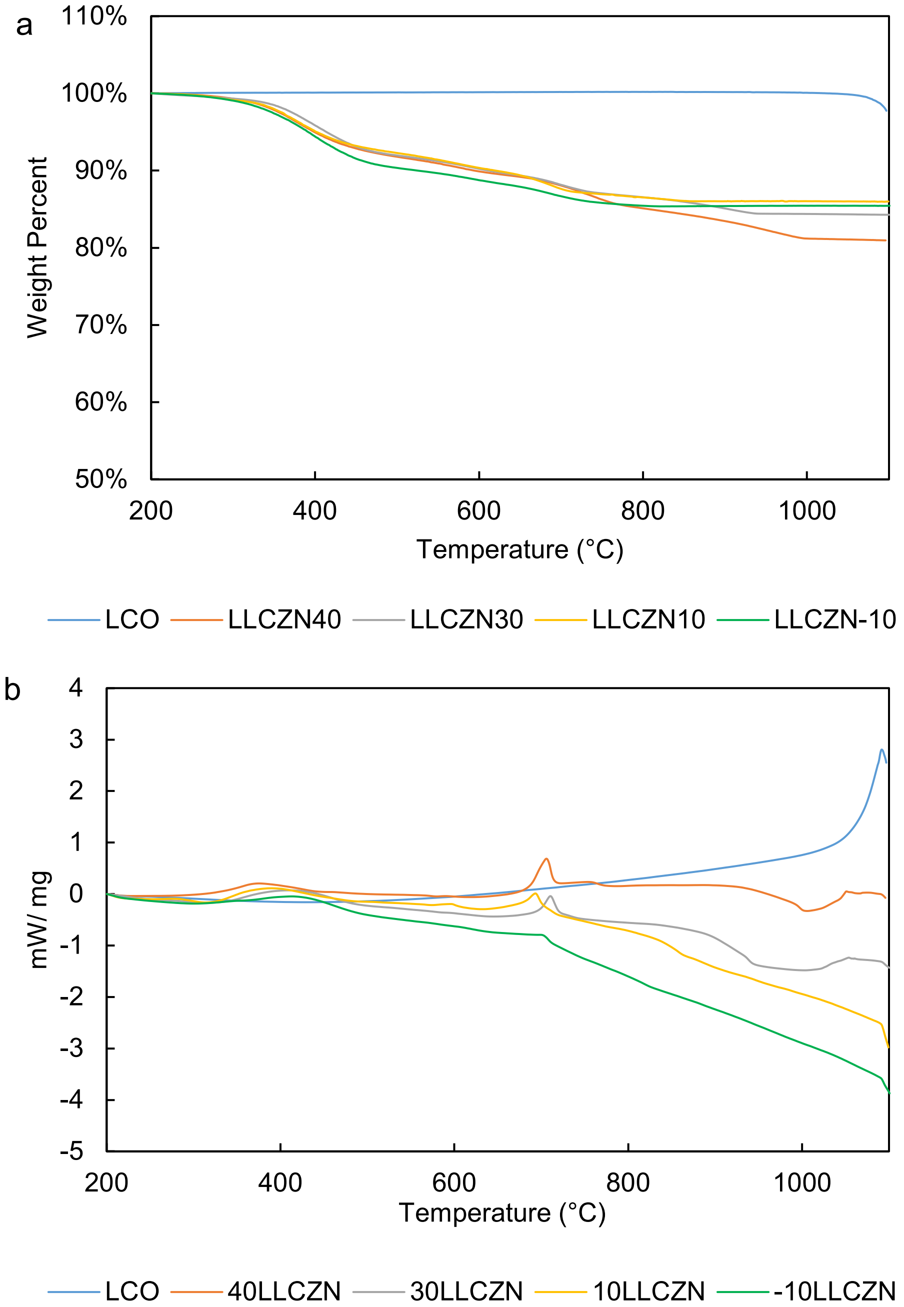

Figure S45a. TGA Data for all the separate powders before co-sintering. **S45b.** DSC Data of all the separate powders before heat treating them together.

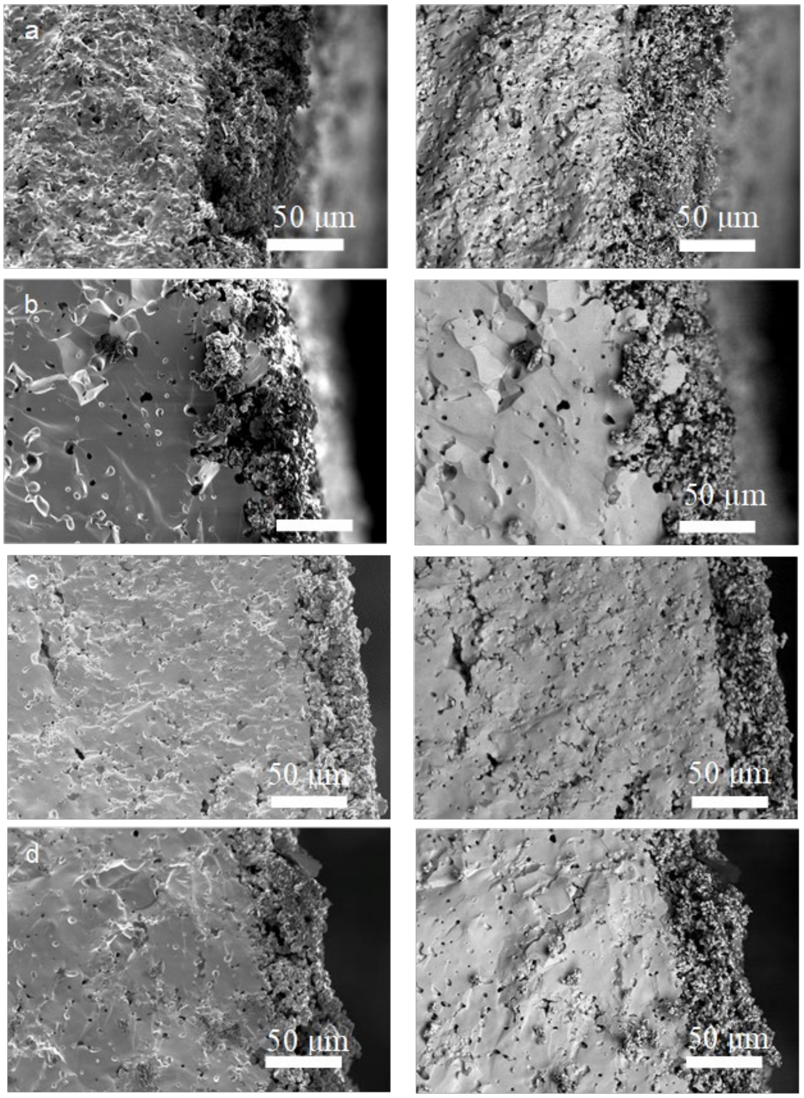

Figure S46. Cross section edge SEM (left) and BSE (right) images of pressed composite pellets of 50/50 weight mixtures of LLCZNX/LCO, with a) x=-10, b: x=0, c) x=10, d) x=40.

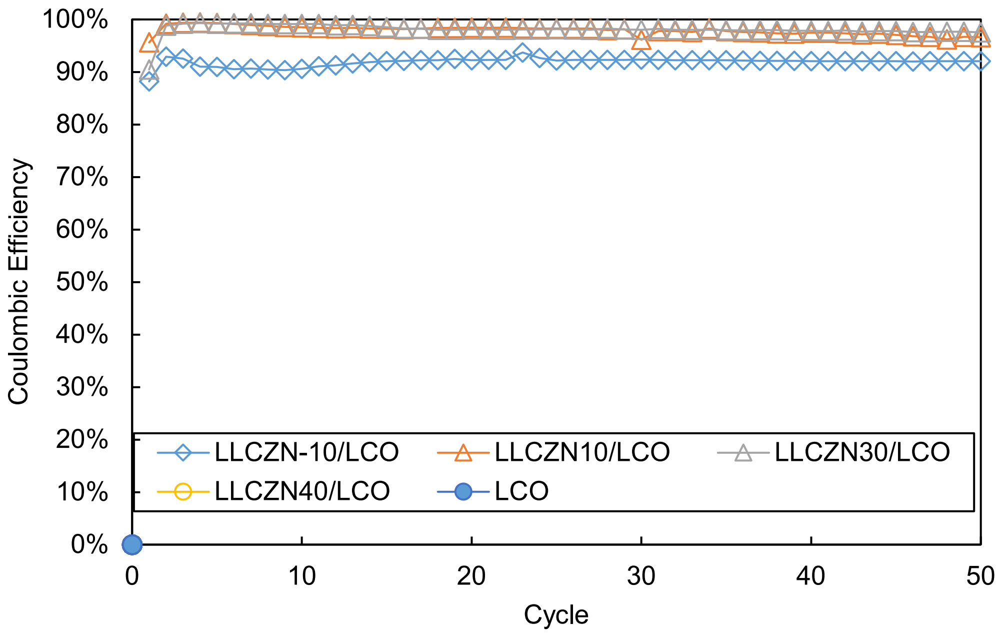

Figure S47. Coulombic efficiency of the cycle life data

After co-sintering LLCZNX/LCO powder at 1050°C for 4 hours, half cells with the co-sintered powder and liquid electrolyte were constructed and then charged and discharged. A baseline cell with LCO was also constructed and measured a capacity of 125 mAhr g^{-1}.

LLCZN10/LCO and LLCZN30/LCO half-cells show faster capacity degradation (95% and 96% original capacity after 50 cycles respectively) versus LLCZN40/LCO which shows 98% original capacity after 50 cycles. Oxide coatings on LCO have been previously used to inhibit cobalt oxide dissolution during charging and increasing structural stability for longer cycle life[331]. LLCZN and excess lithium may be acting as a coating on the LCO particles which appears to be inhibiting cycle life degradation when $LaCoO_3$ is minimally formed. It is presumed co-sintering LLCZN40 and LCO does not have a deleterious effect on electrochemical cycle life performance. This is crucial for operation in solid state cells.

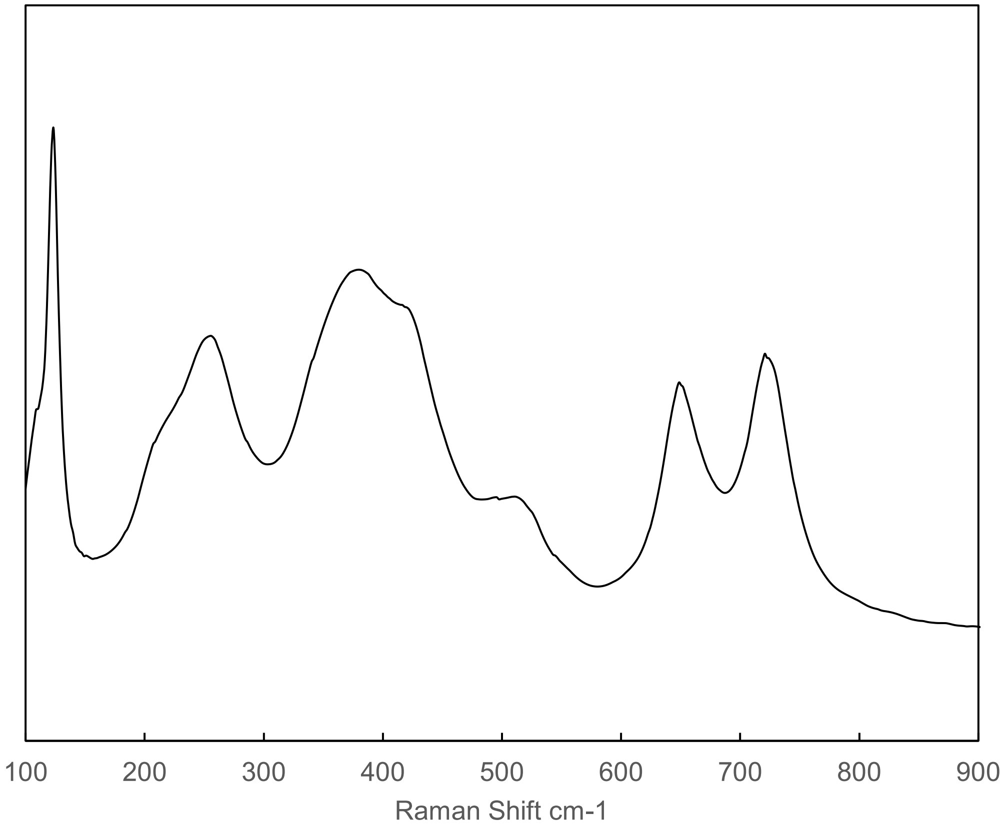

Figure S48. Raman spectroscopy data of sintered LLCZN5

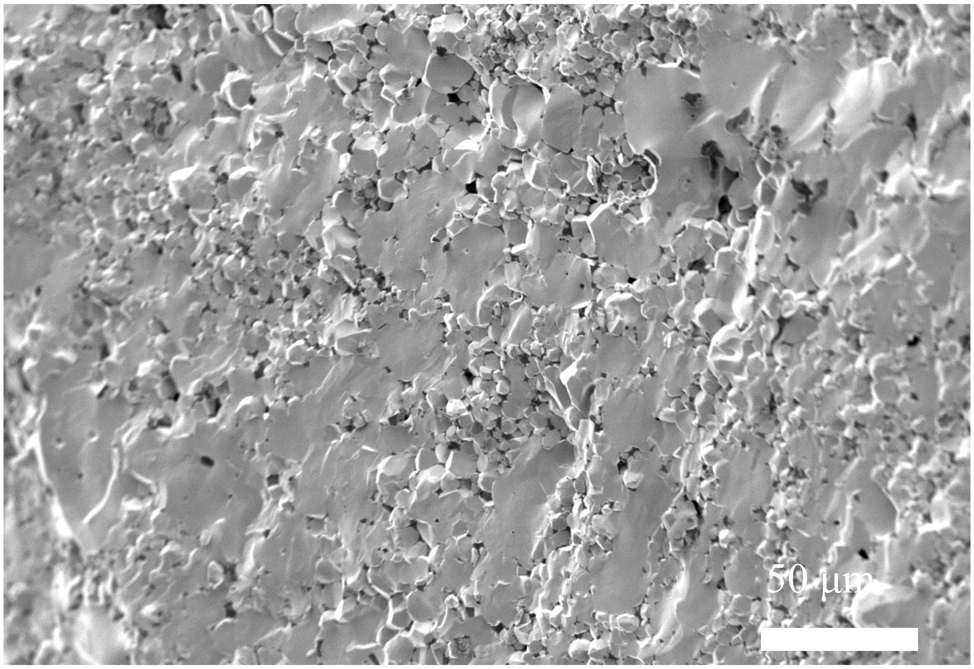

Figure S49. Fractured Edge SEM image of sintered LLCZN5

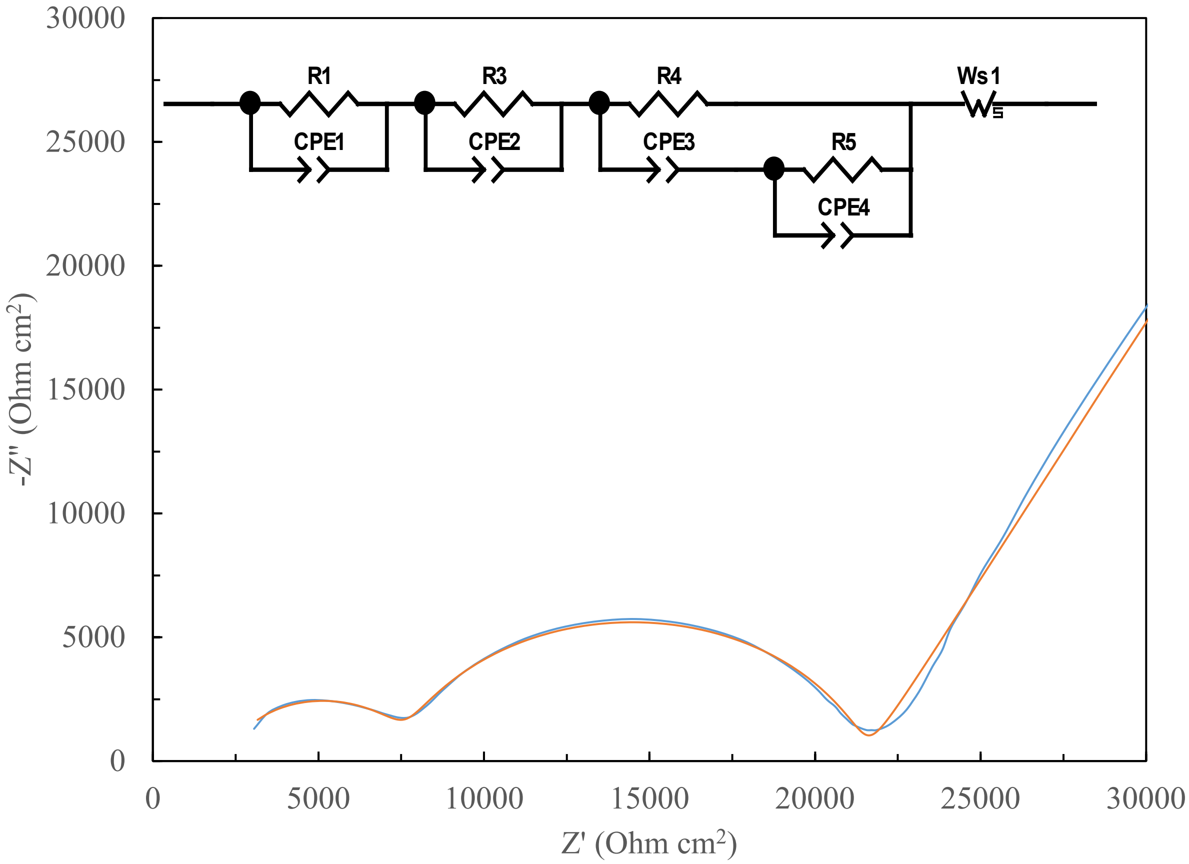

Figure S50. EIS and fit data for LLCZN-10/LCO.

Sample	**Rbulk (Ohms)**	**Cbulk (F)**	**RGB (Ohms)**	**CGB (F)**	**RInt (Ohms)**	**CInt (F)**
LLCZN-10/LCO	2240	1.53E-11	1436	4.17E-10	17941	4.44E-09
LLCZN10/LCO	2254	2.50E-11	4198	4.17E-10	7965	3.83E-09
LLCZN30/LCO	1898	1.48E-10	4717	2.41E-08	1301	4.06E-06
LLCZN40/LCO	3760	8.22E-11	519.9	1.58E-09	4501	2.84E-08

Table S20. EIS fitting results

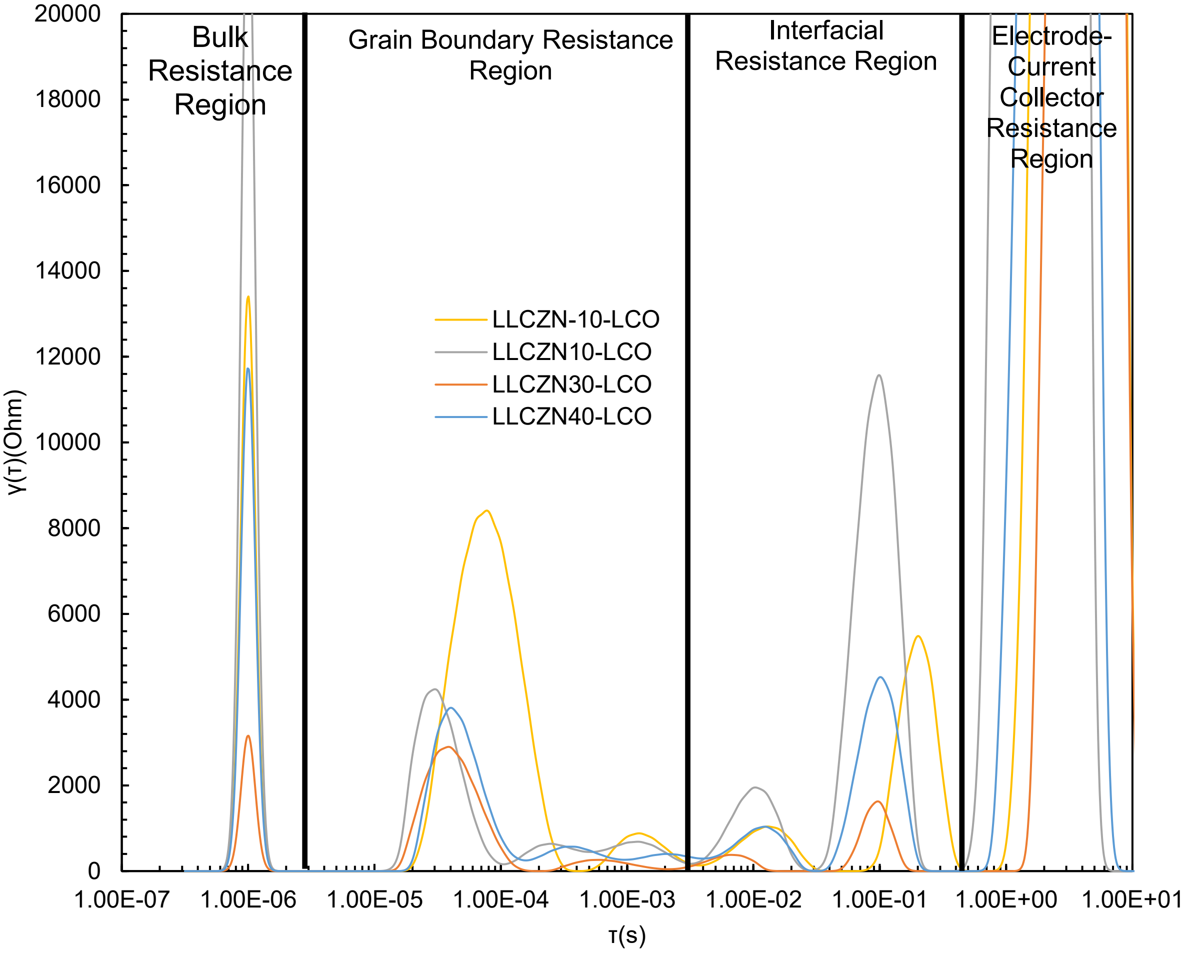

Figure S51. DRT results of EIS data

Sample	**Relaxation Frequency 1 (Hz)**	**Relaxation Frequency 2 (Hz)**	**Relaxation Frequency 3 (Hz)**	**Relaxation Frequency 4 (Hz)**
LLCZN-10/LCO	4.64E+06	2.66E+05	2.00E+03	7.70E-06
LLCZN10/LCO	2.82E+06	9.09E+04	5.21E+03	2.41E-04
LLCZN30/LCO	5.65E+05	1.40E+03	3.01E+01	5.97E-03
LLCZN40/LCO	5.15E+05	1.94E+05	1.25E+03	5.78E-05

Table S21. Calculated relaxation frequencies

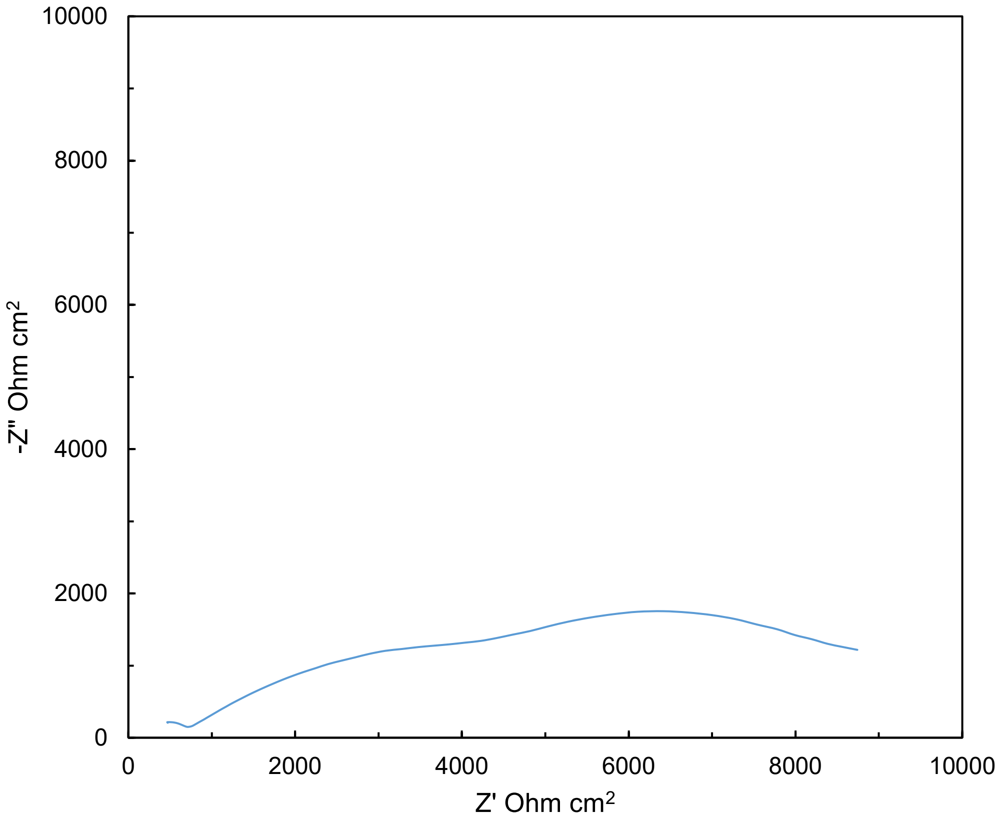

Figure S52. EIS of full cell of LLCZN40/LCO

Appendix C: Supplementary Information For Chapter 4

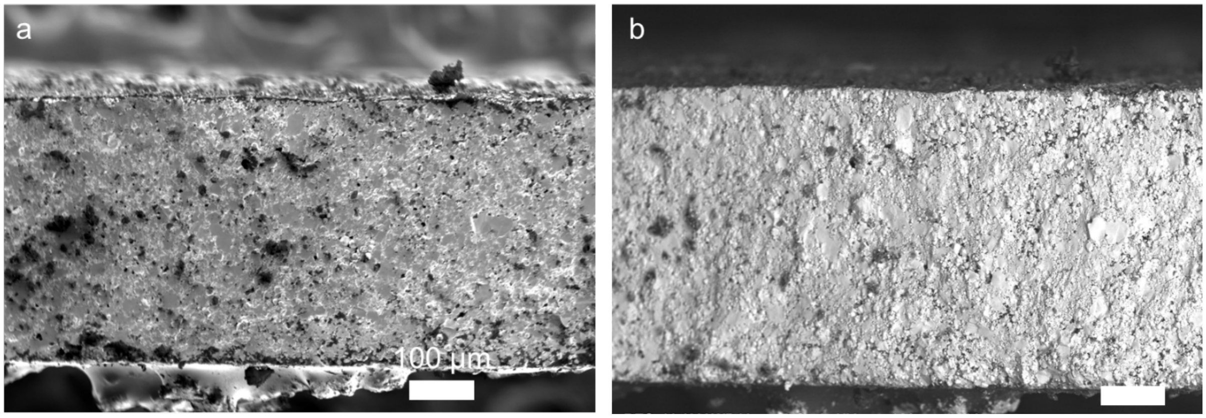

Figure S53a. Fractured edge SEM Images of LLCZN. **Figure S53b.** BSE Images of LLCZN.

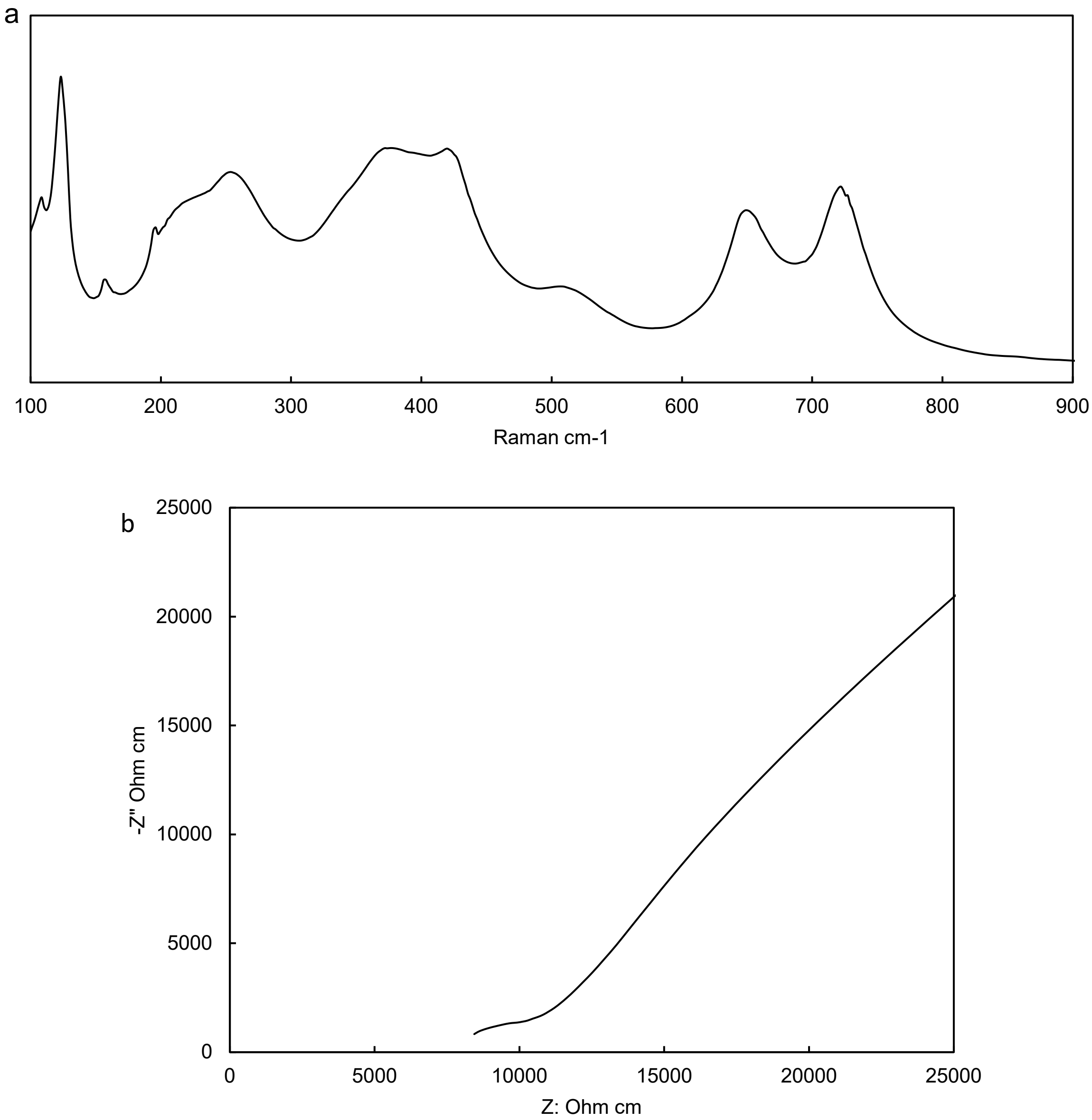

Figure S54. Raman Spectra of LLCZN Pellet. **Figure S54b**. EIS of LLCZN pellet.

LLCZN pellets were prepared by applying Au paste to both side and then heating to 750°C for 1 hour to remove the organics. The pellet was then placed between two stainless steel plates and ran EIS at 10 mV between 10 kHz and 0.1 Hz.

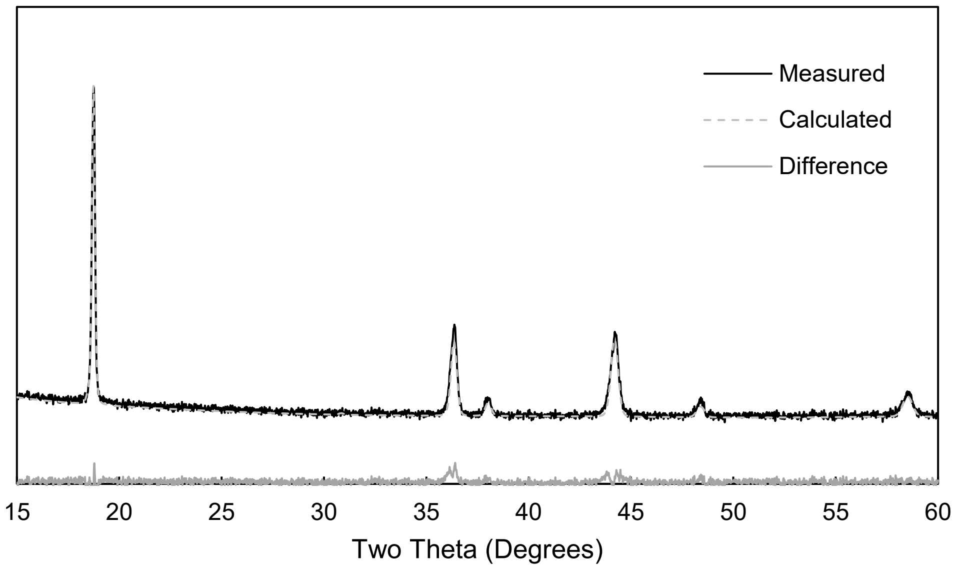

Figure S55. Example of Rietveld refinement fit

	LMO	**LM-Cl**	**LMC**	**LMFC**	**LMNFC**
Li 8a (0,0,0) Occupancy	1	1	1	1	1
Mn 16d (0.675,0.675,0.675) Occupancy	1	1	0.975	0.950	0.925
Ni 16d (0.675,0.675,0.675) Occupancy	0	0	0	0	0.025
Fe 16d (0.675,0.675,0.675) Occupancy	0	0	0	0.025	0.025
Co 16d (0.675,0.675,0.675) Occupancy	0	0	0.025	0.025	0.025
O 32e (0.390,0.390,0.390) Occupancy	1	0.990	0.990	0.990	0.990
Cl 32e (0.390,0.390,0.390) Occupancy	0	0.010	0.010	0.010	0.010
Lattice Parameter (Å)	8.189	8.215	8.203	8.206	8.196
Lattice Volume (Å^3)	533.76	554.45	552.05	552.48	550.28
Rwp(%)	5.233	2.980	3.160	3.370	3.290
X^2	4.347	1.376	1.204	1.832	1.589

Table S22. XRD refinement parameters

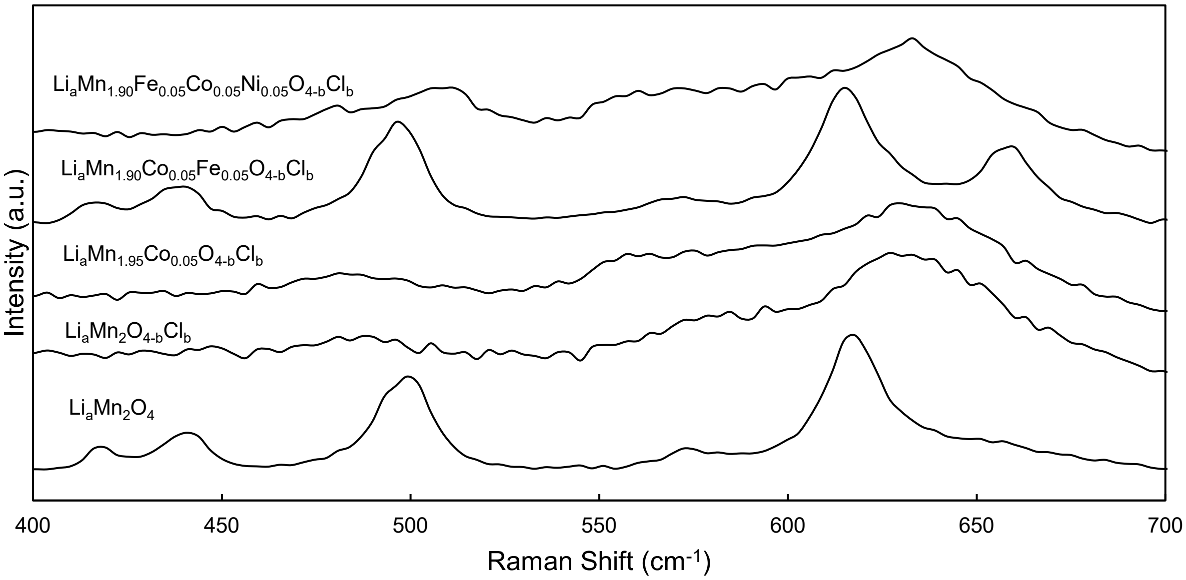

Figure S56. Raman spectroscopy of all the samples. Magnified into closer sections of the data set. The order vs. disorder can be seen in LMO and LMCFO vs all the other samples.

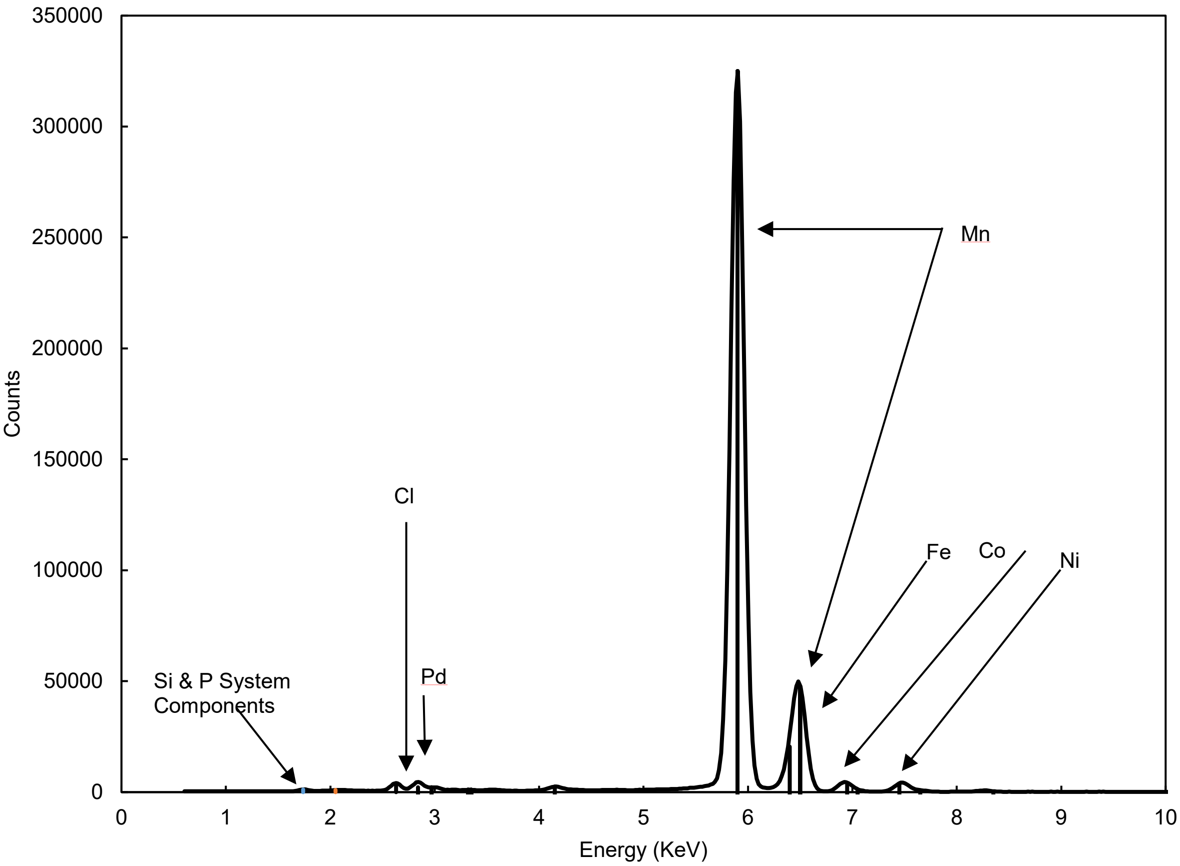

Figure S57. X-ray florescence spectra of LMNCF where the chlorine is identified as being in the powder.

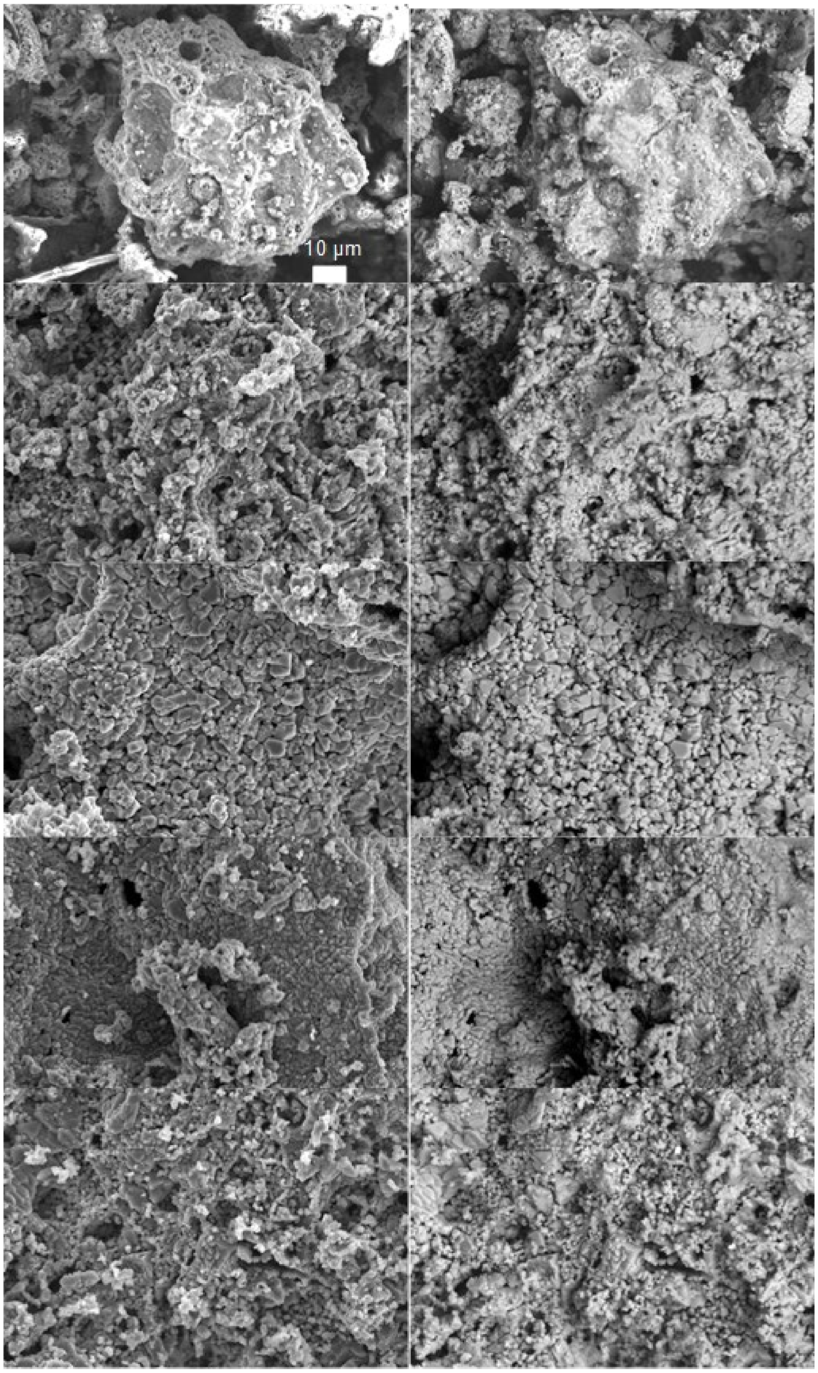

Figure S58. Scanning electron microscope images of all the samples (left column) and back scatter images of the samples (right column). First rows is LM, second row is LM-CL, third row is LMC, fourth row is LMFC, and the last row is LMNFC.

The SEM images of all the samples indicates no major changes in the microstructure of the materials meaning it is independent of the dopants used but it is dependent on the formation method. The method allows for high surface area material to be made and the phases to be stable under appropriate circumstances (Cl addition, Fe addition with Ni addition).

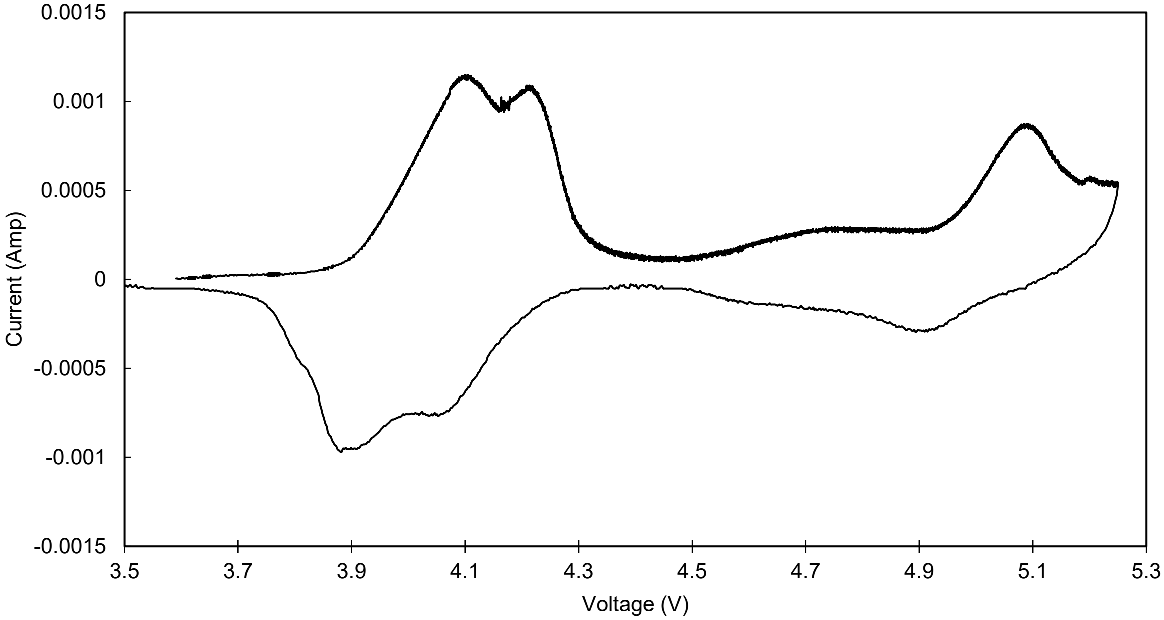

Figure S59. Cyclic voltammetry curve of LMNFC.

The cyclic voltammetry (CV) is shown here to elucidate the difference between actual capacity that can be accessed at 5.25 V and the measured capacity at 4.5 V. There appears to be about 20-30% more capacity above 4.5 V. However, there are limitations in the electrolyte that make cycling to this voltage difficult. The overcharge seen above 5 V is largely the electrolyte degradation with more lithium which will increase cell resistance making high rate cycling challenging without a specific electrolyte designed.

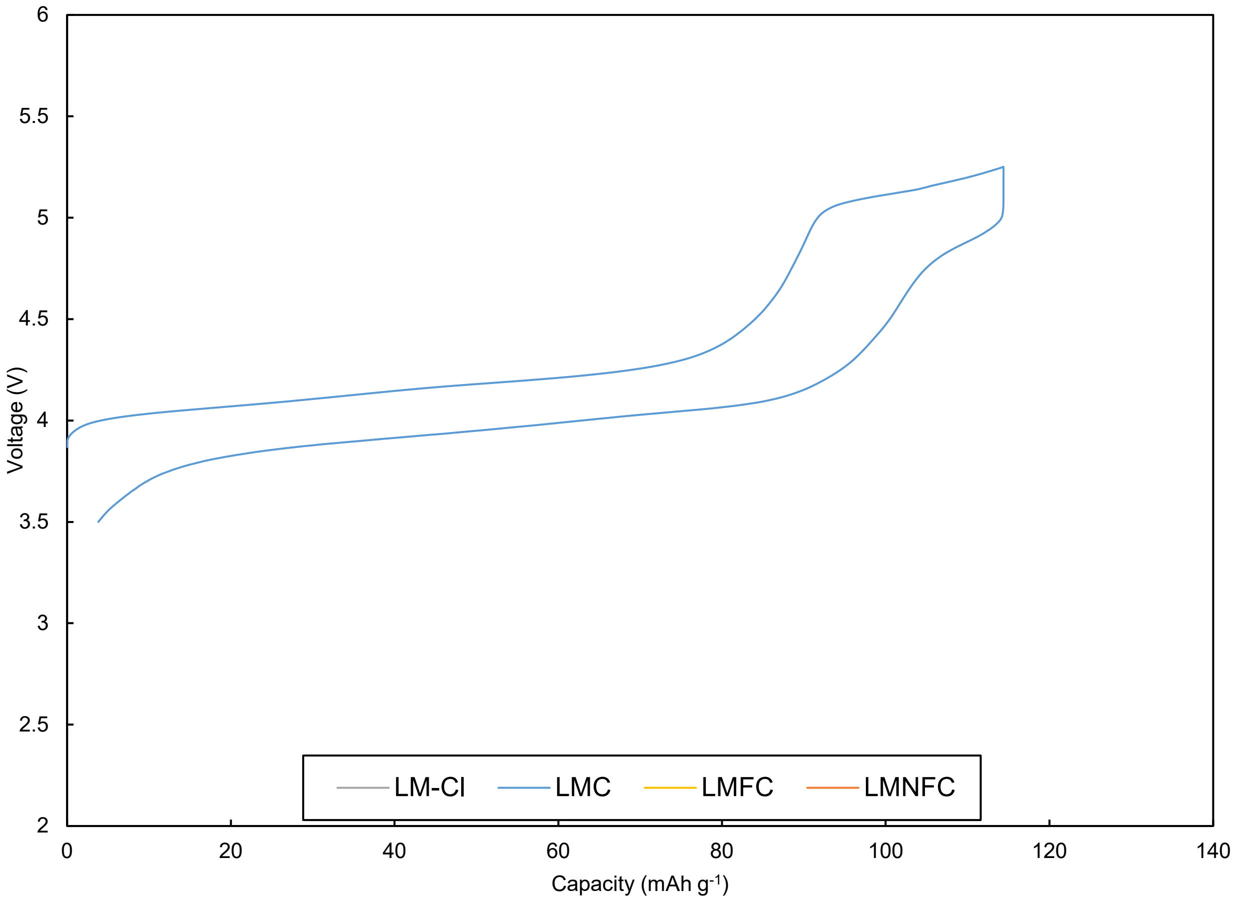

Figure S60. Voltage vs capacity for succeeding cycle of results

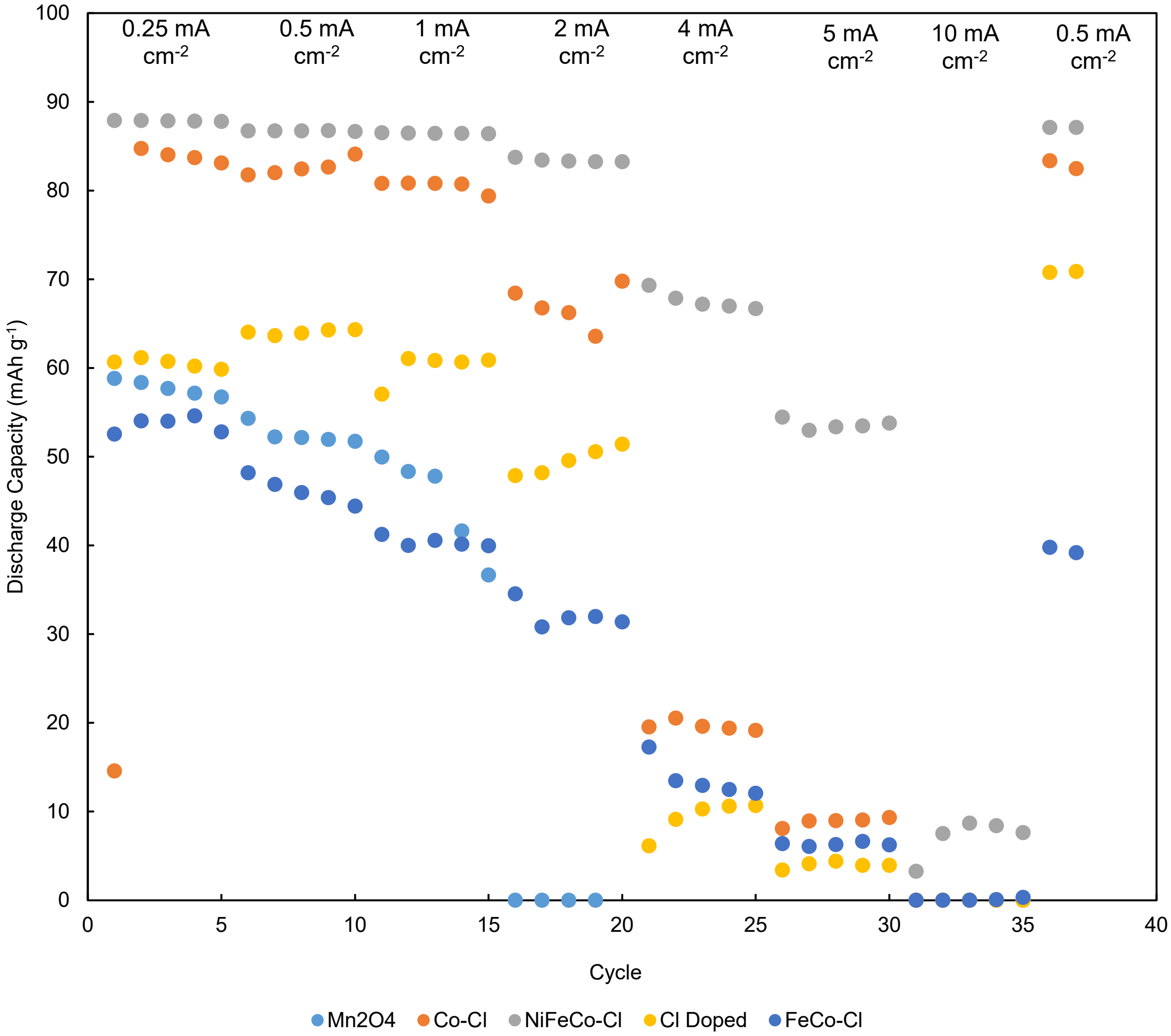

Figure S 61. Capacity vs. cycle number for varying charge and discharge rates (~C/10 to 4C)

Figure S60 compares the rate capability of the material. The cathode loading of the material was ~25 mg cm^{-2} of active material. Chlorine doping shows that it helps maintain the structure by increasing the disorder of the B-site. LMNFC has the best rate capability due to the iron inclusion and the other dopants which handle the lithium insertion and extraction without manganese dissolution. The increasing dopants do show better rate capability as more dopants are added but the LMFCO has lower capacity because of the nonreactive $LiMn_2O_3$ formation but still retains capacity as well as LMCO.

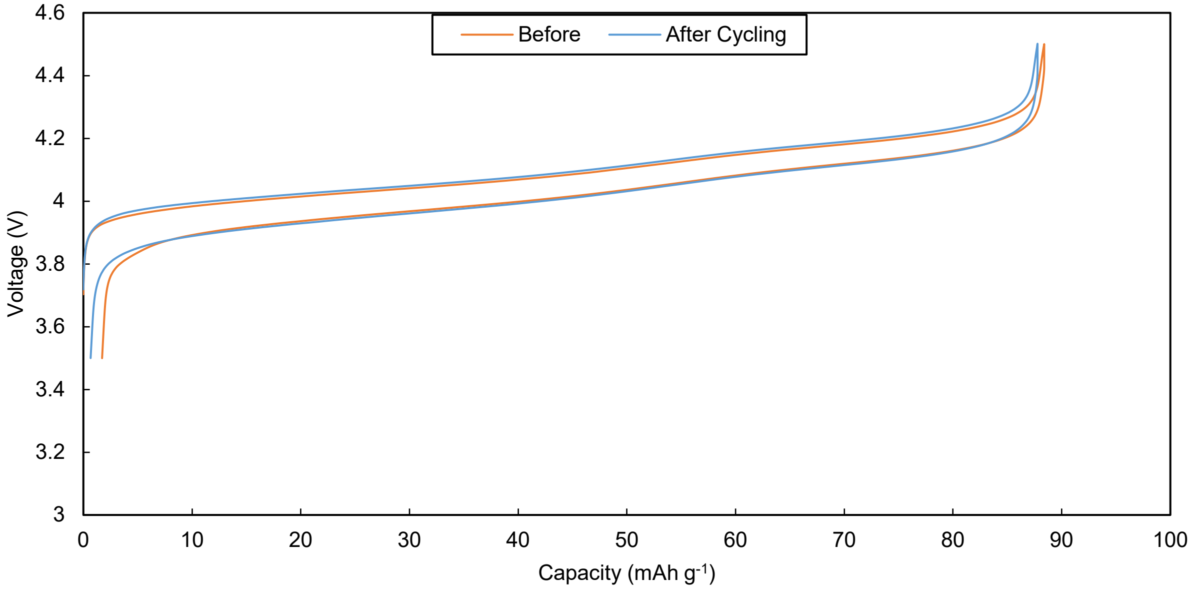

Figure S62. Voltage vs. capacity before and after LMNCF rate testing at 0.5 mA cm^{-2}

The voltage vs capacity plot before and after rate testing did not indicate any major changes for the LMNCF material which is because the dopants enabled faster discharging and charging because of the transition metals charge compensating when quickly charged.

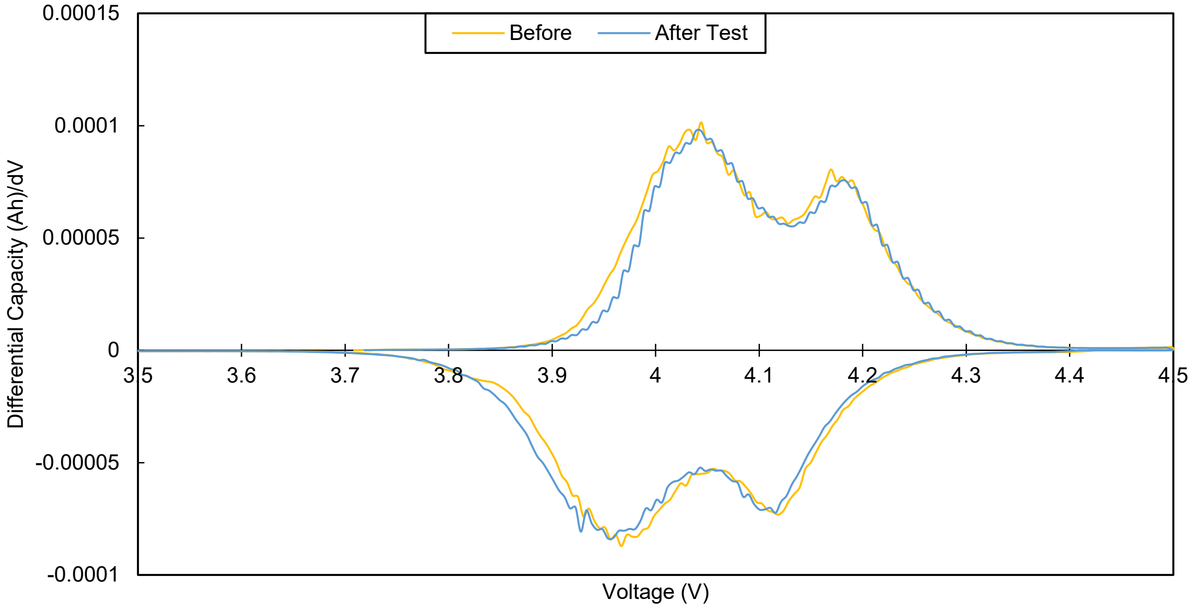

Figure S63. Differential capacity vs. voltage of LMNCF before and after rate testing at 0.5 mA cm^{-2}.

Differential capacity enables the cathode structure and cell kinetics to be examined without taking apart the cell. The curve specifies no changes in structure or kinetics between the before and after testing; meaning the cathode material still is intact and can cycle.

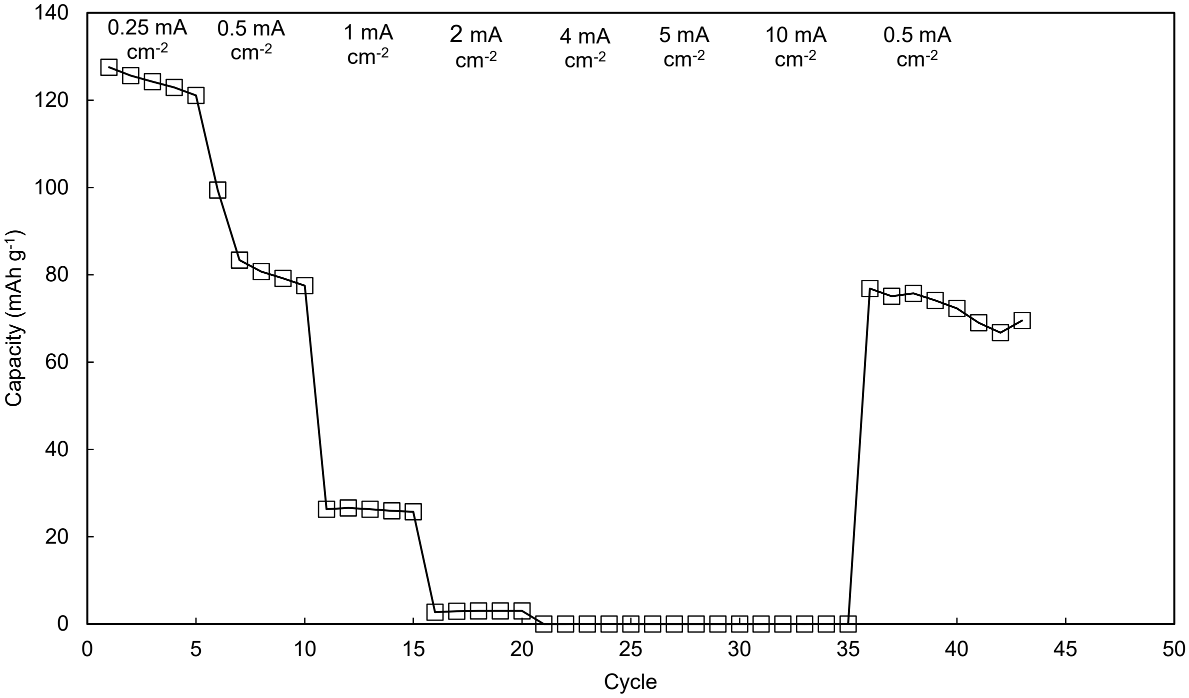

Figure S63. Cycle at rates vs. discharge capacity of LMNCF.

The cell was unable to discharge at high rates when above 4.5 V which indicates a large internal resistance. The cyclic voltammetry indicates cell gelling which will increase resistance within the cell, leading to premature cell failure at high rates.

	Initial	**Final**
R_{soln}	7.091	5.847
R_p	54.41	20.88
C_{dl}	2.2E-05	0.00015
A_{dl}	0.7798	0.5977
R_{ad}	0.00049	121.1
C_a	1.6E-06	1.2E-06
R_a	2.14	2.037
C_{ad}	0.04873	0.03563
A_{ad}	0.09563	1
R_{total}	63.6415	149.864

Table S23. Fitting results for EIS from Figure 32a

	Initial	**Final**
R_{soln}	7.346	6.746
R_p	1.26E-05	86.2
C_{dl}	8.39E-05	1.63E-04
A_{dl}	6.46E-01	7.10E-01
R_{ad}	151.7	44.15
C_a	2.12E-06	1.49E-06
R_a	2.161	2.485
C_{ad}	2.96E-02	1.56E-02
A_{ad}	1	7.89E-01
R_{total}	161.207	139.581

Table S24. Fitting results for EIS from Figure 32b

	Initial	**Final**
R_{soln}	8.198	4.782
R_p	85.66	116.5
C_{dl}	1.31E-04	1.32E-04
A_{dl}	7.22E-01	5.57E-01
R_{ad}	37.5	35.54
C_a	1.67E-06	2.08E-04
R_a	2.693	54.46
C_{ad}	1.59E-02	9.93E-03
A_{ad}	7.25E-01	6.66E-01
R_{total}	134.051	211.282

Table S25. Fitting Results for EIS from Figure 66a

	Initial	**Final**
R_{soln}	6.077	6.826
R_p	124.000	23.560
C_{dl}	6.68E-05	4.65E-04
A_{dl}	0.623	0.601
R_{ad}	53.370	282.000
C_a	1.73E-04	2.50E-06
R_a	46.220	1.888
C_{ad}	0.012	0.004
A_{ad}	0.835	1.000
R_{total}	229.667	314.274

Table S26. Fitting Results for EIS from Figure 66b

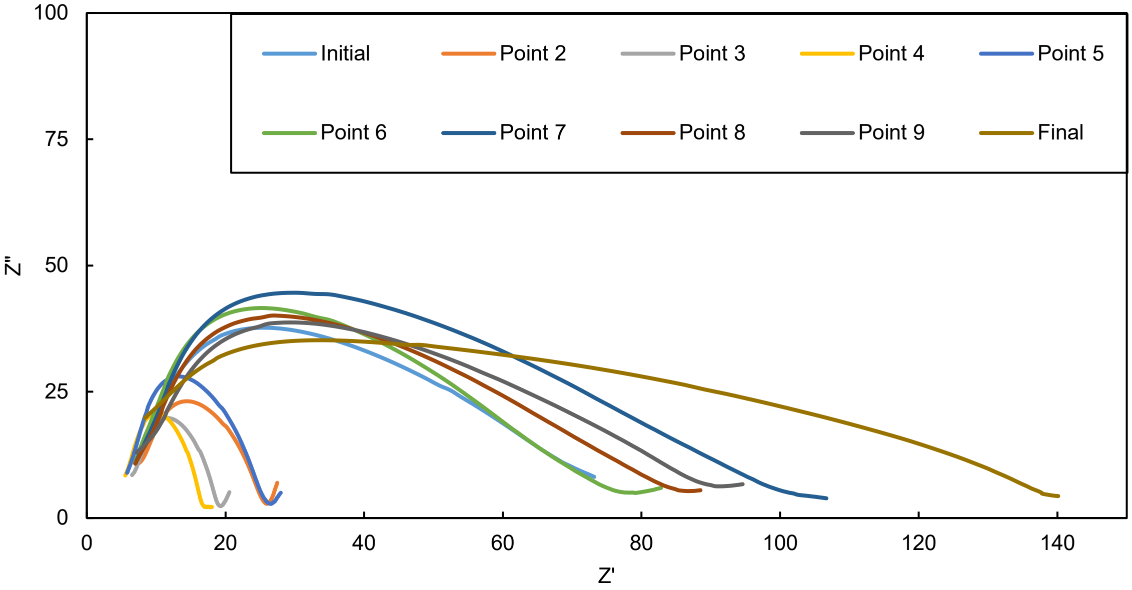

Figure S64. Example of the EIS results during cycling between 5 V and 2.5 V.

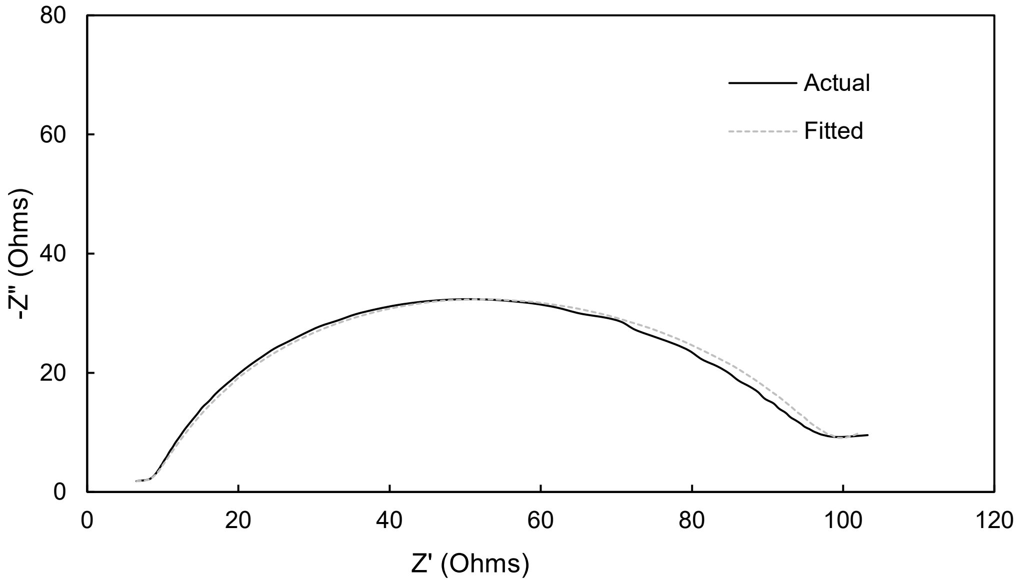

Figure S65. Example of fit of the EIS data

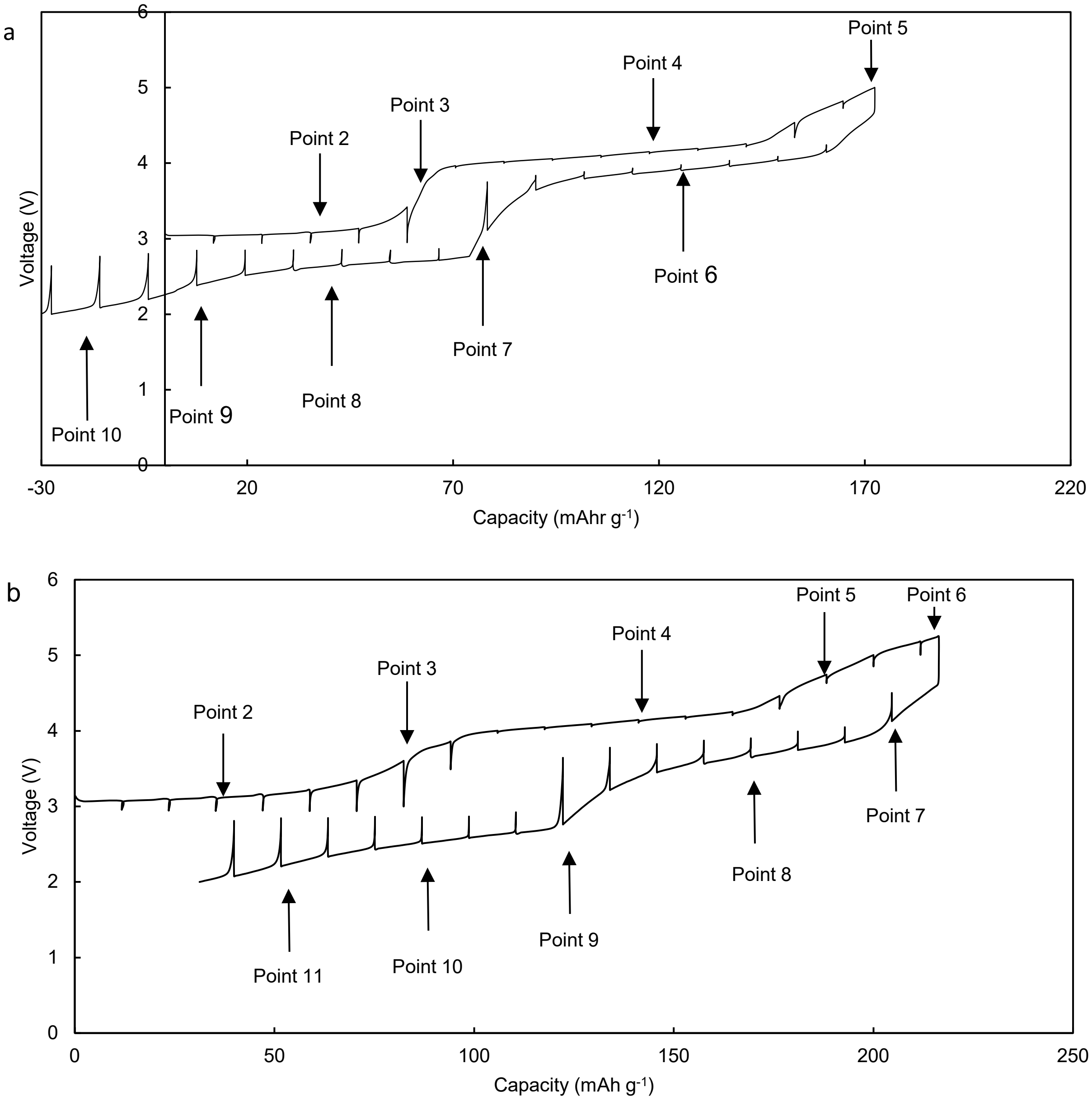

Figure S66a. Voltage vs. capacity for LMNCF between 5 and 2V at60.2 mA cm^{-2} (~C/10 for 120 mAh g^{-1}) with EIS measurements every hour for a second time. **S66b.** Voltage vs. capacity for LMNCF between 5.25 and 2V at 0.2 mA cm^{-2} with EIS measurements every hour for a second time.

Bibliography

Chapter 1 References

[1] Ding, Y.; Cano, Z.P.; Yu, A.; Lu, J.; Chen, Z.. Automotive Li-Ion Batteries: Current Status and Future Perspectives. *Electrochem. Energ. Rev.* **2019,** 2**,** 1–28 DOI: 10.1007/s41918-018-0022-z

[2] Hirtenstein, A. Move over Tesla, Europe's building its own battery gigafactories. *Bloomberg.com*, 22 May 2017, www.bloomberg.com/news/articles/2017-05-22/move-over-tesla-europe-s-building-its-own-battery-gigafactories

[3] Peters, J.F.; Baumann, M.; Zimmerman, D.; Braun, J.; Weil, M. The environmental impact of Li-Ion batteries and the role of key parameters – A review. *Renewable and Sustainable Energy Reviews*. **2017,** 67, 491–506, DOI:10.1016/j.rser.2016.08.039

[4] Robinson, A.L.; Whittingham, S.L. Pushing the frontiers of lithium-ion batteries raises safety questions. *MRS Bulletin*. **2016**, 41 (3), 188–189, DOI:10.1557/mrs.2016.30

[5] Dewulf, J.O. Vorst, G.; Denturck, K.; Langenhove, H.; Ghyoot, W.; Tytgat, J.; Vandeputte, K. Recycling rechargeable lithium-ion batteries: Critical analysis of natural resource savings. *Resources, Conservation and Recycling*. **2010,** 54, 229–234, DOI:10.1016/j.resconrec.2009.08.004

[6] Dai, K.; Wang, Z.; Ai, G.; Zhao, H.; Yuan, W.; Song, X.; Battaglia, V.; Sun, C.; Wu, K.; Liu, G. The transformation of graphite electrode materials in lithium-ion batteries after cycling. *Journal of Power Sources.* **2015,** 298, 349-354 DOI:10.1016/j.powsour.2015.08.055

[7] Babu, B.V.;Babu, K.V.; Aregi, G.T.; Devi, L.S.; Latha, B.M.; Reddi, M.S.; Samatha, K.; Veeraiah, V. Structural and electrical properties of $Li_4Ti_5O_{12}$ anode material for lithium-ion batteries. *Results in Physics*. **2018,** 9, 284-289. DOI:10.1016/j.rinp.2018.02.050

[8] Chiu, H.; Lu, X.; Zhou, J.; Gu, L.; Reid, J.; Gauvin, R.; Zaghib, K.; Demopoulos, G.P. Annealing-regulated elimination of residual strain-induced structural relaxation for stable high-power $Li_4Ti_5O_{12}$ nanosheet anodes. *Nano Energy*. **2017,** 32, 533–541. DOI:10.1016/j.nanoen.2016.12.063.

[9] Wang, C.; Wang, S.; He, Y.; Tang, L.; Han, C.; Yang, C.; Wagemaker, M; Li, B.; Yang, Q.; Kim, J.; Kang, F. Combining Fast Li-Ion Battery Cycling with Large Volumetric Energy Density: Grain Boundary Induced High Electronic and Ionic Conductivity in $Li_4Ti_5O_{12}$ Spheres of Densely Packed Nanocrystallites. *Chemistry of Materials*. **2013,** 27, 5647–5656. DOI:10.1021/acs.chemmater.5b02027

[10] Li, Y.; Chen, Q.; Meng, Q.; Lei, S.; Li, C.; Li, X.; Ma, J. One-Step Synthesis of a Nanosized Cubic Li_2TiO_3-Coated Br, C, and N Co-Doped $Li_4Ti_5O_{12}$ Anode Material for Stable High-Rate Lithium-Ion Batteries. *ACS Applied Materials & Interfaces*. **2019,** 11, 25804–25816. DOI: 10.1021/acsami.9b04041

[11] Dhaiveegan, P.; Peng, H.;Michalska, M.; Xiao, Y.; Lin, J.; Hseich, C. Investigation of carbon coating approach on electrochemical performance of $Li_4Ti_5O_{12}$/C composite anodes for high-rate

---

lithium-ion batteries. *Journal of Solid State Electrochemistry*. **2018,** 22, 1851–1861. DOI:10.1007/s10008-018-3886-2

[12] Ding, K.; Zhao, J.; Sun, Y.; Chen, Y.; Wei, B.; Zhang, Y.; Pan, J. Using potassium ferricyanide as a dopant to prepare K and Fe co-doped $Li_4Ti_5O_{12}$ *Ceramics International*. **2016,** 42, 19187–19194. DOI:10.1016/j.ceramint.2016.09.082

[13] Chen, C.; Guo, H.; Zhao, Z.; Li, S.; Jian, Z.; Luo, D.; Wang, Y. A robust strategy for engineering Li4Ti5O12 hollow micro-cube as superior rate anode for lithium-ion batteries. *Electrochimica Acta*. **2019,** 293, 141–148. DOI:10.1016/j.electacta.2018.09.201

[14] Macdowell, M.; Lee, S.W.; Nix, W.D.; Cui, Y. 25th Anniversary Article: Understanding the Lithiation of Silicon and Other Alloying Anodes for Lithium-Ion Batteries. *Advanced Materials.* **2013,** 25, 4966-4985. DOI: 10.1002/adma.201301795

[15] Schmerling, M.; Schwenzel, J.; Busse, M. Investigation of the degradation mechanisms of silicon thin film anodes for lithium-ion batteries. *Thin Solid Films*. **2018,** 655, 77-82. DOI:10.1016/j.tsf.2018.03.037

[16] Rezqita, A.; Kathribail, A.; Kahr, J.; Jahn, M. Layered oxide, graphite and silicon-graphite electrodes for Lithium-ion cells: Effect of electrolyte composition and cycling windows. *Journal of The Electrochemical Society*. **2019,** 166, (2019), DOI:10.1149/2.0671903jes

[17] Wei, Q.; Liu, G.; Zhang, C.; Hong, X.; Song, C.; Yang, Y.; Zhang, M.; Huang, W.; Cai, Y. Novel honeycomb silicon wrapped in reduced graphene oxide/CNT system as high-stability anodes for lithium-ion batteries. *Electrochimica Acta*. **2019,** 317, 583–593. DOI:10.1016/j.electacta.2019.06.024

[18] Wang, J.; Liao, L.; Lee, H.; Shi, F.; Huang, W.; Zhao, J.; Pei, A.; Tang, J.; Zheng, X.; Chen, W.; Cui, Y. Surface-engineered mesoporous silicon microparticles as high-Coulombic-efficiency anodes for lithium-ion batteries. *Nano Energy*. **2019,** 61, 404–410, DOI:10.1016/j.nanoen.2019.04.070

[19] Xu, W.; Wang, J.; Ding, F.; Chen, X.; Nasybulin, E.; Zhang, Y.; Zhang, J. Lithium metal anodes for rechargeable batteries. *Energy & Environmental Sciences.* **2014,** 7, 513–537 DOI: 10.1039/C3EE40795K

[20] Fang, C.; Wang, X.; Meng, S. Key Issues Hindering a Practical Lithium-Metal Anode. *Trends in Chemistry*. **2019,** 1, 152-158. doi: 10.1016/j.trechm.2019.02.015

[21] Thirumalraj, B.; Hagos, T.; Huang, C.; Teshager, M.; Cheng, J.; Su, W.; Hwang, B. Nucleation and Growth Mechanism of Lithium Metal Electroplating. *Journal of American Chemical Society.* **2019,** 141, 18612-18623. DOI: 10.1021/jacs.9b10195

[22] Chen, K.; Wood, K.; Kazyak, E.; LePage, W.S.; Davis, A.L.; Sanchez, A.J.; Dasgupta, N.P. Dead lithium: mass transport effects on voltage, capacity, and failure of lithium metal anodes. *Journal of Materials Chemistry A*. **2017,** 5, 11671-11681. DOI: 10.1039/C7TA00371D

[23] Liu, Y.; Lin, D.C.; Yuen, P.Y.; Liu, K.; Xie, J.; Dauskardt, R.H.; Cui, YAn Artificial Solid Electrolyte Interphase with High Li-Ion Conductivity, Mechanical Strength, and Flexibility for Stable Lithium Metal Anodes. *Advanced Materials*. **2017,** 29, 1605531 DOI: 10.1002/adma.201605531

[24] Tikekar, M.D.; Choudhury, S.; Tu, Z.; Archer, L.A. Design principles for electrolytes and interfaces for stable lithium-metal batteries. *Nature Energy*. **2016,** 1, 16114 DOI:10.1038/nenergy.2016.114

[25] Lu, Y.; Tu, Z.; Archer, L.A. Stable lithium electrodeposition in liquid and nanoporous solid electrolytes. *Nature Materials*. **2014,** 13, 961-969. DOI: 10.1038/nmat4041

---

[26] Lu, Y.; Xu, S.; Shu, J.; Aladat, W.I.A.; Archer, L.A. High voltage LIB cathodes enabled by salt-reinforced liquid electrolytes. *Electrochemistry Communications*. **2015,** 51, 23-26. doi: 10.1016/j.elecom.2014.11.010

[27] Lu, Y.; Tu, Z.; Shu, J.; Archer, L.A. Stable lithium electrodeposition in salt-reinforced electrolytes. *Journal of Power Sources*. **2015,** 279, 413-418, DOI: 10.1016/j.jpowsour.2015.01.030

[28] Mizuno, F.; Arthur, T.S.; Takechi, K. Water in Ionic Liquid for Electrochemical Li Cycling. *ACS Energy Letters.* **2016,** 1, 542-547. DOI: 10.1021/acsenergylett.6b00200

[29] Yang, C.; Zhang, L.; Liu, B.; Zu, S.; Hamann, T.; McOwen, D.; Dai, J.; Luo, W.; Wachsman, E.D.; Hu, L. Continuous plating/stripping behavior of solid-state lithium metal anode in a 3D ion-conductive framework. *Proceedings for the National Academy of Sciences*. **2018,** 115, 3770-3775. doi:10.1073/pnas.1719758115

[30] Lyu, P. ;Liu, X.; Qu, J.; Zhao, J.; Huo, Y.; Qu, Z.; Rao, Z. Recent Advances of thermal safety of lithium ion battery for energy storage. *Energy Storage Materials*. **2020**, 31, 195-220, doi:10.1016/j.ensm.2020.06.042

[31] Balakrishnan,, P.G.; Ramesh, R.; Kumar, T.P. Safety mechanisms in lithium-ion batteries. *Journal of Power Sources*. **2006**, 155, 401-414, doi:10.1016/j.jpowsour.2005.12.022

[32] Tobishima, S.; Yamaki, J. A consideration of lithium cell safety. *Journal of Power Sources.* **1999,** 81, 882-886, doi: 10/1016/S0378-7753(98)00240-7

[33] Liu, K.; Kiu, Y.; Lin, D.; Pei, A.; Ciu, Y. Materials for lithium-ion battery safety. *Science Advances*. **2018**, 4, doi:10.1126/sciadv.aas9820

[34] Feng, X.; Zheng, S.; Ren, D.; He, X.; Wang, L.; Cui, H.; Liu, X.; Jin, C.; Zhang, F.; Xu, C.; et. al. Investigating the thermal runaway mechanisms of lithium-ion batteries based on thermal analysis database. *Applied Energy.* **2019.** 246, 53-64, doi:10.1016/j.spenergy.2019.04.009

[35] Leising, R. A.; Palazzo, M.J.; Takeuchi, E. S.; Takeuchi, K.J. Abuse testing of lithium-ion batteries: Characterization of the overcharge reaction of $LiCoO_2$/ Graphite Cells. *Journal of the Electrochemical Society*. **2001.** 148, A838-A844, doi:10.1149/1.1379740

[36] Gao, Z.; Rao,, T.; Li, W.; Yang, X.; Chen, Y.; Zheng, Y.; Ding, Y.; Dong, T.; Li, S.; Design strategies of flame-ratrdant additives for lithium ion electrolyte. *Journal of Electrochemical Energy Conversion and Storage.* **2022.** 19, doi: 10.1115/1.4053968

[37] Hastie. J.W. Molecular basis of flame inhibition. *Journal of Research of the National Bureau of Standards- A Physics and Chemistry.* **1973,** 77, 733-754

[38] Walton, J.J.; Hiasa, T.; Kumita, H.; Takeshi, K. Sandford, G. Flurocyanoesters as additives for lithium-ion battery electrolytes, *ACS Applied Materials & Interfaces,* **2020,** 12, 15893-15902, doi:10.1021/acsami.9b23028

[39] Feng, J.; Lu, L. A novel bifunctional additives for safer lithium ion batteries, *Journal of Power Sources,* **2013,** 243, 29-32, doi:10.1016/j.jpowsour.2013.05.170

[40] Jin, Y.l Kneusels, N. H.; Magusin, P.C.M.M.; Kim, G.; Castillo-Martinez, E.; Marbella, L.E.; Kerber, R.N.; Howe, D.J.; Paula, S.; Grey, C.P. Identifying the structural basis for the increased stability of the solid electrolyte interphase formed on silicon with the additive fluorethylene carbonate. *Journal off the American Chemical Society,* **2017.** 139, 14992-15004, doi: 10.1021/jacs.7b06834

[41] Janssen, P.; Streipert, B.; Krafft, R.; Murmann, P.; Wagner, R.; Lewos-Alleye, L.; Roschenthaler, G.-V.; Winter, M.; Cekic-Laskovic, I. Shutdown potential adjustment of modified carbene adducts as additives for lithium ion battery electrolytes. *Journal of Power Sources.* **2017.** 367, 72-79, doi: 10.1016/j.jpowsour.2017.09.023

---

[42] Johnson, K. E. What's an ionic liquid? *The Electrochemical Society Interface.* **2007.** 16, 38-41, doi:10.1149/2.F04071F

[43] Eshetu, G.G.; Grugeon, S.; Laruelle, S.; Boyanov, S.; Lecocq, A.; Bertrand, J.-B.; Marlair, G. In-depth safety docused analysis of solvents used in electrolytes for large scale lithium ion batteries. *Physical Chemistry Chemical Physics*. **2013**, 23, 9145-9155, doi:10.1039/c3cp51315g

[44] MarcFarlan, D. R.; Tachikawa, N.; Forsyth, M.; Pringle, J. M.; Howlett, P. C.; Elliot, G.D.; Davis, J.H.; Watanabe, M.; Simon, P.; Angel, C.A. Energy applications of ionic liquids. *Energy and Environmental Science.* **2014,**7, 232-250, doi:10.1039/c3ee42099j

[45] Balduci, A. Ionic liquids in lithium ion batteries. *Topics in Current Chemistry.* **2017,** 20, doi:10.1007/s41061-017-0109-8

[46] Angell, C. Austen, Ansari, Y.; Zhao, Z. Ionic liquids: past, present, and future. *Faraday Discussions.* **2012.** 154, 9-27, doi: 10.1039/C1FD00112D

[47] Goodenough, J.B.; Youngsik, K. Challenges for Rechargeable Li Batteries. *Chemistry of Materials*. **2010,** 22, 587–603. DOI:10.1021/cm901452z

[48] Bohnke, O.; Bohnke, C.; Sid'Ahmed, J.; Crosnier-Lopez, M.P.; Duroy, H.; Le Berrre, F.; Fourquet, J.L. Lithium Ion Conductivity in New Perovskite Oxides $[Ag_yLi_{1-y}]_{3x}La_{2/3-x1/3-2x}TiO_3$ ($x = 0.09$ and $0 \leq y \leq 1$). *Chemistry of Materials*. **2001,** 13, 1593–1599. doi:10.1021/cm001207u

[49]Alpen, U.v. Li_3N: A promising Li ionic conductor. *Journal of Solid State Chemistry*. **1979,** 29, 379–392. doi:10.1016/0022-4596(79)90195-6

[50] Kanno, R. Synthesis of a new lithium ionic conductor, thio-LISICON–lithium germanium sulfide system. *Solid State Ionics*. **2000,** 130, 97–104. DOI:10.1016/s0167-2738(00)00277-0

[51] Badot, J.C.; Panabiere, E.; Emery, N.; Dubrunfaut, O.; Bach, S.; Pereira-Ramos, P.P. Percolation behaviors of ionic and electronic transfers in $Li_{3-2x}Co_xN$. *Physical Chemistry Chemical Physics*. **2019,** 21, 2790–2803. DOI:10.1039/c8cp06770h

[52] Fix, M.; Jesche, A.; Jantz, S.G.; Brauninger, S.A.; Klaus, H.; Manna, R.S.; Pietsch, I.M.; Hoppe, H.A.; Canfield, P.C. Ferromagnetism versus slow paramagnetic relaxation in Fe-doped. *Physical Review B*. **2018,** 97, 064419. doi: 10.1103/physrevb.97.064419

[53] Guiton, B.S.; Davies, P.K. Nano-chessboard superlattices formed by spontaneous phase separation in oxides. *Nature Materials*. **2007,** 6, 586–591. doi:10.1038/nmat1953

[54] Gao, X.; Fisher, C.A.J.; Ikuhara, Y.H.; Fujiwara, Y.; Kobayashi, S.; Moriwake, H.; Kuwabera, H.; Hosikawa, K.; Kohama, K.; Iba, H.; Ikuhara, Y. Cation ordering in A-site-deficient Li-ion conducting perovskites $La_{(1-x)/3}Li_xNbO_3$. *Journal of Materials Chemistry A*. **2015,** 3, 3351–3359. doi:10.1039/c4ta07040b

[55] Belous, A.; Pashkova, E.; Gavrilenko, O.; V'yunov, V.; Kovalenkoa, K. Solid electrolytes based on lithium-containing lanthanum metaniobates and metatantalates with defect-perovskite structure. *Ionics*. **2003,** 9, 21–27. DOI:10.1007/bf02376532

[56] Li, W.; Wu, G.; Araujo, C.M.; Scheider, R.H.; Blomqvist, A.; Ahuja, R.; Xiong, Z.; Feng, Y.; Chen, P. Li^+ ion conductivity and diffusion mechanism in α-Li_3N and β-Li_3N. *Energy & Environmental Science*. **2010,** 3, 1524. doi:10.1039/c0ee00052c

[57] Bates, J.B.; Dudney, N.J.; Gruzalski, G.R.; Zuhr, R.A.; Choudhury, A.; Luck, C.F.; Robertson, J.D. Electrical properties of amorphous lithium electrolyte thin films. *Solid State Ionics*. **1992,** 53-56, 647-654, doi: 0.1016/0167-2738(92)90442-R

[58] Suzuki, N.; Inaba, T.; Shiga, T. Electrochemical properties of LiPON films made from a mixed powder target of Li_3PO_4 and Li_2O. *Thin Solid Films*. **2012,** 520, 1821–1825. doi:10.1016/j.tsf.2011.08.107

---

[59] Bruce, P.G.; West, A.R. Ionic conductivity of LISICON solid solutions, $Li_{2+2x}Zn_{1-x}GeO_4$. *Journal of Solid State Chemistry*. **1982,** 44, 354–365. doi:10.1016/0022-4596(82)90383-8

[60] Bruce, P.G.; West, A.R. Ion trapping and its effect on the conductivity of LISICON and other solid electrolytes. *Journal of Solid State Chemistry*. **1982,** 53, 430–434. doi:10.1016/0022-4596(84)90122-1

[61] Macneil, J.H.; Massi, D.M.; Zhang, J.H.; Rosmus, K.A.; Brunetta, C.D.; Gentile, T.A.; Aitken, J.A. Synthesis, structure, physicochemical characterization and electronic structure of thio-lithium super ionic conductors, Li_4GeS_4 and Li_4SnS_4. *Journal of Alloys and Compounds*. **2014,** 586, 736–744. doi:10.1016/j.jallcom.2013.10.011

[62] Hartmann, P.; Leichtweiss, T.; Busche, M,; Schneider, M.; Reich, M.; Sann, J.; Adelhelm, P.; Janek, J. Degradation of NASICON-Type Materials in Contact with Lithium Metal: Formation of Mixed Conducting Interphases (MCI) on Solid Electrolytes. *The Journal of Physical Chemistry C*. **2013,** 117, 21064–21074. doi:10.1021/jp4051275

[63] Thangadurai, V.; Kaack, H.; Weppner, W.J.F. Novel Fast Lithium Ion Conduction in Garnet-Type $Li_5La_3M_2O_{12}$ (M = Nb, Ta). *Journal of the American Ceramic Society.* **2003,** 86, 437-440. doi: 10.1111/j.1151-2916.2003.tb03318.x

[64] Murugan, R.; Thangadurai, V.; Weppner, W. Fast Lithium Ion Conduction in Garnet-Type $Li_7La_3Zr_2O_{12}$. *Angewandte Chemie*. **2007,** 38, 7778-7781. doi:10.1002/chin.200750009

[65] Shin, D.O.; Oh, K.; Kim, K.M.; Park, K.; Lee, B.; Lee, Y.; Kang, K. Synergistic multi-doping effects on the Li7La3Zr2O12 solid electrolyte for fast lithium ion conduction. *Scientific Reports.* **2005,** 5,18053. doi: 10.1038/srep18053

[66]Ohta, S.; Kobyashi, T.; Assoka, T. High lithium ionic conductivity in the garnet-type oxide $Li_{7-X}La_3(Zr_{2-X}, Nb_X)O_{12}$ (X = 0–2). *Journal of Power Sources*. **2011,** 196, 3342–3345. doi:10.1016/j.jpowsour.2010.11.089

[67] Cussen, E.J. Structure and ionic conductivity in lithium garnets. *Journal of Materials Chemistry*. **2010,** 20, 5167.doi:10.1039/b925553b

[68] Nemori, H.; Matsuda, Y.; Matsui, M.; Yamamoto, O.; Takeda, T.; Imanshi, N. Relationship between lithium content and ionic conductivity in the $Li_{5+2x}La_3Nb_{2-x}Sc_xO_{12}$ system. *Solid State Ionics*. **2014,** 266, 9–12. doi:10.1016/j.ssi.2014.08.001

[69] Kotobuki, M.; Munakta, M.; Kanamura, K.; Sato, Y.; Yoshida, T. Compatibility of Li7La3Zr2O12 Solid Electrolyte to All-Solid-State Battery Using Li Metal Anode. *Journal of The Electrochemical Society*. **2010,** 157, doi:10.1149/1.3474232

[70] Reimers, J.N. Electrochemical and In Situ X-Ray Diffraction Studies of Lithium Intercalation in Li_xCoO_2 *Journal of The Electrochemical Society*. **1992,** 139, 2091, doi:10.1149/1.2221184

[71] Basch, A.; de Campo, L.; Albering, J.H.; White, J.W. Chemical delithiation and exfoliation of Li_xCoO_2. *Journal of Solid State Chemistry*. **2014,** 220, 102–110. doi:10.1016/j.jssc.2014.08.011

[72] Doeff, M. Batteries: Overview of Battery Cathodes. *SpringerReference*. **2011**, doi:10.1007/springerreference_308749.

[73] Laveda, J.V.; Low, J.; Pagani, F.; Stilp, E.; Dilger, S.; Baran, V.; Heere, M.; Battaglia, C. Stabilizing Capacity Retention in NMC811/Graphite Full Cells via TMSPi Electrolyte Additives. *ACS Applied Energy Materials.* **2019,** *2*, 7036-7044. doi: 10.1021/acsaem.9b00727

[74] Patoux, S.; Sannier, L.; Lignier, H.; Reynier, Y.; Bourbon, C.; Jouanneau, S.; Le Cras, F.; Martinet, S. High voltage nickel manganese spinel oxides for Li-ion batteries. *Electrochimica Acta*. **2008,** 53,4137-4145,DOI: 10.1016/j.electacta.2007.12.054

---

[75] Lai, Y.; Xu, M.; Zhan, Z.; Gao, C.; Wang, P.; Yu, Z. Optimized structure stability and electrochemical performance of $LiNi_{0.8}Co_{0.15}Al_{0.05}O_2$ by sputtering nanoscale ZnO film. *Journal of Power Sources*. **2016,** 309, 20–26. doi:10.1016/j.jpowsour.2016.01.079

[76] Li, W.; Ericksin, E. M., Manthiram, A. High-nickel layered cathodes for lithium-based automotive batteries. *Nature Energy.* **202**, 5, 26-34, doi:10.1038/s41560-019-0513-0

[77] Li, J.; Harlow, J.; Stakheiko, N.; Zhang, N.; Paulsen, J.; Dahn, J. Dependence of cell failure on cut-off voltage ranges and observation of kinetic hinderance in $LiNi_{0.8}Co_{0.15}Al_{0.05}O_2$. *Journal of Electrochemical Society.* **2018**, 165, A2682-A-2685, doi:10.1149/s.0491811jes

[78] Prager, Y.; Barkholtz, H.M.; Fresquez, A.; Campbell, D.L.; Juba, B. W.; Roman-Kustas, J.; Ferreira, S. R.; Chalamala, B.Degradation of commercial lithium-ion cells as a function of chemistry and cycling conditions, *Journal of the Electrochemistry*. **2020,** 167, 120532, doi:10.1149/1945

[79] Marker, K. Xu, C.; Grey, C.P. Operando NMC of NMC 811/graphite lithium-ion batteries: structure, dynamics, and lithium metal deposition. *Journal of the American Chemical Society.* **2020,** 142, 17447-17456, doi:10.1021/jacs.0c06727

[80] Li, J.; Ma , C.; Chi, M.; Liang, C.; Dudney, N.J. Solid Electrolyte: the Key for High-Voltage Lithium Batteries. *Adv Energy Mater.* **2015,** 5:1401408. doi: 10.1002/aenm.201401408

[81] Ding, Z.; Li, J.; Li, J.; An, C. Key Issue to Be Solved for All Solid-State Lithium Battery Technologies. *Journal of Electrochemical Society*. **2020,** 167, 079541, doi:10.1149/1945-7111/ab7f84

[82] Liu, Q.; Geng, Z.; Han, C.; Fu, Y.; Li, S.; He, Y.; Kang, F.; Li, B. Challenges and perspectives of garnet solid electrolytes for all solid-state lithium batteries. *Journal of Power Sources*. **2015,** 389(15) , 120–134. doi: 10.1016/j.jpowsour.2018.04.019

[83] Liu, C.; Rui, K.; Shen, C.; Badding, M.E.; Zhang, G.; Wen, Z. Reversible ion exchange and structural stability of garnet-type Nb-doped $Li_7La_3Zr_2O_{12}$ in water for applications in lithium batteries. *Journal of Power Sources*. **2015,** 282, 286–293. doi:10.1016/j.jpowsour.2015.02.050

[84] Wolfenstine, J.; Allen, J.L.; Read, J.; Sakamoto, J. Chemical stability of cubic Li7La3Zr2O12 with molten lithium at elevated temperature. *Journal of Materials Science*. **2013,** 48 (17), 5846–5851. doi:10.1007/s10853-013-7380-z

[85] Xu. S.; Hu, L. Towards a high-performance garnet-based solid-state Li metal battery: A perspective on recent advances. *Journal of Power Sources*. **2020,** 472, 228751 doi: 10.1016/j.jpowsour.2020.228571

[86] Hu, Y. Batteries: Getting solid. *Nature Energy*. **2016,** 1, 16042, doi:10.1038/nenergy.2016.42

[87] Ting, T.; Zhang, Y.; Chen, R.; Zhao, S.X.; Lin, Y.; Wen, C.; Shen, Y. Non-successive degradation in bulk-type all-solid-state lithium battery with rigid interfacial contact. *Electrochemistry Communications*. **2017,** 79, 1–4. doi:10.1016/j.elecom.2017.03.016

[88] Xiao, Y.; Wang, Y.; Bo, SH.;. Kim, J.C.; Miara, L.J.; Ceder, G. Understanding interface stability in solid-state batteries. *Nature Review Materials.* **2020,** 5, 105–126. doi: 10.1038/s41578-019-0157-5

[89] Ohta, S.; Seki, J.; Yagi, Y.; Kihira, Y.; Tani, T.; Asaoka, T. Co-sinterable lithium garnet-type oxide electrolyte with cathode for all-solid-state lithium ion battery. *Journal of Power Sources.* **2014,** 265, 40-44. doi: 10.1016/j.jpowsour.2014.04.065

[90] Ren, Y.; Liu, T.; Shen, Y.; Lin, Y.; Nen, C. Chemical compatibility between garnet-like solid state electrolyte $Li_{6.75}La_3Zr_{1.75}Ta_{0.25}O_{12}$ and major commercial lithium battery cathode materials. *Journal of* Materiomics. **2016,** 2, 256-264. doi: 10.1016/j.jmat.2016.04.003

[91] Carmichael, R.S. *Practical Handbook of Physical Properties of Rocks and Minerals,* (1989)

---

[92] Lee, B.; Chu, C.T.; Krajewski, M.; Michalska, M.; Lin, J. Temperature-controlled synthesis of spinel lithium nickel manganese oxide cathode materials for lithium-ion batteries. *Ceramics International.* **2020,** 45, 20856-20864, doi: 10.1016/j.ceramint.2020.05.124

[93] Xiao, Y.; Fan, J.; Zhang, X.; Zhang, D.; Chang, C. Li2Ni0.5Mn1.5O4, spinel type cathode material with high reversible capacity. *Electrochimica Acta*. **2019,** 311(1), 170–177. doi:10.1016/j.electacta.2019.04.162

[94] Gummow, R.J.; Kock, A.; Thackery, M.M. Improved capacity retention in rechargeable 4 V lithium/lithium-manganese oxide (spinel) cells. *Solid State Ionics*. **1994,** 69, 59–67. doi:10.1016/0167-2738(94)90450-2

[95] Lu, J.; Less, K.S. Spinel cathodes for advanced lithium ion batteries: a review of challenges and recent progress. *Materials Technology*. **2016,** 31, 628-641. doi: 10.1080/10667857.2016.1208957

[96] Hagh, N.M; Amatucci, G.G. Effect of cation and anion doping on microstructure and electrochemical properties of the $LiMn_{1.5}Ni_{0.5}O_{4-\delta}$ spinel. *Journal of Power Sources*. **2014,** 256, 457–469. doi:10.1016/j.jpowsour.2013.12.135

[97] Shin, Y.; Manthiram. A. Influence of the Lattice Parameter Difference between the Two Cubic Phases Formed in the 4 V Region on the Capacity Fading of Spinel Manganese Oxides. *Chemistry of Materials*. **2003,** 15, 2954–2961. doi:10.1021/cm0341787

[98] Oh, S.H.; Jeon, S.H.; Coo, W.; Kim, C.S.; Cho, B.W. Synthesis and characterization of the metal-doped high-voltage spinel $LiNi_{0.5}Mn_{1.5}O_4$ by mechanochemical process. *Journal of Alloys and Compounds*. **2008,** 452, 389–396. doi:10.1016/j.jallcom.2006.10.153

[99] Song, J.; Shin, D.W.; Lu, Y.; Amos, C.D.; Manthiram, A.; Goodenough, J.B. Role of Oxygen Vacancies on the Performance of $Li[Ni_{0.5-x}Mn_{1.5+x}]O_4$ (x = 0, 0.05, and 0.08) Spinel Cathodes for Lithium-Ion Batteries. *Chemistry of Materials.* **2014,** *24*, 3101-3109. doi: 10.1021/cm301825h

[100] Kunduraci, M.; Amatucci, G.G. The effect of particle size and morphology on the rate capability of 4.7 V $LiMn_{1.5+\delta}Ni_{0.5-\delta}O_4$ spinel lithium-ion battery cathodes. *Electrochimica Acta*. **2008,** 53, 4193–4199. doi:10.1016/j.electacta.2007.12.057

[101] Wan, L.; Deng, Y.; Yang, C.; Xu, H.; Qin, X.; Chen, G. Ni/Mn ratio and morphology-dependent crystallographic facet structure and electrochemical properties of the high-voltage spinel $LiNi_{0.5}Mn_{1.5}O_4$ cathode material. *RSC Advances*. **2015,** 5, 25988–25997. doi:10.1039/c5ra03602j

[102] Liu, D.; Zhu, W.; Gagnon, C.; Barray, F.; Guefi, A.; Mauger, A.; Groult, H.; Julien, C.M; Goodenough, J.B.; Zaghib, K. Spinel materials for high-voltage cathodes in Li-ion batteries. *RSC Advances*. **2014,** 4, 154–167. doi:10.1039/c3ra45706k

[103] Dai, J.; Zhou, L.; Han, X.; Carter, M.; Hu, L. Improving the High-Voltage $Li_2FeMn_3O_8$ Cathode by Chlorine Doping. *ACS Applied Materials & Interfaces*. **2016,** *8*, 10820-10825. doi: 10.1021/acsami.6b00288

[104] Kong, F.; Liang, C.; Longo, R.C.; Yeon, D.; Zheng, Y.; Park, J.; Doo, D.; Cho, K. Conflicting Roles of Anion Doping on the Electrochemical Performance of Li-Ion Battery Cathode Materials. *Chemistry of Materials.* **2018,** *28*, 6942-6952. doi: 10.1021/acs.chemmater.6b02627

[105] ThBolek, K. "The Effect of Excess Lithium on the Phase Formation, Structure and Electrical Properties of LLZO Garnet Structured Solid-State Electrolyte" **2020**, All Theses. 3405. https://tigerprints.clemson.edu/all_theses/3405

[106] Miara, L.; Windmüller, A.; Tsai, C.; Richards, W.D.; Ma, Q.; Uhlenbruck, S.; Guillon, O.; Ceder, G. About the Compatibility between High Voltage Spinel Cathode Materials and Solid

---

Oxide Electrolytes as a Function of Temperature. *ACS Applied Materials & Interfaces.* **2016,** *8*, 26842-26850 doi: 10.1021/acsami.6b09059

[107] Brewer, L.; Margrav J. The Vapor Pressures of Lithium and Sodium Oxides. *The Journal of Physical Chemistry,* **1955,** *59* (5), 421-425. doi: 10.1021/j150527a010

[108] Cohn, G. Reactions in the Solid State. *Chemical Reviews.* **1948,** *42*, 527-579. doi: 10.1021/cr60133a002

[109] Huang, M; Liu, T.; Deng, Y.; Geng, H.; Shen, Y.; Lin, Y.; Nan, C. Effect of sintering temperature on structure and ionic conductivity of $Li_{7-x}La_3Zr_2O_{12-0.5x}$ ($x = 0.5 \sim 0.7$) ceramics. *Solid State Ionics.* **2011,** 204-205, 41-45. doi: 10.1016/j.ssi.2011.10.003

[110] Sintering. (n.d.). Retrieved February 19, 2021, from https://www.sciencedirect.com/topics/engineering/sintering

[111] Jow, R.T.; Delp, S.A.; Allen, J.L.; Jones, J.P.; Smart, M.C. Factors Limiting Li + Charge Transfer Kinetics in Li-Ion Batteries. *Journal of The Electrochemical Society*. **2018,** 165, A361. doi:10.1149/2.1221802jes

[112] Jow, T. R., Delp, S. A., Allen, J. L., Jones, J., & Smart, M. C. (2018). Factors limiting Li+ chage transfer kinetics in lithium-ion batteries in innovations in army energy and power materials. In *Innovations in army energy and power materials technologies* (pp. 84-98). MILLERSVILLE: MATERIALS Science FORUM.

[113] Jow, T.R.; Marx, M.B.; Allen, J.L. Distinguishing Li+ Charge Transfer Kinetics at NCA/Electrolyte and Graphite/Electrolyte Interfaces, and NCA/Electrolyte and LFP/Electrolyte Interfaces in Li-Ion Cells. *Journal of The Electrochemical Society*. **2012,** 159, A604. doi:10.1149/2.079205jes

[114] Nakayama, N.; Nozawa, T.; Iriyama, Y.; Abe, T.; Ogumi, Z.; Kikuchi, K. Interfacial lithium-ion transfer at the $LiMn_2O_4$ thin film electrode/aqueous solution interface. *Journal of Power Sources*. **2007,** 174, 695–700. doi:10.1016/j.jpowsour.2007.06.113

[115] Chen, L.; X. Quo, Z. Bai, L. Fan, *Journal of Energy Chemistry,* 52, 210-217, (2020)., doi: 10.1016/j.jechem.2020.03.052

[116] Kim, A.;Woo, S.; Kang, M.; Park, H.; Kang, B. Research Progresses of Garnet-Type Solid Electrolytes for Developing All-Solid-State Li Batteries. *Frontiers in Chemistry.* **2020,** 8, 468. doi: 10.3389/fchem.2020.00468

[117] Zhang, Y.; Luo, D.; Luo, W.; Du, S.; Deng, Y.; Deng, J. High-purity and high-density cubic phase of Li7La3Zr2O12 solid electrolytes by controlling surface/volume ratio and sintering pressure. *Electrochemica Acta.* **2020,** 359, 136965, doi: 10.1016/j.electacta.2020.136965

[118] Dimesso, L.; Pechini Processes: An Alternate Approach of the Sol–Gel Method, Preparation, Properties, and Applications. In: Klein L., Aparicio M., Jitianu A. (eds) Handbook of Sol-Gel Science and Technology. Springer, Cham. (2016) doi: 10.1007/978-3-319-19454-7_123-1

[119] Selbach, S.M.; Einarsrud, M.-A.; Tybell, T.; Grande, T. Synthesis of BiFeO3 by Wet Chemical Methods. *Journal of the American Ceramic Society*. **2007,** 90: 3430-3434. doi: 10.1111/j.1551-2916.2007.01937.x

[120] Dinnebier, R. E.; Billinge, S.J.L. *Powder Diffraction: Theory and Practice*. Royal Society of Chemistry, 2015.

[121] Nave, R. “Bragg's Law.” *Bragg's Law*, 2000, hyperphysics.phy-astr.gsu.edu/hbase/quantum/bragg.html.

[122] Will, G.. *Powder Diffraction: the Rietveld Method and the Two Stage Method to Determine and Refine Crystal Structures from Powder Diffraction Data*. Springer, 2011.

---

[123] Marguí Eva, and R. van. Grieken. *X-Ray Fluorescence Spectrometry and Related Techniques: An Introduction*. Momentum Press, LLC, 2013.

[124] "What Is X-Ray Fluorescence Spectroscopy (XRF)." *HORIBA*, www.horiba.com/scientific/products/x-ray-fluorescence-analysis/tutorial/x-ray-fluorescence-the-basic-process/.

[125] Quinzeni, I.; Capsoni, D.; Berbenni, V.; Mustarelli, P.; Sturini, M.; Bini, M. Stability of low-temperature Li7La3Zr2O12 cubic phase: The role of temperature and atmosphere. *Materials Chemistry and Physics*. **2017,** 185, 55–64. doi:10.1016/j.matchemphys.2016.10.004

[126] Thomas, Robert. *Practical Guide to ICP-MS: a Tutorial for Beginners*. CRC Press, 2013.

[127] Mahaffy, P. "Mass Spectrometer: The Detector." *NASA*, NASA, attic.gsfc.nasa.gov/huygensgcms/MS_Detector_1.htm.

[128] Vandenabeele, P. *Practical Raman Spectroscopy: an Introduction*. Wiley, 2013

[129] "What Is Raman Spectroscopy?" *HORIBA*, www.horiba.com/en_en/raman-imaging-and-spectroscopy/.

[130] Goldstein, J. I., Newbury, D. E., Echlin, P., Joy, D. C., Lyman, C. E., Lifshin, E., Michael, J. R. (2003). *Scanning Electron Microscopy and X-ray Microanalysis: Third Edition*. Boston, MA: Springer US.

[131] Scanning Electron Microscopy. (n.d.). Retrieved April 24, 2020, from https://www.nanoscience.com/techniques/scanning-electron-microscopy/

[132] *SEM Scanning Electron Microscope A to Z: Basic Knowledge for using the SEM*. (n.d.). JEOL. Retrieved from https://www.jeol.co.jp/en/applications/pdf/sm/sem_atoz_all.pdf

[133] Napchan, E. Backscattered Electrons in the SEM. *Microscopy and Analysis*. **2001**

[134] Kersten, K. (2018, June 14). SEM working principle: The detection of backscattered electrons. Retrieved April 24, 2020, from https://blog.phenom-world.com/backscattered-electrons-sem

[135] Yale University. (n.d.). Retrieved April 24, 2020, from https://ywcmatsci.yale.edu/edx-principle

[136] Hughes, S.W. *Physics Education, 40*, 468-474. (2005). doi:10.1088/0031-9120/40/5/008

[137] Basics of Electrochemical Impedance Spectroscopy. (n.d.). Retrieved April 24, 2020, from https://www.gamry.com/application-notes/EIS/basics-of-electrochemical-impedance-spectroscopy/

Chapter 2 References

[138] Shionuma, K.; Yokokawa, M.; Nagaura, T. Characteristics of lithium-ion rechargeable battery. *Proc. Abstracts 32nd Battery Symp.* **1991**, 1, 33-34.

---

[139] Inaguma, Y.; Liquan C.; Itoh M.; Nakamura, T.; Uchida, T.; Ikuta, H.; Wakihara, M. High ionic conductivity in lithium lanthanum titanate. *Solid State Commun.* **1993**, 86, 689-93. doi: 10.1016/0038-1098(93)90841-A

[140] Ming'en, L.; Zhu, X.; Jiang, Y.; Zhu, J. Comparative study of solid-state reaction and sol-gel process for synthesis of Zr-doped $Li_{0.5}La_{0.5}TiO_3$ solid electrolytes. *Ionics.* **1996**, 22, 2151-2156. doi: 10.1007/s11581-016-1744-8

[141] Slater, P.R.; Greaves, C. Synthesis and conductivities of sulfate/selenate phases related to nasicon: $Na_xM(III)_{2-x}(SO_4)_{3-y}(SeO_4)_y$. *J Solid State Chem.* **1993**, 107, 12-18. doi:10.1006/jssc.1993.1317

[142] Aono, H.; Sugimoto, E.; Sadaoka, Y.; Imanaka, N.; Adachi, G.-y. Ionic conductivity of solid electrolytes based on lithium titanium phosphate. *J. Electrochem. Soc.* **1990**, 137, 1023–1027. doi:10.1149/1.2086597

[143] Arbi, K.; Mandal, S.; Rojo, J.M.; Sanz, J. Dependence of Ionic Conductivity on Composition of Fast Ionic Conductors $Li_{1+x}Ti_{2-x}Al_x(PO_4)_3$, $0 \leq x \leq 0.7$. A Parallel NMR and Electric Impedance Study. *Chem. Mater.* **1990**, 14, 1091-1097. doi: 10.1021/cm010528i

[144] Kanno, R. Synthesis of a new lithium ionic conductor, thio-LISICON–lithium germanium sulfide system. *Solid State Ion.* **2000**, 130, 97-104. doi:10.1016/S0167-2738(00)00277-0

[145] Feng Jk. Lu L.Lai Mo. Lithium storage capability of lithium ion conductor $Li_{1.5}Al_{0.5}Ge_{1.5}(PO_4)_3$. *J. Alloys and Compd.* **2010**, 501, 255-258. doi:10.1016/j.jallcom.2010.04.084

[146] Thangadurai, V.; Weppner, W. $Li_6ALa_2Ta_2O_{12}$ (A = Sr, Ba): Novel Garnet-Like Oxides for Fast Lithium Ion Conduction. *Adv. Funct. Mater.* **2005**, 15, 107-112. doi:10.1002/adfm.200400044

[147] Ohta, S.; Kobayashi, T.; Asaoka, T. High lithium ionic conductivity in the garnet-type oxide $Li_{7-X}\,La_3(Zr_{2-X}, Nb_X)O_{12}$ (X = 0-2). *J. Power Sources.* **2011**, 196, 3342-3345. doi: 10.1016/j.jpowsour.2010.11.089

[148] Murugan, R.; Thangadurai, V.; Weppner, W. Fast Lithium Ion Conduction in Garnet-Type $Li_7La_3Zr_2O_{12}$. *Angew. Chem Int. Ed. Engl..* **2011**, 46, 7778-7781. doi:10.1002/anie.200701144

[149] Xie, H.; Alonso, J.A.; Li, Y.; Fernández-Díaz, M.T.; Goodenough, J.B. Lithium Distribution in Aluminum-Free Cubic $Li_7La_3Zr_2O_{12}$. *Chem. Mater.* **2011**, 23, 3587–3589. doi: 10.1021/cm201671k

[150] Kumazaki, S.; Iriyama, Y.; Kim, K.-H.; Murugan, R.; Tanabe, K.; Yamamoto, K.; Hirayama, T.; Ogumi, Z. High lithium ion conductive $Li_7La_3Zr_2O_{12}$ by inclusion of both Al and Si. *Electrochem. Commun.* **2011**, 13, l 509-512. doi:10.1016/j.elecom.2011.02.035

[151] Xia, W.; Xu, B.; Duan, H.; Guo, Y.; Kang, H.; Li, H.; Liu, H. Ionic Conductivity and Air Stability of Al-Doped $Li_7La_3Zr_2O_{12}$ Sintered in Alumina and Pt Crucibles. *ACS Appl. Mater. Interfaces.* **2016**, 8, 5335-3542. doi: 10.1021/acsami.5b12186

[152] Narayanan, S.; Hitz, G.T.; Wachsman, E.D.; Thangadurai, V. Effect of Excess Li on the Structural and Electrical Properties of Garnet-Type Li6La3Ta1.5Y0.5O12. *Journal of the Electrochemical Society*. **2015**, 162, A1772. doi:10.1149/2.0321509jes.

[153] Aono, H.; Sugimoto, E.; Sadaoka, Y.; Imanak Adachi, N. G.-y. The Electrical Properties of Ceramic Electrolytes for $LiM_xTi_{2-x}(PO_4)_3$+yLi_2O, M=Ge,Sn,Hf, and Zr Systems. *J. Electrochem. Soc*. **1993**, 140, 1827-1833. doi:10.1149/1.2220723

[154] Liu K. Ma JT. Wang CA. Excess lithium salt functions more than compensating for lithium loss when synthesizing $Li_{6.5}La_3Ta_{0.5}Zr_{1.5}O_{12}$ in alumina crucible. *J. Power Sources*. **2014**, 260, 109-114. doi: 10.1016/j.jpowsour.2014.02.065

[155] Jin, Y.; Mcginn, P.J. Al-doped $Li_7La_3Zr_2O_{12}$ synthesized by a polymerized complex method.

J. Power Sources. **2011**, 196(20), 8683-8687. doi:/10.1016/j.jpowsour.2011.05.065

[156] Skokan, A. PHASE STABILITY INVESTIGATIONS IN THE CERAMIC BREEDER SYSTEMS Li_2O-Al_2O_3 and Li_2O-ZrO_2. *Fus. Technol.* **1991**, 772-776. doi:10.1016/B978-0-444-88508-1.50139-0.

[157] Navarro, R.; Carolina, N.; Miura, A.; Higuchi, M.; Tadanaga, K. Optimization of Al_2O_3 and Li_3BO_3 Content as Sintering Additives of $Li_{7-x}La_{2.95}Ca_{0.05}ZrTaO_{12}$ at Low Temperature. *Journal of Electronic Materials*. **2016**, 46, 497-501. doi: 10.1007/s11664-016-4924-4

[158] Kulkarni, N.S.; Besmann, T.M.; Spear, K.E. Thermodynamic Optimization of Lithia–Alumina. *J. Am. Ceram. Soc.* **2008**, 91, 4074-083. doi: 10.1111/j.1551-2916.2008.02753.x

[159] Kudo, H.; Wuo, C.H.; Ihle, H.R. The effect of radiation upon diffusion in metals. *J. Nucl. Mater*. **1978**, 78, 380-389. doi:10.1016/0022-3115(78)

[160] Kontoyannis, C.G.; Vagenas, N.V. Calcium carbonate phase analysis using XRD and FT-Raman spectroscopy. Analyst. **2020**, 125, 251-255. doi:10.1039/A9086091

[161] Li,Y.Q.; Wang, Z.; Li, C.L.; Cao, Y. Guom, X.X. Densification and ionic-conduction improvement of lithium garnet solid electrolytes by flowing oxygen sintering. *J. Power Sources*. **2014**, 248, 642–646. doi:10.1016/j.jpowsour.2013.09.140

[162] Fu., Z.; McOwen, D.; Zhang, L.; Gong, Y.; Ren, Y.; Gritton, J.E.; Godbey, G.; Dai, J.; Hu, L. Wachsman, E.D. Predicting the flexural strength of Li-ion-conducting garnet type oxide for solid-state-batteries. *J. Am. Ceram. Soc.* **2020**, 103, 5186-5195. doi:10.1111/jace.17177

[163] Ji, Y.; Zhou, C.; Lin, F.; Li, B.; Yang, F.; Zhu, H.; Duan, J.; Chen, Z. Submicron-Sized Nb-Doped Lithium Garnet for High Ionic Conductivity Solid Electrolyte and Performance of Quasi-Solid-State Lithium Battery. *Materials*. **2020**, 13, 560. doi:10.3390/ma13030560

[164] Yamamoto, O.; Ohira, T.; Alvarez, K.; Fukuda, M. Antibacterial characteristics of $CaCO_3$-MgO composites *Mater. Sci. Eng. B*. **2010**, 173, 208-212. doi:10.1016/j.mseb.2009.12.007

[165] Zhao, L.; Liu, P.; Sun, G.; Fu, Z. Nanopowders preparation and dielectric properties of low-fired $Li_3Mg_2NbO_6$ ceramics *J. Mater. Sci. Mater. Electron*. **2018**, 29, 5873-5877. doi:10.1007/s10854-018-8559-5

[166] Jiang, Y.; Zhou, Y.; Hu, Z.; Juang, Y.; Zhu, X. MgO or Al_2O_3 crucible: Which is better for the preparation of LLZ-based solid electrolytes? *Ceram. Int*. **2020**, 46, 3367-3373. doi:10.1016/j.ceranubt.2019.10.046

[167] Larraz, G.; Orera, A.; Sanjuán, M.L. Cubic phases of garnet-type $Li_7La_3Zr_2O_{12}$: the role of hydration. *J. Mater. Chem. A*. **2013**, *1*, 11419-11428. doi:10.1039/c3ta11996c

[168] Hubaud, A.A.; Schroeder, D.J.; Kay, B.; Ingram, B.; Dogan, F.; Vaughey, J.T. Low temperature stabilization of cubic $(Li_{7-x}Al_{x/3})La_3Zr_2O_{12}$: role of aluminum during formation. *J. Mater. Chem. A*. **2013**, 1, 8813-8818. doi:10.1039/C3TA11338H

[169] Shannon, R.D. Revised effective ionic radii and systematic studies of interatomic distances in halides and chalcogenides. *Acta Crystallogr.* **1976**, A32, 751-761. doi:10.1107/S0567739476001551

[170] Hubaud, AA.; Schroeder, D.J.; Ingram, B.J.; Okasinski, J.S.; Vaughey, J.T. Thermal expansion in the garnet-type solid electrolyte $(Li_{7-x}Al_{x/3})La_3Zr_2O_{12}$ as a function of Al content. *J. Alloys Compd.* **2015**, 644, 804-807. doi:10.1016/j.jallcom.2015.05.067

[171] Huang, X.; Luo, Y.; Song, Z.; Xiu, T.; Badding, M. E.; Wen, Z. Preparation of dense Ta-LLZO/MgO composite Li-ion solid electrolyte: Sintering, microstructure, performance and the role of MgO. *J. Energy Chem*. **2019**, 39, 8-16. doi:10.1016/j.echem.2019.01.013

---

[172] Murugan, R.; Thangadurai, V.; Weppner, W. Effect of lithium ion content on the lithium ion conductivity of the garnet-like structure $Li_{5+x}BaLa_2TaO_{11.5+0.5x}$ (x=0-2) *Appl. Phys. A.* **2000**, 91, 615-620. Doi:10.1007/s00339-008-4494-2

[173] Huang, Z.; Chen, L.; Huang, B.; Xu, B.; Shao, G.; Wang, H.; Li, Y. Wang, C. Enhanced Performance of $Li_{6.4}La_3Zr_{1.4}Ta_{0.6}O_{12}$ Solid Electrolyte by the Regulation of Grain and Grain Boundary Phases. *ACS Appl. Mater. Interfaces*. **2020**, 12, 56118-56125. doi:10.1021/acsami.0c18674

[174] Wang, Y.; Yan, P.; Xiao, J.; Zhang, J.; Sprenkle, VL. Effect of Al_2O_3 on the sintering of garnet-type $Li_{6.5}La_3Zr_{1.5}Ta_{0.5}O_{12}$. *Solid State Ion.* **2016**, 294, 108-115. doi:10.1016/j.ssi.2016.06.013

[175] Fleig J. The grain boundary impedance of random microstructures: numerical simulations and implications for the analysis of experimental data. *Solid State Ion.* **2002**, 150, 181-193. doi:10.1016/S0167-2738(02)00274-6

[176] Irvine JTS. Sinclair DC. West AR. Electroceramics: Characterization by Impedance Spectroscopy. *Adv. Mater.* **1990***,* 2, 132-138. doi:10.1002/adma.1990020304

[177] Pesci F.; Bertei A.; Brugge R.H.; Emge S. P.; Hekselman A.K. O.; Marbella, L.E.; Grey C. G.; Aguadero A. Establishing Ultralow Activation Energies for Lithium Transport in Garnet Electrolytes. *ACS Appl. Mater. Interfaces.* **2020,** 12, 32806-32816, doi:10.1021/acsami.0c08605

[178] Wan T.H.; Saccoccio M.; Chen C.; Ciucci F. Influence of discretization methods on the distribution of relaxation times deconvolution:implements radial basis functions with DRTools. *Electrochim. Acta.* **2015**, 184, 483-499. doi: 10.1016/j.electacta.2015.09.097

[179] Zhuang L.; Huang X.; Lu Y.;Tang J.; Zhou Y.; Ao X.; Yang Y.; Tian B. Phase transformation and grain-boundary segregation in Al-doped $Li_7La_3Zr_2O1_2$ ceramics. *Ceram. Int.* **2021,** 47, 22768-22775. doi:10.1016/j.ceramint.2021.04.0295

[180] Percival J. ; Kendrick E.; Smith R.I.; Slater P.R. Cation ordering in Li containing garnets:synthesis and structural characterization of the tetragonal system, $Li_7La_3Sn_2O_{12}$. *Dalton Trans.* **2009,** 26, 5177-5181. doi:10.1039/B907331K

[181] Zheng H.; Li G.; Liu J.; Wu S.; Zhang X.; Wu S.; Zhu H.; Liu H.; Duan H. A rational design of garnet-type $Li_7La_3Zr_2O_{12}$ with ultrahigh moisture stability. *Energy Stor. Mater.* **2022,** 49, 278-290, doi: 10.1016/j.ensm.2022.04.027

[182] Hahn M.; Rosenbach D.; Krimalowski A.; Nazarenus T.; Moos R.; Thelakkat M.; Danzer M.A. Investigating solid polymer and ceramic electrrolytes for lithium-ion batteries by means of an extended Distribution of Relaxation Times analysis. *Electrochim. Acta*. **2020,** 344, 136060. doi:10.1016/j.electacta.2020.136060

[183] El-Shinawai, H.; Cussen. E. J.; Corr, S. A. Enhancement of the lithium ion conductivity of Ta-doped $Li_7La_3Zr_2O_{12}$ by incorporation of calcium. *Dalton Trans.* **2017**, 46, 9415-9419. doi: 10.1039/C7DT01573A

[184] Luo, Y.; Feng, W.; Meng, Z.; Wang, Y.; Jiang, X.; Xue, Z. Interface modification in solid-state lithium batteries based on garnet-type electrolytes with high ionic conductivity. *Electrochim. Acta.* **2021**, 397, 139285. doi:10.1016/j.electacta.2021.139285

[185] Huang, X.; Lu, Y.; Guo, H.; Song, Z.; Xiu, T.; Badding, M.E.; Wen, Z. None-Mother-Powder Method to Prepare Dense Li-Garnet Solid Electrolytes with High Critical Current Density. *ACS Appl. Energy Mater.* **2018**, 1,5355-5365. Doi:10.1021/acsaem.8b00976

Chapter 3 References

[186] C. Yang, L. Zhang, B. Liu, S. Xu, T. Hamann, D.W. McOwen, J. Dai, W. Luo, Y. Gong, et. al. *Proc. Natl. Acad. Sci. U.S.A.,* **115**, 3770-3775 (2018).

---

[187] B. Ramkuma, K. So-young, N. Chan-woo, V. Aravindan, L. Yun-Sung, *Electochem. Acta.,* **359**, 136955 (2020).

[188] H. Gao, Q. Wu, Y. Hu, J.P. Zheng, K. Amine, Z. Chen, *J. Phys. Chem. Lett.,* **9**, 5100-5104 (2018).

[189] R. Chen, Y. Zhang, T. Liu, B. Xu, Y. Shen, L. Li, Y. Lin, C. Nan, *Solid State Ion*. **310**, 44-49 (2017)

[190] G. Hitz, D.W. McOwen, L. Zhang, Z. Ma, Z. Fu, Y. Wen, Y. Gong, J. Dai, T.R. Hamann, L. Hu, E.D. Wachsman, *Mater. Today*., **22,** 50-57 (2020).

[191] Q. Liu, Z. Geng, C. Han, Y. Fu, S. Li, Y. He, F. Kang, B. Li, *Journal of Power Sources*., **389**, 120–134 (2018).

[192] C. Liu, K. Rui, M.E. Badding, G. Zhang, Z. Wen, *J. Power Sources*, **282**, 286–293 (2015).

[193] Y.S. Hu. *Nat. Energy*. ,**1**, 16042 (2016). Doi:10.1038/energy.2016.42

[194] J. Kim, M. Eom, S. Noh, D. Shin, *J. Power Sources*. , **244**, 476–481 (2013).

[195] D. Hlushkou, A.E. Reising, Ni. Kaiser, S. Spannenberger, S. Schlabach, Y. Kato B. Roling, U. Tallarek, *J.Power Sources*. **396**, 363-370 (2018).

[196] X. Yang, Q. Sun, C. Zhao, X. Gao, K.R. Adair, Y. Liu, J. Luo, X. Lin, J. Liang, H. Huang, L. Zhang, R,.Yang, S. Lu, R. Li, X. Sun, *Nano Energy*., **61**, 567–575 (2019).

[197] T. Yamaguchi, H. Shimada, U. Honda, H. Kishimoto, T. Ishiyama, K. Hamamoto, H. Sumi, T. Suzuki, Y. Fujishiro, *Solid State Ion*. **288**, 347–350 (2016).

[198] D. Han, K. Shinoda, S. Tsukimoto, H. Takeuchi, C. Hiriawa, M. Majima, T. Uda. J. Mat. Chem. A., 2, 12552 (2014).

[199] J. Tong, D. Clark, M. Hoban, R. O'Hayre, C*Solid State Ion*., **181**, 496–503 (2010).

[200] S. Harboe, P. Lupetin, O. Guillon, N. Menzler, *J. Eur. Ceram. Soc.,* **40**, 3618-3631 (2020).

[201] M. Finsterbusch, T. Danner, C. Tsia, S. Uhlenbruck, A. Latz, O. Gullion O. *ACS App. Mat. Interfaces*. **10**, 22329–22339 (2018).

[202] J. Wakasugi, H. Munakata, K. Kanmura. *Electrochem*. **85**, 77–81 (2017).

[203] S. Uhlenbruck, J. Dornseiffer, S. Lobe. C. Dellen, C. Tsia, B. Gotzen, D. Sebold, M. Finsterbusch, O. Guillon, *J. Electroceramics*. **8**, 197–206 (2017).

[204] Y. Zhu, X. He, Y. Mo, *ACS Appl. Mater. Interface.* **7**, 23685-23693 (2015).

[205] A. M. Nolan, E.D. Wachsman, Y. Mo, *Energy Stor. Mater*. **41**, 571-580 (2021).

[206] G. Vardar, W.J. Bowman; Q. Lu, J. Wang, R.J. Chater, A. Aguadero, R. Seibert, J. Terry, A. Hunt, I. Waluyo, D. Fong, A. Jarry, E. Crumlin, H. Hellstron, Y. Chiang, B. Yildiz, *Chem. Materials*. **30**, 6259–6276 (2018).

[207] S. Ohta, J. Seki, Y. Yagi, Y. Kihira, T. Tani, T. Asaoka, *J. of Power Sources*., **265**, 40–44 (2014).

[208] F. Han, J. Yue, C. Chen, N. Zhao, X. Fan, Z. Ma, T. Gao, F. Wang, X. Guo, C. Wang, *Joule*. **2**, 497–508 (2018).

[209] Y. Ren, T. Liu, Y. Shen, Y. Lin, C.W. Nan, *J. Materiomics*. **2**, 256–264 (2016).

[210] K.H. Kim, Y. Iriyama, K. Yamamoto, S. Kumazaki, T. Asaka, K. Tanbe, C. Fisher, T. Hirayama, R. Murugan, Z. Oguami, *J. Power Sources*. **196**, 764–767 (2011).

[211] K. Park, B.C. Yu , J.W. Jung, Y. Li, W. Zhou, H. Gao, H. Son, J.B. Goodenough, *Chem. Mater.* **28**, 8051–8059 (2016).

[212] D. Wang, Q. Sun, J. Luo, J. Liang, Y. Sun, R. Li , K. Adair, L. Zhang, R. Yang, S. Lu, H. Huang, X. Sun, *ACS Appl. Mater. Interfaces*. , **11**, 4954-4961 (2019).

[213] X. Guo, L. Hao, Y. Yang, Y. Wang, Y. Lu, H. Yu, *J. Mater. Chem. A*. **7**, 25915–25924 (2019).

---

[214] V. Thangadurai and W. Weppner, *J. Power Sources*., **142**, 339–344 (2005).

[215] M. A. Limpert, T. B. Atwater, T. Hamann, G. Luh, G. T. Hitz, D. W. McOwen, E. D. Wachsman, *Chem. Mater.* , **34**, 9468-9478 (2022).

[216] S. Sharif-Asi, F.A. Soto, A. Nie, Y. Yuan, H. Asayesh-Ardakani, T. Foroozan, V. Yurkiv, B. Song, F. Mashayek, R. F. Klie, K. Amine, J. Lu, P. B. Balbuena, R. Shahbazain-Yassar, *Nano Lett.,* **17,** 2165-2171 (2017).

[217] S. Levasseur, M. Menetrier, Y. Shao-Horn, Gautier, A. Audemer, G. Demazeau, A. Largeteau, C. Delmas, *Chem. Mater.,* **15**, 348-354 (2003).

[218] N. Zhang, X. Long, Z. Wang, P. Yu, F. Han, J. Fu, G. Ren, Y. Wu, S. Zheng, W. Huang, C. Wang, H. Li, X. Liu, *ACS Appli. Energy Mater.,* **1**, 5968-5976 (2018).

[219] W. Luo, Y. Gong, Y. Zhu, K.K. Fu, J. Dia, S. Lacey, C. Wang, B. Liu, X. Han, Y. Mo, E.D. Wachsman, L. Hu, *J. Am. Chem. Soc.* **, 138**, 12258–12262 (2016).

[220] S.A. Delp, I. Borodin, M. Olugin, C.G. Eisner, J.L. Allen, T.R. Jow, *Electrochim. Acta.* **209**, 498-510 (2016).

[221] Gates-Rector, S.; Blanton, T. The Powder Diffraction File: A Quality Materials Characterization Database. Powder Diffr. **2019**, 34 (4), 352–360. https://doi.org/10.1017/S0885715619000812.

[222] P. Pasierv, S. Komornicki, M. Rokita, M. Rekas, *J. Mol. Struct.,* 596, 151-156 (2001).

[223] L. Truong and V. Thangadurai, *Inorg. Chem. ,* **51**, 1222-1224 (2012).

[224] G. Larraz,A. Orera, M.L. Sanjuán, *J. of Mater. Chem. A.* **, 1**, 11419 (2013).

[225] F. Tietz, T. Wegener, M. Gerhards, M. Giarola, G. Mariotto, *Solid State Ion.,* **230**, 77-82 (2013).

[226] M. Inaba, Y. Iriyama, Z. Oguymi, Y. Todzuka, A. Tasaka, *J. Raman Spectrosc*. **28**, 613-617 (1998).

[227] C. Julien, M. Camacho-Lopez, L. Escobar-Alarcon, E. Haro-Poniatowski, *Mater. Chem. Phys.* , **68**, 210-216 (2001). 2

[228] S. Chen, X. Hu, W. Bao, Z. Weng, Q. Yang, L. Nie, X. Zhang, J. Zhang, Y. Jiang, Y. Han, C. Wan, J. Xie, Y. Yu, W. Liu, *Cell Rep. Phys. Sci.* **, 2**, 100569 (2021).

[229] P. Wakudkar and A.V. Deshpande, *J. Phys. Chem. Solids.* **, 155**, 110092 (2021).

[230] N.C. Rosero-Navarro, T. Yamashita,A. Miura, M. Higuchi, K. Tadanaga, *J. Am. Ceram. Soc.*, **100**, 276-285 (2017).

[231] X. Yang, D. Kong, Z. Chen, Y. Sun, Y. Liu, *J. Mater. Sci.: Mater. Elec*.**, 29**, 1523-1529 (2017).

[232] X. Cheng, J. Huang, W. Qiang, B. Huang B. *Ceram. Int.* **, 46**, 3731-3737 (2019).

[233] JTS. Irvine, D.C. Sinclair, A.R. West, *Adv. Mater.,* **2**, 132-138 (1990).

[234] Y. Zhu, J. Connel, S. Tepavcevic, P.l. Zapol, R. Garcia-Mendez, N.J. Taylor, J. Sakamoto, B.J. Ingram, L.A. Curtiss, J.W. Freeland, D.D. Dong, N.M, Markovic, *Adv. Energy Mater.*, **9**, 1803440 (2019).

[235] T.H. Wan, M. Saccoccio, C. Chen, F. Ciucci, *Electrochim. Acta.* **,184**, 483-499 (2015).

[236] H. Zheng, G. Li, J. Liu, S. Wu, X. Zhang, S. Wu, H. Zhu, H. Liu, H. Duan, *Energy Stor. Mater.* **, 49**, 278-290 (2022).

---

[239] K. Mizushima, et al., *Solid State Ionics,* vol. 3-4, 1981, pp. 171–174., doi:10.1016/0167-2738(81)90077-1.

[240] A. Hirtenstein "Move Over Tesla, Europe's Building Its Own Battery Gigafactories." *Bloomberg.com*, Bloomberg, 22 May 2017, www.bloomberg.com/news/articles/2017-05-22/move-over-tesla-europe-s-building-its-own-battery-gigafactories

[241] J.F. Peters, et al. *Renewable and Sustainable Energy Reviews*, vol. 67, 2017, pp. 491–506., doi:10.1016/j.rser.2016.08.039.

[242] A. L Robinson, M. S. Whittingham. *MRS Bulletin*, vol. 41, no. 03, 2016, pp. 188–189., doi:10.1557/mrs.2016.30.

[243] J. Dewulf, et al. *Resources, Conservation and Recycling*, vol. 54, no. 4, 2010, pp. 229–234., doi:10.1016/j.resconrec.2009.08.004.

[244] R.S. Carmichael, (1989) *Practical Handbook of Physical Properties of Rocks and Minerals*

[245] S. Jang, et al. *Journal of Power Sources*, vol. 88, no. 2, 2000, pp. 274–277., doi:10.1016/s0378-7753(00)00374-8.

[246] F.L. Cras, et al. *Solid State Ionics*, vol. 106, no. 1-2, Jan. 1998, pp. 1–10., doi:10.1016/s0167-2738(97)00490-6.

[247] R.J. Gummow, et al. *Solid State Ionics*, vol. 69, no. 1, 1994, pp. 59–67., doi:10.1016/0167-2738(94)90450-2.

[248] J. Lu, K.S. Less, *Materials Technology*, Vol. 31, no. 11, 2016, pp. 628-641, doi: 10.1080/10667857.2016.1208957

[249] N. M. Hagh, G. G. Amatucci. *Journal of Power Sources*, vol. 256, 2014, pp. 457–469., doi:10.1016/j.jpowsour.2013.12.135.

[250] D. Andre , et al. *Journal of Materials Chemistry A*, vol. 3, no. 13, 2015, pp. 6709–6732., doi:10.1039/c5ta00361j.

[251] Y. Shin, A. Manthiram. *Chemistry of Materials*, vol. 15, no. 15, 2003, pp. 2954–2961., doi:10.1021/cm0341787.

[252] S. H. Oh, et al. *Journal of Alloys and Compounds*, vol. 452, no. 2, 2008, pp. 389–396., doi:10.1016/j.jallcom.2006.10.153.

[253] J. Song, et al. *Chemistry of Materials*, vol. 24, no. 15, 2012, pp. 3101–3109., doi:10.1021/cm301825h.

[254] M. Kunduraci., G. G. Amatucci. *Electrochimica Acta*, vol. 53, no. 12, 2008, pp. 4193–4199., doi:10.1016/j.electacta.2007.12.057.

[255] Y. Xiao, et al. *Electrochimica Acta*, vol. 311, 2019, pp. 170–177., doi:10.1016/j.electacta.2019.04.162.

[256] F. Luo, C. Wei, C. Zhang, H. Gao, J. Niu, W. Ma, Z. Peng, Y. Bai, Z. Zhang, *Journal of Energy Chemistry,* vol. 44, 2020, pp. 138-146., doi:10.1016/j.j.echem.2019.09.011

[257] C. Zuo, Z. Hu, R. Qi, J. Liu, C. Dong, K. Yang, W. Huang, C. Chen, Z. Song, Y. Yu, J. Zheng, F. Pan, *Advanced Energy Materials,* vol. 10, no. 34, 2020, pp. 2000363., doi:10.1002/aenm.202000363

[258] W. Che, X. Wan, D. Zhang, C. Chang, *Advanced Powder Technology,* vol. 32, no. 5, 2021, pp. 1802-1809., doi:10.1016/j.spt.2021.03.038

[259] L. Xiong, Y. Xu, T. Tao. J.B. Goodeneough, *Journal of Power Sources,* vol. 199, pp. 214-219., doi:10.1016/j/jpowersour/2011.09.062

[260] R. Chen, B. We., H. Li, M. Wang, C. Su, J. Guo, W. Bai, Z. Sa, *Vacuum*, vol. 187, 2021, pp. 110077, doi: 10.1016/j.vacuum.2021.110077

---

[261] S. Wang, H. Liu, M. Xiang, J. Guo, W. Bai, Bai, X. Liu, X. Su, *New Journal of Chemistry*, vol.44, 2020, pp 10569-10577., doi:10.1039/DONJ02190D

[262] Z. Cai, MY. Ma, X. Huang, X. Yan, Z. Z. Yu, C. Zhang, G. Song, Y. Xu, W. Cuje, W. Yang, *Journal of Energy Storage,* vol. 27, 2020, 101036, doi:10.1016/j.est.101036

[263] L. Wan, et al. *RSC Advances*, vol. 5, no. 33, 2015, pp. 25988–25997., doi:10.1039/c5ra03602j.

[264] D. Liu, et al. *RSC Adv.*, vol. 4, no. 1, 2014, pp. 154–167., doi:10.1039/c3ra45706k.

[265] J. Zhu, Q. Liu, M. Ziang, J. Guo, H. Bai, X. Liu, C. Su, W. Bai, *Ceramics International,* vol. 46, issue 10, part A, pp. 14516-14522, doi:10.1016/jceramint.2020.02.250

[266] P. Taddesse, C. Tsona, N. Murali, K. V. Babu, *Scientific African,* vol. 14, 2021, e00975, doi:10.1016/j.sciaf.2021.e00975

[267] O.O. Normakhmedov, O. A. Brylev, D. II. Petukhov, K.A. Kurilenko, T. L. Kulova, E. K. Tuseeva, A. M. Skundin, *Materials,*vol. 11, no. 17, 2018, pp. 1162, doi:10.3390/ma11071162

[268] F. Kong, et al. *Chemistry of Materials*, vol. 28, no. 19, 2016, pp. 6942–6952., doi:10.1021/acs.chemmater.6b02627.

[269] J. Dai, et al. *ACS Applied Materials & Interfaces*, vol. 8, no. 17, 2016, pp. 10820–10825., doi:10.1021/acsami.6b00288.

[270] JJ. Xao, H. Zhu, Z. Chen, Z. Peng, G. Hu, *Transactions of Nonferrous Metals Society of China*, vol. 16, no. 2, 2006, pp/ 467-472, doi:10.1015/s1003-6326(06)60080-0

[271] W. Wang, H. Hanzawa, K. Machida, K. Miyazaki, T. Abe, *Electrochemistry,* vol. 90, no. 1, 2022, pp. 017010, doi:10.5796/e;ectrochemistry.21-00119

[272] X. Zeng, J. Wu, Q. Hu, *Micro and Nano Letters,* vol. 11, no. 12, 2016, pp 789-791, doi:10.1049/mnl.2016.0445

[273] P. Arora, B.N. Popov, R.E. White, *Journal of Electrochemical Society*, vol. 145, no. 3, 1998, pp. 807-815.

[274] K. Tucchemiuk, D. Bondarev, G. G. Amatucci, G. Yushin, *Materials Today,* vol. 42, 2021, pp. 57-72., doi:10.1016/j.mattod.2020.09.027

[275] Z. Fu, D. McOwen, L. Zhang, Y. Gong, Y. Ren. J, E. Gritton, G. Godbey, J. Dai, L. Hu, E. Wachsman, *Journal of the American Ceramic Society,* 2020, doi:10.1111/jace.17177

[276] S.A. Delp, O. Borodin, et al., *Electrochmica Acta,* vol. 209, 2016, pp. 498-510, doi:10.1016/j.electa.2016.05.100

[277] R.D. Shannon. *Acta Crystallographica Section A*, vol. 32, no. 5, 1976, pp. 751–767., doi:10.1107/s0567739476001551.

[278] K. Mukai, T. Uyama, .. *ACS Omega,* vol. *2*, no. 8, 2017, pp. 5142-5149. doi:10.1021/acsomega.7b00948

[279] C.M. Julien, F Gemdron, A. Armdouni, M. Masscot, *Material Science and Engineering:B,* vol. 130, iss. 1-3, 2006, pp.41-48., doi:10.1016/j.mseb.2006.02.003

[280] Y. J. Wei, L. Y. Yan, C.Z. Wang, X. G. Xu, F. Wu, G. Chen, *Journal of Physical Chemistry B,* vol. 108, 2004, pp. 18547-18551., doi:10.1021/jp05479522

[281] K. Dokko, N. Abzuem, M. Mohaedmi, T. Itoh, I. Uchida, *Electrochemistry Communications,* vol. 6, iss. 4, 2004, pp. 384-388 doi:10.1016/j.elecom.2004.02.005

[282] G. B. Zhong, YY. Wang, Y. Q. Yu, C.H. Chen, *Journal of Power Sources,* vol. 205, 2021, pp. 385-392., doi:20.2016/j.jpowsour.2011.12.037

[283] Y. Chen, K. Xie, Y. Pan, C. Zheng, *Journal of Power Sources*, vol. 196, no. 15, 2011, pp. 6493-6497, doi:10.1016/j.jpowsour.2011.03.081

---

[284] R. Dizmiebja, M. Molenda, *Journal of Power Sources,* vol. 119-121, 2003, pp. 121-124, doi:10.1016/S0378-7753(03)00139-3

[285] P.J. Masset, *Journal of Thermal Analysis and Calorimetery*, vol. 96, pp. 439-441, doi:10.1007/s10973-008-9399-y

[286] Y. Huang, Y. Dong, S. Li, J. Lee, C. Wang, Z. Zhu, W. Xue, Y. Li, J. Li, *Advanced Energy Materials,* vo. 11, iss. 2, 2021, pp 2000997, doi:10.1012/aenm.202000997

[287] Y. Gao, K. Myrtle, M. Zhang, J.N. Reimers, J.R. Dahn, *Phys. Rev. B*, vol. 54, 1996, pp. 16670

[288] F. Bonino, S. Panero, D. Satolli, B. Scrosati, *Journal of Power Sources,* vol. 97, 2001, pp. 389-392.

[289] J. Liu, A. Manthiram. *The Journal of Physical Chemistry C*, vol. 113, no. 33, 2009, pp. 15073–15079., doi:10.1021/jp904276t

[290] H. Liu, R. Tian, Y. Jiang, X. Tun, J. Chen, L. Zhang, Y. Guo, H. Wang, K. Sun. W. Chu, *Electrochimica Acta,* vol. 180, 2015, pp. 138-146., doi:10.1016/j.electacta.2015.08/0123

[291] D.-W. Han, W.-H. Ryu, W.-K. Kim, J.-Y. Eom, H.-S. Kwon, *Journal of Physical Chemistry C,* vol. 117, no. 10, 2013, pp. 4913-4919, doi:10.1021/jp310011m

[292] T.B. Atwater, P. C. Taveras. "45th Power Sources Conference." Curran Associates, Inc., *45th Power Sources Conference 2012* , vol. 1, 2014, pp. 37–40.

[293] U. Westerhoff, K. Kurbach, F. Lienesch, M. Kurrat, *Energy Technology,* vol. 4, no. 12, 2016, pp. 1620-1630, doi:10.1002/ente.201600154

[294] L. Suo, et al., *Proceedings of the National Academy of Sciences of the the United States of America,* vol: 115, no:6, pp. 1156-1161, 2018, doi:10.1073/pnas.1712895

[295] D. Pritzl, A. Bumberger, M. Wetjen, J. Landesfeind, S. Solchenbach, H.A. Gasteiger, *Journal of Electrochemical Society,* vol:166, pp. A582, 2018, doi:10.1149/2.0451904jes

Chapter 5 References

[296] Wood, M.; Gao, X.; Shi, R.; Heo, T.W.; Espitia, J. A.; Duoss, E.B.; Wood, B.C.; Ye, J. Exploring the relationship between solvent assisted ball milling, particle size, and sintering temperature in garnet-type solid electrolytes. *J. Power Sources.* **2022**, 484, 229252. DOI:10.1016/j.jpowsour.2020.229252

[297] Gu, Y.; She, S.; Hong, Z.; Huang, Y.; Wu, Y. Enabling lithium metal battery with flexible polymer/garnet type solid oxide composite electrolyte. *Solid State Ion.* **2021,** 368, 115710. DOI: 10.1016/j.ssi.2021.115710

[298] Yu, S.; Schmidt, R.D.; Garcia-Mendez, R.; Herbert, E.; Dudney, N. K., Wolfenstein, J.B.; Sakamoto, J.; Siegel, D. J. Elastic Properties of the SSolid Electrolyte $Li_7La_3Zr_2O_{12}$ (LLZO). *Chem. Mater.* **2016,** 28, 197-206. DOI:10.1021/acs.chemmater.5b02854

[299] Inada, R.; Yasuda, S.; Tojo, M.; Tsuritani, K.; Tojo, T.; Sakurai, Y. Development of Lithium-Stuffed Garnet-Type Oxide Solid Electrolytes with High Ionic Conductivity for Application to All-Solid-State Batteries. *Front. Energy Res.* **2016,** 4. DOI:10.3389/fenrg.2016.00028

[300] Xu, L.; Li, G.; Guan, J.; Wang, L.; Chen, J.; Zheng, J. Garnet-doped composite polymer electrolyte with high ionic conductivity for dendrite free lithium batteries. *J. Energy Storage.* **2019,** 24, 100767, DOI:10.1016/j.est.2019.110767

[301] Hitz, G.T.; McOwen, D. W.; Zhang, L.; Ma, Z.; Fu, Z.; Wen, Y.; Gong, Y.; Dai, J.; Hamann, T.R.; Hu, L.; Wachsman, E.D. High rate lithium cycling in scalable trilayer Li-garnet-electrolyte architecture. *Mater. Today Commun..* **2018,** 22, 50-57, DOI:10.1016.2018.04.004

---

[302] Sastre, J.; Futscher, M.H.; Pompizi, L.; Aribia, A.; Priebe, A.; Overbeck, J.; Stiefel, M.; Tiwari, A.N.; Romanyuk, J. Blocking lithium dendrite growth in solid-state batteries with an ultrathin amorphous Li-La-Zr-O solid electrolyte. *Communications Materials.* **2021,** 2, doi:10.1038/s43246-012-00177-4

[303] Frankel, T.C. Cobalt mining for lithium ion batteries has a high human cost. *Washington Post,* September 30, 2016, https://www.washingtonpost.com/graphics/business/batteries/congo-cobalt-mining-for-lithium-ion-battery/

[304] Wentker, M.; Greendwood, M.; Leker, J. A bottom-up approach to lithium-ion battery cost modeling with a focus on cathode active materials. *Energies,* **2019**, 12, 504, DOI:10.3390/en12030504

[305] Miara, L.; Windmuller, A,; Tsai, C.-L.; Richards, W.D.; Ma, Q.; Uhlenbruck, S.; Guillon, O.; Ceder, G. About the compatibility between high voltage spinel cathode materials and solid oxide electrolytes as a function of temperature. *ACS Appl. Mater. Interfaces.* **2016,** 8, 26842-26850, DOI:10.1021/acsami.6b09059

[306] Yu, C.-Y.; Choi, J.; Han, J.; Lee, E.; Kim, J.-H. Phase stability of garnet solid-electrolyte interfacing with various cathodes in all-solid state batteries. *J. Electrochem. Soc.* **2022**, 169, 020520, DOI:10.1149/1945-7111/ac4e5b

[307] Fey, G. T.-K.; Lin, Y.Y.; Kumar, T.P. Enhanced cyclability and thermal stability of LiCoO2 coated with cobalt oxides. *Surf. Coat. Technol.* **2005**, 191, 68-75, DOI:10.1016/j.surfcoat.2004.06.007

[308] Yi, T.; Dai, C.; Gao, K.; Hu, X. Effects of synthetic parameters on structure and electrochemical performance of spinel lithium manganese oxide by citric acid-assisted sol-gel method. *J. Alloys and Compd.* **2006,** 425, 343-347, DOI:10.1016/j.jallcom.2006.01.054

[309] Rezvani, S.J.; Parmar, R.; Maroni, F.; Nobili, F.; Di Cicco, A.; Gunnella, R. Does Alumina Coating Alter the Solid Permeable Interphase Dynamics in $LiMn_2O_4$ Cathodes? *J. Phys. Chem. C.* **2020,** 124, 26670-26677, DOI:10.1021/acs.jpcc.0c08449

[310] Zhou, H.-M.; Zhu, Y.-H.; Li, J.; Sun, W.-J.; Liu, Z.Z. Electrochemical performance of Al_2O_3 pre-coated spinel $LiMn_2O_4$. *Rare Met.* **2019,** 38, 128-135, DOI: 10.1007/s12598-014-0418-9

[311] Thackeray, M.M.; Mansuetto, M.E.; Dees, D.W.; Vissers, D.R. The Thermal Stability of lithium-manganese-oxide spinel phases. *Mater. Res. Bull.* **1996,** 31, 133-140, DOI:10.1016/0025-5408(95)00190-5

[312] Lee, H.R.; Lee, B.; Chung, K. Y.; Cho, B.Y.; Lee, W.Y.; Oh, S.H. Scalable synthesis and electrochemical investigations of fluorine-doped lithium manganese spinel oxide. *Electrochim. Acta.* **2014,** 136, 396-403, DOI:10.1016/j.electacta.2014.05.106

[313] Li, H.;Luo, Y.; Xie, J.; Zhang, Q.; Yan, L. Effect of lithium and fluorine doping on the electrochemical and thermal stability of $LiNi_{0.5}Mn_{1.5}O_4$ spinel cathode materials. *J. Alloys Compd.* **2015,** 639, 346-351, DOI:10.1016/j.jallcom.2015.03.114

[314] Nguyen, C.C.; Bae, Y. S.; Lee, K.-H.; Song, J.-W,; Min, J.-H.; Kim, J.-S.; Paik, Y. Roles of Fluorine-doping in Enhancing Intial Cycle Efficiency and SEI Formation of Li-, Al-cosubstituted Spinel Battery Cathodes. *Bull. Korean Chem. Soc.* **2013,** 34, 384-388, DOI:10.5012/bkcs.2013.34.2.384

[315] Bakierska, M.; Molenda, M.; Dziembaj, R. Optimization of Sulphur content in $LiMn_2O_{4-y}S_y$ spinels as cathode materials for lithium-ion batteries. *Procedia Eng.* **2014,** 98, 20-27, DOI:10.1016/j.proeng.2014.12.482

---

[316] Bakierska, M.; Swietoslawski, M.; Dziembaj, R.; Molenda, M. Nature of Electrochemical Properties of Sulphur Substituted $LiMn_2O_4$ Spinel Cathode Material Studied by Electrochemical Impedance Spectroscopy. *Mater.* **2016,** 9, 696, DOI:10.3390/ma9080696

[317] Molenda, M.; Bakierska, M.; Majda, D.; Swietoslawski,M.; Dziembaj, R. Structural and electrochemical characterization of Sulphur-doped lithium manganese spinel cathode materials for lithium ion batteries. *Solid State Ion.* **2015,** 272, 127-132, DOI:10.1016/j.ssi.2015.01.012

[318] Larraz, G.; Orera, A.; Sanjuán, M.L. Cubic phases of garnet-type $Li_7La_3Zr_2O_{12}$: the role of hydration. *J. Mat. Chem. A.* **2013,** 1, 11419-11428, doi:10.1039/c3ta11996c

[319] Tietz, F.; Wegener, T.; Gerhards, M.; Giarola, M.; Mariotto, G. Synthesis and Raman micro-spectroscopy investigation of $Li_7La_3Zr_2O_{12}$. *Solid State Ion.* **2013,** 230, 77-82. doi:10.1016/j.ssi.2012.10.021

[320] Xu, Z.; He, L.; Zhong, X.; Zhang, J.; Chen, X.; Ma, H.; Cao, X. Effects of Y_2O_3 addition on the phase evolution and thermophysical properties of lanthanum zirconate. *J. Alloys Compd.* **2009**, 480, 220-224. doi: 10.1016/j.jallcom.2009.02.048

[321] Boobalan, K.; Varun, A.; Vijayaraghavan, R.; Chidambaram, K.; Kamachi Mudali, U. Facile, scalable synthesis of nanocrystalline calcium zirconate by the solution combustion method. *Ceram. Int.* 40, 5781-5786, (2014). doi: 10.1016/j.ceramint.2013.11.017

[322] Brewer, L.; Margave, J. The Vapor Pressures of Lithium and Sodium Hydroxides. *J. Phys. Chem.* **1955**, 59, 421-425. doi:10.1021/j150527a010

[323] Schnell, J.; Knozer, H.; Imbsweiler, A.J.; Reinhart, G. Solid versus Liquid-A Bottom-Up Calculation Model to Analyze the Manufacturing Cost of Future High-Energy Batteries. *Energy Technol.*. **2020**; 8, 1901237. doi:10.1002/ente.201901237

[324] Li, Y.; Wang, Z.; Li, C.; Cao, Y.; Guom, X. Densification and ionic-conduction improvement of lithium garnet solid electrolytes by flowing oxygen sintering. *J. Power Sources*. **2014**, 248, 642–646. doi:10.1016/j.jpowsour.2013.09.140

[325] Dobrestov, E.A.; Mateyshina, Y.G.; Uvarov, N.F. Influence of lithium oxide excess and alumina on grain boundary resistance of $Li_{6.75}La_3Zr_{1.75}Nb_{0.25}O_{12}$ solid electrolyte. *Solid State Ion.* **2017**, 299, 55-59. doi:10.1016/j.ssi.2016.09.014

[326] Johnson, R.A.; Yi, E.; Shen, F.; Tucker, M.C. Optimization of Tape Casting for Fabrication of $Li_{6.25}Al_{0.25}La_3Zr_2O_{12}$ Sheets. *Energy Fuels.* **2021**, 35, 8982-8990. doi:10.1021/acs.energyfuels.1c00566

[327] Xu, S.; McOwen, D.W.; Wang, C.; Zhang, L.; Luo, W.; Chen, C.; Li, Y.; Gong, Y.; Dia, J.; Kuang, Y. et al. Three-dimensional, solid-state mixed electron-ion conductive framework for lithium metal anode. *Nano Lett*. **2018**, 18, 3926-3933. doi:10.1021/acs.nanolett.8b012

[328] Huang, Z.; Chen, L.; Huang, B.; Xu, B.; Shao, G.; Wang, H.; Li, Y.; Wang. C. Enhanced Performance of $Li_{6.4}La_3Zr_{1.4}Ta_{0.6}O_{12}$ Solid Electrolyte by the Regulation of Grain and Grain Boundary Phases. *ACS Appl. Mater. Interfaces*. **2020**, 12, 56118-56125. doi:10.1021/acsami.0c18674

[329] Bordia, R.K.; Kang, S.L.; Olevsky, E.A. Current understanding and future research directions at the onset of the next century of sintering science and technology. *J. Am. Ceram. Soc*. **2017**, 100, 2134-2352. doi: 10.1111/jace.14919

[330] Gates-Rector, S.; Blanton, T. The Powder Diffraction File: A Quality Materials Characterization Database. Powder Diffr. **2019**, 34 (4), 352–360. https://doi.org/10.1017/S0885715619000812.

[331] Wang, L., Chen, B., Ma, J., Cui, G., Chen, L. (2018). *Chemical Society Reviews, 47*(17), 6505-6602. doi:10.1039/c8cs00322j